HAL
open science

Observation of a BEH-like boson decaying into two photons with the ATLAS detector at the LHC

Nansi Andari

To cite this version:

Nansi Andari. Observation of a BEH-like boson decaying into two photons with the ATLAS detector at the LHC. Other [cond-mat.other]. Université Paris Sud - Paris XI, 2012. English. NNT : 2012PA112191 . tel-00744847

HAL Id: tel-00744847

https://theses.hal.science/tel-00744847

Submitted on 24 Oct 2012

HAL is a multi-disciplinary open access archive for the deposit and dissemination of scientific research documents, whether they are published or not. The documents may come from teaching and research institutions in France or abroad, or from public or private research centers.

L'archive ouverte pluridisciplinaire **HAL**, est destinée au dépôt et à la diffusion de documents scientifiques de niveau recherche, publiés ou non, émanant des établissements d'enseignement et de recherche français ou étrangers, des laboratoires publics ou privés.

LAL 12-300

UNIVERSITE PARIS-SUD XI

THESE DE DOCTORAT

pour obtenir le grade de

Docteur ès sciences

Spécialité: Physique des Particules

Observation of a BEH-like boson decaying into two photons with the ATLAS detector at the LHC

Soutenue le 26/09/2012
par

Nansi ANDARI

Devant la Comission d'examen composée de MM.:

Glen COWAN	*Rapporteur*
François ENGLERT	
Louis FAYARD	*Directeur de Thèse*
Achille STOCCHI	*Président du Jury*
Guillaume UNAL	
Patrice VERDIER	*Rapporteur*
Tejinder VIRDEE	

A vous, papa et maman.
A toi, ma soeur.

Abstract:

In this thesis, I show my contribution to the observation of a new boson at the Large Hadron Collider with the ATLAS detector in the diphoton decay channel. This boson is compatible with the long-searched scalar boson of the Standard Model and has a mass of 126.0 ± 0.4 (stat) ± 0.4 (sys) GeV obtained when combining the decay channels $\gamma\gamma$ and ZZ. The data used were collected in the ATLAS experiment during 2011 with a center-of-mass energy $\sqrt{s} = 7$ TeV and during the first three months of the 2012 run with a center-of-mass energy of $\sqrt{s} = 8$ TeV. The total corresponding luminosity is ~ 10 fb^{-1}. The observed excess has a local significance of 4.5σ in the $\gamma\gamma$ channel and has a significance of 5.9σ when combining all the channels used in the analysis. Moreover, diverse contributions to the $H \to \gamma\gamma$ analyses of the data from 2009 to 2012 are also shown.

Keywords:

LHC - ATLAS - BEH boson - Standard Model - photon - electromagnetic calorimeter- significance - limits - energy - luminosity - mass.

Résumé:

Dans cette thèse, je présente ma contribution à l'observation d'un nouveau boson au LHC avec le détecteur ATLAS dans le canal de désintégration en deux photons. Ce boson est compatible avec le boson scalaire du Modèle Standard longtemps recherché et a une masse de 126.0 ± 0.4 (stat) ± 0.4 (sys) GeV obtenue en combinant les canaux $\gamma\gamma$ et ZZ. Les données utilisées sont celles collectées par l'expérience ATLAS durant l'année 2011 avec une énergie de centre de masse $\sqrt{s} = 7$ TeV et durant les trois premiers mois du run en 2012 avec une énergie de centre de masse $\sqrt{s} = 8$ TeV. La luminosité totale correspondante est de ~ 10 fb^{-1}. L'excès observé a une significance locale de 4.5σ dans le canal $\gamma\gamma$ et de 5.9σ en combinant tous les canaux analysés. De même, diverses contributions aux analyses des données, dans le canal $H \to \gamma\gamma$, depuis l'année 2009 jusqu'en 2012 sont aussi montrées.

Mots-clés:

LHC - ATLAS - BEH boson - Modèle Standard - photon - calorimètre électromagnétique - significance - limites - énergie - luminosité - masse.

Contents

Introduction **v**

1 Spontaneous Symmetry Breaking **1**
1.1 Historical Survey . . . 1
1.2 Electroweak theory . . . 5
1.3 Limits on the scalar boson mass . . . 12
1.3.1 Theoretical limits . . . 12
1.3.2 Experimental limits . . . 15
1.4 SM Scalar Boson Searches at LHC . . . 20
1.4.1 SM Scalar Boson Production . . . 20
1.4.2 SM Scalar Boson Decays . . . 24
1.5 Beyond the SM . . . 28

2 Statistical Methods for LHC **33**
2.1 Test Statistic . . . 33
2.2 χ^2 approximation . . . 39
2.3 Asymptotic formulae . . . 42
2.4 Profiling . . . 46
2.5 Look-elsewhere effect . . . 47
2.6 Energy scale uncertainties . . . 49

3 ATLAS Detector **51**
3.1 LHC . . . 51
3.1.1 LHC machine . . . 51
3.1.2 LHC running . . . 53
3.1.3 LHC performances . . . 53
3.2 ATLAS Detector . . . 57
3.2.1 The ATLAS Coordinate System . . . 58
3.2.2 The Inner Detector . . . 60
3.2.3 Calorimeters . . . 65
3.3 CMS Detector . . . 74

4 Calibration of electrons and photons **77**
4.1 LAr Calorimeter electronic calibration . . . 77
4.1.1 Electronic readout of the ATLAS LAr Calorimeter . . . 77
4.1.2 Optimal Filtering . . . 80
4.1.3 Autocorrelation matrix . . . 82
4.1.4 Energy reconstruction . . . 86
4.2 MC-based calibration . . . 86

4.2.1 Birks' Law 89
4.3 In-situ calibration 92

5 Photon Performance **101**
5.1 Photon Reconstruction 101
5.2 Photon Identification 102
5.2.1 Discriminating variables 102
5.2.2 Loose and Tight Selections 106
5.3 Photon Isolation 107
5.4 Purity of single prompt photons 112
5.5 Purity of single converted photons 114
5.6 Purity in $H \to \gamma\gamma$ 117
5.7 Photon efficiency 119
5.7.1 Fudge Factors 119
5.7.2 Photon efficiency and uncertainty 120

6 $H \to \gamma\gamma$ Analysis **127**
6.1 Analysis of 2010 data 127
6.1.1 Aspen 2011 127
6.1.2 Moriond 2011 131
6.2 Analysis of 2011 data 136
6.2.1 PLHC 2011 136
6.2.2 EPS 2011 142
6.2.3 Council 2011 152
6.3 Improved Analysis of 2011 data 156
6.3.1 Improved selections and corrections 157
6.3.2 Event categorization 158
6.4 Analysis of 2012 data 165
6.5 Conclusion 168

7 Observation of a BEH-like particle **173**
7.1 Evolution of the $H \to \gamma\gamma$ search 173
7.2 BEH-like particle decaying to a pair of photons 178
7.2.1 Statistical procedure 178
7.2.2 Background modeling 184
7.2.3 Observation Results 185
7.3 BEH-like particle in the combined channels 198

8 ATLAS-CMS comparison **209**
8.1 Observation of the BEH-like particle decaying into a pair of photons with the CMS detector 209
8.2 ATLAS-CMS comparison in the $H \to \gamma\gamma$ channel 214
8.3 ATLAS-CMS comparison in the combined channels 216

Conclusion i

Bibliography iii

Appendix xxi

Remerciements xxv

Introduction

One of the enigmas searched for at the Large Hadron Collider (LHC) is the only remaining unobserved particle predicted by the Standard Model, the scalar boson. The search for the scalar boson is one of the main topics in Particle Physics nowadays. Thanks to the outstanding performance of the LHC, important progress in this search has been made from the beginning of the data taking in December 2009. In July 2012, CERN announced the discovery of a new boson at the LHC with a mass around 126 GeV, compatible with the long-searched for scalar boson. In this thesis, I will show my own contribution to the search and the observation of this new boson within the ATLAS detector in the channel when it decays into a pair of photons.

A brief review of the history of the spontaneous symmetry breaking mechanism is presented in Chapter 1. The derivation of the electroweak theory is recalled. The theoretical and experimental constraints on the mass of the predicted scalar boson are discussed. The Standard Model scalar boson production and decay at the LHC are summarized. Finally, a brief summary of what is beyond the Standard Model is given.

Chapter 2 presents the statistical methods used at the LHC. A description of the test statistic used for establishing a discovery or setting an exclusion limit is given. I discuss my personal contribution in the validation of the asymptotic approximation down to low luminosities by a redefinition of the test statistic. The asymptotic formulae used are recalled. The look-elsewhere effect is briefly presented together with the impact of the energy scale systematic on the validity of the asymptotic approximations.

Chapter 3 briefly describes the LHC machine. It gives a review of its running in the past and some possible thoughts for the future. The luminosity and the pile-up are defined and given for the 2011 and 2012 runs. The ATLAS detector is then detailed with its different parts focusing mainly on the description of the inner detector and the electromagnetic calorimeter. Finally, the CMS detector is briefly described.

Chapter 4 explains the calibration of the electrons and photons in ATLAS in three different steps: the electronic calibration, the Monte Carlo-based calibration and the in-situ calibration. My personal contribution in a comparison of the noise autocorrelation matrix for different pile-up configurations

and different regions of the detector is discussed. Moreover, the study on understanding the discrepancy between data (collected in 2010) and Monte Carlo in the presampler at high energies is described together with the definition of Birks' law.

Chapter 5 describes the reconstruction and the identification of the photons. The discriminating variables and the cuts used to identify the photons are briefly recalled and compared between different analyses. The photon isolation is then described, recalling the difference between the track and calorimetric isolation together with the evolution of the methods used in the analyses. The first measurement of the purity of single prompt photons is recalled. My personal contribution to the purity of single converted photons using the 2010 dataset is shown. The diphoton purity in the $H \rightarrow \gamma\gamma$ analysis estimated for the full 2011 dataset corresponding to a luminosity of 4.8 fb^{-1} and a 2012 dataset with a luminosity of 5.9 fb^{-1} is summarized. Finally, the photon efficiency measurement is discussed. The method to correct for discrepancies in shower shape variables between data and Monte Carlo is explained. The photon efficiency and its uncertainty are compared between 2011 and 2012.

Chapter 6 presents the evolution of the analyses in the $H \rightarrow \gamma\gamma$ channel from 2010 to 2012, starting with Aspen 2010. The systematic uncertainties on the signal yield and on the mass resolution are detailed. The signal and background modeling are defined. The number of expected signal yields and the mass resolution are given for the various analyses. The improved 2011 analysis and the 2012 analysis are detailed.

Chapter 7 recalls the results for the $H \rightarrow \gamma\gamma$ search from 2010 to 2012. The results presented at ICHEP 2012 are discussed. The statistical procedure used for this analysis is given with a detailed likelihood. An excess over the background is observed in this channel with a local significance of 4.5σ at a mass of 126.5 GeV while the expected significance is about 2.5σ. Finally, the results for the combined channels are briefly summarized. The maximum observed local significance is 5.9σ for a mass of 126.5 GeV while the expected significance is 4.9σ.

Chapter 8 summarizes briefly the $H \rightarrow \gamma\gamma$ search within the CMS experiment. Main differences between ATLAS and CMS analyses and results are derived. The differences in results for the combined channels are also given.

Chapter 1

Spontaneous Symmetry Breaking

Contents

1.1 Historical Survey **1**

1.2 Electroweak theory **5**

1.3 Limits on the scalar boson mass **12**

1.3.1 Theoretical limits 12

1.3.2 Experimental limits 15

1.4 SM Scalar Boson Searches at LHC **20**

1.4.1 SM Scalar Boson Production 20

1.4.2 SM Scalar Boson Decays 24

1.5 Beyond the SM **28**

1.1 Historical Survey

The human mind has persistently been fascinated by the observation of symmetries which manifest themselves through various natural phenomena. In particular, physical phenomena offer several famous examples, to such an extent that it has become common among physicists to try and characterize new phenomena in terms of some symmetry. Correspondingly, the concept of symmetry has generated several branches of mathematics, in particular for what concerns us here, group theory. In the twentieth century, the Galilean symmetry discovered in mechanics has undergone a spectacular evolution through a careful reinvestigation of the concept of simultaneity of events, which has led to Einstein's theory of special relativity. There, the invariance of physical laws under their observation in different regions of space, at different times is characterized by the Lorentz symmetry group. Following the evolution in the formulation of the laws of mechanics, through a variational principle (Lagrangian and Hamiltonian mechanics), it was observed by Emmy Noether that to each continuous symmetry there corresponds a conserved quantity: e.g the invariance under space and time translations entails the conservation of momentum and energy. The Lagrangian framework of classical mechanics, together with its Hamiltonian companion, have proved essential in the

discovery and formulation of quantum mechanics which describes atomic, nuclear and subnuclear physics. In these realms, many other symmetries were discovered, besides those associated with the homogeneity of space and time. These symmetries were called "internal" symmetries (e.g U(1) electromagnetic symmetry leading to charge conservation, isotopic spin symmetry). In Lagrangian field theories, e.g electrodynamics of charged scalar or Dirac spinor fields, Noether's theorem produces conserved or partially conserved currents depending whether the symmetries are exact or approximate.

It is worthwile pointing out a distinction between two classes of symmetries that have been known in particle physics: *physical* symmetries which generate observable effects and *formal* symmetries which act on fields not all of which are observable. Gauge symmetries, i.e symmetries which depend on the position in space and time (local symmetries), are of the latter type. The prototype is electrodynamics: at the classical level the system of Maxwell and Maxwell-Lorentz equations can be written in terms of the observable Maxwell fields $\{F_{\mu\nu}\} = \{\vec{E}, \vec{H}\}$, the particle positions and velocities. Whereas it is technically helpful to parametrize the field strength $\{F_{\mu\nu}\}$ in terms of the unobservable potential vector A_μ, $(F_{\mu\nu} = \partial_\mu A_\nu - \partial_\nu A_\mu)$, it is not in principle necessary. The quantum analog, as it is known nowadays, associates fields to particles in such a way that the introduction of the potential vector becomes necessary. The dynamics of the charged fields and the potential vector, described in terms of a local field interaction gives sensible physical results provided it is invariant under the U(1) gauge group. Whereas the principle of gauge invariance attached to the choice of unphysical field variables was recognized by Weyl, it was later extended to compact Lie non-Abelian groups by Yang and Mills [1] in 1954. Gauge invariance is therefore not a real physical symmetry by itself but its introduction into the theory does lead to a meaningful "renormalizable" quantum field theory (i.e computable in terms of a finite number of parameters- masses, coupling constants).

Furthermore, physicists have shown that symmetries of physical laws could be broken explicitly or spontaneously. This thesis will be focused namely on the class of spontaneous symmetry breaking (SSB). There, it happens that the Lagrangian is invariant under a given symmetry while the physical fundamental state, the so-called "vacuum" state, is not. The notion of SSB originates from condensed matter and statistical physics although the name of SSB was introduced later by Baker and Glashow [2]. A canonical example was already provided by Heisenberg in 1928 [3] for a ferromagnet where below the Curie temperature (T_C) the ground state is a completely ordered configuration in which all dipoles are aligned in some arbitrary direction, breaking spontaneously the symmetry of rotation O(3) down to O(2). Later Ginzburg-Landau (GL) [4] introduced the notion of order parameter to describe phase transitions in superconducting materials, and the "mexican hat" form of the

free energy for temperatures below T_C.

The concept of SSB was transferred from condensed matter physics to quantum field theory for elementary particles in 1960's by Y. Nambu (in [5, 6] and with G. Jona-Lasinio in [7, 8]). Nambu was inspired by the microscopic theory of superconductivity by J. Bardeen, L. Cooper and R. Schrieffer [9], the so-called BCS theory where the electromagnetic (EM) gauge invariance was found to be spontaneously broken. Nambu put forward a scheme for the theory of the strong interactions. The scheme was motivated by the observation of an interesting analogy between the properties of Dirac particles and quasi-particle excitations of the BCS theory. In addition to being spontaneously broken, Nambu suggested that the global chiral symmetry is not exact and thus that the axial current is an approximately conserved quantity in the limit $q^2 >> m_\pi^2$, where m_π is the mass of the pion. The nucleon mass is generated by a SSB of the chiral symmetry, and the pion is the corresponding pseudoscalar boson which should become massless in the limit of exact conservation.

In 1960, J. Goldstone showed in [10] that the appearance of massless bosons as a consequence of spontaneously broken continuous global symmetry is a general theorem. He gave the example of a simple model using a complex scalar field, $\phi = (\phi_1 + i\phi_2)/\sqrt{2}$, with U(1) symmetry. The Lagrangian

$$L = \partial^\mu \phi^* \partial_\mu \phi - V(\phi^*\phi) \tag{1.1}$$

with

$$V(\phi^*\phi) = \mu^2 \phi^*\phi + \frac{\lambda}{6}(\phi^*\phi)^2, \quad \lambda > 0 \ \text{ and } \ \mu^2 < 0, \tag{1.2}$$

is invariant under $\phi \to e^{i\alpha}\phi$.

The potential $V(\phi^*\phi)$ has the "mexican hat" form and it has an infinite number of minima. Thus, the theory has several vacuum states, but there is a "superselection rule" which allows the choice of one of them. The infinitesemal oscillations (χ) around one of these minima are quantized using the canonical transformation:

$$\phi = \phi' + \chi, \quad |\chi|^2 = -\frac{3\mu^2}{\lambda}. \tag{1.3}$$

Fixing the undetermined phase of χ breaks the symmetry. With χ real, the new Lagrangian becomes:

$$L = \frac{1}{2}(\partial^\mu \phi_1' \partial_\mu \phi_1' + 2\mu^2 \phi_1'^2) + \frac{1}{2}\partial^\mu \phi_2' \partial_\mu \phi_2' - \frac{\lambda\chi}{6}\phi_1'(\phi_1'^2 + \phi_2'^2) - \frac{\lambda}{24}(\phi_1'^2 + \phi_2'^2)^2. \tag{1.4}$$

The particle corresponding to the ϕ_2' field has zero mass. This corresponds to the so-called Nambu-Goldstone (or Goldstone) boson. In addition, it is interesting to note the appearance of a new massive particle ϕ_1' corresponding to oscillations in the direction of χ which has a mass of $\sqrt{-2\mu^2}$. In the hadronic world, described for instance by QCD (quantum chromodynamics)

where the pion is essentially the Goldstone boson of a chiral symmetry, the massive particle turns out to be the so-called sigma meson or $f_0(600)$, thus corresponding to a physical state. The general Goldstone theorem was proved by Goldstone, Salam and Weinberg the following year in [11].

The prediction of new massless particles, which were ruled out experimentally, seemed to close off the opportunities provided by SSB. Motivated by this disappointment, R. Brout and F. Englert [12], P. Higgs [13, 14], and G. Guralnik, D. Hagen and T. Kibble [15] were all led to look for an exception to Goldstone's theorem. The exception was found to be in theories where both SSB and local gauge invariance are included. This was actually argued earlier by P. Anderson [16], on the basis of the non-relativistic BCS theory, the scalar zero-mass excitations of a superconducting neutral Fermi gas become longitudinal plasmon modes of finite mass when the gas is charged. Note that the idea that gauge fields could acquire a mass through interactions seems to originate from Schwinger [17, 18].

Englert and Brout, in 1964, first discovered the phenomenon when trying to understand whether the strong interactions might be mediated by massive gauge vector meson i.e Yang-Mills field. They found that breaking the symmetry in a non Abelian Yang-Mills theory don't lead to massless Nambu-Goldstone bosons, but rather to massive vector gauge bosons. Almost at the same time in 1964, Higgs argued that the presence of gauge fields allows avoiding massless bosons. He gave the example of Abelian QED-like case in a linear approximation and a specific non-covariant gauge and extended it to the non-Abelian case based on SU(3). In the same year, Guralnik, Hagen and Kibble showed that after SSB, the vector field becomes massive and the Goldstone boson decouples. A more complete understanding was presented by Higgs in 1965 [19] where he found a gauge transformation in the abelian case which transforms the initial Lagrangian into a Lagrangian with only physical degrees of freedom, a massive scalar boson and massive vector fields, explicitly showing the presence of a new massive scalar (with a mass of $\sqrt{-2\mu^2}$). It was generalized to the non-Abelian case in 1967 by Kibble [20]. The above described phenomenon was baptized Brout-Englert-Higgs (BEH) mechanism and the scalar boson is called BEH boson or more commonly "Higgs boson".

It is only in 1967 that the BEH mechanism was applied to the weak leptonic interactions by S. Weinberg [21] and in 1968 by A. Salam [22] independently. The gauge symmetry group $SU(2) \times U(1)$ was chosen to describe weak and electromagnetic interactions, based on earlier work by S. Glashow [23] and by Salam and Ward [24]. Remarkably, this model unifies the weak interactions with electromagnetism in a single larger gauge theory called the electroweak (EW) theory. Three of the gauge symmetries of $SU(2) \times U(1)$ are spontaneously broken, creating three Goldstone bosons. A massless vector boson has two physical polarization states whereas a massive vector boson

has three physical polarization states. The gauge bosons acquire three extra degrees of freedom by "eating" the Goldstone bosons. By analogy with the Goldstone theorem, the BEH boson is formed by the transverse excitations around the minima of the potential $V(\phi^*\phi)$. A detailed calculation for the electroweak theory will be presented in section 1.2. The spontaneous breakdown of $SU(2) \times U(1)$ to the $U(1)$ of ordinary EM gauge invariance give masses to three of the four vector gauge bosons: the charged bosons $W^{\pm}$, and a neutral boson Z. The fourth boson would automatically remain massless, and is identified as the photon. The quantization of non-abelian gauge theories was finally achieved in 1967 by Faddeev and Popov [25] and in 1971 't Hooft showed [26, 27] that the electroweak theory is renormalizable. The proof was subsequently completed by Lee and Zinn-Justin [28, 29, 30] and by 't Hooft and Veltman [31], and later in an elegant formalism by Becchi, Rouet and Stora [32, 33, 34] and by Tyutin [35]. Following the introduction of quarks (especially the fourth quark by Glashow, Iliopoulos and Maiani [36]) and the cancellation of the triangle anomalies (Bouchiat, Iliopoulos and Meyer [37]), the Standard Model was defined. Afterwards, many experiments were aiming to understand and to confirm the Standard Model. I only quote here the discovery at CERN of the neutral currents by the Gargamelle experiment [38, 39, 40], the measurement at SLAC of parity non-conservation in inelastic electron scattering in 1978 [41] and the discovery at CERN by UA1 and UA2 of the W [42, 43] and Z [44, 45] bosons. More details on the history of the Standard Model making can be found in [46, 47, 48, 49].

1.2 Electroweak theory

Let us begin with a simple Lagrangian invariant under an $SO(4)$ symmetry group, which is equivalent to $SU(2) \times SU(2)/Z_2$.

$$L = \partial^\mu \phi^\dagger \partial_\mu \phi - V(\phi^\dagger \phi) \tag{1.5}$$

with

$$V(\phi^\dagger \phi) = \mu^2 \phi^\dagger \phi + \lambda(\phi^\dagger \phi)^2; \quad \lambda > 0 \ \text{ and } \ \mu^2 < 0, \tag{1.6}$$

where the scalar field is represented by a doublet of complex fields with four real components.

$$\phi = \frac{1}{\sqrt{2}} \begin{pmatrix} \phi_1 + i\phi_2 \\ \phi_3 + i\phi_4 \end{pmatrix} \tag{1.7}$$

The particularity of this potential $V(\phi^\dagger \phi)$ is that the mass term $\mu^2 \phi^\dagger \phi$ has a negative sign, thus there is a nonzero field configuration with lowest potential. The vacuum configurations of the system are determined as solutions of the equations of motion, i.e when the potential is at its minimum, equivalently

when:

$$\frac{\partial V}{\partial \phi} = 2\mu^2|\phi| + 4\lambda|\phi|^3 = 0. \tag{1.8}$$

The non-trivial solutions are the only stable ones:

$$|\phi|^2 = \phi^\dagger\phi = -\frac{\mu^2}{2\lambda}. \tag{1.9}$$

These solutions represent a sphere in a 4-dim space invariant under $SO(4)$. The classical minimum of the potential is degenerate, we can go from one minimum to another one by acting with the symmetry group. If we choose a particular minimum such as:

$$\phi_0 = \frac{1}{\sqrt{2}}\begin{pmatrix}0\\ \upsilon\end{pmatrix}; \quad \upsilon = \sqrt{\frac{-\mu^2}{\lambda}} \tag{1.10}$$

the global symmetry is spontaneously broken leaving the ground state invariant only under a subgroup of $SO(4)$ ($SU(2)\times SU(2)$) which is $SO(3)$ ($SU(2)$). Note that the Lagrangian is still invariant under the total symmetry $SO(4)$ ($SU(2)\times SU(2)$).

Perturbation theory is constructed around the minimum, i.e in terms of a set of fields which vanish when equation 1.9 is satisfied:

$$\phi(x) = \frac{1}{\sqrt{2}}e^{i\pi^a(x)\theta_a/\upsilon}\begin{pmatrix}0\\ \rho(x)+\upsilon\end{pmatrix} \tag{1.11}$$

where $\rho(x)$ and $\pi(x)$ are zero when the system is in the lowest energy state and θ_a denote the three generators of the Lie algebra of SU(2), $a = 1, 2, 3$. In the following, we consider one general field $\pi(x)$ for simplicity and the conclusion is extended to the three fields $\pi^a(x)$. We can rewrite the Lagrangian as:

$$L = \frac{1}{2}\partial^\mu\rho\partial_\mu\rho + \frac{1}{2}(1+\frac{\rho}{\upsilon})^2\partial^\mu\pi\partial_\mu\pi - \frac{\mu^2}{2}(\rho+\upsilon)^2 - \frac{\lambda}{4}(\rho+\upsilon)^4 \tag{1.12}$$

Substituting υ by its value given in equation 1.10, we obtain:

$$L = \frac{1}{2}\partial^\mu\rho\partial_\mu\rho + \frac{1}{2}\partial^\mu\pi\partial_\mu\pi + \frac{\mu^4}{4\lambda} + \mu^2\rho^2 - \sqrt{-\lambda\mu^2}\rho^3 - \frac{\lambda}{4}\rho^4 + \frac{1}{\upsilon}\rho\partial^\mu\pi\partial_\mu\pi + \frac{1}{2\upsilon^2}\rho^2\partial^\mu\pi\partial_\mu\pi. \tag{1.13}$$

The interpretation of this langrangian shows that the first two terms are kinetic terms for the fields ρ and π. In addition, the ρ field acquires a mass through the term $\mu^2\rho^2$ with a positive sign, indicating a physical particle. The absence of mass terms for π (recalling π^a) indicates the presence of three massless particles. The physical consequence is that the SSB of the continuous symmetry implies the appearance of three massless bosons and one massive scalar boson. The three massless bosons are the Nambu-Goldstone bosons.

In particular, if the general $SU(2) \times SU(2)$ group symmetry was that of the chiral symmetry in hadrodynamics, we get back the results of Nambu: the three massless bosons will represent the three pions π^0, π^+, π^- (in fact the pions have a mass but this is due to the approximate and not exact chiral symmetry) and the massive scalar boson the σ meson (now called $f_0(600)$).

This, the so-called "linear σ model" [50], was first used by Weinberg and Salam to describe the weak and EM interactions. The general group $SU(2) \times SU(2)$ is reduced to $SU(2) \times U(1)$ to take into account for the differences between left (L) and right (R) fermions (there is no R chirality neutrinos). It models the L fermions using $SU(2)_L$ and R fermions using a subgroup of $SU(2)_L \times SU(2)_R$: the $U(1)_Y$ group where the index Y refers to the weak hypercharge. The SSB of the global symmetry $SU(2) \times U(1)$ due to the particular choice of vacuum configuration reduces the group under which the ground state is invariant to a $U(1)_{EM}$. Note that the associated global symmetry is broken and not the local gauge symmetry. The gauge symmetry is broken ad-hoc afterwards in order to show the renormalizability of the theory and has nothing to do with the BEH mechanism. The impossibility of breaking down naturally the local symmetry was proven in [51] on lattice gauge fields.
We can rewrite the Lagrangian 1.5 requiring the symmetry to be local in order to simulate the BEH mechanism as:

$$L = D^\mu \phi^\dagger D_\mu \phi - V(\phi^\dagger \phi) \tag{1.14}$$

where the covariant derivative is obtained similarly to the one of QED $D_\mu = \partial_\mu + iqA_\mu$ with the only difference which is the distinction between the L and R parts when acting on fermions. It is given by:

$$\begin{aligned} D_{L\mu} &= \partial_\mu - ig\frac{\tau^a}{2}A^a_\mu - ig'(q - \frac{\tau_3}{2}B_\mu), \\ D_{R\mu} &= D_{L\mu}|_{\tau=0}. \end{aligned} \tag{1.15}$$

where τ^a are the Pauli matrices and the hypercharge Y given by the Gell-Mann-Nishijima relation $Y = 2(Q - \tau_3)$. The fields A_μ and B_μ are the gauge fields of $SU(2)$ and $U(1)$ respectively. Since the $SU(2)$ and $U(1)$ factors of the gauge group commute with one another, the coupling constants g and g' can be different. The Lagrangian is invariant under the following gauge transformations:

$$\phi(x) \to U_L(x) e^{i\beta(x)Y/2}\phi(x) \tag{1.16}$$

where $U_L(x) = e^{i\alpha^a(x)\tau^a}$

$$\frac{\tau^a}{2}A^a_\mu \to U_L \frac{\tau^a}{2}A^a_\mu U_L^\dagger - \frac{i}{g}\partial^\mu U_L . U_L^\dagger \tag{1.17}$$

$$B_\mu(x) \to B_\mu(x) + \frac{1}{g'}\partial_\mu \beta(x) \tag{1.18}$$

The gauge-invariant kinetic terms corresponding to these gauge fields are $F^i_{\mu\nu}F^i_{\mu\nu}$ and $G_{\mu\nu}G_{\mu\nu}$ with:

$$F^i_{\mu\nu} = \partial^\mu A^i_\nu - \partial_\nu A^i_\mu + g\varepsilon^{ijk}A^j_\mu A^k_\nu, \quad i = 1, 2, 3 \tag{1.19}$$

$$G_{\mu\nu} = \partial_\mu B_\nu - \partial_\nu B_\mu, \tag{1.20}$$

which transform like:

$$\frac{\tau^a}{2}F^a_{\mu\nu} \to U_L \frac{\tau^a}{2}F^a_{\mu\nu}U^\dagger_L \tag{1.21}$$

and

$$G_{\mu\nu} \to G_{\mu\nu}. \tag{1.22}$$

The kinetic part to be included in the Lagrangian is:

$$L_{kin} = -\frac{1}{4}F^i_{\mu\nu}F^{i\mu\nu} - \frac{1}{4}G_{\mu\nu}G^{\mu\nu}. \tag{1.23}$$

The scalar complex doublet field ϕ is choosen to have one neutral member in order to have a possibility to have a $U(1)_{EM}$-invariant ϕ_0 where the latter is given by equation 1.10:

$$\phi = \begin{pmatrix} \phi^+ \\ \phi^0 \end{pmatrix} \tag{1.24}$$

As previously, we can perform a change of variable replacing $\phi(x)$ by $\phi_0 + \chi(x)$:

$$\phi(x) = e^{i\theta(x).\tau/\upsilon}\begin{pmatrix} 0 \\ \frac{\upsilon+\chi(x)}{\sqrt{2}} \end{pmatrix} \tag{1.25}$$

The original two complex fields $\phi^+(x)$ and $\phi^0(x)$ are parametrized in terms of four real fields $\theta_i(x)$ and $\chi(x)$. We can make a specific choice of gauge, for example the unitary gauge and obtain:

$$\phi'(x) = \begin{pmatrix} 0 \\ \frac{\upsilon+\chi(x)}{\sqrt{2}} \end{pmatrix} \tag{1.26}$$

We replace ϕ by ϕ' in the scalar Lagrangian:

$$\begin{aligned} L &= |(\partial_\mu - ig\tau^a A'^a_\mu - i\frac{g'}{2}B'_\mu)\phi'|^2 + \mu^2|\phi'|^2 - \lambda\phi'^4 \\ &= \frac{(\upsilon+\chi)^2}{8}\{g^2|A'^1_\mu - iA'^2_\mu|^2 + |gA'^3_\mu - g'B'_\mu|^2\} + \frac{1}{2}(\partial_\mu\chi)^2 + \mu^2\chi^2 - \lambda\upsilon\chi^3 - \frac{\lambda}{4}\chi^4 \end{aligned} \tag{1.27}$$

where

$$\begin{aligned} \frac{\tau^a}{2}A'^a_\mu &= U(\theta)\frac{\tau^a}{2}A^a_\mu U^{-1}(\theta) - \frac{i}{g}(\partial_\mu U(\theta))U^{-1}(\theta), \\ B'_\mu &= B_\mu. \end{aligned} \tag{1.28}$$

Note the appearance of the physical mass term $\mu^2\chi^2$ which identifies the BEH boson mass as $\sqrt{-2\mu^2}$. At the first order in g, the first term in the Lagrangian tends to: $\frac{(\upsilon)^2}{8}\{g^2[(A'^1_\mu)^2+(A'^2_\mu)^2]+(gA'^3_\mu-g'B'_\mu)^2\}$. Furthermore, we can do the following identifications:

$$\begin{aligned} M_W^2 W^+_\mu W^{-\mu} &= \frac{g^2\upsilon^2}{8}[(A'^1_\mu)^2+(A'^2_\mu)^2], \\ \frac{1}{2}M_Z^2 Z_\mu Z^\mu &= \frac{\upsilon^2}{8}(gA'^3_\mu - g'B'_\mu)^2 \end{aligned} \tag{1.29}$$

For the charged vector mesons, we thus have:

$$W^\pm_\mu = \frac{A'^1_\mu \mp A'^2_\mu}{\sqrt{2}} \tag{1.30}$$

and

$$M_W^2 = \frac{g^2\upsilon^2}{4}. \tag{1.31}$$

The linear combination $gA'^3_\mu - g'B'_\mu$ is also massive while the orthogonal combination remains massless and corresponds to a gauge boson associated to the unbroken $U(1)_{EM}$ group, i.e the photon. We will diagonalize this term in another basis:

$$\begin{aligned} \frac{1}{2}M_Z^2 Z_\mu Z^\mu &= \frac{\upsilon^2}{8}(A'^3_\mu, B'_\mu)\begin{pmatrix} g^2 & -gg' \\ -gg' & g'^2 \end{pmatrix}\begin{pmatrix} A'^3_\mu \\ B'_\mu \end{pmatrix} \\ &= \frac{1}{2}(Z_\mu, A_\mu)\begin{pmatrix} M_Z^2 & 0 \\ 0 & 0 \end{pmatrix}\begin{pmatrix} Z^\mu \\ A^\mu \end{pmatrix} \end{aligned} \tag{1.32}$$

where

$$\begin{pmatrix} Z_\mu \\ A_\mu \end{pmatrix} = \begin{pmatrix} \cos\theta_W & -\sin\theta_W \\ \sin\theta_W & \cos\theta_W \end{pmatrix}\begin{pmatrix} A'^3_\mu \\ B'_\mu \end{pmatrix}. \tag{1.33}$$

θ_W is called the weak mixing angle and is related to the coupling constants by:

$$\cos\theta_W = \frac{g}{\sqrt{g^2+g'^2}}, \qquad \sin\theta_W = \frac{g'}{\sqrt{g^2+g'^2}} \tag{1.34}$$

We can deduce the mass of the neutral gauge bosons:

$$M_Z^2 = \upsilon^2(g^2+g'^2)/4, \quad M_A^2 = 0. \tag{1.35}$$

One can easily see that the masses of the weak gauge bosons are not independent:

$$M_W = M_Z\cos\theta_W = \frac{1}{2}\upsilon g, \tag{1.36}$$

which can also be written as:

$$\rho = \frac{M_W^2}{M_Z^2\cos^2\theta_W} = 1. \tag{1.37}$$

From equation 1.36, we conclude $\upsilon = \frac{2M_W}{g} = (G_F\sqrt{2})^{-1/2}$ where G_F is the Fermi constant determined from muon decay and one gets $\upsilon = 246$ GeV. The vacuum expectation value of the scalar field is then $\frac{\upsilon}{\sqrt{2}} \sim 174$ GeV.

In order to introduce the leptons into the model, we introduce the left-handed "weak-isospin" doublet:

$$L = \begin{pmatrix} \psi_{\nu_l} \\ \psi_l \end{pmatrix}_L, \quad l = e, \mu, \tau \tag{1.38}$$

where

$$L = \frac{1}{2}(1 - \gamma_5)\begin{pmatrix} \psi_{\nu_l} \\ \psi_l \end{pmatrix} \tag{1.39}$$

and the only right-handed "weak-isospin" singlet (assuming the non-existence of neutrinos right-handed states, which is not completely true if we consider the very small neutrino mass deduced from the measurement of neutrino oscillations):

$$R = (\psi_l)_R = \frac{1}{2}(1 + \gamma_5)\psi_l \tag{1.40}$$

The corresponding gauge-invariant Lagrangian can be written as:

$$L_{leptons} = i\bar{\psi}\gamma^\mu D_\mu \psi \tag{1.41}$$

where the covariant derivative is given by equation 1.15. In addition, in order to make the leptons massive, we can introduce an interaction term between the field ψ and the scalar ϕ:

$$L_{Yukawa} = -g_l(\bar{L}\phi R + \bar{R}\phi^\dagger L) \tag{1.42}$$

where g_l are the Yukawa couplings of the scalar to the fermions. Replacing ϕ from equation 1.26, we rewrite L_{Yukawa} as:

$$L_{Yukawa} = -g_l\frac{\upsilon + \chi}{\sqrt{2}}(\bar{\psi}_R\psi_L + \bar{\psi}_L\psi_R) \tag{1.43}$$

or $\bar{\psi}_R\psi_L + \bar{\psi}_L\psi_R = \bar{\psi}\psi$, so:

$$L_{Yukawa} = -\frac{g_l\upsilon}{\sqrt{2}}\bar{\psi}\psi - \frac{g_l\chi}{\sqrt{2}}\bar{\psi}\psi \tag{1.44}$$

The first term of the Yukawa Lagrangian shows that the lepton has acquired a mass:

$$m_l = \frac{g_l\upsilon}{\sqrt{2}}. \tag{1.45}$$

The second term represents the interaction between the lepton and the BEH boson.

After the GIM mechanism, the quarks were introduced in the theory. Left-handed doublets are defined similarly as for the case of leptons:

$$\begin{pmatrix}\psi_u\\ \psi_{d'}\end{pmatrix}_L \begin{pmatrix}\psi_c\\ \psi_{s'}\end{pmatrix}_L \begin{pmatrix}\psi_t\\ \psi_{b'}\end{pmatrix}_L \tag{1.46}$$

where

$$\begin{pmatrix}\psi_{d'}\\ \psi_{s'}\\ \psi_{b'}\end{pmatrix} = V_{CKM}\begin{pmatrix}\psi_d\\ \psi_s\\ \psi_b\end{pmatrix}. \tag{1.47}$$

The matrix V_{CKM} is the Cabibbo - Kobayashi - Maskawa matrix:

$$V_{CKM} = \begin{pmatrix}V_{ud} & V_{us} & V_{ub}\\ V_{cd} & V_{cs} & V_{cb}\\ V_{td} & V_{ts} & V_{tb}\end{pmatrix}. \tag{1.48}$$

The left-handed matrices of quarks can also be written as:

$$\begin{pmatrix}\psi_u\\ \psi_{d'}\end{pmatrix}_L = \frac{1-\gamma_5}{2}\begin{pmatrix}\psi_u\\ \psi_{d'}\end{pmatrix} \tag{1.49}$$

and similarly for $\binom{\psi_c}{\psi_{s'}}_L$ and $\binom{\psi_t}{\psi_{b'}}_L$. The right-handed parts are given by:

$$\psi_{u_R} = \frac{1+\gamma_5}{2}\psi_u, \quad \psi_{d_R} = \frac{1+\gamma_5}{2}\psi_d \tag{1.50}$$

and similarly for ψ_c, ψ_s and ψ_t, ψ_b. The most general Yukawa coupling between scalars and quarks can be written as:

$$L_{Yukawa_quarks} = -g_d(\bar{\psi_u}\bar{\psi_{d'}})_L\begin{pmatrix}\phi^+\\ \phi^0\end{pmatrix}\psi_{d_R} - g_u(\bar{\psi_u}\bar{\psi_{d'}})_L\begin{pmatrix}-\bar{\phi^0}\\ \phi^-\end{pmatrix}\psi_{u_R} + h.c \tag{1.51}$$

For ϕ given by equation 1.26, this is rewritten to:

$$L_{Yukawa_quarks} = -m_d\bar{\psi_d}\psi_d(1+\frac{\chi}{\upsilon}) - m_u\bar{\psi_u}\psi_u(1+\frac{\chi}{\upsilon}) \tag{1.52}$$

with the quark masses given by:

$$m_u = \frac{g_u\upsilon}{\sqrt{2}} \quad m_d = \frac{g_d\upsilon}{\sqrt{2}} \tag{1.53}$$

and similarly for ψ_c, ψ_s and ψ_t, ψ_b. Note that the masses of fermions are dependent of their Yukawa couplings to the scalar boson and therefore the masses are not predicted by the EW theory.

The total gauge-invariant Lagrangian of the Electroweak Model (EWM) can be written as:

$$\begin{aligned} L_{EWM} = & -\frac{1}{4}F^{i}_{\mu\nu}F^{i\mu\nu} - \frac{1}{4}G_{\mu\nu}G^{\mu\nu} \\ & + i\bar{\psi}\gamma^{\mu}D_{\mu}\psi \\ & + (D_{\mu}\phi)^{\dagger}(D^{\mu}\phi) - V(\phi^{\dagger}\phi) \\ & - g_{l}\bar{L}\phi R - g_{u}(\bar{\psi_{u}}\bar{\psi_{d'}})_{L}\begin{pmatrix}\phi^{+}\\ \phi^{0}\end{pmatrix}\psi_{d_R} + h.c \end{aligned} \tag{1.54}$$

and the total Lagrangian for the Standard Model (SM):

$$L_{SM} = L_{EWM} + L_{QCD}. \tag{1.55}$$

The first term of equation 1.54 represents the W, Z, γ kinetic energies and self interactions. The second term contains the lepton and quark kinetic energies and their interactions with W, Z, γ. In the third term, one has the W, Z, γ masses and couplings with the scalar boson. The lepton and quark masses and couplings to the scalar boson are in the last term.

1.3 Limits on the scalar boson mass

1.3.1 Theoretical limits

Since in the SM the mass of the scalar boson is a free parameter, constraints on its mass were derived from theoretical assumptions: unitarity of scattering amplitudes, triviality of the scalar boson self coupling and stability of the EW vacuum. For more details, see [52, 53].

Unitarity of scattering amplitudes

In the limit of high energies, the longitudinal components of the massive gauge bosons, $W^{\pm}_{L}$ and Z_{L}, can be approximated as scalar Goldstone bosons $w_0, w_{\pm}$. The cross sections of processes involving such longitudinal components increase with the energy and could lead to a violation of perturbativity at some stage [54, 55, 56], a known example is the scattering process $W^{+}W^{-} \to W^{+}W^{-}$ (an historical account with the original references can be found in [57]). The amplitude for this process in the limit of high energies in the Goldstone boson approximation is given by:

$$\mathcal{A}\left(w_{+}w_{-} \to w_{+}w_{-}\right) = -\left[2\frac{M_H^2}{v^2} + (\frac{M_H^2}{v})^2\frac{1}{s - M_H^2} + (\frac{M_H^2}{v})^2\frac{1}{t - M_H^2}\right] \tag{1.56}$$

where s, t are the Mandelstam variables.

In order to study the unitarity of this amplitude, it is decomposed into partial waves a_k of orbital angular momentum k on the Legendre polynomials basis:

$$\mathcal{A} = 16\pi \sum_{k=0}^{\infty} (2k+1) P_k(\cos\theta) a_k \tag{1.57}$$

where P_k are the Legendre polynomials and θ is the scattering angle in the center-of-mass frame. Since the cross section of a $2 \to 2$ process is given by $d\sigma/d\Omega = |\mathcal{A}|^2/(64\pi^2 s)$ with $d\Omega = 2\pi d\cos\theta$, we can write:

$$\sigma = \frac{8\pi}{s} \sum_{k=0}^{\infty} \sum_{l=0}^{\infty} (2k+1)(2l+1) a_k a_l^* \int_{-1}^{1} d\cos\theta P_k(\cos\theta) P_l(\cos\theta) = \frac{16\pi}{s} \sum_{k=0}^{\infty} (2k+1)|a_k|^2 \tag{1.58}$$

On the other hand, the total cross section is proportional to the imaginary part of the amplitude in the forward direction, this is the optical theorem which can be written as:

$$\sigma = \frac{1}{s} Im(\mathcal{A}(\theta = 0)) = \frac{16\pi}{s} \sum_{k=0}^{\infty} (2k+1)|a_k|^2 \tag{1.59}$$

This leads to the unitarity conditions:

$$|a_k|^2 < Im(a_k) \Rightarrow (Re(a_k))^2 + (Im(a_k))^2 < Im(a_k) \Rightarrow (Re(a_k))^2 + \left(Im(a_k) - \frac{1}{2}\right)^2 < \frac{1}{4} \tag{1.60}$$

This is the equation of a circle of radius $\frac{1}{2}$ and center $(0, \frac{1}{2})$ in the plane [Re(a_k, Im(a_k)], so we have:

$$|Re(a_k)| < \frac{1}{2} \tag{1.61}$$

The amplitude for $k = 0$ is thus given by:

$$\begin{aligned} a_0 &= \frac{1}{16\pi s} \int_{-s}^{0} \mathrm{d}t |\mathcal{A}| = -\frac{1}{16\pi s} \int_{-s}^{0} \mathrm{d}t \frac{M_H^2}{\upsilon^2} \left[2 + \frac{M_H^2}{s - M_H^2} + \frac{M_H^2}{t - M_H^2} \right] \\ &= -\frac{M_H^2}{16\pi\upsilon^2} \left(2 + \frac{M_H^2}{s - M_H^2} - \frac{M_H^2}{s}\, log\, \left(1 + \frac{s}{M_H^2} \right) \right) \\ &\sim -\frac{M_H^2}{16\pi\upsilon^2} \left(2 + \mathcal{O}(\frac{M_H^2}{s}) \right) \end{aligned} \tag{1.62}$$

and if the mass of the BEH boson is much smaller than $\sqrt{s}$:

$$a_0 \xrightarrow{s \gg M_H^2} -\frac{M_H^2}{8\pi\upsilon^2} \tag{1.63}$$

So, one obtains the following upper bound from the unitarity condition in equation 1.61:

$$\frac{M_H^2}{8\pi\upsilon^2} < \frac{1}{2} \rightarrow M_H^2 < 4\pi\upsilon^2 = (870 \text{ GeV})^2 \tag{1.64}$$

If the scattering channel $W_L^+W_L^-$ is coupled with other channels: Z_LZ_L, HH, Z_LH, W_L^+H and $W_L^+Z_L$, the upper bound reduces to:

$$M_H^2 < \frac{8\pi}{3}\upsilon^2 = (710 \text{ GeV})^2 \tag{1.65}$$

Thus, if the BEH boson mass exceeds values of $\mathcal{O}(700)$ GeV, unitarity is violated unless new physics appear to restore it. Note that the above calculations are performed assuming that the SM remains perturbative at high energies and that higher-order corrections are not very large.

Triviality of the scalar boson self coupling

The mass of the BEH boson is given by its self coupling:

$$M_H^2 = \frac{8\lambda(\upsilon)M_W^2}{g^2}. \tag{1.66}$$

The variation of the quartic BEH coupling with the energy scale Q is described by the Renormalization Group Equation (RGE):

$$\frac{d\lambda(Q^2)}{dlog\ (Q^2)} = \frac{3}{4\pi^2}\lambda^2(Q^2) + \text{higher orders} \tag{1.67}$$

The solution of this equation is given by:

$$\frac{1}{\lambda(Q^2)} = -\frac{3}{4\pi^2}\ log\ (Q^2) + C \tag{1.68}$$

If we define a boundary condition $\lambda(Q^2 = \upsilon^2) = \lambda_0$ we find:

$$\lambda(Q^2) = \frac{\lambda_0}{1 - \frac{3}{4\pi^2}\lambda(\upsilon^2)\ log\ \frac{Q^2}{\upsilon^2}} \tag{1.69}$$

If $Q^2 \ll \upsilon^2$, the quartic coupling becomes very small and eventually vanishes, while for high energies $Q^2 \gg \upsilon^2$ it grows until it actually hits a pole at:

$$\begin{aligned} 1 - \frac{3}{4\pi^2}\lambda(\upsilon^2)\ log\ \frac{Q_C^2}{\upsilon^2} = 0 \Leftrightarrow log\ \frac{Q_C^2}{\upsilon^2} = \frac{4\pi^2}{3\lambda_0} \\ \Leftrightarrow Q_C = \upsilon \exp\left(\frac{2\pi^2}{3\lambda_0}\right) = \upsilon\ \exp\left(\frac{4\pi^2\upsilon^2}{3M_H^2}\right) \end{aligned} \tag{1.70}$$

This is the Landau pole which gives the maximum scale beyond which we cannot rely on our perturbative theory anymore. This limit is the triviality

bound because it states that for these theories to remain perturbative at all scales one needs to have a zero coupling everywhere. If the energy scale reaches for instance the Planck scale, i.e $Q_C \sim 10^{19}$ GeV, the BEH boson is required to be light $M_H \lesssim 145$ GeV (keeping in mind that these perturbative calculations are non-consistent at high energy scale), if instead the energy scale is choosen to be small $\sim 10^3$ GeV, the BEH boson can be heavier $M_H \lesssim 750$ GeV.

Stability of the vacuum

The vacuum stability gives a lower bound on the BEH boson mass as a function of the "cut-off" scale, called the stability bound. It is estimated by including in addition to the self-BEH coupling (which was the only one considered for estimating the triviality bound) the contributions of top quarks and massive gauge bosons. The solution of the new RGE is then:

$$\lambda(Q^2) = \lambda_0 + \frac{1}{16\pi^2}\left[-12\frac{m_t^4}{v^4} + \frac{3}{16}(2g^4 + (g^2+g'^2)^2)\right] \; log\; \frac{Q^2}{v^2} \tag{1.71}$$

The negative sign term assigned to the top contribution could lead to a negative coupling $\lambda(Q^2) < 0$ which could make the vacuum unstable. Therefore, in order to keep the coupling positive, the BEH boson has to satisfy:

$$M_H^2 > -\frac{v^2}{8\pi^2}\left[-12\frac{m_t^4}{v^4} + \frac{3}{16}(2g^4 + (g^2+g'^2)^2)\right] \; log\; \frac{Q_C^2}{v^2} \tag{1.72}$$

In other words the BEH potential has a minimum below for energy scales below $Q_C(M_H)$ and the vacuum is stable. For instance, for relatively low and very high values of the "cut-off", we have:

$$\begin{aligned} M_H &> 70 \text{ GeV} \quad \text{for} \quad Q_c = 10^3 \text{ GeV} \\ M_H &> 130 \text{ GeV} \quad \text{for} \quad Q_c = 10^{16} \text{ GeV} \end{aligned} \tag{1.73}$$

A summary of the limits from the triviality and stability bounds [52, 58] is shown in Fig. 1.1.

1.3.2 Experimental limits

Direct searches

The search for a low mass BEH boson started more than 35 years ago [59] and was performed in particular in the decays of various particles, see for instance [60] for a search in K_L decay. The first direct searches for a high mass BEH boson were performed at the Large Electron Positron (LEP) collider: an electron-positron collider at center-of-mass energies up to $\sqrt{s} = 209$ GeV.

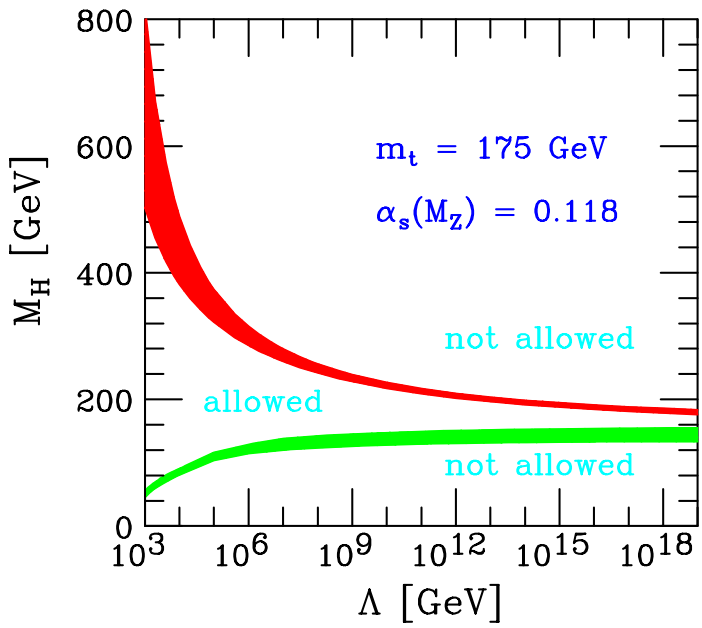

Figure 1.1: The triviality bound (upper) and the vacuum stability bound (lower) on the BEH boson mass as a function of the "cut-off" scale Λ for a top quark mass $m_t = 175 \pm 6$ GeV and $\alpha_s(M_Z) = 0.118 \pm 0.002$. [52].

The main production mechanism at LEP was the BEH-strahlung mode $e^+e^- \to Z^*$[1]$\to ZH$, and the main explored BEH decay mode in the low mass range was the $H \to b\bar{b}$ channel. Fig. 1.2 shows the combined results from the four experiments at LEP (ALEPH, DELPHI, L3 and OPAL) [61]. While the median expected upper limit was $M_H < 115.3$ GeV at 95% C.L. ($CL_s = 5\%$), the observed exclusion was set to $M_H < 114.4$ GeV at 95% C.L.. Among these experiments an excess of $\sim 3\sigma$ for a BEH mass (M_H) around 115 GeV was observed by ALEPH [62].

These searches were continued at Tevatron in Fermilab with CDF and DØ experiments. Proton-antiproton collisions were performed for an integrated luminosity up to 10 fb^{-1}. The main production mechanisms at Tevatron are the gluon-gluon fusion and the associated production of the BEH boson with W/Z bosons. For low masses, i.e $M_H < 135$ GeV, $q\bar{q} \to W^{\pm}H/ZH$ where the BEH boson decays mainly into a pair of b quarks dominates, while for masses $M_H > 135$ GeV $gg \to H$ where the BEH boson decays mainly into a pair of W bosons becomes the dominant process. The most recent combined results [63] exclude the SM BEH boson mass range between 100 and 103 GeV and between 147 and 180 GeV at 95% C.L., as can be seen in Fig. 1.3. One can note an excess in data with respect to the estimated background in the range $115 < M_H < 140$ GeV which explains why the observed limit is not as

[1] Z^* is an off-shell Z boson.

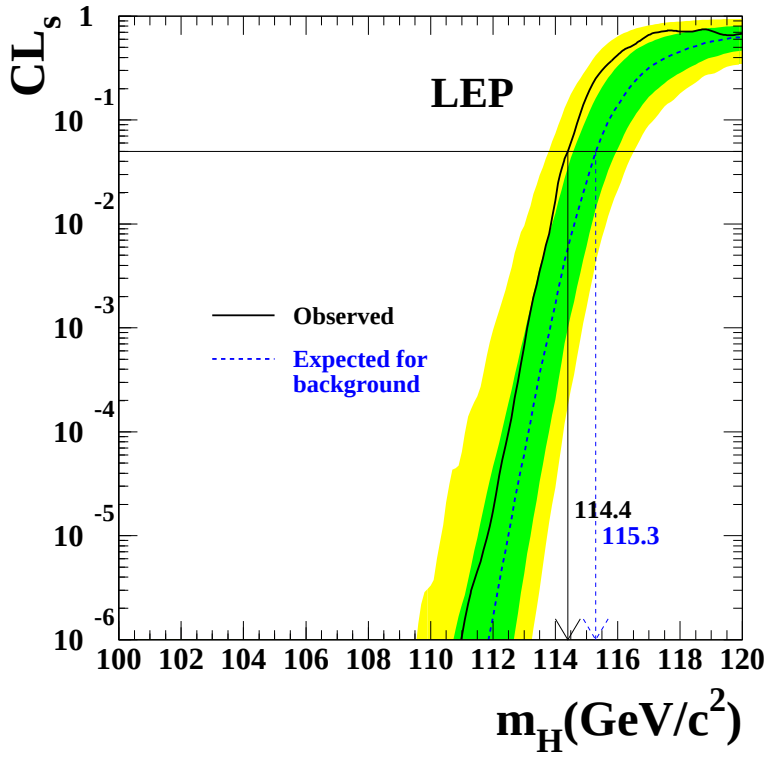

Figure 1.2: The CL_s ratio as a function of the BEH boson mass. The observed exclusion limit is shown in solid line while the expectation is shoen in dashed line. The bands show the 68% and 95% probability bands. The line $CL_s = 0.05$ defines the 95% C.L. [61].

stringent as the expected one. At $M_H = 120$ GeV, a local significance (the difference between local and global significance will be detailed in 2.5) of 3 standard deviations is quoted.

At the Large Hadron Collider (LHC) where proton-proton collisions occured in 2011 at $\sqrt{s} = 7$ TeV, the ATLAS and CMS experiments have performed detailed searches (with more decay channels). For an integrated luminosity of $\sim 5fb^{-1}$, the ATLAS collaboration [64] has excluded a SM BEH cross section for masses going from 111.4 to 116.6 GeV, 119.4 to 122.1 GeV and from 129.2 to 541 GeV at 95% C.L. and from 130.7 to 506 GeV at 99% C.L. as can be seen in Fig. 1.4. While the CMS experiment [65] excluded a SM BEH boson mass from 127.5 to 600 GeV at 95% C.L. and from 129 to 525 GeV at 99% C.L., see Fig. 1.5. An excess of events over the background with a 3.5σ significance at 126 GeV was observed in ATLAS. Similarly, an excess of 3.1σ at 124 GeV was observed in CMS. The results with the 2012 dataset at $\sqrt{s} = 8$ TeV will be shown in Chapter 7 of this thesis.

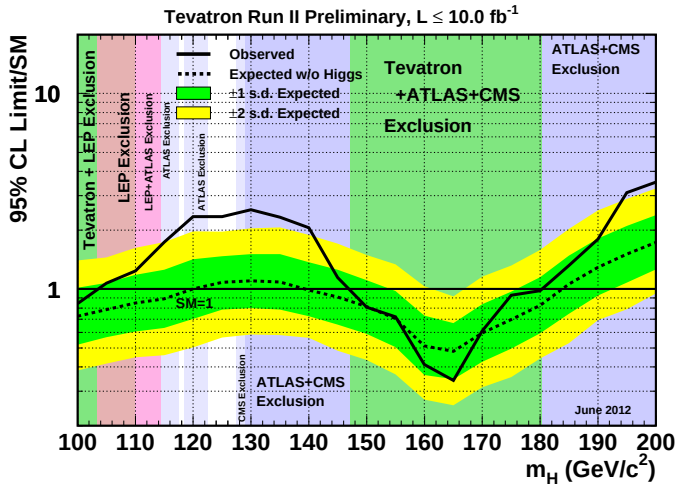

Figure 1.3: Observed and expected 95% C.L. upper limits on the ratios to the SM cross section as a function of the BEH boson mass for the combined CDF and DØ analyses estimated using a Bayesian calculation. The bands indicate the 68% and 95% probability regions where the limits can fluctuate in the absence of the signal [63].

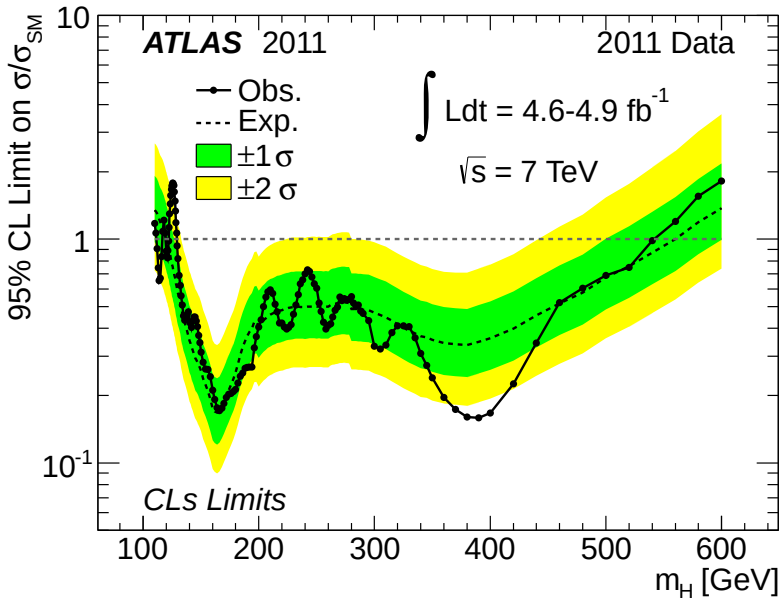

Figure 1.4: Observed and expected 95% C.L. upper limits on the ratios to the SM cross section as a function of the BEH boson mass for the ATLAS experiment estimated using a frequentist approach. The bands indicate the 68% and 95% probability regions where the limits can fluctuate in the absence of the signal [64].

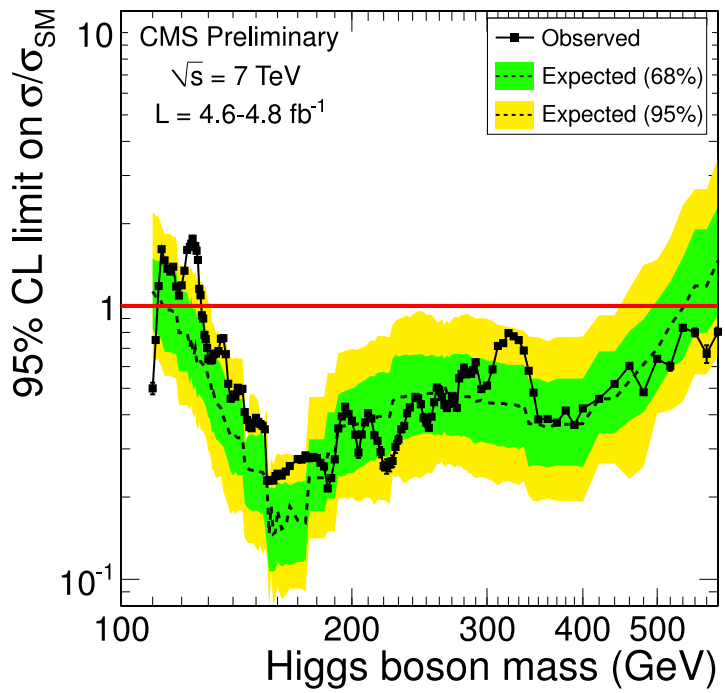

Figure 1.5: Observed and expected 95% C.L. upper limits on the ratios to the SM cross section as a function of the BEH boson mass for the CMS experiment in the range $110-600$ GeV [65].

Indirect searches

The BEH boson contributes to the radiative corrections to the high-precision EW observables; an example of its contribution to the gauge boson self-energy is shown in Fig. 1.6. Thus constraints on its mass could be derived from high-precision measurements of these EW observables (the constraints are weak since the dependence on the BEH mass is only logarithmic). This was done at LEP, Stanford Linear Collider (SLC), Tevatron and in low energies experiments such as ν_{μ^-} and $\bar{\nu}_{\mu^-}$-nucleon deep-inelastic scattering. The measured parameters are for instance the mass of the W, Z bosons, the effective weak mixing angle as measured in forward-backward and polarization asymmetries using the strong and the EM coupling constants, the mass of the top and the Fermi coupling constant. The $\Delta\chi^2 = \chi^2 - \chi^2_{min}$ of the fit on the combined data performed by the LEP Electroweak Working Group [66] is shown in Fig. 1.7 depending on the BEH boson mass. The left and right yellow bands are the excluded limits by the LEP2 and LHC

experiments respectively. The fitted SM BEH boson mass is then:

$$M_H = 94^{+29}_{-24} \text{ GeV} \tag{1.74}$$

and the 95% C.L. upper bound (derived from $\Delta\chi^2 = 2.7$ for the blue band, thus including both experimental and theoretical uncertainties) is:

$$M_H \leq 152 \text{ GeV}. \tag{1.75}$$

Similar results however including both direct and indirect data into the fit were obtained by the GFitter collaboration in [67].

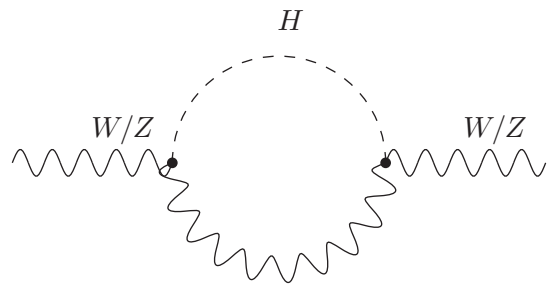

Figure 1.6: BEH boson contribution to the EW gauge boson self energy (correction logarithmically dependent on the BEH mass).

1.4 SM Scalar Boson Searches at LHC

1.4.1 SM Scalar Boson Production

In the SM, the main production mechanisms for BEH bosons at hadron colliders make use of the fact that the BEH boson couples preferentially to the heavy particles, that is the massive W and Z vector bosons, the top quark and to, a lesser extent, the bottom quark. The four dominant production processes are: the gluon-gluon fusion mechanism, the weak vector boson fusion, the associated production with W/Z bosons and the associated production with heavy top or bottom quark pair. The corresponding Feynman diagrams are shown in Fig. 1.8.

Gluon-gluon fusion is the main production mechanism of the SM BEH bosons at hadron colliders. As can be seen in Fig. 1.9, at high energy i.e at small fraction of momenta x, the gluonic density dominates [68]. This mechanism occurs through a triangular loop of heavy quarks, mainly top quarks and to a lesser extent, bottom quarks due to their large Yukawa couplings to the BEH boson. Since this process is controlled by strong interactions, the calculation of QCD radiative corrections up to higher orders is necessary. The cross section is computed up to next-to-leading (NLO) order with the

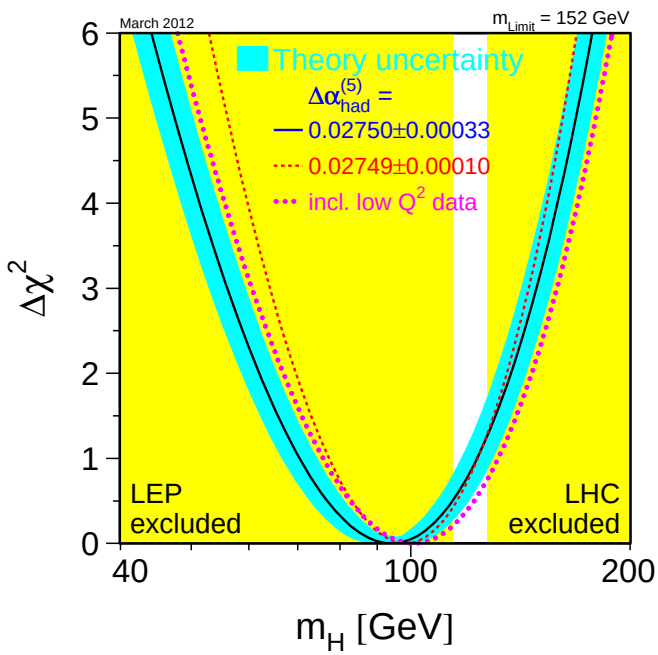

Figure 1.7: The $\Delta\chi^2$ of the fit to EW precision data as a function of M_H. The blue-band represents the theoretical uncertainties from unknown higher-order corrections. The effect of including the low Q^2 and of using different values of $\Delta\alpha_{\rm had}$ are also shown [66].

exact top (and bottom) quark mass effects. The next-to-next-to-leading order (NNLO) corrections were added in an effective approach i.e in the limit of large top quark mass [69, 70, 71]. It was shown at NLO that the large-m_t limit is a good approximation, to better than 1% for a relatively light BEH boson i.e $M_H < 300$ GeV. The NNLO calculation was improved by including the next-to-next-to-leading logarithm (NNLL) resummation of the soft-gluon contributions using the same approximation [72]. In addition electroweak (EW) corrections were evaluated. One of the most important sources of uncertainty on the partonic cross section comes from uncalculated higher order QCD radiative corrections. This uncertainty is evaluated in general by varying the factorization and renormalization scales from $\mu_0 = M_H/2$ to $\mu_0 = 2M_H$. However in some computations, e.g. in [70], the effect of the soft-gluon resummation is mimicked by chosing the central value of the factorization and normalization scales as $\mu_R = \mu_F = M_H/2$ (there is an official prescription to compute the uncertainties in [73]). At $\sqrt{s} = 7$ (14) TeV, the scale uncertainty is about $+12 - 8\%$ ($+12 - 8\%$) in the range $M_H = 100 - 300$ GeV. Other uncertainties come from the missing EW corrections and from the large-m_t approximation, both of which are estimated to be about $\pm 1\%$ for $M_H < 300$

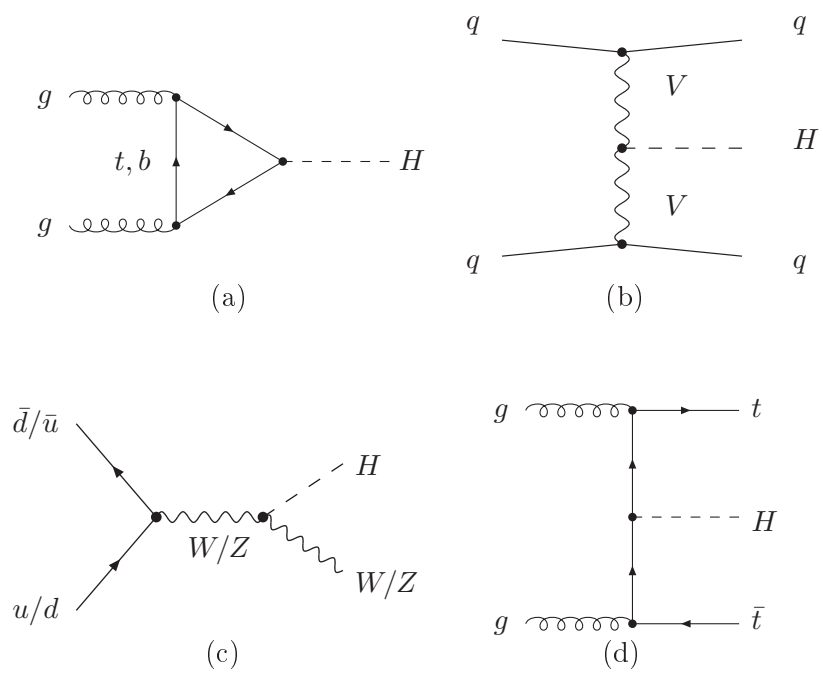

Figure 1.8: Feynman diagrams for BEH production processes: (a) gluon fusion, (b) vector boson fusion, (c) associated vector boson production,(d) associated production with heavy top quarks.

GeV. A final important source of uncertainty is the one coming from PDFs and from the value of the QCD coupling. The combined effect of PDF$+\alpha_s$ uncertainties was estimated to be about $+8-7\%$ in the range $M_H = 100-300$ GeV for both $\sqrt{s} = 7$ and 14 TeV [74]. Adding quadratically these uncertainties, the total theoretical uncertainty is found to be about $+14.1 - 10.7\%$ for $M_H = 125$ GeV at $\sqrt{s} = 7$ TeV. There is a discussion in [75] of a possible underestimation of these uncertainties.

Vector boson fusion (VBF) is a three-body production process, with two hard jets in the forward and backward regions of the detector and the BEH boson. It is mediated by gauge boson exchange and it plays a very important role in the BEH searches at LHC since it has a power to discriminate the signal from many large QCD backgrounds. In addition, the VBF channel is important for the determination of the BEH-boson couplings, especially the HWW and HZZ couplings. This process has been computed fully at NLO (with EW and QCD corrections). Approximate NNLO QCD corrections have been computed using the structure-function approach. This leaves an uncertainty of $\pm 1-2\%$ due to the scale dependence and another one estimated at the same level due to the parton distributions.

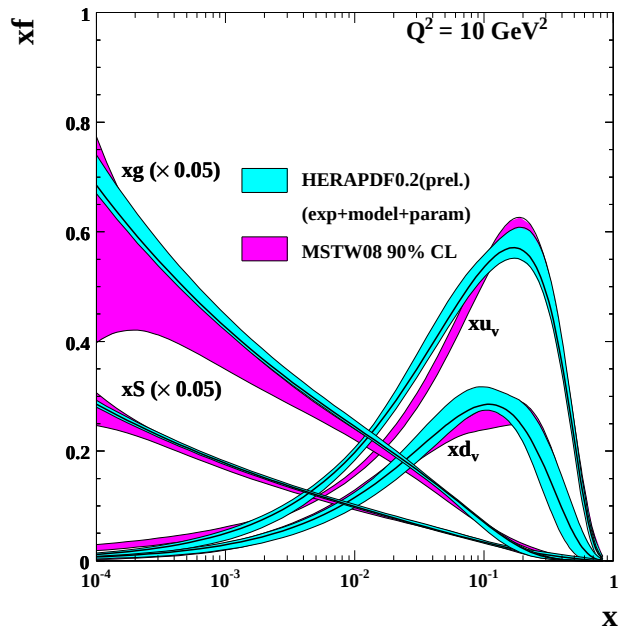

Figure 1.9: The HERA Parton Distribution Function (PDF) compared to Martin-Stirling-Thorne-Watt (MSTW) PDFs [68].

The cross section calculation of the associated $W^{\pm}$, Z production modes, also called BEH-strahlung processes, included NNLO QCD and NLO EW corrections. The uncertainties coming from scale variation and from the PDF+α_s contribution vary from 3% to 5% and from 4% to 6% respectively for WH (ZH) with 90 GeV $< M_H <$ 150 GeV. The scale uncertainties for the ZH production are consistently larger than those for WH production because they are dominated by the uncertainties of the gg channel (see diagram (c) of Fig.1.10). The associated vector boson production mode is quite interesting for the BEH searches in the $H \to b\bar{b}$ channel, where the associated production of high transverse momentum scalar boson rescues this decay mode [76] (due to the reduction in background and the improved signature provided by the leptonic decays of the vector boson). It is also of interest for the estimation of the BEH coupling to b quarks.

The $t\bar{t}H$ production mode plays a role for light BEH masses, below 150 GeV, as well as in the determination of the BEH - top quark Yukawa coupling. Its production cross section has been computed at NLO. The cross sections for $\sqrt{s} = 14$ TeV are $7 - 10$ times larger than the corresponding values for $\sqrt{s} = 7$ TeV. The scale uncertainties are of the order of $\pm 5 - 10\%$ while the PDF+α_s uncertainties range between $\pm 8 - 10\%$ depending on the mass of the BEH boson. The total uncertainty amounts to typically $\pm 10 - 15\%$ but becomes slightly larger for BEH masses beyond 200 GeV.

The SM BEH production cross sections for $\sqrt{s} = 7$ TeV at LHC for the

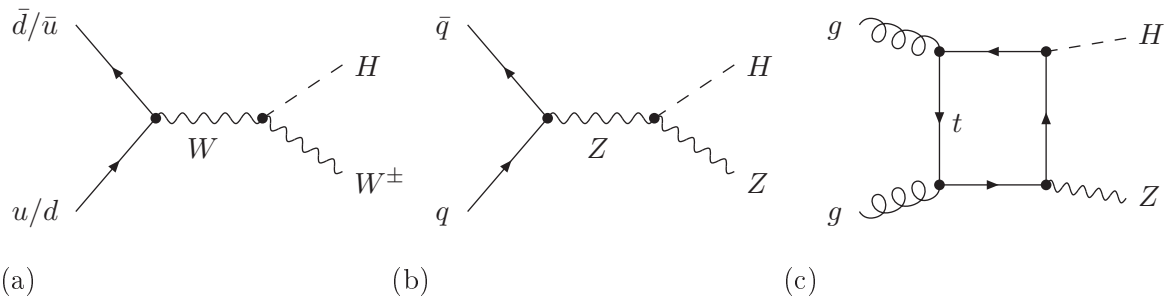

Figure 1.10: (a), (b) LO diagrams for the partonic processes $pp \to VH$ ($V = W, Z$); (c) diagram contributing to the $gg \to HZ$ channel.

individual channels are shown in Fig. 1.11 (top). The bands illustrate the combined parametric and theoretical uncertainties. A comparison of the total SM BEH production cross section at $\sqrt{s} = 7$ TeV and the nominal energy, $\sqrt{s} = 14$ TeV, is shown in Fig. 1.11 (bottom). More details can be found in [73].

1.4.2 SM Scalar Boson Decays

The total width and the decay branching ratios of the SM BEH boson are shown in Figs. 1.12 and 1.13 (for more details, see [77]). They were calculated using the programs HDECAY [78] and PROPHECY4F [79]. HDECAY calculates the decay widths and branching ratios of the SM BEH boson including all kinematically allowed channels and all relevant higher-order QCD corrections to decays into quark pairs and gluons. EW NLO corrections to the decays $H \to \gamma\gamma$ and $H \to gg$ are implemented in HDECAY in form of grids based on the calculation of [80, 81]. PROPHECY4F is a Monte Carlo (MC) generator for $H \to WW/ZZ \to 4f$ final states. It includes the complete NLO QCD and EW corrections and all interferences at LO and NLO which are not computed by HDECAY. For instance, the interference between $H \to Z^*Z^* \to e^+e^-\nu\bar{\nu}$ and $H \to W^*W^* \to e^+\nu e^-\bar{\nu}$ is important for $M_H < 2M_{W,Z}$ (since above this threshold, the small widths of on shell $W's$ and $Z's$ give a small interference effect) and is taken into account in PROPHECY4F. The resulting BEH total width is therefore:

$$\Gamma_H = \Gamma^{HD} - \Gamma^{HD}_{ZZ} - \Gamma^{HD}_{WW} + \Gamma^{Proph}_{4f}, \tag{1.76}$$

where Γ_H is the total BEH width, Γ^{HD} the BEH width obtained with HDECAY, Γ^{HD}_{ZZ} and Γ^{HD}_{WW} are the partial widths to ZZ and WW computed with HDECAY, while Γ^{Proph}_{4f} represents the partial width for $H \to 4f$ calculated with PROPHECY4F and is given by equation 1.77.

$$\Gamma^{Proph}_{4f} = \Gamma_{H\to W^*W^*\to 4f} + \Gamma_{H\to Z^*Z^*\to 4f} + \Gamma_{WW/ZZ-int}. \tag{1.77}$$

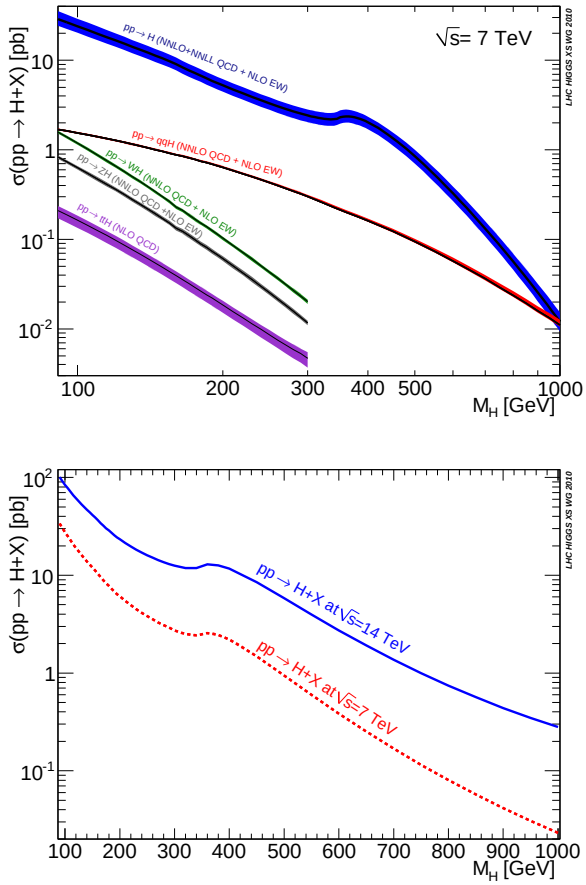

Figure 1.11: (Top) SM BEH boson production cross section for individual channels at the LHC at $\sqrt{s} = 7$ TeV and (bottom) the total production cross section at $\sqrt{s} = 7$ TeV and $\sqrt{s} = 14$ TeV [73].

The total decay width of the BEH boson is very narrow in the low mass range, $\Gamma_H < 10$ MeV, where therefore the experimental resolution (which is of the order of a GeV in the best cases where the BEH boson decays to $\gamma\gamma$ or $4l$) dominates. As the mass increases, the width becomes considerably wider: for example, for $M_H \sim 130$ GeV, Γ_H is equal to few MeV and for $M_H \backsim 1$ TeV, it reaches $\Gamma_H \backsim 700$ GeV.

In the low mass range, $110 \lesssim M_H \lesssim 130$ GeV, the BEH boson decays into a $b\bar{b}$ pair with the highest branching fraction of $\backsim 75-50\%$ for $M_H = 115-130$ GeV. However the QCD background is far too large for this decay channel to be useful at the LHC in the gluon-gluon fusion production mode. The associated production of the BEH boson with an EW boson is likely to be a more promising process to identify $H \to b\bar{b}$ decays [76]. The $H \to \tau^+\tau^-$ channel has a smaller branching ratio, about 7%, but offers a signature which can be discriminated from QCD background processes. The sensitivity is

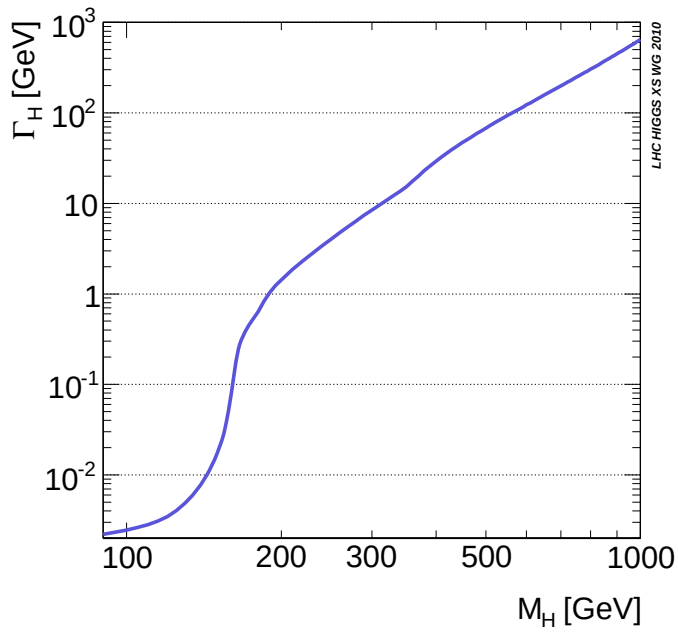

Figure 1.12: The SM BEH boson total decay width decay as a function of M_H [73].

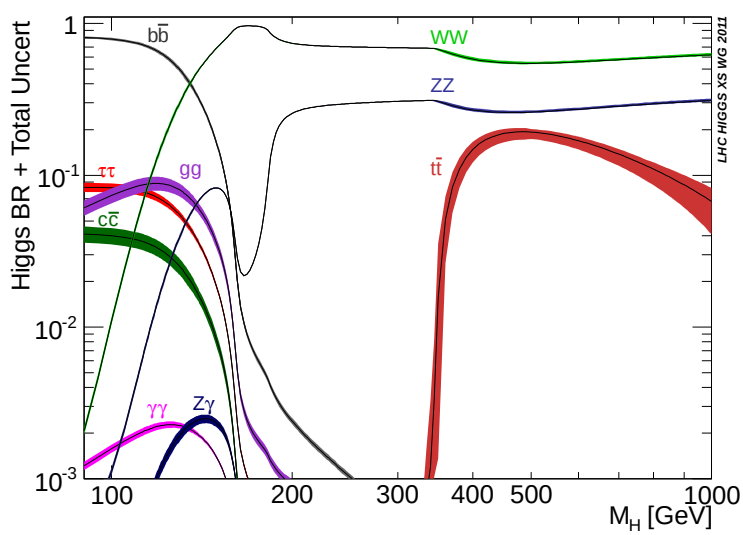

Figure 1.13: The SM BEH boson decay branching ratios as a function of M_H [77].

enhanced by requiring that the BEH boson is produced in association with jets, at NLO in the gluon fusion process and at LO in the VBF process. Despite its small branching ratio, about 0.2%, the $H \to \gamma\gamma$ is one of the most promising search channels at the LHC because it provides a good experimental

sensitivity. The signal would appear as a narrow peak over a continuum of background. This channel has been a key channel since the beginning of prospective studies at the LHC. The first analysis was done on Monte Carlo by C. Seez and J. Virdee in 1990 [82] in CMS, followed by several studies in ATLAS [83]. There were also some other studies (without proper detector simulation) at that time (and before) at SSC [84, 85, 86, 87]. All these studies follow the first papers on $H \to \gamma\gamma$ decay [88, 59, 89]. The decay of the SM scalar boson into two photons is mediated by a W boson and heavy charged fermion (mainly top) loops. The two corresponding Feynman diagrams interfer (with different signs), the amplitude corresponding to the W loop being larger.

In the intermediate mass range, 130 GeV $\lesssim M_H \lesssim$ 180 GeV, the WW decay mode of the BEH boson starts to dominate at $M_H \backsim$ 130 GeV and becomes gradually overwhelming, in particular for $2M_W \lesssim M_H \lesssim 2M_Z$ where the W boson is real while the Z boson is still virtual, strongly suppressing the $H \to ZZ^*$ mode and leading to a WW branching ratio of almost 100% as can be seen in Fig. 1.13.

In the high mass range, 180 GeV $\lesssim M_H \lesssim$ 1 TeV, $H \to WW \to l\nu qq$ becomes important, and has an advantage over the $H \to WW^{(*)} \to l\nu l\nu$ which is the ability to fully reconstruct the BEH boson mass. However the large W+jets background makes this channel less sensitive than $H \to WW^{(*)} \to l\nu l\nu$. Also a significant fraction of BEH bosons decay into two Z bosons. The $H \to ZZ^{(*)} \to l^+l^-l'^+l'^-$ decay mode, where $l, l' = e, \mu$, has the cleanest signature for the search for the BEH boson. In this "golden" channel, an excellent energy and transverse momentum resolution of the reconstructed electrons and muons, respectively, leads to a narrow four-lepton invariant mass peak on top of a smooth background. For $M_H >$ 200 GeV, $H \to ZZ \to llqq$ and $H \to ZZ \to ll\nu\nu$ become also important. Above $2m_t$, the $H \to t\bar{t}$ branching ratio is at the level of $\backsim$ 20% but it starts to decrease again to fall below 10% for $M_H \backsim$ 800 GeV, because the partial decay width into gauge bosons increases as M_H^3 while it increases as M_H when it decays into a top pair. Note that the coupling of the BEH boson to a fermion pair is $\sim g\frac{M_f}{2M_W}$ while the coupling to a W or Z pair is $\sim gM_W$ or $\sim g\frac{M_Z}{2cos\theta_W}$.

The uncertainties on the branching ratios and the total width of the SM BEH boson originate from uncertainties on the parameters α_s, m_c, m_b and m_t and from approximations in the theoretical calculations, mainly from missing high orders. The total parametric uncertainties are obtained adding the parametric errors from the four parameters variations in quadrature. The individual theoretical uncertainties for the branching ratios are added linearly. Finally, the total uncertainties are obtained by adding linearly the total parametric uncertainties and the total theoretical uncertainties. The theoretical uncertainties are more relevant for the $H \to gg$, $H \to Z\gamma$ and $H \to t\bar{t}$ branch-

ing ratios reaching 10%. Parametric uncertainties are relevant mostly for the $H \to c\bar{c}$ and $H \to gg$ branching ratios reaching 10% and 5% respectively. For the $H \to \gamma\gamma$ channel [77], the total uncertainty can reach up to about 5% in the relevant mass range, while the total uncertainty on the $H \to ZZ$ and $H \to WW$ branching ratios remains at the level of a few % over the whole mass range. The bands around the lines in Fig. 1.13 show the corresponding total uncertainties.

1.5 Beyond the SM

In spite of the impressive successes of the SM, some problems remain unexplained like the neutrino masses, baryogenesis, and dark matter. Theorists think that the SM has to be embedded within a broader theory that includes the gravitational interactions as well. The quantization of gravitation has so far led to non renormalizable local field theories. In addition, the radiative corrections to the mass of the BEH boson predicted by the SM are quadratically divergent as a function of the "cut-off" scale, Λ, and they become very large when Λ reaches the Planck scale $\sim 10^{19}$ GeV. In this latter case, the counter-term used for the renormalization needs a "fine-tuning" of about 16 orders of magnitude to obtain a BEH boson with $M_H < 1$ TeV.

Many solutions were proposed to go beyond the SM. One of the most impressive extensions of the SM is the introduction of Supersymmetry (SUSY). SUSY predicts for every type of boson a corresponding type of fermion with the same mass and internal quantum numbers and vice-versa. However, this mass spectrum is not experimentally observed, which requires to explicitly break SUSY in order to remove mass degeneracy among supersymmetric partners. Indeed, the hierarchy problem is solved in SUSY, the quadratic divergences are cancelled because of the opposite sign terms induced by the fermionic and the associated bosonic (partners of the fermions) loops, leaving only a logarithmic dependence as a function of Λ. Note that in the simplest models of SUSY, five fundamental scalar bosons are predicted, 2 charged BEH bosons ($H^{\pm}$) and 3 neutral ones (H, h, A). In addition, SUSY often predicts the dark matter whose existence is confirmed by astrophysical observations, and is not described in the SM. Indeed most of the supersymmetric models include a conserved number called R-parity [90, 91], which is 1 for ordinary matter and -1 for superpartners. There is therefore a lightest supersymmetric partner (LSP), which is often a mixture of the superpartners of weak and BEH bosons and is called the lightest neutralino. This is a stable and neutral massive particle which is a good candidate for the dark matter component of the Universe. Furthermore, in SUSY, the three couplings of $SU(3)_c$, $SU(2)_L$ and $U(1)_Y$ are better unified at high energy than in the SM, see for instance Fig. 1.14 from [92]. Finally, if SUSY is local, it incorporates gravity naturally;

this gives rise to the gauge theory of supergravity, whose ultraviolet behaviour seems to exhibit remarkable cancellations.

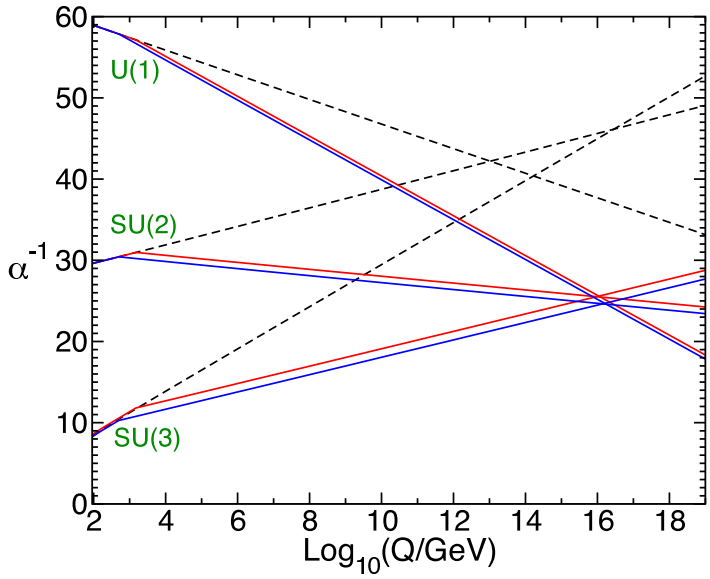

Figure 1.14: The two-loop renormalization group evolution of the inverse gauge couplings in the SM (dashed lines) and MSSM (solid lines) [92].

In addition, there are various models of composite BEH, based on an analogy with QCD and the chiral symmetry, evolving from the work of Weinberg [93] and Susskind [94]. These models will not be discussed in this thesis.

For completeness, I will say few words about two other extensions of the SM that have been studied at LHC:

- The SM4 scalar boson: an extension of the SM including a fourth generation of fermions (see for instance [95]). The additional heavy quarks in the quark loop associated with the $gg \to H$ process greatly enhance the production cross section, while other production mechanisms are not affected. Based on SM4 benchmark parameters [77], exclusion limits have been published. At the time of Moriond 2012, the most stringent limit is found by CMS [65] as shown in Fig. 1.15: the SM4 scalar boson is excluded at 95% C.L. in the range $120 - 600$ GeV.

- The fermiophobic scalar boson: in some models (see for instance [96]), the scalar boson responsible for the EW symmetry breaking does not couple to fermions therefore the production modes $gg \to H$ and $gg \to t\bar{t}H$ disappear. Direct decays $H \to \tau\tau$ and $H \to b\bar{b}$ become impossible while the branching fractions of $H \to \gamma\gamma$, $H \to WW$ and $H \to ZZ$ enhance significantly at low mass of the BEH boson. Using cross sections of [97], at the time of summer 2012, the best limit is found by CMS [98] as shown in Fig. 1.16: the fermiophobic scalar boson is excluded in the mass range $110 - 194$ GeV at

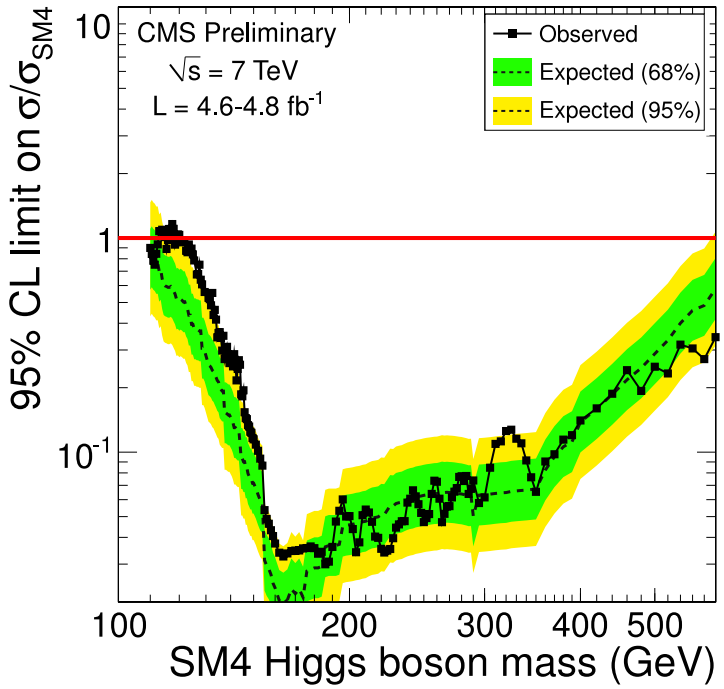

Figure 1.15: The observed and expected 95% C.L. upper limits on the ratios to the SM4 cross sections for a SM4 BEH boson hypothesis as a function of M_H [65].

95% C.L..

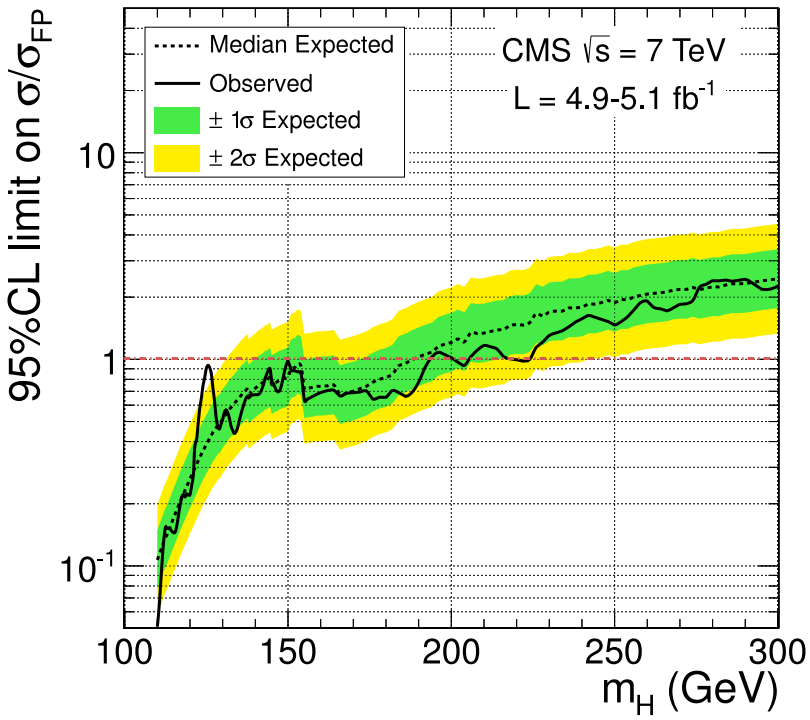

Figure 1.16: The observed and expected 95% C.L. upper limits on the ratios to the fermiophobic cross sections for a fermiophobic BEH boson hypothesis as a function of M_H [98].

Chapter 2

Statistical Methods for LHC

Contents

2.1 Test Statistic 33
2.2 χ^2 approximation 39
2.3 Asymptotic formulae 42
2.4 Profiling 46
2.5 Look-elsewhere effect 47
2.6 Energy scale uncertainties 49

The statistical procedure for data analyses in high energy physics (HEP) is crucial for excluding or discovering a new phenomena. It consists to determine whether the observed data are compatible or not with a given hypothesis and to define the degree of incompatibility. The exclusion of a given hypothesis requires a minimum confidence level of 95% i.e mostly 5% of the experiments with signal and background would be wrongly excluded (i.e being as "background-like" as the actually observed data). The discovery has even more stringent requirements. The minimal significance required to claim a discovery of a signal is set by convention to 5σ i.e among 3×10^6 background experiments, only one could fluctuate to give a similar excess. In the following, I describe briefly the statistical methods used at the LHC for discovery and setting upper limits on the scalar boson production process. For more details, see for instance [99].

2.1 Test Statistic

One of the continuous dilemmas in statistics is the Bayesian-frequentist interpretation of the probability. The Bayesian approach introduces a subjective degree of belief in a given hypothesis. It is therefore possible to consider the probability of finding the true value of an unknown parameter in a given fixed interval. However this statement does not make sense in the frequentist approach since the parameter is believed to have one and only one assigned value and cannot be represented by a probability density function (pdf). The frequentist probability is interpreted as the frequency of an outcome of a repeatable experiment. Hence, if we repeat an experiment depending on

a physical parameter whose exact value is not known, then the probability to find it in a given fixed interval would be either zero or one. For many inference problems, the frequentist and Bayesian approaches give similar numerical answers, even though they are based on fundamentally different interpretations of probability. In the HEP field, it was agreed that it is more convenient to avoid a prior knowledge assumption in the interpretation of physical results and therefore a frequentist approach is adopted. However Bayesian approach is used as a cross-check for setting exclusion limits.

The classical frequentist approach begins from defining a test statistic, t_μ, aiming to make a statement about how well the observed data stand in agreement with given predicted probabilities. It is used to test a hypothesized value of the strength parameter μ which acts as a scaling to the total rate of signal events. We often write $\mu = \sigma/\sigma_{\rm SM}$, where $\sigma_{\rm SM}$ is the SM production cross section. μ scales in general the branching ratio, the efficiency, the luminosity and the acceptance. The signal strength is defined so that $\mu = 0$ corresponds to the background-only model and $\mu = 1$ is the SM signal. In our case, the test statistic is used to discriminate signal-like from background-like events. From the Neyman-Pearson lemma, the ratio of likelihoods is the most powerful discriminator. Consider a histogram with n_i entries in the ith bin, where n_i follows a Poisson distribution with mean $\mu s_i + b_i$ with s representing the signal modeling and b the background. The binned likelihood function is written as the product of these Poisson probabilities to observe n_i (s_i signal and b_i background) events in a given bin i (N is the total number of bins):

$$L(data|\mu s + b) = \prod_{i=1}^{N} \frac{(\mu s_i + b_i)^{n_i}}{n_i!} e^{-(\mu s_i + b_i)} \tag{2.1}$$

or for an unbinned likelihood over N_{evt} events in the data sample:

$$L(data|\mu s + b) = \frac{1}{N_{evt}!} e^{-(\mu s_{tot} + b_{tot})} \prod_{i=1}^{N_{evt}} (\mu s_{tot} f_s(x_i) + b_{tot} f_b(x_i)) \tag{2.2}$$

where s_{tot} and b_{tot} are the total number of signal and background events, $f_s(x)$ and $f_b(x)$ are pdfs of signal and background of some observable x, and $data$ is either the actual observed experimental data or the generated pseudo-experiments i.e Monte Carlo simulations. The best one-dimensional test statistic in the sense of maximum power is given by the likelihood ratio:

$$\lambda_{\rm best}(\mu) = \frac{L(\mu)}{L(\mu = 0)} \tag{2.3}$$

From the definition of $\lambda_{\rm best}(\mu)$, one can see that $0 \leq \lambda_{\rm best} \leq \infty$, with $\lambda_{\rm best} > 1$ implying a better agreement between the data and the hypothesized value of

μ. Equivalently, it is more convenient to use the statistic:

$$t_{\mu,\text{best}} = -2ln\lambda_{\text{best}}(\mu) \tag{2.4}$$

as the basis of a statistical test. Lower values of $t_{\mu,\text{best}}$ correspond to an increasing compatibility between the data and the hypothesized μ.

In general, s and b are affected by systematic uncertainties (experimental and theoretical). These systematic uncertainties are treated as nuisance parameters $\boldsymbol{\theta}$ so that signal and background expectations become functions of those nuisance parameters i.e $s(\boldsymbol{\theta})$ and $b(\boldsymbol{\theta})$. There are different possible ways to treat these nuisance parameters in the statistical analysis. A hybrid Bayesian-frequentist approach was used at LEP and Tevatron. Pseudo-experiments are generated randomizing the nuisance parameters (equivalent to Bayesian marginalization) around their expected values (taken from Monte Carlo at LEP and from the best fit to the observed data at Tevatron). These nuisance parameters are then fitted at Tevatron or not at LEP. At LHC, a fully frequentist approach is used [101]. The differences between the test statistics used at LEP, Tevatron and LHC are explained in [100]. At the LHC, pseudo-experiments are generated using best fit of nuisance parameters to the observed data i.e the nuisance parameters are fixed in the generation to their conditional maximum likelihood estimate (CMLE) $\hat{\hat{\boldsymbol{\theta}}}(\mu, obs)$ for a given μ. The procedure for choosing specific values of the nuisance parameters for a given value of μ is often referred to as "profiling", $\hat{\hat{\boldsymbol{\theta}}}$ is often called the "profiled value" of $\boldsymbol{\theta}$. The nuisance parameters are constrained with constraint terms originating from auxiliary measurements which are usually modelized by a gaussian distribution $G(\boldsymbol{\theta}_0|\boldsymbol{\theta}, \delta)$ where $\boldsymbol{\theta_0}$ is the auxiliary measurement, δ the value of the uncertainty. In the generation of the pseudo-experiments, $\boldsymbol{\theta}_0$ is randomized according to $G(\boldsymbol{\theta}_0|\hat{\hat{\boldsymbol{\theta}}}(\mu, obs), \delta)$. This is the so-called "unconditional ensemble". When fitting the generated pseudo-experiments, like when fitting the observed data, the nuisance parameters are allowed to float constrained to their nominal values by the constraint terms.

Taking into account the nuisance parameters, a profile likelihood ratio is defined as:

$$\lambda_0(\mu) = \frac{L(\mu, \hat{\hat{\boldsymbol{\theta}}}(\mu))}{L(\mu = 0, \hat{\hat{\boldsymbol{\theta}}}(\mu = 0))} \tag{2.5}$$

equivalently:

$$t_\mu^0 = -2ln\lambda_0(\mu) \tag{2.6}$$

This profile likelihood ratio is used at Tevatron analyses. However, at the LHC, another profile likelihood ratio is used [102] due to its known asymptotic

properties discussed later in section 2.2 and 2.3.

$$\lambda(\mu) = \frac{L(\mu, \hat{\hat{\boldsymbol{\theta}}})}{L(\hat{\mu}, \hat{\boldsymbol{\theta}})} \tag{2.7}$$

where $\hat{\mu}$ and $\hat{\boldsymbol{\theta}}$ denote the values of the parameters that maximize the likelihood function $L(\mu, \boldsymbol{\theta})$ so-called the maximum likelihood estimator (MLE) of μ and $\boldsymbol{\theta}$. While $\hat{\hat{\boldsymbol{\theta}}}$ is the CMLE of $\boldsymbol{\theta}$ for a fixed μ. In the following, we will consider the profile likelihood ratio used at the LHC.

For purposes of discovering a new signal process, one tests the background-only hypothesis $\mu = 0$ against an alternative hypothesis including both signal and background. The test statistic t_μ with $\mu = 0$ is constructed as:

$$t_0 = \begin{cases} -2ln\frac{L(0,\hat{\hat{\boldsymbol{\theta}}}(\mu=0))}{L(\hat{\mu},\hat{\boldsymbol{\theta}})} & \text{for } \hat{\mu} \geq 0, \\ 0 & \text{if } \hat{\mu} < 0 \end{cases} \tag{2.8}$$

The condition $t_0 = 0$ if $\hat{\mu} < 0$ is imposed because one is not interested to test the downward fluctuations of the background when willing to discover a signal process. Removing this condition leads to a change of the test statistics from being one-sided to double-sided. The level of compatibility between data and $\mu = 0$ hypothesis is quantified by the following p-value:

$$p_0 = \int_{t_{0,\text{obs}}}^{\infty} f\left(t_0|0, \hat{\hat{\boldsymbol{\theta}}}(\mu = 0)\right) dt_0 \tag{2.9}$$

where $f(t_0|0)$ is the sampling distribution of the test statistic t_0 under the assumption of $\mu = 0$ obtained from background-only generated pseudo-experiments and $t_{0,\text{obs}}$ is the value of t_0 observed from the data. It is also needed to know the expectation from the SM hypothesis. This is represented by the median p_0, the so-called expected p_0, which maps one-to-one onto the expected significance. For an expected p_0, $t_{0,\text{exp}}$, that replaces $t_{0,\text{obs}}$ in equation 2.9, would be the median of $f(t_0|\mu)$ from signal+background pseudo-experiments. $\hat{\hat{\boldsymbol{\theta}}}(\mu = 0)$ are the profiled values of the nuisance parameters determined by fitting the observed data with $\mu = 0$. p_0 is the probability under the assumption of $\mu = 0$ to observe data with equal or lesser compatibility with the hypothesis $\mu = 0$ relative to the data actually obtained. A small value of p_0 is interpreted as an evidence against $\mu = 0$ i.e more signal-like data. It is more convenient to convert the p-value into an equivalent significance defined using the quantile of a unit Gaussian. It is given by:

$$Z = \Phi^{-1}(1 - p) \tag{2.10}$$

where Φ^{-1} is the inverse of the cumulative distribution for a unit Gaussian. The rejection of the $\mu = 0$ hypothesis with a significance of at least $Z = 5$ ensures a claim of discovery, this is a convention. Fig. 2.1 shows the relation between the p-value and the test statistic t_μ with $\mu \geq 0$ (left) as well as its relation with the significance Z (right). Table 2.1 gives some often used values of p-values to quantify discovery along with the corresponding significances Z.

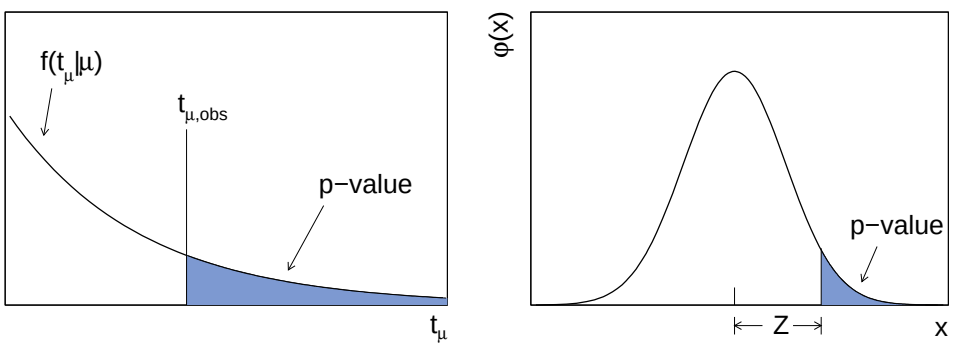

Figure 2.1: Illustration of the relation between the p-value obtained from an observed value of the test statistic t_μ (left) and its relation with the significance (right).

p-value	Z
1.587×10^{-1}	1σ
2.275×10^{-2}	2σ
1.350×10^{-3}	3σ
3.167×10^{-5}	4σ
2.867×10^{-7}	5σ
9.866×10^{-10}	6σ
1.280×10^{-12}	7σ

Table 2.1: Some often used p-values and their corresponding significances for the discovery.

For purposes of establishing an upper limit on the strength parameter μ, we consider the test statistic t_μ (equivalent to $\tilde{q}_\mu$ of [103]) defined as:

$$t_\mu = \begin{cases} -2ln\frac{L(\mu,\hat{\hat{\boldsymbol{\theta}}}(\mu))}{L(\hat{\mu},\hat{\boldsymbol{\theta}})} & \text{if } 0 \leq \hat{\mu} \leq \mu, \\ 0 & \text{if } \hat{\mu} > \mu \end{cases} \tag{2.11}$$

The reason for setting $t_\mu = 0$ for $\hat{\mu} > \mu$ is that when setting an upper limit, the relevant alternative to the μ being tested is $\mu = 0$. So the critical region of

the test is taken as values of the data that are characteristic for $\mu = 0$, i.e low values of $\hat{\mu}$. As for discovery, one quantifies the level of agreement between the data and the hypothesized μ with the p-value computed as:

$$p_\mu = \int_{t_{\mu,\text{obs}}}^{\infty} f\left(t_\mu|\mu, \hat{\hat{\boldsymbol{\theta}}}(\mu, \text{obs})\right) dt_\mu \tag{2.12}$$

where $f(t_\mu|\mu)$ is the sampling distribution of the test statistic t_μ under the assumption of the signal strength μ obtained from signal+background generated pseudo-experiments and $t_{\mu,\text{obs}}$ is the value of t_μ observed from the data. For establishing the expected upper limit, $t_{\mu,\text{obs}} \equiv t_{\mu,\text{exp}}$ would be the median of $f(t_\mu|0)$ from background-only pseudo-experiments. One also can compute the error bands integrating $f(t_\mu|\mu)$ from the median$\pm 1(2)\sigma$ ($\sim 68\%$ and $\sim 95\%$ bands) of $f(t_\mu|0)$. The confidence level (C.L.) is defined as $1 - p$-value. Typically for setting an upper limit a confidence level of at least 95% is required corresponding to an exclusion of a signal + background fluctuation with a significance of 1.64σ. Table 2.2 shows some often used values of C.L. and their corresponding significances in case of setting an exclusion limit.

C.L.	*Z*
0.90	1.282σ
0.95	1.645σ
0.975	1.960σ
0.99	2.326σ

Table 2.2: Some often used C.L. values and their corresponding significances for setting upper limits.

The method using p_μ to set exclusion limits is called CL_{s+b} method. While this method represents the right coverage and the best frequentist approach, it suffers from a problem in the limit of very small number of signal events, especially when is it is equal to zero. When $\mu = 0$, one expects, by construction, 5% of experiments will end up excluding a signal of zero strength. This is interpreted as an exclusion of a downward fluctuation of the background. Therefore, for the 2σ band, we can exclude a $\mu = 0$ hypothesis at a C.L. greater than 95% C.L.. Another technique was introduced at the time of LEP and used also later at Tevatron to prevent the exclusion of a parameter value for which one has no sensitivity is the CL_s [104, 105]. The CL_s method is a modified frequentist approach estimated from a ratio of probabilities: p_μ and $1-p_b$, where p_b is the p-value of the t_μ distribution under the background-only hypothesis:

$$p_b = 1 - \int_{t_{\mu,\text{obs}}}^{\infty} f\left(t_\mu|0, \hat{\hat{\boldsymbol{\theta}}}(\mu = 0, \text{obs})\right) dt_\mu \tag{2.13}$$

The CL_s upper limit is defined using the p-value p'_μ:

$$p'_\mu = \frac{p_\mu}{1 - p_b} \tag{2.14}$$

The procedure results in a coverage probability that is in general greater than $1 - p'_\mu$. The amount of over coverage is not immediately obvious; however, for small values of μ the coverage is near 97.5% (due to $\langle p_b \rangle \sim 1/2$) and for large values of μ the coverage is near the nominal 95% (due to $\langle p_b \rangle \sim 0$). Another technique which was used at some point is the modified CL_{s+b} where the $+2\sigma$ band of the CL_{s+b} is truncated. It is called the power constrained limit (PCL) [106]. In addition the observed limit is not allowed to go below the expected median limit for a 50% power recommendation.

2.2 χ^2 approximation

The prescription described above using the pseudo-experiments is not practical from the computational point of view due to the high CPU demand: one would have to generate more than 10^7 pseudo-experiments to test a 5σ fluctuation corresponding to a p-value of 2.85×10^{-7}. Therefore it was very important to find an asymptotic approximation of the sampling distributions $f(t_0|0)$ and $f(t_\mu|\mu)$. For a sufficiently large data sample and in case $\hat{\mu}$ is Gaussian distributed, Wilks' theorem [107] states that the pdf of a test statistic $f(t_\mu|\mu)$ with $\mu \geq 0$ follows a χ^2 distribution for one degree of freedom given by:

$$f_{\chi^2_1}(t_\mu) = \frac{1}{\sqrt{2\pi}} \frac{1}{\sqrt{t_\mu}} e^{-t_\mu/2} \tag{2.15}$$

This theorem generalizes to more than one parameter of interest. For n parameters of interest, the test statistic follows a χ^2 distribution for n degrees of freedom. The condition $t_0 = 0$ ($t_\mu = 0$) if $\hat{\mu} < 0$ ($\hat{\mu} > \mu$) for discovery (setting upper limits) leads to a delta function $\delta(t_0)$ ($\delta(t_\mu)$) at 0 in half of the cases. Therefore the test statistic is described by a sum of a delta function and a χ^2 weighted by 0.5:

$$f(t_\mu|\mu) = \frac{1}{2}\delta(t_\mu) + \frac{1}{2} f_{\chi^2_1}(t_\mu) \tag{2.16}$$

(similarly for $f(t_0|0)$).

This approximation is valid for sufficiently large data samples i.e for high luminosities experiments. In the case of low statistics, important deviations of the test statistic distribution $f(t_\mu|\mu)$ with $\mu > 0$ from the one half-chi-square function ($1/2\ f_{\chi^2_1}(t_\mu)$) are observed, breaking down the validity of the approximation. In this thesis, a study was made to show that this could be avoided, following the original idea by M. Kado, by redefining the test statistic

allowing the estimator $\hat{\mu}$ to take on negative values [108]. The redefined test statistic q_μ can therefore be written as:

$$q_\mu = \begin{cases} -2ln\frac{L(\mu,\hat{\hat{\boldsymbol{\theta}}}(\mu))}{L(\hat{\mu},\hat{\boldsymbol{\theta}})} & \text{if } -\infty < \hat{\mu} \leq \mu, \\ 0 & \text{if } \hat{\mu} > \mu \end{cases} \tag{2.17}$$

The study was based on the spirit of setting exclusion limits. The signal and background probability density functions were chosen according to the $H \rightarrow \gamma\gamma$ analysis. A signal model of Crystal-Ball + gaussian and a simple exponential for the background are used. The normalization of background and the slope of the exponential are considered as nuisance parameters. In order to validate the approximation down to low luminosities, the redefined test statistic distribution from signal+background Monte Carlo generated samples are compared to the 1/2 $f_{\chi_1^2}(q_\mu)$ function. Monte Carlo samples with N_{bkg} background events and $N_{sig} = \mu' S_{SM}$ signal events (where μ' is the strength parameter in the generation), are simulated in both cases of $\mu' = \mu$ (sigToys) and $\mu' = 0$ (bkgToys). The fit of these generated samples is made once by fixing μ and once by leaving μ floating. Fig. 2.2 shows the q_μ distributions for sigToys and bkgToys for luminosities of 0.2 fb^{-1} (top) and 0.05 fb^{-1} (bottom). A 1/2 $f_{\chi_1^2}(q_\mu)$ function is superimposed to the sigToys distribution. One can see the good fitting of the sigToys q_μ distribution with the 1/2 $f_{\chi_1^2}(q_\mu)$ function even at low luminosities.

In order to quantify the validity of this approximation, p-values are compared between two methods. The first method relies on Monte Carlo simulated events, it consists on counting the number of sigToys events from the median of bkgToys distribution up to infinity. Normalizing this number to the total number of sigToys, one obtains the corresponding p_μ. The second method integrates the 1/2 $f_{\chi_1^2}(q_\mu)$ function from the median of the bkgToys to infinity. This integral is divided by the total integral to obtain the p-value. Moreover, the same procedure is done from the median+1σ and median+2σ of the bkgToys to see the impact on the error bands.

Table 2.3 shows the $1-p$-values or C.L.(%) for both methods for a luminosity of 0.2 fb^{-1}. A comparison between the test statistics t_μ and q_μ for each method is also shown. The median expected limit is in a good agreement between all the cases. However if one considers the C.L.(1σ) and C.L.(2σ) for t_μ, one sees the breaking of the approximation validity while it is recovered with the new test statistic q_μ.

Another study was made to compare the test statistics q_μ and t_μ^0 defined in equation 2.6. The correlation between these two statistics is shown in Fig. 2.3 for $\mu = 1$ for q_μ (t_μ^0) values of sigToys above the median of q_μ (t_μ^0) of bkgToys. The computed p-values were found to be almost equal for both test statistics. They give similar median values for exclusion limits as well as for the band

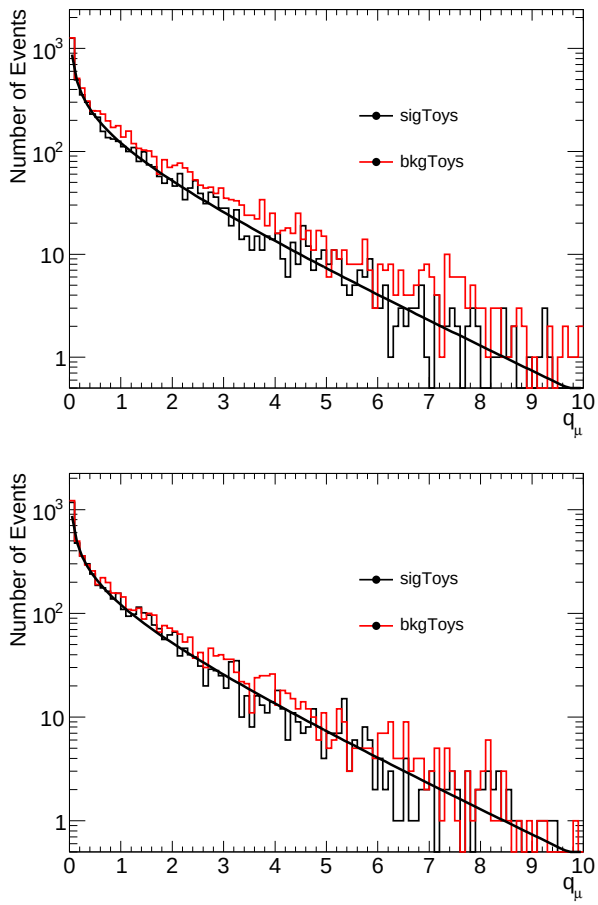

Figure 2.2: Redefined test statistic distribution q_μ for signal+background (sigToys) and background-only Monte Carlo simulations (bkgToys) for a luminosity of 0.2 fb^{-1} (top) and 0.05 fb^{-1} (bottom). A 1/2 $f_{\chi^2_1}(q_\mu)$ distribution is superimposed to the distribution corresponding to signal+background simulated events.

	t_μ		q_μ	
	Counting	1/2 $f_{\chi^2_1}(t_\mu)$	Counting	1/2 $f_{\chi^2_1}(q_\mu)$
Median	60.04	60.07	60.03	60.10
Median+1σ	89.22	76.63	89.12	89.37
Median+2σ	98.86	84.16	98.87	98.86

Table 2.3: Comparison of C.L. values (%) for t_μ and q_μ test statistics computed using two methods: counting the Monte Carlo signal+background simulated events and integrating $\frac{1}{2}$ $f_{\chi^2_1}(t_\mu)$ ($\frac{1}{2}$ $f_{\chi^2_1}(q_\mu)$)approximation from the median (+1σ, +2σ) of the background-only samples.

errors. For high values of μ, i.e around 16, a small difference is seen but has a negligible impact on the final results. However t_μ^0 is not used in the LHC statistical analyses, it is used at Tevatron.

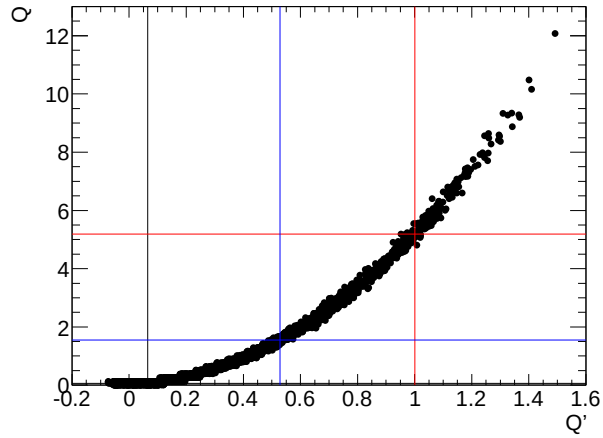

Figure 2.3: The correlation between t_μ^0 (Q) and q_μ (Q') for $\mu = 1$.

2.3 Asymptotic formulae

As described above, it is convenient to approximate the distributions $f(q_0|0)$ and $f(q_\mu|\mu)$ with a 1/2 $f_{\chi_1^2}(q_\mu)$ distribution. In order to estimate the observed p_0 or to set an observed upper limit, it would be sufficient to integrate the χ^2 distribution from the value $q_{0,\text{obs}}$ or $q_{\mu,\text{obs}}$ up to infinity normalized to the total integral. However to estimate the expected p_0 or to set an expected upper limit, it would be necessary to generate signal+background pseudo-experiments (for discovery) and background-only pseudo-experiments (for setting upper limits) in order to determine the corresponding median from which one would integrate the χ^2 distribution. The generation of pseudo-experiments remains time and CPU consuming. Therefore, another important approximation was the so-called "Asimov dataset".

The "Asimov dataset" is a single artificially reconstructed representative dataset in which all the statistical fluctuations are suppressed. The values of n in equation 2.1 are replaced by their expectation values for a given integrated luminosity and a hypothesized strength parameter μ_A. Usually, for discovery $\mu_A = 1$ and for setting upper limits $\mu_A = 0$. Note also that an unbinned likelihood can be interpreted as a limiting case of a binned likelihood when the bin size goes to zero, as it is the case for the $H \to \gamma\gamma$ analysis at the LHC. The Asimov dataset is generated with a number of

events proportional to the fitted nuisance parameters on data for a given value of μ (this will be discussed in the next section).
The expected test statistic is therefore obtained from the profile likelihood ratio for an Asimov defined as:

$$\lambda_A(\mu) = \frac{L_A(\mu, \hat{\hat{\boldsymbol{\theta}}})}{L_A(\hat{\mu}, \hat{\boldsymbol{\theta}})} = \frac{L_A(\mu, \hat{\hat{\boldsymbol{\theta}}})}{L_A(\mu', \boldsymbol{\theta})} \tag{2.18}$$

where $\hat{\mu}$ is supposed to follow a Gaussian distribution with a mean μ' and a standard deviation σ. The final equality says explicitly that the estimators for the parameters are equal to their hypothesized values.
In the following, I will introduce the asymptotic formulae for discovery and setting upper limits using an Asimov dataset and the observed data, taken from [103].

Consider a test of the strength parameter μ, which can either be zero (for discovery) or nonzero (for an upper limit), and suppose the data distributed according to a strength parameter μ' (which is in general $\mu' = \mu$), the distribution $f(q_\mu|\mu')$ can be found using a result due to Wald [109], who showed that for the case of a single parameter of interest:

$$q_\mu = -2ln\lambda(\mu) = \frac{\mu - \hat{\mu}}{\sigma^2} + \mathcal{O}(1/\sqrt{N}) \tag{2.19}$$

where $\hat{\mu}$ follows a Gaussian distribution with a mean μ' and a standard deviation σ and N represents the data sample size. In the limit of large N, the test statistic follows a noncentral χ^2 distribution for one degree of freedom with the noncentrality parameter $\Lambda = (\mu - \mu')^2/\sigma^2$. For the special case $\mu' = \mu$, the test statistic follows a χ^2 distribution ($\Lambda = 0$) for one degree of freedom, one gets back the Wilks' theorem.

To determine the variance of the $\hat{\mu}$ distribution, one may use the method of Fisher matrix constructed from the second derivatives of the log-likelihood function or use the formula of Wald:

$$\sigma^2 = \frac{(\mu - \mu')^2}{q_\mu} \tag{2.20}$$

This is usually used to find the exclusion sensitivity for the hypothesis μ assuming that there is no signal i.e $\mu' = 0$.

From equation 2.19, one can rewrite the test statistic q_0 for discovery as:

$$q_0 = \begin{cases} \hat{\mu}^2/\sigma^2 & \text{if } \hat{\mu} \geq 0, \\ 0 & \text{if } \hat{\mu} \leq 0 \end{cases} \tag{2.21}$$

The pdf of q_0 has the form:

$$\begin{aligned} f(q_0|\mu') &= \left(1 - \Phi\left(\frac{\mu'}{\sigma}\right)\right)\delta(q_0) \\ &+ \frac{1}{2}\frac{1}{\sqrt{2\pi}}\frac{1}{\sqrt{q_0}}\exp\left[-\frac{1}{2}\left(\sqrt{q_0} - \frac{\mu'}{\sigma}\right)^2\right] \end{aligned}$$

The corresponding cumulative distribution is written as:

$$F(q_0|\mu') = \Phi\left(\sqrt{q_0} - \frac{\mu'}{\sigma}\right) \tag{2.22}$$

For the important case $\mu' = 0$, one can write the distribution as in equation 2.16:

$$f(q_0|0) = \frac{1}{2}\delta(q_0) + \frac{1}{2}\frac{1}{\sqrt{2\pi}}\frac{1}{\sqrt{q_0}}e^{-q_0/2} \tag{2.23}$$

The corresponding cumulative distribution is therefore written as:

$$F(q_0|0) = \Phi(\sqrt{q_0}) \tag{2.24}$$

The p-value of the $\mu = 0$ hypothesis is:

$$p_0 = 1 - F(q_0|0) \tag{2.25}$$

and therefore the corresponding significance can be written as:

$$Z_0 = \Phi^{-1}(1 - p_0) = \sqrt{q_0} \tag{2.26}$$

To summarize, for the observed test statistic $q_{0,\text{obs}}$ one obtains the observed value of $p_{0,\text{obs}}$ using the following equation:

$$p_{0,\text{obs}} = 1 - \Phi(\sqrt{q_{0,\text{obs}}}) \tag{2.27}$$

and the corresponding observed significance is given by:

$$Z_{0,\text{obs}} = \sqrt{q_{0,\text{obs}}} \tag{2.28}$$

The median significance is deduced from the test statistic $q_{0,A}$ obtained from the Asimov dataset (generated with $\mu_A = 1$):

$$Z_{0,\text{exp}} = \sqrt{q_{0,A}} \tag{2.29}$$

Similarly for establishing upper limits, one can write:

$$q_\mu = \begin{cases} (\mu - \hat{\mu})^2/\sigma^2 & \text{if } \hat{\mu} < \mu, \\ 0 & \text{if } \hat{\mu} > \mu \end{cases} \tag{2.30}$$

The distribution of q_μ is given by:

$$\begin{aligned} f(q_\mu|\mu') &= \Phi\left(\frac{\mu'-\mu}{\sigma}\right)\delta(q_\mu) \\ &+ \frac{1}{2}\frac{1}{\sqrt{2\pi}}\frac{1}{\sqrt{q_\mu}}\exp\left[-\frac{1}{2}\left(\sqrt{q_\mu}-\frac{\mu-\mu'}{\sigma}\right)^2\right] \end{aligned}$$

The corresponding cumulative distribution is written as:

$$F(q_\mu|\mu') = \Phi\left(\sqrt{q_\mu}-\frac{\mu-\mu'}{\sigma}\right) \tag{2.31}$$

For the important case $\mu' = \mu$, one can write the distribution as in equation 2.16:

$$f(q_\mu|\mu) = \frac{1}{2}\delta(q_\mu) + \frac{1}{2}\frac{1}{\sqrt{2\pi}}\frac{1}{\sqrt{q_\mu}}e^{-q_\mu/2} \tag{2.32}$$

The corresponding cumulative distribution is written as:

$$F(q_\mu|\mu) = \Phi(\sqrt{q_\mu}) \tag{2.33}$$

The p-value of the μ hypothesis is:

$$p_\mu = 1 - F(q_\mu|\mu) \tag{2.34}$$

and therefore the corresponding significance can be written as:

$$Z_\mu = \Phi^{-1}(1-p_\mu) = \sqrt{q_\mu} \tag{2.35}$$

For setting an observed CL_{s+b} upper limit we solve the following equation:

$$p_{\mu,\text{obs}} = 1 - \Phi(\sqrt{q_{\mu,\text{obs}}}) = \alpha \tag{2.36}$$

equivalently,

$$\sqrt{q_{\mu,\text{obs}}} = \Phi^{-1}(1-\alpha) \tag{2.37}$$

and since $\sqrt{q_{\mu,\text{obs}}} = (\mu-\hat{\mu})/\sigma$,

$$\mu_{\text{up,obs}} = \hat{\mu} + \sigma\Phi^{-1}(1-\alpha) \tag{2.38}$$

The CL_s upper limit is obtained by solving the equation:

$$p'_{\mu,\text{obs}} = \frac{p_{\mu,\text{obs}}}{1-p_b} = \alpha \tag{2.39}$$

$1 - p_b = CL_b$ is equal to $F(q_0|0)$ (see equation 2.34). Replacing $\mu' = 0$ in equation 2.31, one gets:

$$CL_b = \Phi\left(\frac{\mu}{\sigma} - \sqrt{q_{\mu,\text{obs}}}\right) \tag{2.40}$$

σ is obtained from equation 2.20 using the Asimov dataset generated with $\mu_A = \mu' = 0$. Finally we have:

$$CL_b = \Phi\left(\sqrt{q_{\mu,A}} - \sqrt{q_{\mu,\text{obs}}}\right) \tag{2.41}$$

and:

$$p'_{\mu,\text{obs}} = \frac{1 - \Phi(\sqrt{q_{\mu,\text{obs}}})}{\Phi\left(\sqrt{q_{\mu,A}} - \sqrt{q_{\mu,\text{obs}}}\right)} = \alpha \tag{2.42}$$

For setting an expected CL_{s+b} median upper limit we solve the following equation:

$$p_{\mu,\text{exp}} = 1 - \Phi(\sqrt{q_{\mu,A}}) = \alpha \tag{2.43}$$

Recalling that $\sqrt{q_{\mu,A}} = \mu_{\text{up,exp}}/\sigma$, one gets:

$$\mu_{\text{up,exp}} = \sigma\Phi^{-1}(1 - \alpha) \tag{2.44}$$

The median CL_s upper limit is obtained by solving:

$$p'_{\mu,\text{exp}} = \frac{p_{\mu,\text{exp}}}{1 - p_b} = \alpha \tag{2.45}$$

where $1 - p_b = 1/2$. One obtains therefore:

$$\mu_{\text{up,exp}} = \sigma\Phi^{-1}(1 - 0.5\alpha) \tag{2.46}$$

Moreover, one can deduce the $N\sigma$ (with N a negative or positive integer) error CL_{s+b} bands for which $\hat{\mu} = N$ and therefore $\sqrt{q_\mu} = (\mu_{\text{upN}\sigma} - N)/\sigma$:

$$\mu_{\text{upN}\sigma} = \sigma(\Phi^{-1}(1 - \alpha) + N) \tag{2.47}$$

and the CL_s error bands:

$$\mu_{\text{upN}\sigma} = \sigma(\Phi^{-1}(1 - \alpha\Phi(N)) + N) \tag{2.48}$$

since $CL_b = \Phi(N)$.
Usually one sets α to 0.05 to get the threshold of 95% C.L. upper limits.

2.4 Profiling

As already described above, the nuisance parameters are profiled for a given value of the strength parameter μ in the generation of the Asimov dataset. There could be several ways to profile the nuisance parameters *i.e* for different

hypotheses μ. Fig. 2.4 shows the comparison of different profiling methods when testing $\mu = 0$. This plot is based on the ATLAS $H \to \gamma\gamma$ analysis described in details in section 6.2.3. A spurious signal term (SS) is added to the signal part of the considered likelihood to take into account for the bias of fitting the data with an exponential to model the background. This SS is fixed to zero in the generation of the Asimov unless otherwise specified.

Profiling at $\mu = 0$ all the nuisance parameters and fixing the spurious signal term to zero in the generation of the Asimov is the baseline procedure in the ATLAS $H \to \gamma\gamma$ analysis.
Another way of profiling is to choose $\mu = \hat{\mu}$, this gives similar results as the profiling at $\mu = 0$ if the signal-related nuisance parameters were fixed to zero in the generation of the Asimov. If not, the curve shows small fluctuations around the one where the profiling is done at $\mu = 0$.
Larger fluctuations are observed when profiling at $\mu = 1$ (fixing or not the spurious signal term). This can be explained by looking at the fitted values of μ. For instance, for masses around 126 GeV where an excess of events was observed in this channel, the value of $\hat{\mu}$ is about twice larger than the SM hypothesis $\mu = 1$. In order to compensate for this difference ($\mu = 1$ and $\hat{\mu} = 2$), the fit tends to increase the values of the parameters which are scaled by μ, for example the efficiency. The efficiency will take therefore a value larger than the one nominally computed for a SM BEH boson. This leads to an increase of the number of signal events in the generated Asimov and consequently an increase of the sensitivity, *i.e* a decrease of the p_0. The choice of the profiling method of the nuisance parameters at $\mu = 0$ in the generation of the Asimov was justified by the smoothness of the expected sensitivity curve *i.e* by minimizing its dependence on the data fluctuations.
In the ATLAS combination of different SM BEH decay channels, the profiling of these nuisance parameters is still done at $\mu = 1$. It is also the case for CMS analyses.

2.5 Look-elsewhere effect

When searching for a new resonance within some possible mass range, as it is the case for the scalar boson, the significance of observing a local excess of events has to take into account the probability that an excess of events anywhere in the range could equally be considered as a signal. This is the so-called "look-elsewhere effect" (LEE). The model in this case consists of a background distribution B and a signal distribution $S(m)$ where m is the unkown mass location parameter of the resonance and it is given by $\mu S(m)+B$. The mass m is a nuisance parameter which does not exist under the hypothesis $\mu = 0$ since B does not depend on m. The test statistics in this case does not

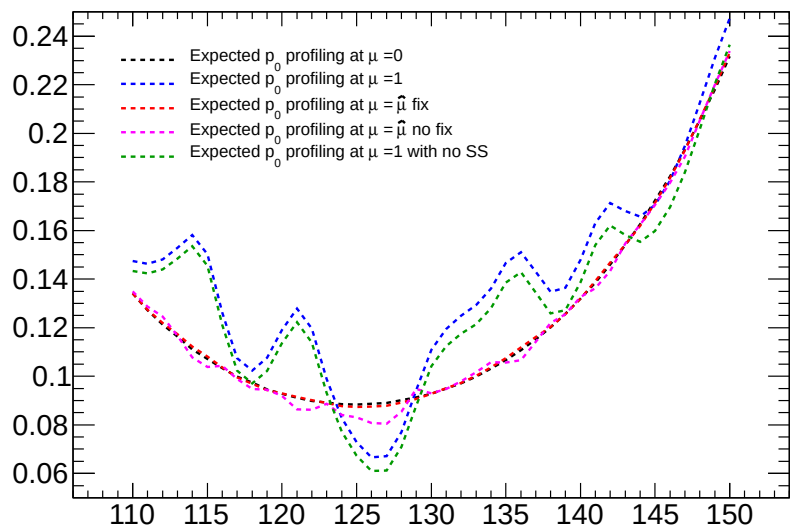

Figure 2.4: Comparison of expected p_0 with different profiling of the nuisance parameters as a function of the BEH mass.

follow the Wilks' theorem because there is a nuisance parameter present only under the alternative. We define $q(m_{\text{fix}})$ as a test statistic for a fixed mass m_{fix}, it follows a χ^2 distribution with s degrees of freedom (in our case $s = 1$). The global test statistic to be associated with the search of the largest excess of events above the background in the entire range is defined by:

$$q(\hat{m}) = max_m[q(m_{\text{fix}})] \tag{2.49}$$

The p-value of the global test statistic can be written as follows:

$$P(q(\hat{m}) > c) \leq P(\chi^2_s > c) + \langle N(c) \rangle \tag{2.50}$$

where $N(c)$ is the number of upcrossings of the level c by the test statistic $q(m_{\text{fix}})$. It is proposed in [110] to express $\langle N(c) \rangle$ as a function of $\langle N(c_0) \rangle >$ defined as the number of upcrossings at some low reference level c_0:

$$P(q(\hat{m}) > c) \leq P(\chi^2_s > c) + \langle N(c_0) \rangle \left(\frac{c}{c_0} \right)^{(s-1)/2} e^{-(c-c_0)/2} \tag{2.51}$$

$\langle N(c_0) \rangle$ is determined by counting the number of upcrossings in a small set of background-only Monte Carlo simulations or by counting the number of upcrossings observed in the data. c_0 is chosen to be as low as possible but still significantly larger than the numerical resolution of $q(m_{\text{fix}})$ and the typical distance between the upcrossings should be kept significantly larger than the

mass resolution. For very large values of c, the bound is expected to become an equality, so the global p-value for the particular case $s = 1$ is given by:

$$P(q(\hat{m}) > c) \sim P(\chi^2 > c) + \langle N(c_0)\rangle e^{-(c-c_0)/2} \tag{2.52}$$

On the other hand, it was noticed in [110] that $\langle N(c)\rangle$ is asymptotically (for very large values of c) propotional to the probability $P(\chi^2_{s+1} > c)$. The global p-value could be written as:

$$P(q(\hat{m}) > c) \sim P(\chi^2_s > c) + \mathcal{N} P(\chi^2_{s+1} > c) \tag{2.53}$$

where $\mathcal{N} = \langle N(c)\rangle / P(\chi^2_{s+1} > c)$ is interpreted as an "effective number" of independent search regions in the considered mass range.

It is also useful to describe the LEE in terms of a trial factor (TF) which is the ratio between the global p-value and the local one. TF is therefore given by:

$$\begin{aligned} TF &= \frac{P(q(\hat{m}) > c)}{P(q(m_{\text{fix}}) > c)} \\ &\sim 1 + \mathcal{N}\frac{P(\chi^2_{s+1} > c)}{P(\chi^2_s > c)} \end{aligned}$$

For $s = 1$, $c = Z^2_{\text{fix}}$ where Z_{fix} is the significance at a given mass. For $c \gg s$ one can write:

$$TF \sim 1 + \sqrt{\frac{\pi}{2}}\mathcal{N} Z_{\text{fix}} \tag{2.54}$$

Asymptotically, the TF is proportional to both the fixed-mass significance and the effective number of independent regions $\mathcal{N}$. This formula was validated using pseudo-experiments in [110] and with more statistics by A. Read in [111, 112]. The agreement is found to be very good at large values of c, as shown in Fig. 2.5, where the signal model used is a Gaussian with a fixed width and the total mass range size is 14 times larger than the width of the signal. The distribution of $q(m_{\text{fix}})$ follows a χ^2 with one degree of freedom while $q(\hat{m})$ is different from $q(m_{\text{fix}})$ and it follows a χ^2 with two degrees of freedom for $Z^2 \gtrsim 4$.

2.6 Energy scale uncertainties

The photon and electron energy scale systematic (ESS) uncertainties, decribed in section 4.3, are applied on the invariant mass peak position. In the limit of very large energy scale uncertainties, an invariant mass peak could occur

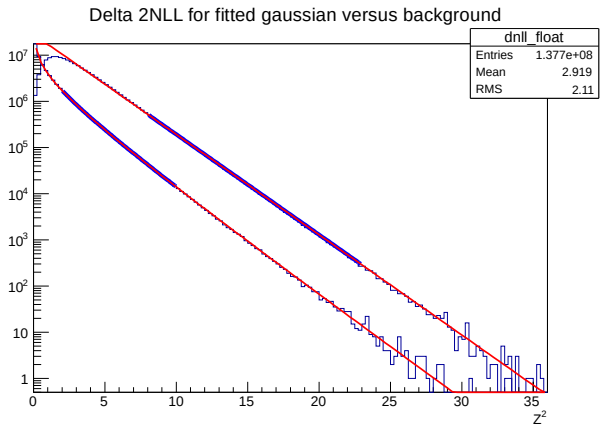

Figure 2.5: $q(m_{\text{fix}})$ and $q(\hat{m})$ distibutions as a function of $c = Z^2$. The fitted regions in blue correspond to a χ^2 function with one degree of freedom for the fit of $q(m_{\text{fix}})$ (bottom) and with two degrees of freedom for the fit of $q(\hat{m})$ (top). The red curves show the extrapolation of the fit in blue [112].

almost anywhere within the uncertainty range [113]. It is essentially equivalent to the look-elsewhere effect. In general, the ESS have only a small impact on the mass position, i.e a mass uncertainty of ~ 0.6 GeV, and therefore the size of the mass range to be considered for LEE is small and equal to this mass uncertainty. The presence of the ESS leads to a small deviation in the distribution of the test statistic from a χ^2 distribution. The minimum local p-value is corrected to the global p-value via equation 2.52. The average number of upcrossings at a given low threshold c_0, $\langle N(c_0)\rangle$, can be estimated by fitting the sum of a χ^2 and a falling exponential to the distribution of the test statistic obtained from a large number of pseudo-experiments. Equation 2.52 is then used to extrapolate the global p-value at higher significance values [114, 115, 116]. There is no more need to generate pseudo-experiments at high significance values which is impractical computationally. This hybrid ensemble-asymptotic approach was validated with a large number of generated pseudo-experiments in [117] and shown to accurately reproduce the p-values.

Chapter 3

ATLAS Detector

Contents

3.1 LHC **51**
3.1.1 LHC machine 51
3.1.2 LHC running 53
3.1.3 LHC performances 53
3.2 ATLAS Detector **57**
3.2.1 The ATLAS Coordinate System 58
3.2.2 The Inner Detector 60
3.2.3 Calorimeters 65
3.3 CMS Detector **74**

3.1 LHC

3.1.1 LHC machine

The Large Hadron Collider (LHC) is the largest instrument ever designed [118, 119] and built for scientific research. It is mainly a proton-proton collider with a nominal center-of-mass energy $\sqrt{s} = 14$ TeV and a design luminosity of $10^{34} cm^{-2} s^{-1}$. A detailed historical review of the LHC can be found in [120, 121]. The LHC is located in the LEP tunnel close to Geneva which has a circumference of 27 km and is lying between 50 and 170 m below the surface. The LHC relies on superconducting magnets cooled down to temperatures below 2 K, using superfluid Helium, and operating at fields of 8.4 T at the nominal center-of-mass energy. The magnet system consists of a total 9593 magnets of which 1232 are main superconducting dipoles (the superconductor material is $NbTi$) each having a length of 14.4 m and a mass of 35 tonnes. The LHC injector complex is shown in Fig. 3.1. The protons produced by a duoplasmatron source at 100 keV are injected in the chain: Linac2 (80 m long linear accelerator) and get accelerated up to 50 MeV - Proton Synchrotron Booster (PSB) (157 m circular accelerator) up to 1.4 GeV - Proton Synchrotron (PS) (628 m ring accelerator) up to 26 GeV - Super Proton Synchrotron (SPS) (6.9 km long circular accelerator lying 50 m underground) up to 450 GeV before reaching the LHC.

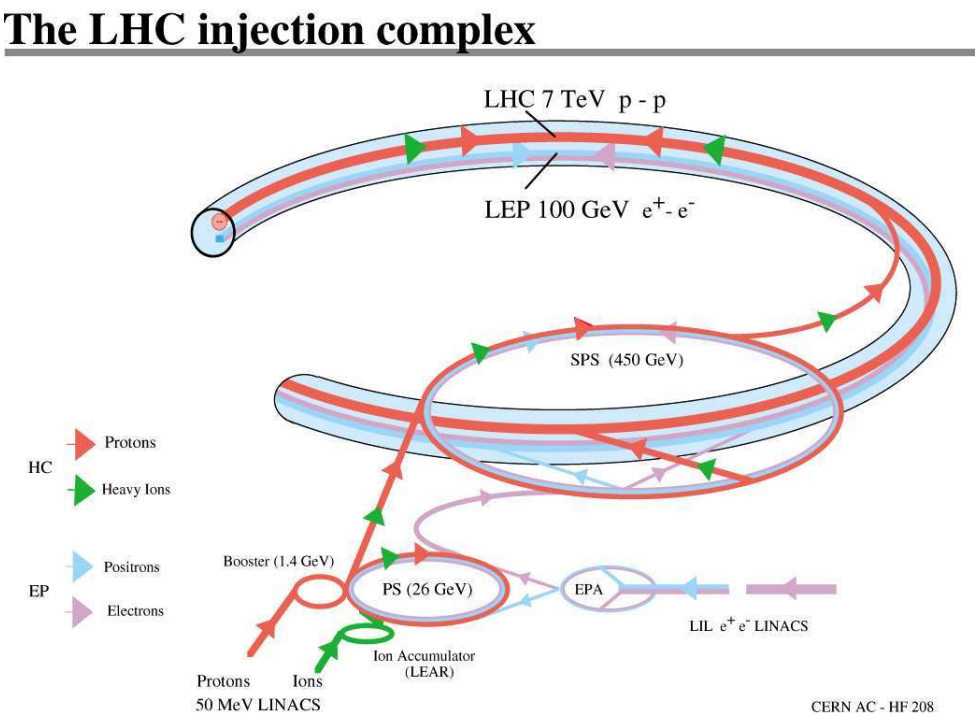

Figure 3.1: The LHC injection complex.

There are six experiments at the LHC:

- Two high luminosity experiments ATLAS [122] (A Toroidal LHC ApparatuS) and CMS [123] (Compact Muon Solenoid) are general purpose experiments: search for new physics, search for the fundamental scalar boson, precision measurements, etc. The description of these detectors will be presented below;

- A lower luminosity experiment LHCb [124] (Large Hadron Collider beauty) aiming for studies about B-physics;

- One heavy ion experiment ALICE [125] (A Large Ion Collider Experiment) optimized for the physics from heavy ions (^{208}Pb) collisions. Its main aim is the study of the quark-gluon plasma;

- LHCf [126] (Large Hadron Collider forward) measuring particles at small angles (very close to the beam line) in order to simulate cosmic rays in laboratory conditions and TOTEM [127] (TOTal cross section, Elastic scattering and diffraction Measurement at the LHC) measuring the total proton-proton cross section and diffractive processes respectively.

3.1.2 LHC running

The first beams in the LHC occured on September 10th 2008. Few days later, on September 19th 2008, a major incident happened due to a failure of superconducting connection between two magnets. This was followed by one year of major repairs and consolidation, with a new quench protection. On 20th of November 2009, first collisions were recorded at a center of mass energy of 900 GeV and in December 2009 the center of mass energy increased to 2.36 TeV. First collisions at 7 TeV occured on March 30th 2010. The total integrated luminosity during 2010 run reached $\sim 40pb^{-1}$. On May 2011, the instantaneous luminosity exceeded 10^{33} $cm^{-2}s^{-1}$, and the total delivered integrated luminosity in 2011 was ~ 5.61 fb^{-1}. During 2012, proton-proton collisions occured at a center-of-mass energy $\sqrt{s} = 8$ TeV and a maximum instantaneous luminosity $\sim 7 \times 10^{33}$ $cm^{-2}s^{-1}$. The proton-proton collisions are scheduled until December 2012 in order to collect an integrated luminosity of ~ 25 fb^{-1} per experiment. A technical stop will follow for the years 2013-2014, in particular for splice consolidation. It will resume in the end of 2014 at (almost) the nominal center-of-mass energy (13 or 14 TeV) and at the nominal luminosity for three years. After a second technical stop during the 2018 year, for injector upgrade, the LHC will resume again for three other years (between 2019 and 2021) at a luminosity about twice the nominal one. Then a two years stop is scheduled (2022-2023) for major upgrades of the CERN accelerator system (and of the experiments) in order to get about 3000 fb^{-1} per experiment for 2030. For further details, see [128]. In addition, there are also long term research and development aiming at having more powerful magnets with Nb_3Sn instead of $NbTi$ and therefore a higher energy [129].

3.1.3 LHC performances

In general, in a particle collider the most important performance parameters are the center-of-mass energy, which is controlled by the colliding beams, and the rate of useful interactions, so-called number of "events" per second. The rate (R_{inel}) is related to the inelastic cross section (σ_{inel}) of the proton-proton collision by a factor of proportionality, the instantaneous luminosity (L):

$$R_{inel} = L.\sigma_{inel} \tag{3.1}$$

The measurement of the instantaneous luminosity is therefore a very important task at the LHC. For the ATLAS detector, the luminosity per bunch crossing ID (BCID) is measured with different ATLAS devices like LUCID (LUminosity using Cerenkov Integrating Detector) and BCM (Beam Condition Monitor):

$$L_{BCID} \sim \frac{\mu_{vis}.f_{rev}}{\sigma_{vis}} \tag{3.2}$$

where:

- μ_{vis} is the average number of visible interactions measured per BCID;
- f_{rev} is the revolution frequency (11.245 kHz corresponding to the circumference of 26.7 km);
- σ_{vis} is the visible inelastic cross section calibrated by Van der Meer scans [130].

For more details, see [131] and [132].

The absolute luminosity (L) of the equation 3.1 is given by (assuming that all the BCIDs have the same luminosity):

$$L = L_{BCID}.\kappa_b \tag{3.3}$$

where κ_b is the number of bunches per beam (nominally 2808 for a 25 ns bunch spacing, at the end of 2011 we had roughly the half of this number since we had 50 ns of bunch spacing).

The relative systematic uncertainty on the luminosity measurement [133] was about 3.7% in the end of 2011 [134] dominated by the uncertainty on the number of protons per bunch. In the spring of 2012, a reanalysis of the 2011 absolute luminosity calibration and its systematic uncertainty was done [135]. The systematic uncertainty has decreased to 1.8% and it is dominated by the Van der Meer calibration procedure. For the 2012 data, the uncertainty is taken as 3.6% and is dominated by preliminary systematics of the Van der Meer calibrations.

In order to calibrate the visible inelastic cross section (σ_{vis}) using Van der Meer scans (done few times per year), the absolute luminosity L is expressed in an alternative way as a function of measured accelerator parameters:

$$\begin{aligned} L &= \frac{N_p^2 \kappa_b f_{rev} \gamma}{4\pi\beta^* \varepsilon_n} F \\ &= \frac{N_p^2 \kappa_b f_{rev}}{4\pi\sigma_x\sigma_y} F \end{aligned} \tag{3.4}$$

where:

- N_p is the number of protons per bunch (nominally 10^{11}, but in the end of 2011, this number exceeded the nominal value at the beginning of the fills to reach 1.4×10^{11} and even $\sim 1.5 \times 10^{11}$ in 2012);
- γ is the relativistic factor E/m_p;
- β^* is the beta function at the collision point, it represents the beam focalization (nominally 1.1 m for 7 TeV (0.55 m for 14 TeV), the value at the end of 2011 was 1 m and for 2012 0.6 m);

- ε_n is the normalized transverse beam emittance which measures the spread of particle coordinates in position and momentum phase space;
- F is the geometric luminosity reduction factor due to the crossing angle at the interaction point (nominally 285 μrad);
- $4\pi\sigma_x\sigma_y$ is the effective area of the beams with σ_x and σ_y representing the transverse sizes of the beam (around 16 microns at the end of 2011 and 12 microns in 2012). σ_x and σ_y are measured in the Van der Meer scans.

The equivalence $\beta^*\varepsilon_n/\gamma = \sigma_x\sigma_y$ shows that the $\beta^*\varepsilon_n$ is proportional to the effective area of the beams while the latter is inversely proportional to the energy of the beam.

Fig. 3.2 (top) shows the peak instantaneous luminosity versus the day for 2011 recorded in the ATLAS detector reaching a maximum value of 3.65×10^{33} $cm^{-2}s^{-1}$. The total integrated luminosity is shown as well in Fig. 3.2 (bottom) reaching a total recorded value of 5.25 fb^{-1} at the end of 2011. Fig. 3.3 shows the same for 2012 up to the technical stop in June 2012, the maximum instantaneous luminosity reached 6.8×10^{33} $cm^{-2}s^{-1}$ and the total integrated luminosity 6.25 fb^{-1}.

A disadvantage of the high luminosity is the increasing number of the so-called "pile-up" events. Most of the triggered bunch crossings contain one hard scattering event while the other additional proton-proton interactions per bunch crossing are referred to as in-time pile-up events. An event display showing the high pile-up in 2012 running of a $Z \to \mu^+\mu^-$ candidate with 25 reconstructed vertices is shown in Fig. 3.4.

The average number of the in-time interactions per bunch crossing, μ_{BCID}, can be computed using the equation:

$$\mu_{BCID} = \frac{\mu_{vis}}{\varepsilon_{meas}} \tag{3.5}$$

where ε_{meas} is the efficiency for one proton-proton inelastic collision to be detected in the luminosity monitor. It can be rewritten using equation 3.2 as:

$$\mu_{BCID} = \frac{L_{BCID}.\sigma_{inel}}{f_{rev}} \tag{3.6}$$

where $\sigma_{inel} = \sigma_{vis}/\varepsilon_{meas}$ is the total inelastic proton-proton cross section, taken as 71.5 mb for 7 TeV and 73 mb for 8 TeV.

Fig. 3.5 shows the luminosity weighted distribution of μ_{BCID} for 2011 and 2012. The mean value of μ_{BCID} increases is about 9.1 for 2011 and 19.5 for 2012.

We can also measure a mean value of μ_{BCID} over all the BCIDs in one lumi-block (LB), $\langle\mu\rangle$, weighted by the luminosity in each BCID. The distribution

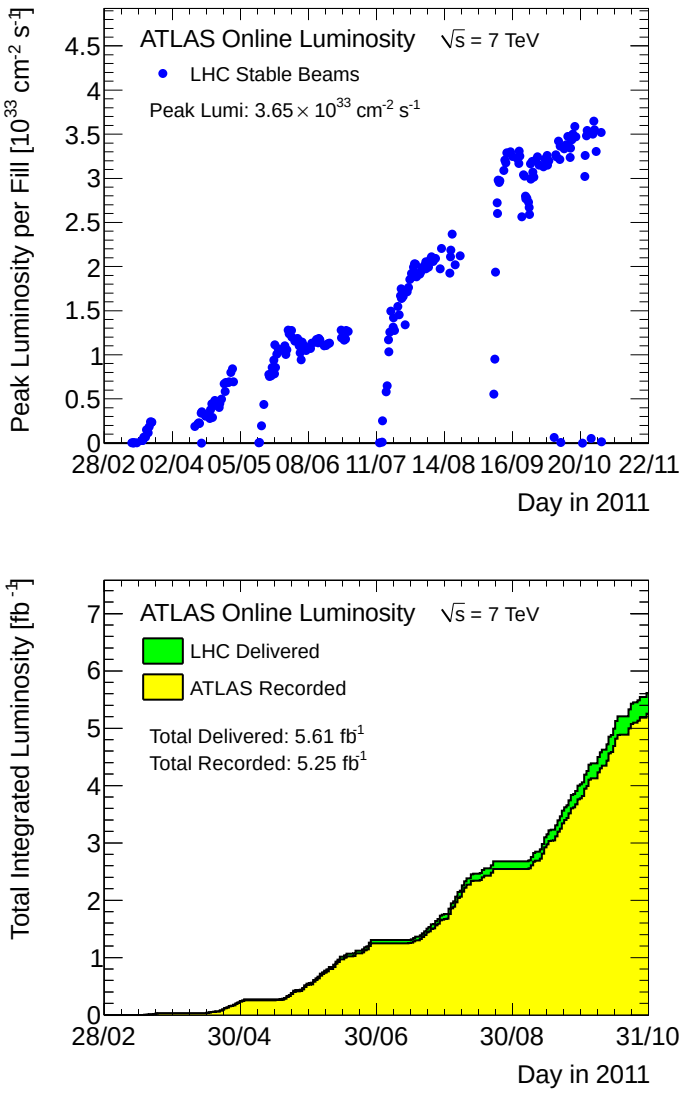

Figure 3.2: (top) The maximum instantaneous luminosity and (bottom) the integrated luminosity per day recorded by ATLAS during stable beams and for pp collisions at $\sqrt{s} = 7$ TeV in 2011 [136].

of $\langle\mu\rangle$ would give an estimation of the in-time and out-of-time mean pile-up of the considered events. The out-of-time pile-up is the consequence of the short bunch spacing (nominally 25 ns): in a given bunch crossing, the detector response can be influenced by the residual effects of previous bunch crossings. Note that in the simulation, for one LB, the BCIDs are considered to have the same luminosity, which is only approximate due to the variation of number of protons between bunches (different L_{BCID} between the BCIDs) and due, to a lesser extent, to the variation of the emittance. However the loss of protons

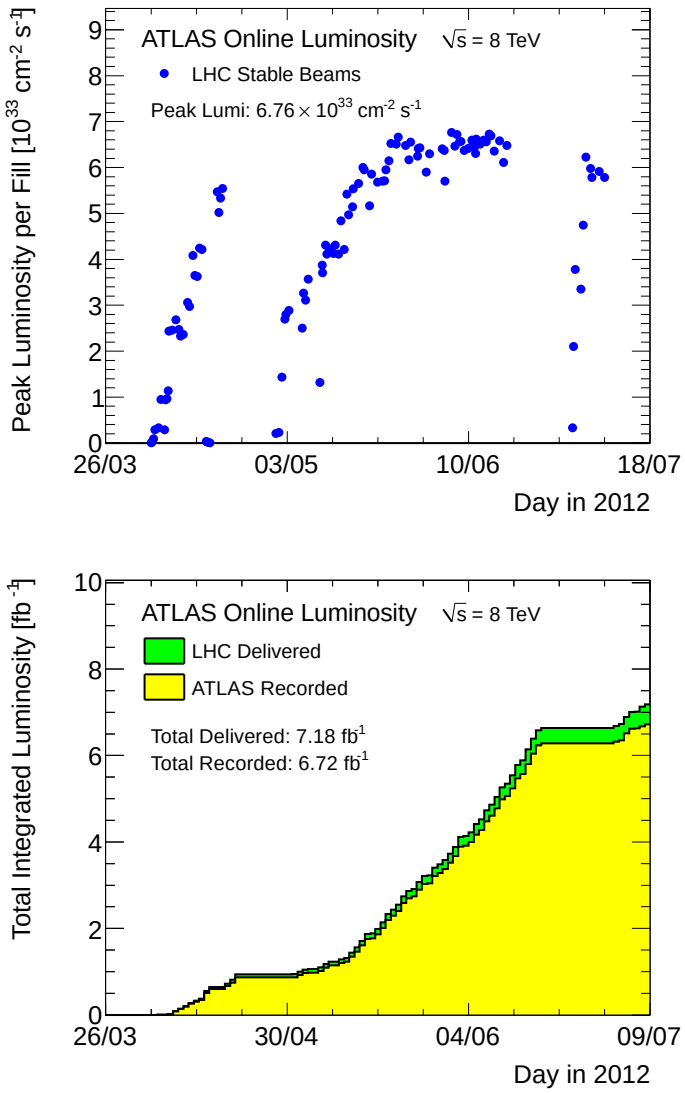

Figure 3.3: (top) The maximum instantaneous luminosity and (bottom) the integrated luminosity per day recorded by ATLAS during stable beams and for pp collisions at $\sqrt{s} = 8$ TeV up to the technical stop in June 2012 [136].

between different LB is taken into account in the simulation by varying $\langle\mu\rangle$.

3.2 ATLAS Detector

The ATLAS detector is shown in Fig. 3.6. It has a length of 44 m, a height of 25 m and a weight of 7000 tonnes. It consists of:

- an Inner Detector which permits the track reconstruction, momentum and vertex measurements, contributes to electron identification and is

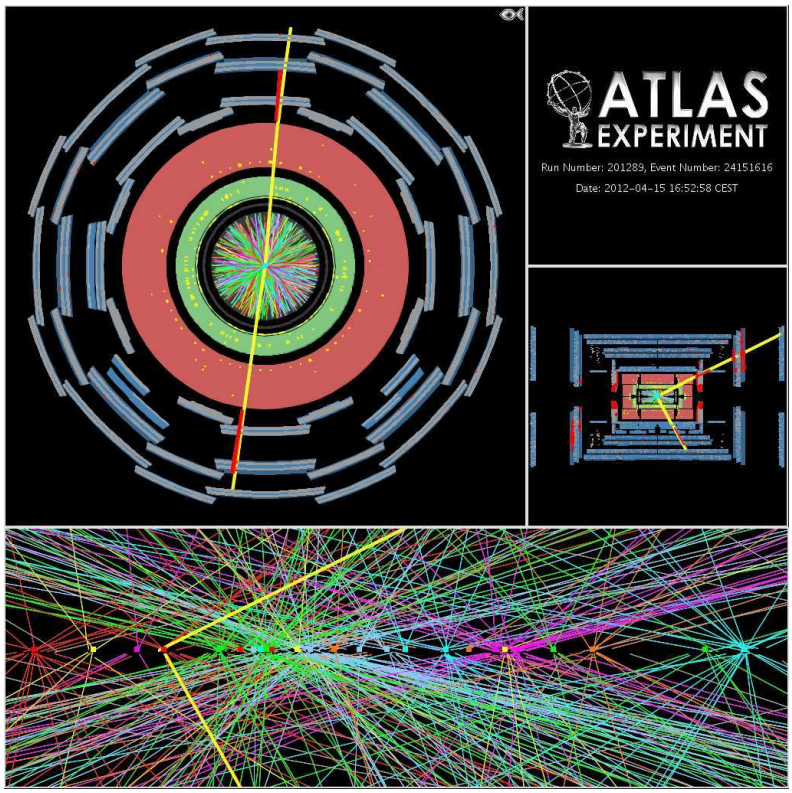

Figure 3.4: Event display of a $Z \rightarrow \mu^+\mu^-$ candidate with 25 reconstructed vertices recorded on April 15th 2012. For this display the track p_T threshold is 0.4 GeV and all tracks are required to have at least 3 Pixel and 6 SCT hits [137].

an essential element for studying photon conversions;

- a liquid-Argon electromagnetic calorimeter ensuring an excellent performance for electrons and photons in terms of energy and position resolution;
- a hadronic calorimeter (steel scintillator in the barrel, liquid-Argon elsewhere) providing a measurement of the jets and the missing transverse energy together with the LAr calorimeter;
- a muon spectrometer providing an excellent muon momentum resolution.

These elements will be discussed in the following, focusing mainly on the relevant ones for photon studies: the tracker and the calorimeters.

3.2.1 The ATLAS Coordinate System

The origin of the coordinate system is defined by the nominal proton-proton interaction point. The beam direction defines the z axis with z positive values

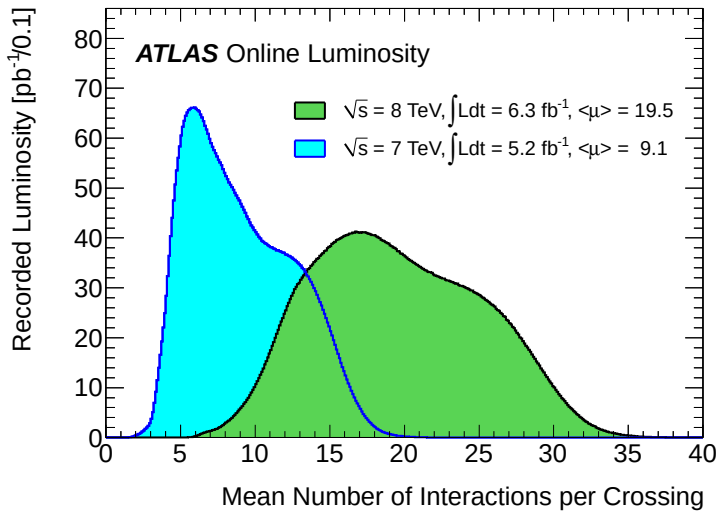

Figure 3.5: The luminosity-weighted distribution of the mean number of interactions per crossing for 2011 and 2012 data [136].

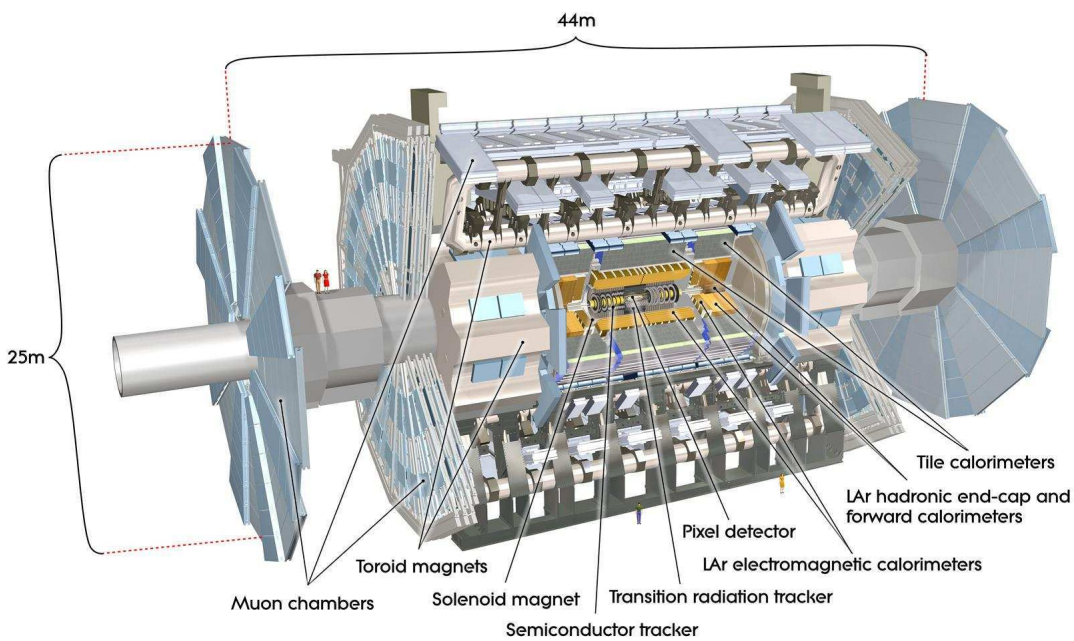

Figure 3.6: View of the ATLAS detector.

pointing counter-clockwise around the ring. The side A of the detector is defined as that with positive z values and the side C is that with negative z.

The $x - y$ plane is transverse to the beam direction, with positive x values pointing towards the center of the ring and positive y values pointing upwards. The azimuthal angle ϕ is defined around the z axis and the polar angle θ is the angle from the z axis. It is more common to use the rapidity:

$$y = \frac{1}{2} ln \left[\frac{E + p_z}{E - p_z} \right] \tag{3.7}$$

(where E and p_z are the energy and the z component of the momentum) or in the limit of massless objects the pseudorapidity:

$$\eta = -ln(tan(\theta/2)) \tag{3.8}$$

where $\eta = 0$ denotes the upward direction ($\theta = 90°$) and $\eta \rightarrow \infty$ for directions close to the beam line ($\theta \rightarrow 0°$). Note that the difference of rapidities Δy is Lorentz invariant (along the z axis). The $\eta - \phi$ is the commonly used plane. The cells of the detector are usually defined in a cone of radius:

$$\Delta R = \sqrt{(\Delta\eta)^2 + (\Delta\phi)^2} \tag{3.9}$$

with $\Delta\eta$ ($\Delta\phi$) is the size in the $\eta(\phi)$ direction.

3.2.2 The Inner Detector

The Inner Detector (ID), shown in Fig 3.7 (a), surrounds the LHC beam pipe and is immersed in a 2 T magnetic field generated by the central solenoid, which has a length of 5.3 m and a diameter of 2.5 m. The ID consists of three sub-detectors, shown in Fig. 3.7 (b)and (c): pixel, silicon microstrip (SCT) trackers and transition radiation tracker (TRT). Each sub-detector consists of a barrel and two end-caps (EC).

The ID was designed to provide a good reconstruction of charged tracks up to $|\eta| < 2.5$ (a reconstructed track in the barrel would typically have 3 pixel hits, 8 SCT strip layers and 36 TRT straw hits) based on the excellent momentum and vertex resolution measurements. The expected resolution on the measurement of the transverse momentum for charged particles is given by (with p_T in GeV):

$$\frac{\sigma_{p_T}}{p_T} = 0.05\% p_T \oplus 1\% \tag{3.10}$$

where 0.05% is due to the ID resolution and 1% describes the effect of multiple scattering in the ID. The track reconstruction efficiency [138] is shown in Fig. 3.8. This efficiency is compared for simulated samples with no pile-up events ($\mu = 1$ and samples with significant pile-up ($\mu = 21$ and $\mu = 41$). Default and robust requirements on reconstructed tracks are also compared. The robust requirements (increased hit requirement which increases the chance that a track that undergoes a hadronic interaction is not

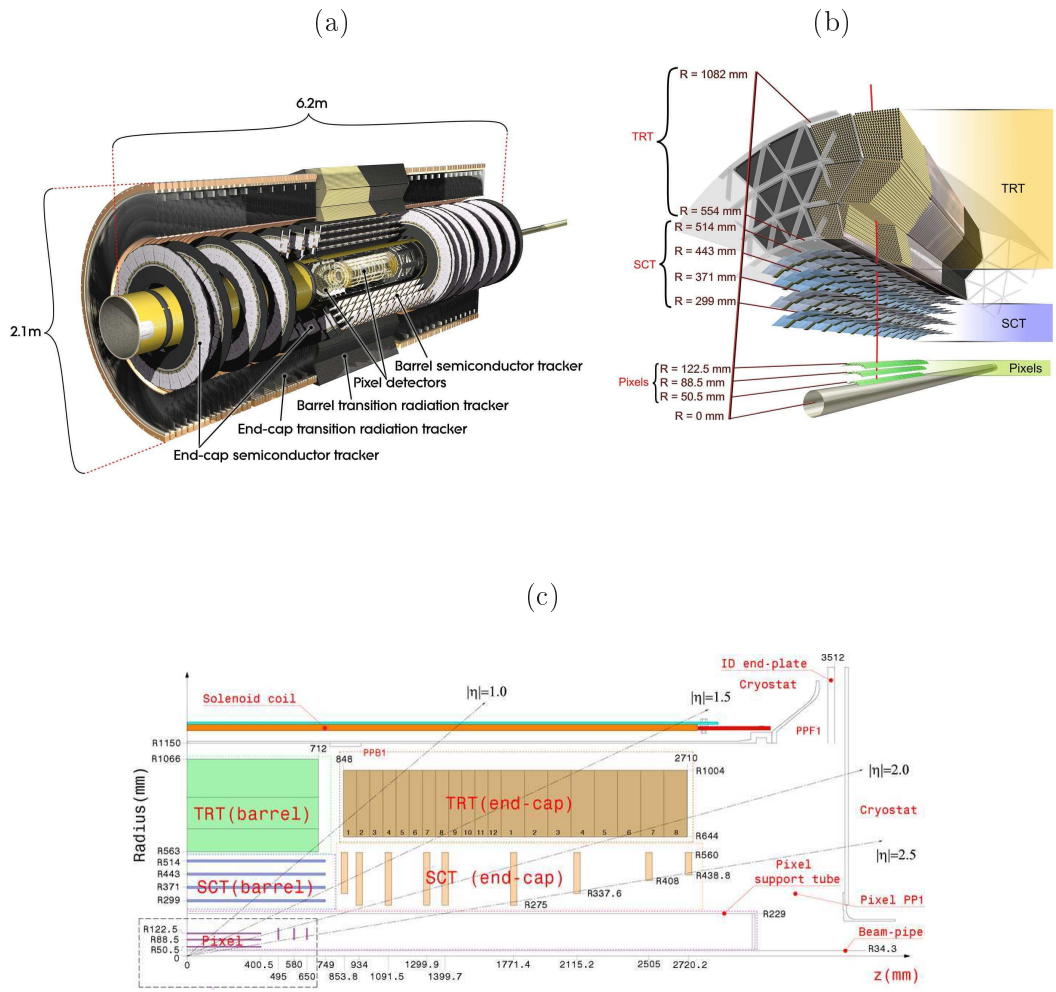

Figure 3.7: (a) View of the ATLAS inner detector, (b) The different sub-detectors of the inner detector, (c) shematical view of the Inner detector.

found) reduce the efficiency by 5%. The efficiency changes with the pile-up by less than 1% for both default and robust requirements. The secondary efficiency is defined as the reconstruction efficiency of particles originating from secondary vertices, usually produced by the desintegration of long-lived particles (life-time $> 3 \times 10^{-11}$ s). The secondary efficiency is stable with increasing pile-up in the central region, and decreases by at most 1% in the forward regions. The robust requirements decrease the secondary efficiency by $1-2\%$. The primary track reconstruction efficiency (default requirements) for hadrons is about 90% in the barrel and 70% in the EC. This low efficiency is due to hadronic interaction. A particle interacting (even elastic scattering) up to the second layer of SCT will not have enough silicon hits to satisfy the

reconstruction quality criteria. Indeed for muons, which have no hadronic interactions, the tracking efficiency is close to 100% [139]. The different parts

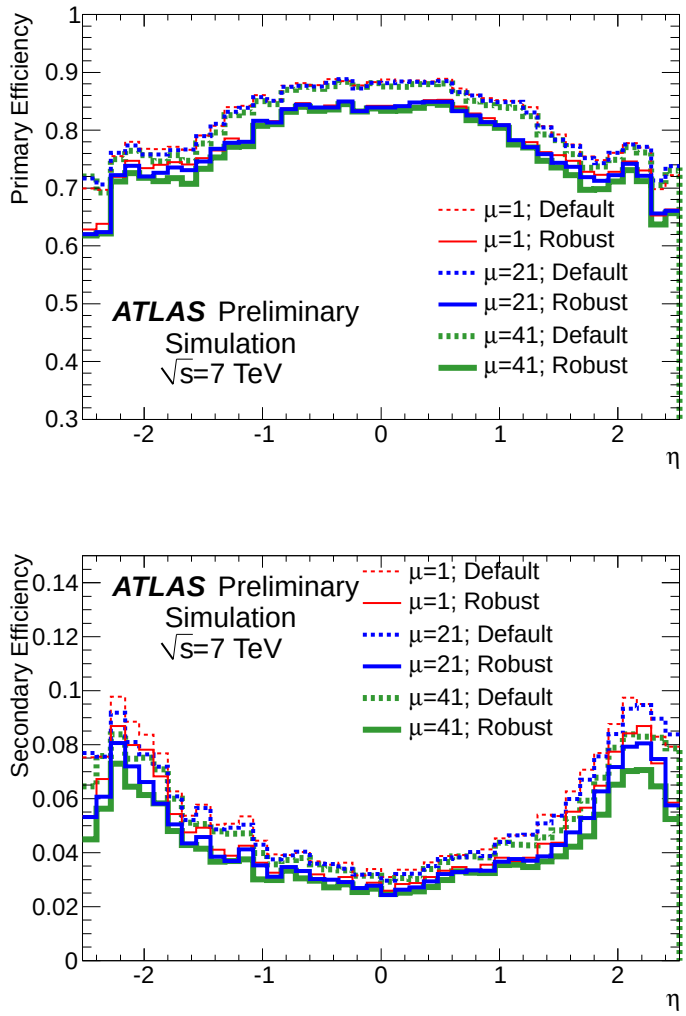

Figure 3.8: The primary (top) and secondary (bottom) track reconstruction efficiency in minimum bias Monte Carlo samples containing exactly one and on average 21 or 41 interactions as a function of η. The distributions are shown for tracks passing the default (dashed) and robust (solid) requirements [138].

of the ID are described below.

Pixel Detector

The highest granularity is achieved with the pixel detector. In the barrel, there are three concentric cylinders around the beam axis (R = 50.5, 88.5, 122.5 mm). The innermost layer is the so-called "B-layer", it provides tagging for

long lived hadrons containing b quarks and allows a discrimination between electrons (generally reconstructed with at least one hit in the B-layer) and converted photons (generally not leaving a hit in the B-layer apart for rare conversions occuring before or in the B-layer). In each EC, there are three disks perpendicular to the beam axis ($z = \pm 495, \ \pm 580, \ \pm 650$ mm), extending the total coverage up to $|\eta| < 2.5$. There are 1744 sensors in the pixel detector, each sensor is made up of 47232 pixels including 46080 readout channels. The nominal pixel size is $50 \times 400\ \mu m^2$ in the $(R\phi) \times z$ plane. The intrinsic $(R\phi)$ accuracy is 10 μm and the instrinsic z (R) accuracy is 115 μm in the barrel (EC).

Semi-Conductor tracker

The SCT is also a precision tracking detector. In the barrel, there are 4 concentric cylindrical layers ($R = 299, \ 371, \ 443, \ 514$ mm) covering the central region up to $|\eta| < 1.1$. In each EC, 9 disks of varying sizes (from $z = \pm 854$ to ± 2720 mm) extend the coverage to $|\eta| < 2.5$. There are 4088 modules (2112 in the barrel and 1976 in the EC) designed as collections of thin strips separated by 80 μm. There are a total of 2×768 active strips of ~ 126 mm length per module. The total number of readout channels in the SCT is therefore ~ 6.3 million. The intrinsic $(R\phi)$ accuracy is 17 μm and the instrinsic z (R) accuracy is 580 μm in the barrel (EC).

Transition Radiation Tracker

The TRT is the outermost tracking detector. Its basic elements are the polyimide drift (straw) tubes of 4 mm diameter, enabling a coverage up to $|\eta| = 2.0$. In the barrel, 144 cm long straw tubes are parallel to the beam axis while in the EC, the 37 cm long straw tubes are arranged radially in wheels. The straws are filled with a gas mixture: 70% of Xe, 27% of CO_2 and 3% of O_2. On the axis of each straw tube runs a gold-plated tungsten wire of 30 μm diameter. This wire plays the role of the anode for electrons coming from the gas ionized by the charged particle passing through the straw tube and it is connected to the analog readout electronics. The total number of TRT readout channels is ~ 351000. In addition, the tubes are surrounded by a radiator material: polypropylene/polyethylene fibers. The particles crossing an interface between two materials of different dielectric constants emit a transition radiation (photons of several keV) which is absorbed by the Xenon gas (for details see [140]). The energy of the transition radiation is proportional to the relativistic factor $\gamma = E/m$. Therefore, the probability of emitting a transition radiation by electrons is significantly larger than

that produced by pions with the same energy (since the mass of the electron is $\sim$ 250 times smaller), which enhances the electron identification and the discriminative power between electrons and pions. A high threshold (HT) has been defined as a measure of the large energy deposit in the TRT due to absorption of a transition radiation. Fig. 3.9 shows the HT fraction for electrons originating from photon conversions and pion candidates in the momentum range $4 < p < 20$ GeV, in the barrel region for 2010 data.

The material distribution at the exit of the ID envelope is obtained

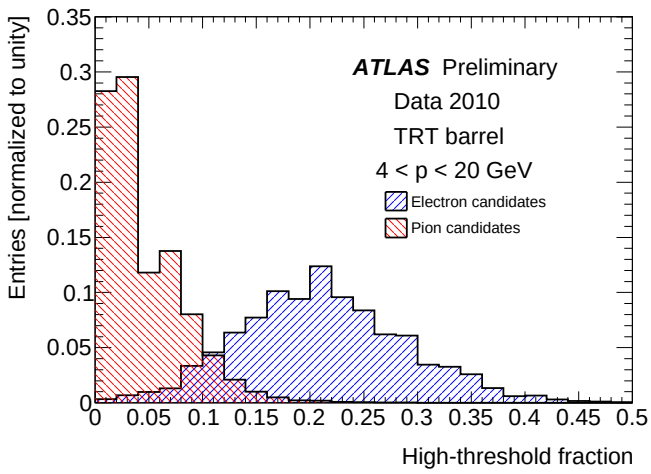

Figure 3.9: High Threshold fraction for electrons and pions in the barrel and for momentum $4 < p < 20$ GeV measured with 2010 data [141].

from simulation as a function of η and averaged over ϕ and it is shown in Fig. 3.10. The radiation length, X_0, is the mean distance over which a high-energy electron loses $\left(1 - \frac{1}{e}\right)$ of its energy by bremsstrahlung, and a high-energy photon has a probability of conversion of $\left(1 - \frac{1}{e}\right)$ before a distance of $\frac{9}{7}X_0$. The knowledge of the material is thus important to simulate the loss of energy by electrons, converted photons (as well to estimate the fraction of conversions), and of low-energy pions through an inelastic hadronic interaction inside the ID. The largest amount of material is found in the so-called "crack" region which is the interface of the barrel and EC regions due to cooling connections and the end of SCT, TRT barrels, TRT electrical connections and SCT and TRT barrel services. Another important amount of material is seen for $|\eta| > 2.7$ due to pixel services.

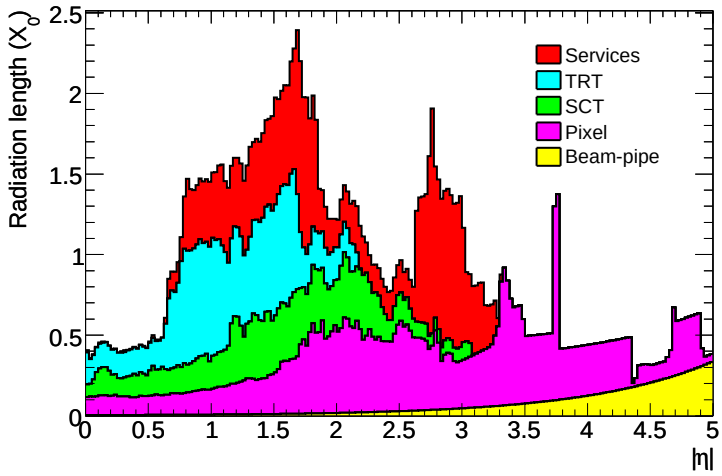

Figure 3.10: The radiation length as a function of η at the exit of the ID envelope.

3.2.3 Calorimeters

An overview of the ATLAS calorimetry system is shown in Fig. 3.11, it consists of:

- a liquid Argon (LAr) electromagnetic calorimeter (ECAL) measuring the energy of the electromagnetically interacting particles (electrons, photons) with an optimized resolution and efficiency measurements;
- a hadronic calorimeter, together with the electromagnetic calorimeter in front, ensuring a reconstruction of hadronic jets and a measurement of missing transverse energy.

The electromagnetic barrel (EMB) calorimeter (two half-barrels separated by a small gap (4 mm) at $z = 0$ and covering $0 < |\eta| < 1.475$) as well as the central solenoid providing the 2 T field for the ID are contained in a barrel cryostat ($0 < |\eta| < 1.7$). Whereas each of the two EC cryostats contains an electromagnetic EC (EMEC) calorimeter (each EC divided into coaxial wheels (outer and inner wheel) covering $1.375 < |\eta| < 3.2$), a hadronic EC (HEC) calorimeter ($1.5 < |\eta| < 3.2$) and a forward calorimeter (FCAL) ($3.1 < |\eta| < 4.9$). One of the EC cryostat is sketched in Fig 3.12. The different parts of the calorimeters, their coverage in $|\eta|$ and the characteristics of their cells ($\Delta\eta \times \Delta\phi$) are shown in Fig. 3.20.

Electromagnetic Calorimeter

The ECAL is a sampling calorimeter with a passive medium made of

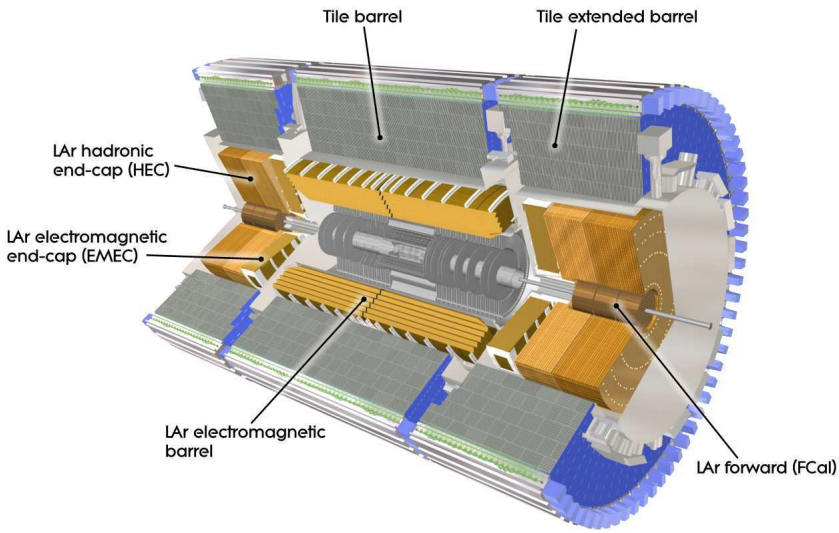

Figure 3.11: Overview of the ATLAS calorimetry system.

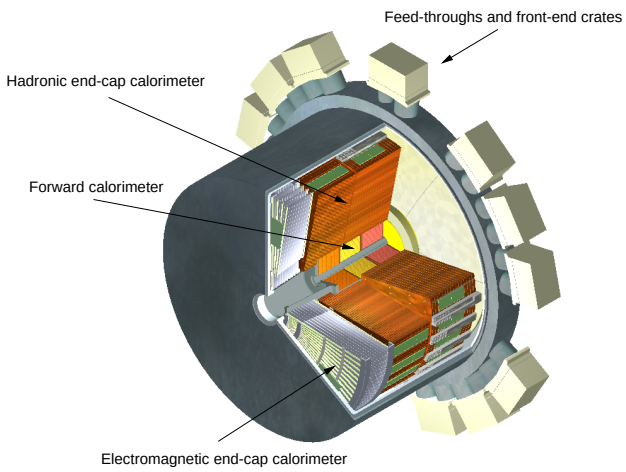

Figure 3.12: Cut-away view of an EC cryostat showing the three EC calorimeters: EMEC, HEC and FCAL.

lead absorber plates and an active medium of LAr. The lead plates in the barrel have a thickness of 1.53 (1.13) mm for $|\eta| < 0.8$ ($|\eta| > 0.8$) while in the EC, the plates have a thickness of 1.7 (2.2) mm for $|\eta| < 2.5$ ($|\eta| > 2.5$). The readout kapton electrodes are located in the LAr gaps (the size of the drift gap on each side of the electrode is 2.1 mm in the barrel) between the grounded absorbers and receive high voltage potential (nominally 2 kV in the barrel). When a high energy electron or photon passes through the

ECAL, the cascade of Bremsstrahlung emissions and pair conversions in the lead-absorbers generates low energy electrons which ionize the LAr atoms. The electrons coming from ionization drift under the electric field created by the difference of voltage between the electrodes and the absorbers. Typically, the drift time in the barrel is $\sim$ 400 ns (2.1 mm of distance and 2 kV of high voltage difference) which is relatively very long comparing to the bunch spacing at the LHC (nominally 25 ns). The solution is to integrate only a fraction of the total charge over a time of $40 - 50$ ns which will degrade the signal-to-noise ratio. Thus minimum number of cables and dead spaces in the calorimeter is needed to optimize the collected signal and to minimize the electronic noise. This problem is solved in ATLAS, following the original idea of D. Fournier [142], with the design of the lead-LAr detector with an accordion geometry. This geometry ensures a complete ϕ symmetry without azimuthal cracks as well as a fast extraction of the signal at the end of the electrodes.

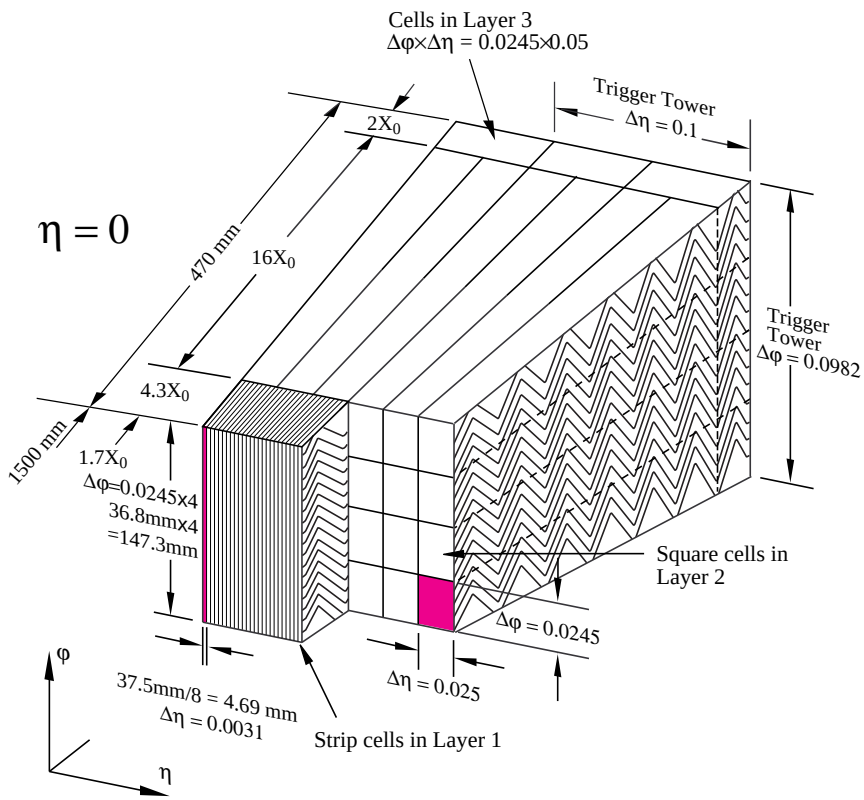

Figure 3.13: A barrel module with the granularity in η and ϕ of the cells are shown.

The LAr calorimeter is separated longitudinally into three layers, see Fig. 3.13:

- the first layer (also known as strip or front layer): it is made of narrow

strips and has the finest segmentation along η, its granularity is $\Delta\eta \times \Delta\phi = 0.025/8 \times 0.1$ in the central region $|\eta| < 1.4$. In the EC, the granularity varies as a function of the η range, it is $0.025/8 \times 0.1$ for $1.5 < |\eta| < 1.8$, $0.025/6 \times 0.1$ for $1.8 < |\eta| < 2.0$ and $0.025/4 \times 0.1$ for $2.0 < |\eta| < 2.4$. The depth of this layer is $\sim 4.4X_0$. The first layer provides an excellent position resolution in η. For photon studies, this layer is of a particular importance since it has the ability to separate two close (in η) photons mainly coming from π^0 (the most important background for photon analysis) and thus ensuring an efficient γ/π^0 separation. An illustration of this separation is shown in the two event displays of Fig. 3.14, where at the left is shown a π^0 candidate and at the right a direct photon isolated candidate (after tight identification selection). One can clearly see the narrow shape in the layer 1 for the photon candidate and a structure with two peaks from two close photons originating from the π^0 decay;

- the second layer (middle layer): it is where the bulk of the energy of the EM shower is deposited. It has a granularity of $\Delta\eta \times \Delta\phi = 0.025 \times 0.025$. The depth of this layer is $\sim 18X_0$. It ensures, together with the first layer, the measurement of the pseudorapidity η of the incident particle and the direction of the photons in the (r, z) plane;

- the third layer (back layer): it collects only the tail of the EM shower and therefore is less segmented in η, it has a granularity of $\Delta\eta \times \Delta\phi = 0.05 \times 0.025$. It is extended up to $|\eta| = 2.5$. The depth of this layer is $\sim 2X_0$.

The EM calorimeter is preceded by a presampler (PS) covering the pseudorapity region up to $|\eta| < 1.8$. The PS consists of an active LAr layer of a thickness of 1.1 cm (0.5 cm) in the barrel (EC) and has a granularity of $\Delta\eta \times \Delta\phi = 0.025 \times 0.1$. It provides shower sampling in front of the active ECAL and inside the cryostat. Its main purpose is to correct for the energy lost by electrons and photons upstream of the calorimeter (*i.e* ID, cryostat and coil). The incident particles will ionize the LAr of the PS, the collected signal from ionization is proportional to the energy lost upstream of the calorimeter [143, 144].

The energy resolution of the EM calorimeter is given by:

$$\frac{\sigma_E}{E} = \frac{a}{\sqrt{E}} \oplus \frac{b}{E} \oplus c \tag{3.11}$$

where:

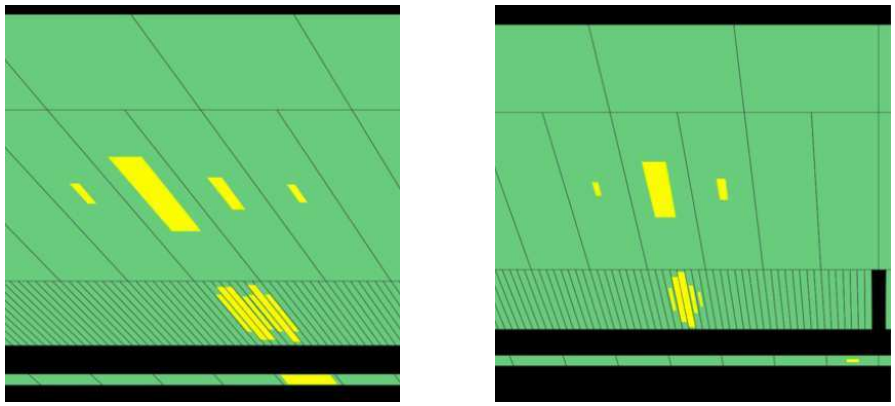

Figure 3.14: Two event displays showing (left) a π^0 candidate and (right) an isolated photon candidate passing tight identification criteria [145].

- **a** is the sampling term (also called the stochastic term) which describes the statistical fluctuations related to the EM shower development in the LAr medium. The design value is 10% in the barrel of the ECAL;

- **b** is the noise term which describes the fluctuations coming mainly from pile-up and electronical noises. The associated factor of $1/E$ shows that this term becomes important at low energies. This term is around 300 MeV;

- **c** is the constant term reflecting non-uniformities in the response of the calorimeter: material non-uniformity, temperature gradient, imperfections in mechanical structures, radiation damages, energy reconstruction scheme and stability in time, etc. The constant term depends on the sampling of the calorimeter. The nominal expected value is around 0.7% in the barrel. This term is very important for high energy studies.

An other important characteristic of the ECAL is the corresponding amount of material in front of it shown in Fig. 3.15. For $|\eta| < 1.5$ ($|\eta| > 1.5$), the material shown is in front of the barrel (EC) presampler and accordion, the radiation length varies between 2 and $4X_0$ up to $|\eta| = 1.4$. The first peak around $|\eta| \sim 1.5$ is due to the material (the PS barrel, end of the cold cryostat wall of the barrel, ID services and cables, cryostat EC) before the EC, see Fig. 3.16. The second peak at $|\eta| \sim 1.7$ is essentially due to the ID services, to the warm wall of the barrel cryostat and to the cables.

Hadronic Calorimeter

The hadronic calorimeter [122] is composed of three independent pieces:

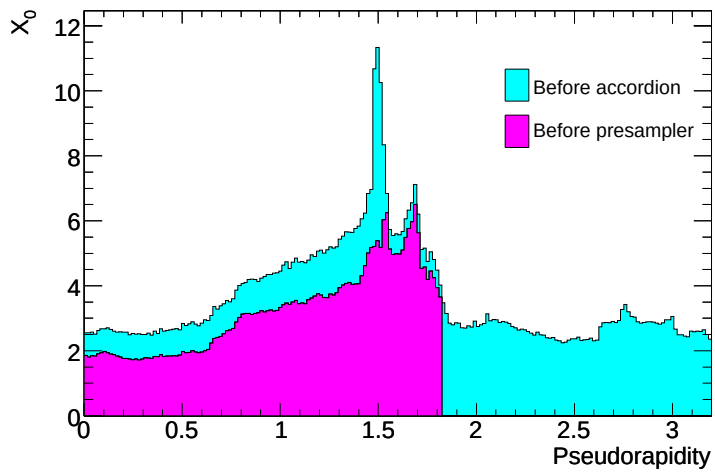

Figure 3.15: The total amount of material in front of the presampler and in front of the accordion as a function of η.

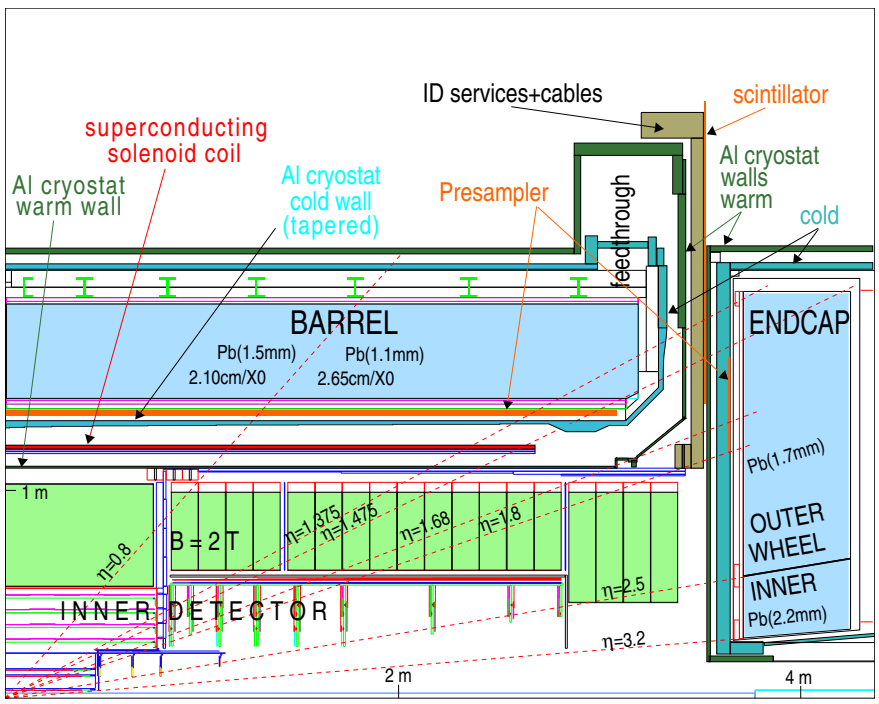

Figure 3.16: Shematical view of the EM calorimeter. The TRT wheel C at large η in the EC shown in the figure has not been installed.

- Tile Calorimeter: it is located just behind the EM calorimeter in the region $|\eta| < 1.7$. It has one barrel, $|\eta| < 1.0$, and two extended barrels $0.8 < |\eta| < 1.7$: each barrel consists of 64 modules in ϕ and of three

layers in depth (the total radial depth is $\sim 7.4\lambda$). The Tile Calorimeter is a sampling calorimeter using steel as the absorber and scintillator tiles as the active medium. The light produced in the scintillating material is collected at the edges of each tile using two wavelength-shifting fibres which are connected to readout photomultiplier tubes converting the light into electrical signal;

- LAr Hadronic EC calorimeter (HEC): it is a copper/LAr sampling calorimeter. It consists of two independent EC wheels located behind the EMEC and sharing the same LAr cryostats: each HEC wheel has 32 modules in ϕ and two layers in depth. It covers the region $1.5 < |\eta| < 3.2$ (overlapping with the Tile Calorimeter and the forward calorimeter);

- Forward Calorimeter (FCAL): it is a LAr sampling calorimeter consisting of three wheels (total depth of 10λ): one EM module having an absorber made of copper and two hadronic modules with a tungsten absorber. These wheels are located in the same cryostats as the EMEC and provide a coverage in pseudorapidity of $3.1 < |\eta| < 4.9$. The FCAL modules are exposed to high particle fluxes, since they are located at high η and at a distance of ~ 4.7 m from the interaction point. This has resulted in a design with LAr gaps much smaller that the 2 mm gap of the EMB calorimeter to avoid ion build-up problems and to provide at the same time the highest possible detector density. The energy resolution of the hadronic and forward calorimeters can be also parametrized by equation 3.11. a is $\sim 50\%$ ($\sim 100\%$) in the hadronic end-cap (forward) calorimeter. The nominal values of the constant term c are below 3 and 10% in the hadronic and forward calorimeters respectively.

Muon spectrometer

The muon spectrometer [122], shown in Fig. 3.17, is the outermost part of the detector and was designed to provide a high-resolution momentum measurement over a wide range of muon momenta in the pseudorapidity range $|\eta| < 2.7$ (except for the innermost wheel where it covers up to $|\eta| < 2.0$) and in addition a capability of triggering on these particles in the region $|\eta| < 2.4$. A transverse momentum resolution of $\sim 10\%$ for 1 TeV tracks is the performance goal. The spectrometer is a combination of large superconducting air-core toroid magnets, instrumented with separate trigger and high-precision tracking chambers. The muons are deflected under a toroidal field delivered by the large barrel toroid over the range $|\eta| < 1.4$ and by two smaller EC magnets for $1.6 < |\eta| < 2.7$. In the transition region, $1.4 < |\eta| < 1.6$, muon tracks are bent by a combination of barrel and EC fields. The magnet system provides a field of 0.5 (1) T in the central (EC) part orthogonal to the muon trajectories. Precise momentum measurement

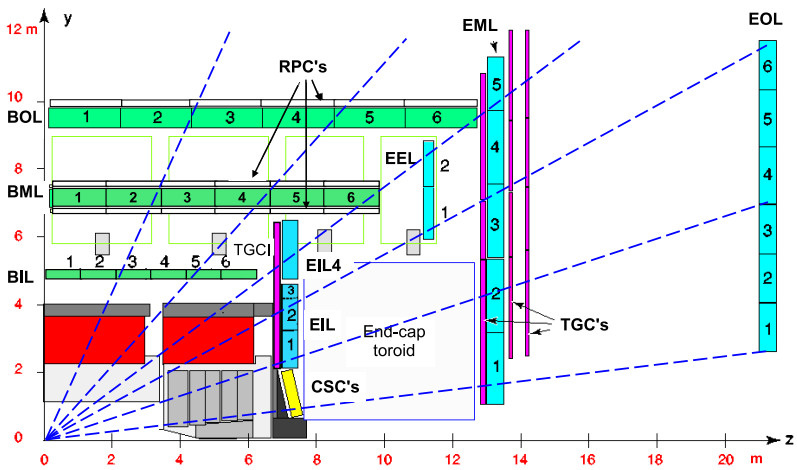

Figure 3.17: Shematical view of the muon system in a plane containing the beam axis.

is performed by determining the track coordinates in the bending plane. Monitored Drift Tubes (MDT), covering the range $|\eta| < 2.7$, are used due to their high measurement accuracy, predictability of mechanical deformations and simplicity of construction. The MDTs consist of three to eight layers of drift tubes of $\sim$ 30 mm operating with Ar (93%) and CO_2 (7%) at an absolute pressure of 3 bar. A resolution of 35 μm per chamber is achieved. In the forward region ($2.0 < |\eta| < 2.7$), Cathode-Strip Chambers (CSC) are used in the innermost EC wheels due to their high rate capability and time resolution. The CSC system consists of two disks with eight chambers each containing four CSC planes. The resolution of a chamber is 40 μm in the bending plane (R direction) and $\sim$ 5 mm in the transverse plane (ϕ direction).

The precision-tracking chambers have been complemented by a system of fast trigger chambers. Resistive Plate Chambers (RPC) in the barrel ($|\eta| < 1.05$) and Thin Gap Chambers (TGC) in the EC ($1.05 < |\eta| < 2.4$) have been selected due to good spatial and time resolution as well as adequate rate capability. Both chamber types deliver signals with a spread much smaller than 25 ns, thus providing the ability to tag the beam-crossing. The trigger chambers provide therefore a bunch-crossing identification, fast tracking information, discrimination on muon transverse momentum, second coordinate measurement in the non-bending ϕ projection and robustness towards random hits due to n/γ background in the experimental hall. Furthermore, the locations of MDT wires and CSC strips must be known with a precision better than 30 microns. To reach this precision goal, a high-precision optical alignment system [146] was built. It relates the position

of each chamber to that of it neighbours and it monitors the position and internal deformations. The optical alignment techniques used are insufficient to reconstruct the absolute positions of the chambers: only variations in relative positions can be determined with the required precision. Therefore track-based alignment algorithms must be used together with the optical system to achieve this desired precision.

Trigger System

In the LHC environment, a very powerful and efficient trigger system is needed to select from the high collision rates (nominal frequency of beam crossings of 40 MHz or in terms of frequency of collisions of 1 GHz) only interesting events with a final maximum output rate of about 200 Hz. The overview of the trigger system is shown in Fig. 3.18. It is a three-tiered system: it consists of a hardware-based trigger in the first tier (Level-1 or L1), followed by a software-based High Level Trigger (HLT) that includes a partial event reconstruction trigger (Level-2 or L2) and an Event Filter (EF or L3) performing the full event reconstruction.

- The L1 trigger processes information from the detector at the full beam-crossing rate of 40 MHz (assuming a bunch crossing each 25 ns). It reduces the ouput rate to 100 kHz based on information from the calorimeters (using a granularity of $\Delta\eta \times \Delta\phi = 0.1 \times 0.1$) and the muon spectrometer (from RPC and TGC). It has a latency of 2.5 μs which is the capacity time of the analogical pipeline to stock the data until the L1 decision is made by the Central Trigger Processor (CTP). After each L1 decision, there is a minimum dead time of five bunch crossings (nominally 125 ns). The minimum dead time corresponding to an output rate of 100 kHz (i.e 10 μs) is $0.125/10 = 1.25\%$. The information is sent to the L2 trigger as a Region-of-Interest (RoI), region in η and ϕ where interesting features were identified;

- The L2 trigger is a RoI-based trigger seeded by the L1 trigger. It is designed to provide a rejection of about a factor of 50 thus with an output rate of $\sim$ 2 kHz. It uses the informations from all the sub-detectors contained in the RoIs regions representing almost 2% of the detector volume. The track information from ID is used and the processing time (limited by the number of processors to be used in the computation) is around 40 ms;

- The EF corresponds to the final event selection leading to a final frequency of $\sim$ 200 Hz, it has an average event processing time of about 4 s. It uses fast versions of offline reconstruction tools (almost the same tools as the ones used for the offline analysis) to look for diphoton and

dilepton events, and for events with high missing transverse energy as well as single-object and multi-object events. The final events selected in this stage are recorded to be used for offline analysis.

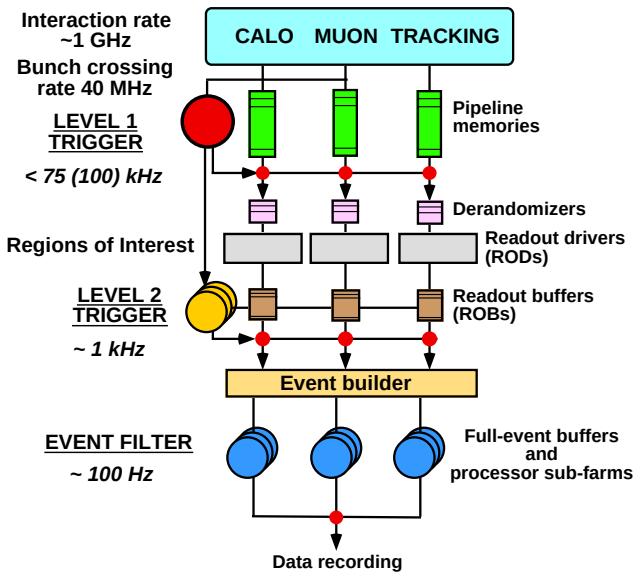

Figure 3.18: The three levels of the ATLAS trigger system.

3.3 CMS Detector

The Compact Muon Solenoid (CMS) [123] is the other multi-purpose apparatus operating at the LHC, its overall layout is shown in Fig. 3.19. It is a detector of 21.6 m long, it has a diameter of 14.6 m and a total weight of 12500 tonnes. The main driving aspect of the design was the choice of the magnetic field configuration for the muon momentum measurement. For this purpose, a superconducting solenoid of 13 m long and of an inner-diameter of 6 m is used to provide a magnetic field of 3.8 T. Four muon stations, each consisting of aluminium drift tubes in the barrel and CSC in the EC complemeted by RPC, are installed to ensure robustness and full coverage. The central coil is large enough to accomodate the inner tracker and the calorimetry inside it. The inner tracker of CMS uses only Si detectors, 10 layers of silicon microstrip detector and 3 layers of silicon pixel detectors. The electromagnetic calorimeter uses lead tungstate ($PbWO_4$) crystals with coverage in pseudorapidity up to $|\eta| < 3.0$. There are 61200 crystals in the central barrel and 7324 crystals in each of the two end-caps. A preshower system is installed in front of the EC ECAL for π^0 rejection (the equivalent in ATLAS is the layer 1 of the ECAL covering the barrel and the EC). Changes in transparency of the

crystals during LHC fills and subsequent recovery are monitored continuously and corrected by using injecting light from a laser and LED system [147]. The ECAL is surrounded by a brass/scintillator sampling hadron calorimeter with coverage up to $|\eta| < 3.0$. Coverage in pseudorapidity up to $|\eta| = 5.0$ is provided by an iron/quartz fibre calorimeter. A detailed comparison between ATLAS and CMS can be found in [148].

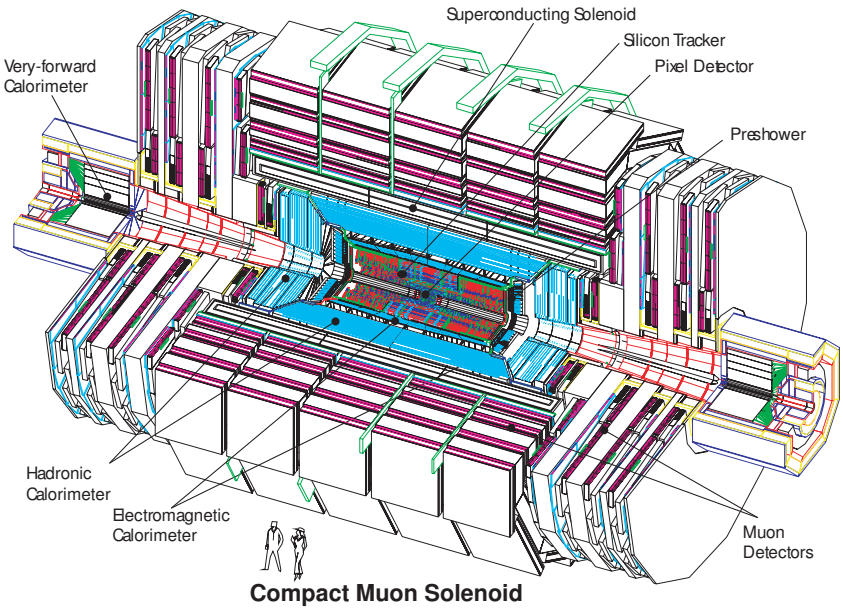

Figure 3.19: An overall layout of the CMS detector

	Barrel		End-cap	
EM calorimeter				
Number of layers and $\|\eta\|$ coverage				
Presampler	1	$\|\eta\| < 1.52$	1	$1.5 < \|\eta\| < 1.8$
Calorimeter	3	$\|\eta\| < 1.35$	2	$1.375 < \|\eta\| < 1.5$
	2	$1.35 < \|\eta\| < 1.475$	3	$1.5 < \|\eta\| < 2.5$
			2	$2.5 < \|\eta\| < 3.2$
Granularity $\Delta\eta \times \Delta\phi$ versus $\|\eta\|$				
Presampler	0.025×0.1	$\|\eta\| < 1.52$	0.025×0.1	$1.5 < \|\eta\| < 1.8$
Calorimeter 1st layer	$0.025/8 \times 0.1$	$\|\eta\| < 1.40$	0.050×0.1	$1.375 < \|\eta\| < 1.425$
	0.025×0.025	$1.40 < \|\eta\| < 1.475$	0.025×0.1	$1.425 < \|\eta\| < 1.5$
			$0.025/8 \times 0.1$	$1.5 < \|\eta\| < 1.8$
			$0.025/6 \times 0.1$	$1.8 < \|\eta\| < 2.0$
			$0.025/4 \times 0.1$	$2.0 < \|\eta\| < 2.4$
			0.025×0.1	$2.4 < \|\eta\| < 2.5$
			0.1×0.1	$2.5 < \|\eta\| < 3.2$
Calorimeter 2nd layer	0.025×0.025	$\|\eta\| < 1.40$	0.050×0.025	$1.375 < \|\eta\| < 1.425$
	0.075×0.025	$1.40 < \|\eta\| < 1.475$	0.025×0.025	$1.425 < \|\eta\| < 2.5$
			0.1×0.1	$2.5 < \|\eta\| < 3.2$
Calorimeter 3rd layer	0.050×0.025	$\|\eta\| < 1.35$	0.050×0.025	$1.5 < \|\eta\| < 2.5$
Number of readout channels				
Presampler	7808		1536 (both sides)	
Calorimeter	101760		62208 (both sides)	
LAr hadronic end-cap				
$\|\eta\|$ coverage			$1.5 < \|\eta\| < 3.2$	
Number of layers			4	
Granularity $\Delta\eta \times \Delta\phi$			0.1×0.1	$1.5 < \|\eta\| < 2.5$
			0.2×0.2	$2.5 < \|\eta\| < 3.2$
Readout channels			5632 (both sides)	
LAr forward calorimeter				
$\|\eta\|$ coverage			$3.1 < \|\eta\| < 4.9$	
Number of layers			3	
Granularity $\Delta x \times \Delta y$ (cm)			FCal1: 3.0×2.6	$3.15 < \|\eta\| < 4.30$
			FCal1: $\sim$ four times finer	$3.10 < \|\eta\| < 3.15$, $4.30 < \|\eta\| < 4.83$
			FCal2: 3.3×4.2	$3.24 < \|\eta\| < 4.50$
			FCal2: $\sim$ four times finer	$3.20 < \|\eta\| < 3.24$, $4.50 < \|\eta\| < 4.81$
			FCal3: 5.4×4.7	$3.32 < \|\eta\| < 4.60$
			FCal3: $\sim$ four times finer	$3.29 < \|\eta\| < 3.32$, $4.60 < \|\eta\| < 4.75$
Readout channels			3524 (both sides)	
Scintillator tile calorimeter				
	Barrel		Extended barrel	
$\|\eta\|$ coverage	$\|\eta\| < 1.0$		$0.8 < \|\eta\| < 1.7$	
Number of layers	3		3	
Granularity $\Delta\eta \times \Delta\phi$	0.1×0.1		0.1×0.1	
Last layer	0.2×0.1		0.2×0.1	
Readout channels	5760		4092 (both sides)	

Figure 3.20: Main parameters of the calorimeter system.

Chapter 4

Calibration of electrons and photons

Contents

4.1 LAr Calorimeter electronic calibration 77

4.1.1 Electronic readout of the ATLAS LAr Calorimeter 77

4.1.2 Optimal Filtering 80

4.1.3 Autocorrelation matrix 82

4.1.4 Energy reconstruction 86

4.2 MC-based calibration 86

4.2.1 Birks' Law 89

4.3 In-situ calibration 92

The calibration of electrons and photons can be divided into three steps:

- The LAr calorimeter electronic calibration [149]: converts the raw signal extracted from each cell (in ADC counts) into a deposited energy;
- MC-based calibration [150], [102]: applies corrections at the cluster level for energy losses (dead material, leakage, etc.);
- The in-situ calibration using physics events recorded by the ATLAS detector [143], [144]: determines the absolute energy scale and intercalibrates the different regions of the calorimeter.

4.1 LAr Calorimeter electronic calibration

4.1.1 Electronic readout of the ATLAS LAr Calorimeter

The overview of the ATLAS LAr readout electronics is shown in Fig. 4.1. The electronic readout system is divided into a Front End (FE) system, including the Front End Boards (FEBs), and a Back End (BE) system containing the Read Out Drivers (RODs). A total of 1524 FEBs are required to read out the 182468 channels of the LAr calorimeter (each FEB processes up to 128 calorimeter channels). The raw signal produced when charged particles

ionize the LAr in the high-voltage potential in the gap between two absorber plates has a triangular shape. Assuming no recombination, the corresponding current is given by:

$$i(t) = \frac{N_e q_e}{t_d}\left(1 - \frac{t}{t_d}\right) \tag{4.1}$$

where t_d is the drift time, N_e is the number of electrons generated in the gap and q_e is the electric charge. The signal passes afterwards through an electronic card in the FEB, where it is amplified by the pre-amplifiers (or the pre-shapers in case of the HEC) to enhance the signal to noise ratio. The pre-amplifier (or pre-shaper) outputs are coupled into three shapers which apply a bipolar $CR-(RC)^2$ analogue filter with a time constant of $\tau = RC = 13$ ns. The shaper is designed to provide a null total integral of the signal to minimize the effects coming from noises (mainly pile-up noise). The triangular input current pulse and the shaped output pulse from the FEB are depicted for the case of a barrel electromagnetic cell in Fig. 4.2. After shaping, the signal is sampled every 25 ns (the nominal bunch spacing at the LHC). Usually the first five samples are read out. In addition the shapers amplify further and split the 16-bit dynamic range signal into three overlapping linear gain scales of 12-bits in the ratio 1/9/93 (low/medium/high gains):

- low gain used for high energies typically between 400 GeV and 4 TeV for the medium layer of the EM calorimeter;
- medium gain for energies typically between 40 GeV and 400 GeV for the same layer;
- high gain for low energies typically up to 40 GeV for the same layer.

The resulting three scaled signals are stored in parallel in the analogical pipelines (Switched Capacitor Array (SCA) chips) during the latency of the trigger L1 (for about 2.5 μs). The sample 2 of the medium gain is first digitized by an Analogical-to-Digital Converter (ADC). If the ADC is less than a first threshold ADC1, the high gain is chosen. If the signal is greater than a second threshold ADC2, the low gain is chosen. Otherwise, the five samples from the medium gain are digitized. For the HEC and the FCAL, the digitization occurs only in the medium and low gains (In 2010 and the beginning of 2011, the high gain was used for the FCAL, it has been changed later to avoid problems of saturation due to the increase of out-of-time pile-up). The digitized samples are then routed via optical fibers from FEBs to RODs.

The RODs process the signal samples for each channel to provide an optimized measurement of the energy using the Optimal Filtering (OF) procedure, detailed in 4.1.2, on Digital Signal Processors (DSPs). The signal is sent in the form of a triplet (energy, time and data quality) from ROD to the Read Out

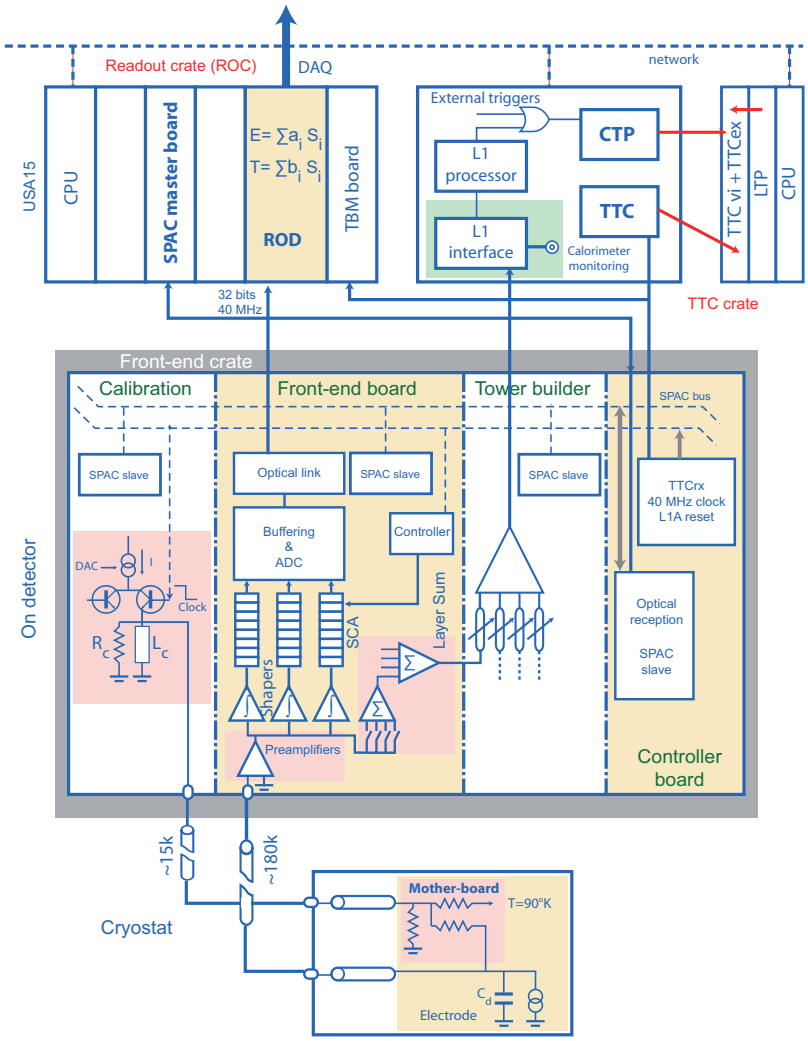

Figure 4.1: Block diagram depicting the architecture of the overall LAr readout electronics.

Buffer (ROB). In addition, for a signal above some threshold, the 5 samples are also sent to the ROB. The ROB gives the input to the Data Acquisition (DAQ) System.

In addition a calibration board is needed to calibrate the response of the front-end electronics boards. The calibration signal measures the gain, the pedestal and the signal shape which is reconstructed using programmable delays. It ensures as well the measurement of the cross-talk [1](since one calibration channel is used every four signal channels) between neighbour cells. The calibration system injects into the detector an exponential shape (approx-

[1]The cross-talk is a phenomenon by which a signal transmitted in a given channel creates an undesirable effect in another channel by some electronic coupling (resistive, inductive or capacitive)

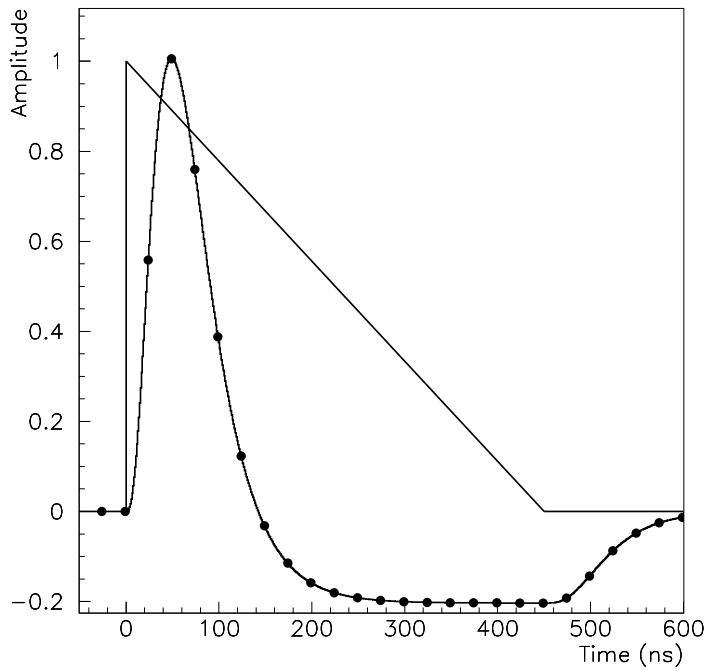

Figure 4.2: Shape of the triangular signal in the LAr barrel EM cell and of the sampled (every 25 ns) impulse response after bi-polar shaping.

imation of the triangular shape of the ionization pulse) generated by means of a digital-to-analog converter (DAC). The calibration signal is then distributed to the calorimeter cells via injection resistors placed at the input of the detector cell with a precision of 0.1% level. A total of 132 calibration boards have been produced. They fulfill the required performance of an integral linearity better than 0.1%, a uniformity better than 0.2%, and a stability as a function of time better than 0.1%. For more details on the description of calibration board, see [151].

4.1.2 Optimal Filtering

The shape of the signal is assumed to be known (shown in Fig. 4.2), except for its amplitude A and its time origin τ. The parameter τ measures the shift in time of the signal relative to $t = 0$ corresponding to a particle coming at the speed of the light from the triggered collision in the center of the detector. This shift could be due to a very massive particle (positive τ) or due to a particle coming from the halo or from a collision at $t = \pm 50$ ns for instance (positive or negative values of τ).

The signal is sampled many times giving a set of measurements $S_0, ..., S_{n-1}$

(in general $n = 5$) with one sample around the maximum. It can be written as:

$$S_i - Ped = Ag(t_i - \tau) + (n(t_i) - Ped), \tag{4.2}$$

where $g(t)$ is the signal waveform normalized to unity. Ped denotes the pedestal value, the mean value of the samples (in ADC counts) in the absence of a signal: $Ped = \langle E_{ADC} \rangle$, it is of the order of 1000 for the high gain (smaller for other gains) in order to be able to measure negative values of signal due to pile-up. $n(t)$ is the function giving the total noise (quadratic sum of electronic and pileup noises) from which a pedestal value has to be substracted. The Taylor expansion gives a linear dependence in τ:

$$S_i - Ped = Ag(t_i) - A\tau g'_{t_i} + (n(t_i) - Ped), \tag{4.3}$$

where g'_{t_i} is the derivative of $g(t_i)$. We define coefficients a and b and form the linear sums U and V as:

$$U = \sum_i a_i(S_i - Ped), \qquad V = \sum_i b_i(S_i - Ped) \tag{4.4}$$

with

$$A = \langle U \rangle, \qquad A\tau = \langle V \rangle. \tag{4.5}$$

The coefficients a_i and b_i are the so-called Optimal Filtering Coefficients (OFC). Using equation 4.3 we can rewrite:

$$A = \langle U \rangle = \sum_i Aa_i g(t_i) - A\tau a_i g'_{t_i} + \langle (n(t_i) - Ped) \rangle, \tag{4.6}$$

and

$$A\tau = \langle V \rangle = \sum_i Ab_i g(t_i) - A\tau b_i g'_{t_i} + \langle (n(t_i) - Ped) \rangle, \tag{4.7}$$

The noise average $\langle n(t_i) - Ped \rangle$ is null. It follows the set of conditions:

$$\sum_i a_i g(t_i) = 1, \qquad \sum_i a_i g'(t_i) = 0 \tag{4.8}$$

and

$$\sum_i b_i g(t_i) = 0, \qquad \sum_i b_i g'(t_i) = -1. \tag{4.9}$$

The variances of U and V are given by:

$$Var(U) = \sum_{ij} a_i a_j \langle (n(t_i) - Ped)(n(t_j) - Ped) \rangle = \sum_{ij} a_i a_j R_{ij}, \tag{4.10}$$

and

$$Var(V) = \sum_{ij} b_i b_j \langle (n(t_i) - Ped)(n(t_j) - Ped) \rangle = \sum_{ij} b_i b_j R_{ij}. \tag{4.11}$$

The matrix $R_{ij} = \langle (n(t_i) - Ped)(n(t_j) - Ped) \rangle$ is the total noise autocorrelation function evaluated at time $t_i - t_j$. The knowledge of the total noise autocorrelation is needed to optimize the OFC in a way to minimize the noise contribution to the amplitude estimator A.
The OFC are obtained by minimizing the variances of U and V using the Lagrange multipliers method and are given by:

$$a = \frac{(g'.R^{-1}g')R^{-1}g - (g.R^{-1}g')R^{-1}g'}{(g.R^{-1}g)(g'.R^{-1}g') - (g.R^{-1}g')^2} \tag{4.12}$$

and

$$b = -\frac{(g.R^{-1}g)R^{-1}g' - (g'.R^{-1}g)R^{-1}g}{(g.R^{-1}g)(g'.R^{-1}g') - (g.R^{-1}g')^2}. \tag{4.13}$$

For more details, see [149], [152], [153].

4.1.3 Autocorrelation matrix

The noise correlation between the sample i and the sample j is given by the symmetric covariance matrix:

$$[C] = \begin{pmatrix} C_{00} & C_{01} & C_{02} & C_{03} & C_{04} \\ C_{10} & C_{11} & C_{12} & C_{13} & C_{14} \\ C_{20} & C_{21} & C_{22} & C_{23} & C_{24} \\ C_{30} & C_{31} & C_{32} & C_{33} & C_{34} \\ C_{40} & C_{41} & C_{42} & C_{43} & C_{44} \end{pmatrix} \tag{4.14}$$

where $C_{ij} = \sigma_i \sigma_j R_{ij}$. σ_i is defined as the RMS of the noise $n_i - Ped$ in the sample i:

$$\sigma_i = \sqrt{\langle (n_i - Ped)^2 \rangle - \langle (n_i - Ped) \rangle^2}. \tag{4.15}$$

The diagonal terms C_{ii} are equal to σ_i^2. In case if the total noise is equal to the electronic noise (no pileup), the diagonal terms are equal to σ_{el}^2 and the covariance matrix is written as:

$$[C] = \sigma_{el}^2 \times \begin{pmatrix} 1 & C_{01} & C_{02} & C_{03} & C_{04} \\ & 1 & C_{12} & C_{13} & C_{14} \\ & & 1 & C_{23} & C_{24} \\ & sym. & & 1 & C_{34} \\ & & & & 1 \end{pmatrix} \tag{4.16}$$

In the presence of pileup noise, it is important to distinguish two cases: in-time and out-of-time pileup. The element C_{22} of the covariance matrix reflects mainly the effect of the in-time pileup, since the maximum of the in-time pileup noise is reached in the sample 2 (but there may still be a small contribution from the out-of-time pileup). In case of large bunch spacing (*i.e*

only in-time pileup), C_{22} acquires the largest value among the matrix elements while C_{00} could be used to estimate the electronic noise. In case of out-of-time pileup, the element C_{00} of the covariance matrix is affected by the out-of-time pileup (in addition to the electronic noise) of the bunch train. In the particular case of a bunch spacing of 25 ns (the time interval between the samples i and $i \pm 1$), the diagonal elements of the covariance matrix are identical because of the equal impact of the pile-up in all the samples.

I have done some studies on 2010 and 2011 early data comparing C_{00} and C_{22} for different pileup configurations and different regions of the detector. The study was done using ZeroBias events. These events are triggered when collisions occured in BCIDs with a trigger rate proportional to the luminosity. In order to not be biased by the trigger itself (here EM10 with 10 GeV threshold), the ZeroBias trigger events within one turn delay. After one turn from the L1 decision, the luminosity is unchanged however the event corresponds to an arbitrary collision and it can be used to measure pile-up noise.

I quote here a comparison between a run with a mean number of interactions per beam crossing $\langle\mu\rangle = 3$ and a bunch spacing of $\Delta t = 150$ ns from 2010 data (Run 167844) and a run from 2011 data (Run 177540) with $\langle\mu\rangle = 4.5$ and no bunch train (therefore only in-time pileup, no out-of-time pileup). Fig. 4.3 shows the autocorrelation element C_{00} for 2010 (circles) and 2011 (triangles) data in different regions of the detector in unit of square ADC values. The first 4 black points represent respectively the first four layers of the EMB. The red points denote the EMEC (Region 4 of the x-axis: layer 0, 5<Region<11: layer 1, 11<Region<17: layer 2, 17<Region<21: layer 3) and the green points the HEC (every couple of points represent one layer).

- In the barrel, the effect of the bunch train present in the 2010 data is not visible, the element C_{00} reflects mainly the electronic noise;
- In the EMEC, this latter effect is seen in particular in layer 1 where $C_{00}(2010) > C_{00}(2011)$ since at large eta the effect of the pile-up (here out-of-time pile-up since we are considering the element C_{00}) dominates;
- In the HEC, no pileup effect is seen since the pileup events are mostly stopped in the EMEC, thus only the electronic noise contributes.

C_{00} is also shown for the FCAL in Fig. 4.4 with a log scale. The same interpretation as for the EMEC holds. In addition, the same comparisons are made for C_{22} in Fig. 4.5 and for the FCAL in Fig. 4.6. The increase of the in-time pileup ($\langle\mu_{2011}\rangle > \langle\mu_{2010}\rangle$) is clearly seen in the EMEC (layer 1) as well as in the FCAL. Some comparisons with Monte Carlo were also done and a reasonnable agreement is found. For 2012 data, the optimized OFCs are computed taking into account the pileup from Monte Carlo and are used in the data analysis.

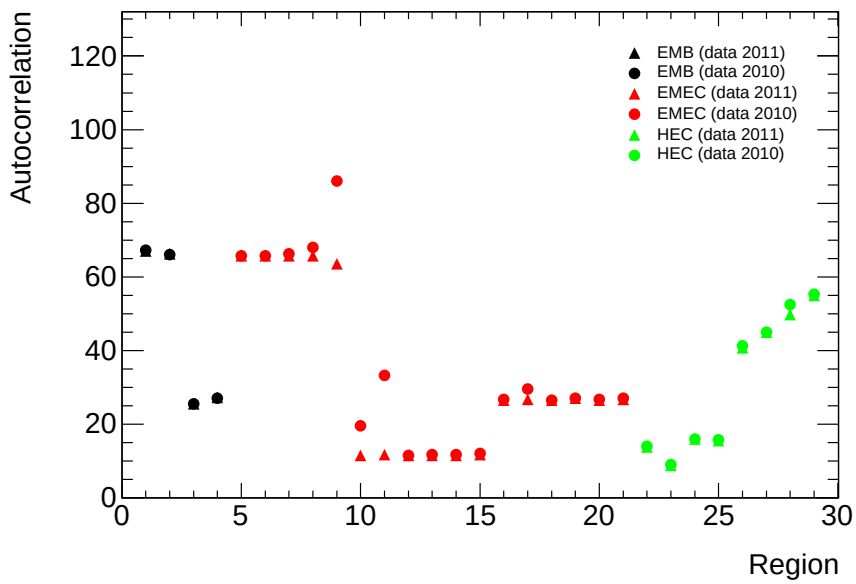

Figure 4.3: C_{00} for Run 167844 of 2010 data (circles) and Run 177540 of 2011 data (triangles) for the different layers (0,1,2,3) of the EMB (black), EMEC (red) and HEC (green).

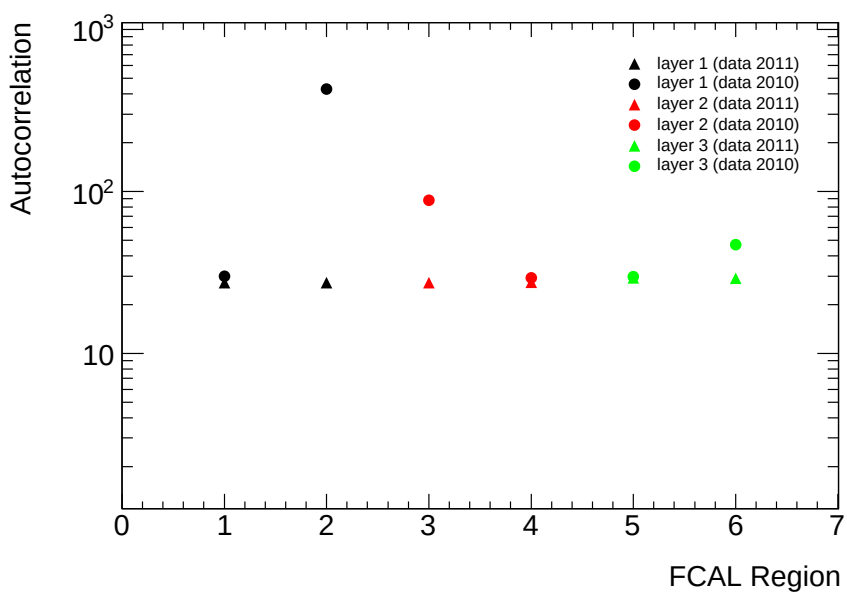

Figure 4.4: C_{00} for Run 167844 of 2010 data (circles) and Run 177540 of 2011 data (triangles) for the different layers (1,2,3) of the FCAL.

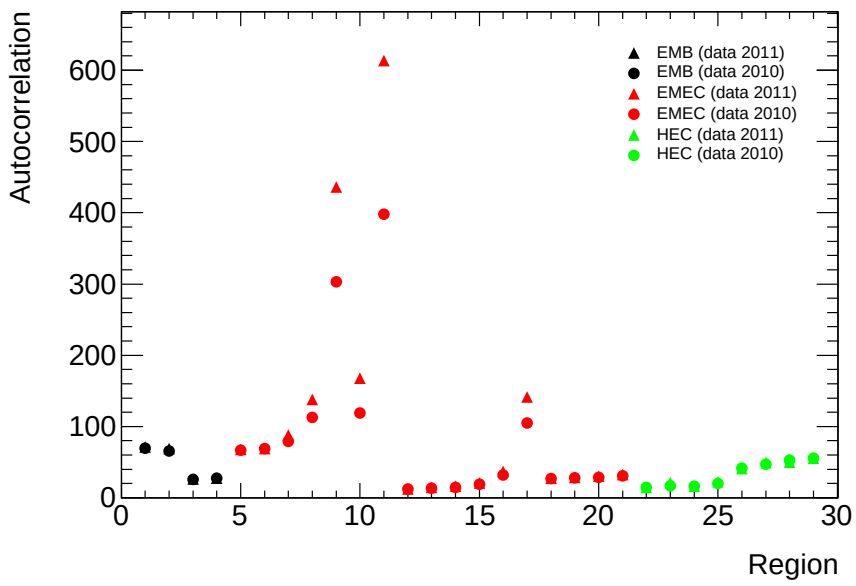

Figure 4.5: C_{22} for Run 167844 of 2010 data (circles) and Run 177540 of 2011 data (triangles) for the different layers (0,1,2,3) of the EMB (black), EMEC (red) and HEC (green).

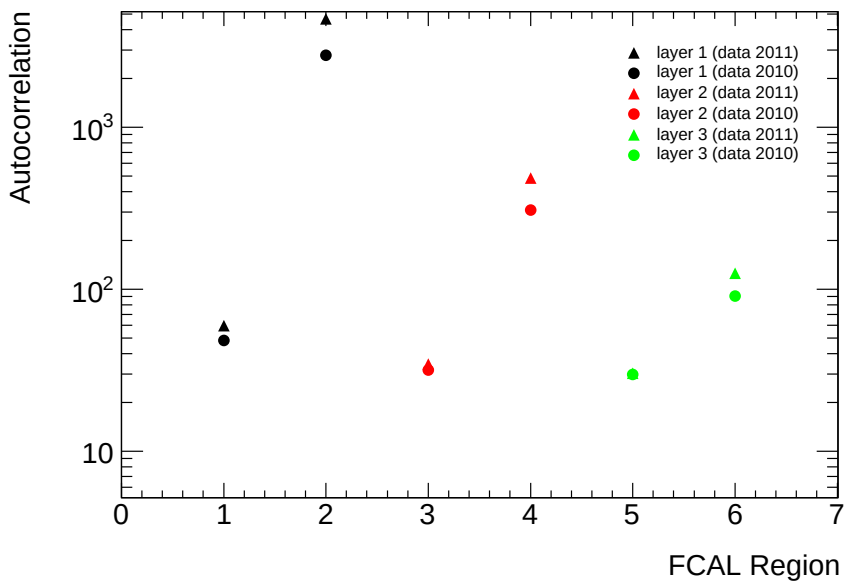

Figure 4.6: C_{22} for Run 167844 of 2010 data (circles) and Run 177540 of 2011 data (triangles) for the different layers (1,2,3) of the FCAL.

4.1.4 Energy reconstruction

The final reconstructed energy of an electromagnetic cell is given by the following equation:

$$E = f_{ADC \to MeV} \sum_i a_i \times (S_i - Ped) \tag{4.17}$$

where $f_{ADC \to MeV}$ is the conversion factor from ADC counts to MeV given by:

$$f_{ADC \to MeV} = \frac{DAC}{ADC} \times \frac{\mu A}{DAC} \times \frac{MeV}{\mu A} \times \left(\frac{M_{phys}}{M_{cal}}\right)^{-1}. \tag{4.18}$$

The subfactors:

- DAC/ADC quantifies the output of the electronics calibration ramp fit;
- $\mu A/DAC$ converts DAC setting of the calibration board to the injected current in the calibration system;
- $MeV/\mu A$ converts the ionization current to the total deposited energy at the EM scale. Its depends on factors such as the sampling fraction of the calorimeter;
- M_{phys}/M_{cal} quantifies the difference between the physical pulse and the calibration pulse.

The time at origin τ is also computed using the following equation:

$$\tau = \frac{\sum_i b_i \times (S_i - Ped)}{\sum_i a_i \times (S_i - Ped)}. \tag{4.19}$$

4.2 MC-based calibration

In this section is described the second step of the calibration dealing with EM clusters. The measured energy and position of the EM clusters are corrected for losses in the upstream material. First, corrections to η and ϕ of the cluster position are applied. Due to the finite granularity of the readout cells, a bias is introduced in the η determination which takes a functional form often referred to as "S-shape". The position (in η) measurements from the first two layers are then combined to define the shower impact point in the calorimeter. In addition, a small bias is introduced in the measurement of the ϕ position which depends on the average shower depth with respect to the accordion structure. The correction to ϕ is applied only in the layer 2 of the calorimeter since it has the best ϕ granularity. Finally, the simulation is used to correct for the energy losses.
The cluster energy is determined by computing and summing four different

contributions: the energy deposited in the presampler and in front of the calorimeter, the energy deposited in the accordion calorimeter, the energy that leaks outside the defined cluster (lateral leakage) and the energy that leaks out of the rear of the EM calorimeter (longitudinal leakage) [143]. The reconstructed energy of an EM object can be written as:

$$E_{e/\gamma} = \Bigg[\underbrace{a(E_{cal},\eta) + b(E_{cal},\eta)E_{PS} + c(E_{cal},\eta)E_{PS}^2}_{Energy \quad in \quad front} + \underbrace{\frac{s_{cl}(X,\eta)}{f_{out}(X,\eta)} \sum_{i=0}^{i=3} E_i}_{Energy \quad in \quad the \quad accordion} \times \underbrace{(1 + f_{leak}(X,\eta))}_{Longitudinal \quad leakage} \Bigg] \times \underbrace{F(\eta,\phi)}_{Energy \quad modulation} \tag{4.20}$$

where:

- $E_{e/\gamma}$ is the electron/photon energy;
- a, b, c are parameters determined as a function of the energy deposited by a particle in the calorimeter (E_{cal}) and η. The coefficient c is set to zero for all η except for $1.55 < |\eta| < 1.8$;
- η is the barycenter of the cluster corrected for the "S-shape" effect described above;
- E_{PS} is the energy deposited in the presampler *i.e* the energy deposited in the active LAr medium divided by an effective sampling fraction (f_{sampl}^{PS}). f_{sampl}^{PS} is fixed to 0.05 in the barrel and to 1/60 in the EC;
- X is the longitudinal barycenter or the shower depth defined by:

$$X = \frac{\sum_{i=0}^{i=3} E_i X_i}{\sum_{i=0}^{i=3} E_i} \tag{4.21}$$

  with E_i the raw energy deposited in the layer i (*i.e* the energy deposited in the LAr medium divided by a region-dependent sampling fraction) and X_i the longitudinal depth of the layer i (in units of radiation length) computed from the center of the detector;
- $s_{cl}(X,\eta)$ is the correction factor to accordion sampling fraction in the cluster;
- $f_{out}(X,\eta)$ is the correction for the lateral leakage *i.e* the energy deposited in the calorimeter outside the cluster;

- $f_{leak}(X, \eta)$ is the longitudinal leakage correction *i.e* the energy deposited by the shower behind the EM calorimeter;
- $F(\eta, \phi)$ is the energy correction reflecting the energy modulation.

Fig. 4.7 shows the fraction of photon cluster raw energy deposited in each layer of the EM calorimeter:

$$f_i = \frac{E_i}{\sum_{i=0}^{i=3} E_i} \tag{4.22}$$

where i=0, 1, 2, 3 denotes the layer 0 (Presampler),1, 2, 3 respectively. The comparison is made between 2010 data with $\sqrt{s} = 900$ GeV and Monte Carlo Pythia [154] Minimum Bias events [155]. The discrepancy between data and simulation for high f_0 (correlated to low f_2) is treated in the next section.

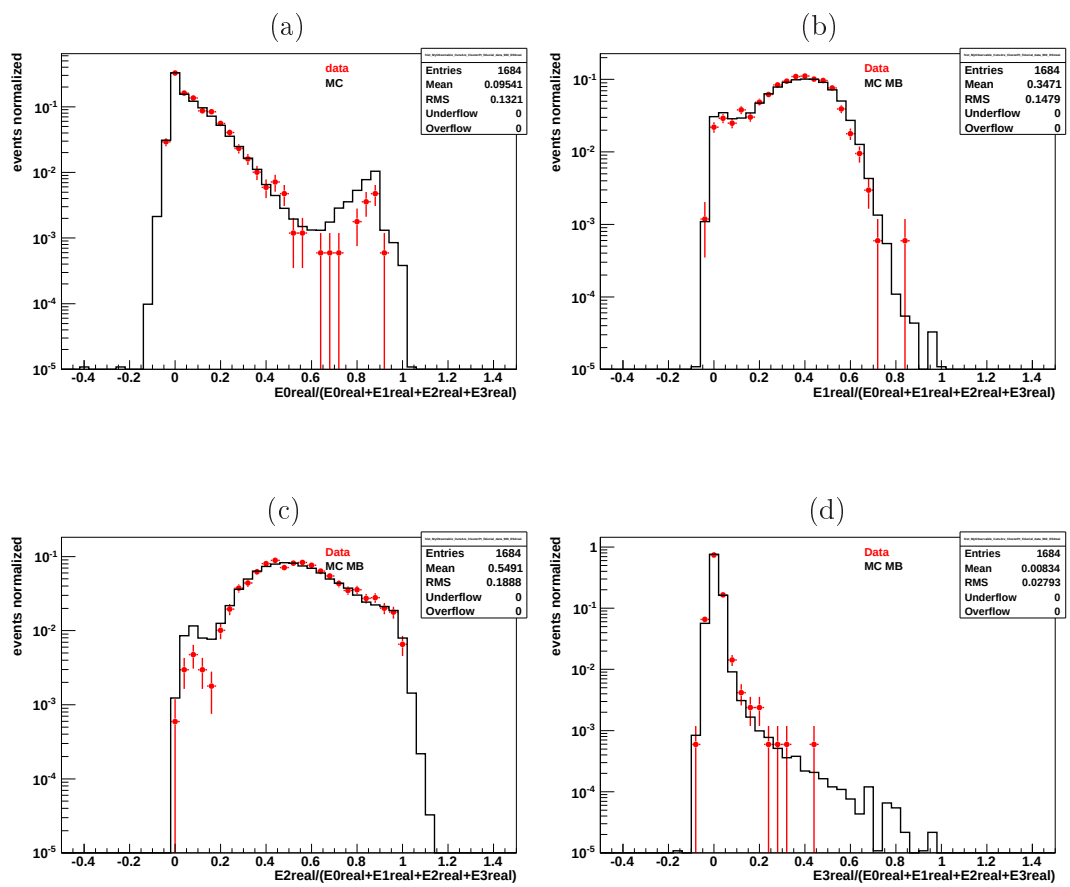

Figure 4.7: Comparison between 2010 data and Pythia MC ($\sqrt{s} = 900$ GeV)for the fraction of the deposited raw energy in (a) layer 0 or Presampler (b) layer 1 (c) layer 2 (d) layer 3.

4.2.1 Birks' Law

In order to understand the discrepancy between data and MC quantified in the presampler at $f_0 > 0.6$, I made various checks. Looking at the corrected energy of photons (by equation 4.20), separating them into converted/unconverted, barrel/EC, applying looser/tighter cuts for the photon selection lead to the same discrepancy. In addition, the same effect was seen for electrons.

A particle identification of the Monte Carlo events in the region $f_0 > 0.6$ is shown in table 4.1. Fig. 4.8 shows the distribution of f_0 from MC minimum-bias with the decomposition into real photons, photons coming from: anti-neutrons, anti-protons and charged pions, and unmatched photons. It is noted that an anti-proton leaves more energy than a proton in the PS. In fact, an anti-proton slows down and leaves energy in the LAr by ionization as much as a proton ($1/\beta^2$ law). The difference remains in the stopped anti-proton which annihilates the proton of a given nuclei producing charged pions. These charged pions contribute to the ionisation energy but also cause the fragmentation of the nuclei into particles like α which leave more local energy. As a result of that, an anti-proton could leave an energy of 50 MeV or even 100 MeV (annihilation+ionisation energy). Similarly, we expect to have more π^+ than π^-. The positive charged pions interact through nuclear interactions like $\pi^+ p \rightarrow \Delta^{++}$ while $\pi^- p \rightarrow$ give neutral bound states (thus giving smaller contribution to the ionisation). We also expect more K_L giving Λ^* which decays in its turn. The real deposited energy in the PS is enhanced by a high sampling fraction that is needed in the PS: 20 in the barrel and 60 in the EC, while in the accordion part of the calorimeter $\sim 20\%$ of the energy is detected in the LAr (thus a factor of 5 is needed to compute the total real energy of the particle). The high PS sampling fraction is necessary for particles like photons and electrons which loose their energy more or less uniformly along their path but not really for a stopped particle like the antiprotons. Thus an antiproton leaving 100 MeV in the barrel PS will be computed as having an energy of ~ 2 GeV. For higher energies, $p_T > 25$ GeV, this problem becomes negligible.

Fig. 4.9 shows two event displays for MC and data respectively with $f_0 > 0.6$. The characteristics of the events are given in table 4.2. In the case of the MC event display, an anti-proton passes through the calorimeter leaving most of its energy in the PS.

The observed disagreement at high f_0 is also partly related to the Birks' law. At the moment of these studies, it was understood that the effect of Birks' law was not implemented in the PS (*i.e* only included in the accordion). The Birks' law describes the recombination effects for ionization energy deposited by particles with high dE/dx in presence of ions. It was noticed in the beginning of the 50's by J. Birks [156] on scintillators. The recombination factor is

PID	Particle	Number
22	γ	607
130	K_L^0	244
211	π^+	506
310	K_S^0	22
321	K^+	51
2112	n	46
2212	p	26
3112	Σ^-	1
3122	Λ	4
3222	Σ^+	1
3312	Ξ^-	2
-3322	$\bar{\Xi}^0$	4
-3222	$\bar{\Sigma}^+$	7
-3122	$\bar{\Lambda}$	74
-3112	$\bar{\Sigma}^-$	3
-2212	$\bar{p}$	384
-2112	$\bar{n}$	642
-321	K^-	144
-211	π^-	373

Table 4.1: Particle identification of events with $f_0 > 0.6$.

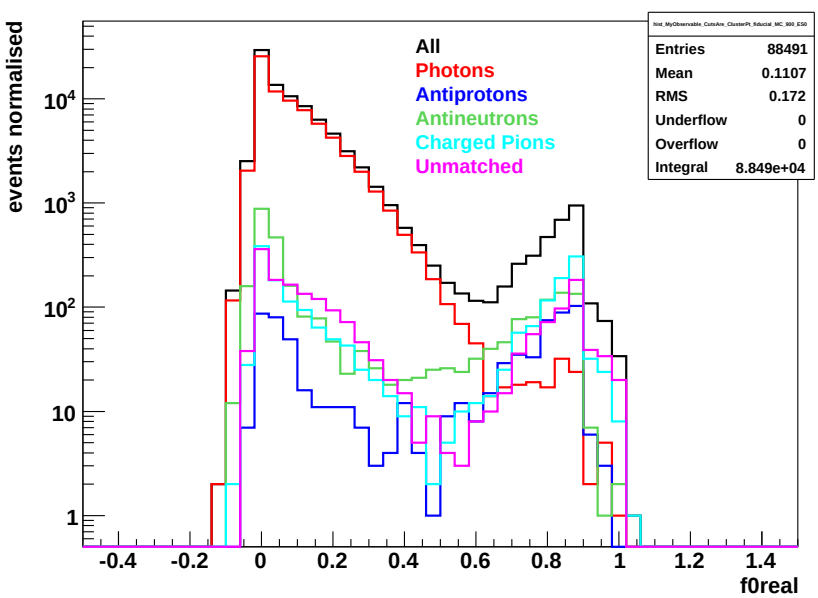

Figure 4.8: Distribution of f_0 obtained from MC minimum-bias with a decomposition showing the mother of the reconstructed photon.

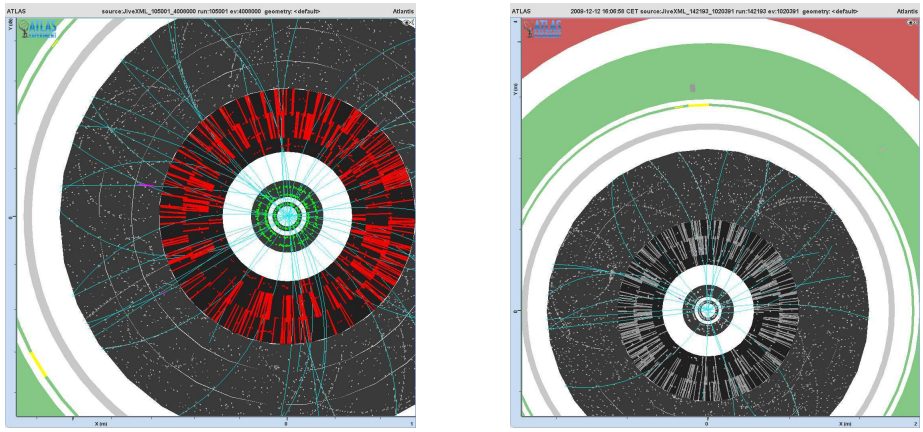

Figure 4.9: Event displays for (left) MC (Pythia 105001 r1023 event 4008000) and (right) data (run 142193 event 1020391) respectively with $f_0 > 0.6$.

Characteristics of the cluster	Value MC	Value Data
ϕ (rad)	-2.59	1.64
η	-0.29	-0.40
p_T (MeV)	3145.65	2504.5
E_0 (MeV)	2617.99	1777.02
E_1 (MeV)	63.62	377.60
E_2 (MeV)	567.77	482
E_3 (MeV)	-48.10	-19.02

Table 4.2: Characteristics of the associated cluster to the event displays for data and MC.

given by:

$$R = \frac{Q}{Q_0} = \frac{A}{1 + \frac{k}{\varepsilon}\frac{dE}{dx}} \tag{4.23}$$

where:

- Q is the measured charge;
- Q_0 is the produced charge;
- $A = 1.0085$;
- $k = 0.0486\ (kV/cm)\ \left(\frac{g}{MeV \cdot cm^2}\right)$ for the Liquid Argon;
- dE is the step energy;
- dx is the step length;
- ε is the electrical field $(= 10\ kV/cm)$.

Fig. 4.10 shows the better agreement between data and MC into which the Birks' law in the PS has been included. Nevertheless, it does not explain all the discrepancy being a probably a combination of three effects:

- inaccurate production of particles in the MC in ATLAS;
- inaccurate G4 simulation: several G4 simulations were checked after discussions with experts [157] and no major change was found;
- inaccurate simulation of the local recombination (Birks' law) in ATLAS: several checks were also made unsuccessfully. Note that even the best studies on local recombination by ICARUS [158] are not going up to the relevant ionization density needed here.

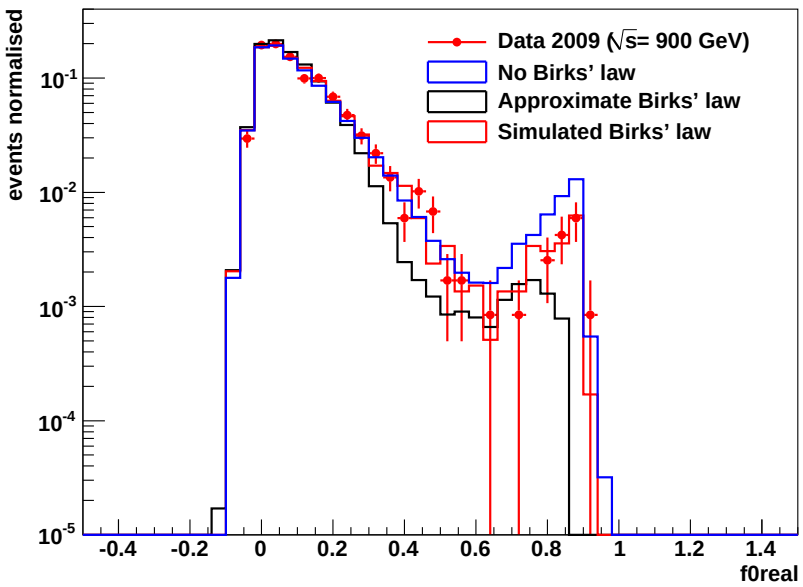

Figure 4.10: Distribution of f_0 in the barrel compared between data 2009, MC without Birks' law in the PS, MC corrected by hand with approximate Birks' law and MC simulated with Birks' law included in the PS.

4.3 In-situ calibration

The third step of the calibration, the "in-situ" calibration, is needed to correct for some long range non uniformities in the calorimeter response which can arise for many reasons: variations in the LAr impurities, high-voltage and temperature effects, amount of upstream material and mechanical deformations. Thanks to the precise knowledge of the Z boson mass from LEP, electron pairs from Z decays can be used for the purpose of intercalibration.

The basic idea of the calibration method is to constrain the di-electron invariant mass distribution to the well-known Z boson line shape. A second goal of the calibration is to provide the absolute EM energy scale. Some results were published in [144] with the 2010 dataset where the calibration was done as a function of η only (not ϕ) because of the limited statistics. The mass of the reconstructed $Z \rightarrow ee$ candidate is computed as:

$$M_{12}^{reco} = \sqrt{2E_1^{reco}E_2^{reco}(1 - cos\theta_{12})} \tag{4.24}$$

where E_1^{reco} and E_2^{reco} are the energies of the two electrons measured in the calorimeter and θ_{12} is the angle between two electrons measured by the tracker. For a given region i of the detector, the electron energy is modified by the non uniformities in the following way:

$$E_i^{reco} = E_i^{true}(1 + \alpha_i) \tag{4.25}$$

where E_i^{reco} is the reconstructed electron energy in the region i, E_i^{true} is the true electron energy and α_i represents the electron energy-scale correction factors. The α_i coefficients are computed from a fit to the reconstructed Z boson mass. Neglecting second order terms and supposing the angle θ_{12} is perfectly known, the reconstructed di-electron invariant mass in a given pair of regions (i, j) is given by:

$$M_{ij}^{reco} = M_{ij}^{true}(1 + \frac{\alpha_i + \alpha_j}{2}) \tag{4.26}$$

where M_{ij}^{true} is the di-electron invariant mass computed from the true electron energies. Fig. 4.11 shows the resulting α values for 40 pb^{-1} of 2010 data. They are within $\pm 2\%$ in the barrel region and $\pm 5\%$ in the forward regions. These α values were recomputed with 2011 data afterwards and additional corrections of the order of 0.5% in the barrel and 1% in the EC were applied to the electrons. Furthermore, a small correction (few per mill) was applied to 2012 data because of the new pileup-optimized OFCs used.

Since electrons and photons interact differently with matter and have different shower profiles, applying the electron energy-scale corrections overcorrect the photon energy-scale if they are due to the material in front of the calorimeter. The uncertainties on the presampler energy scale are also different between electrons and photons since the energy fraction in the presampler is smaller for photons than for electrons.

After applying the electron energy-scale corrections, the energy resolution is measured using the corrected $Z \rightarrow ee$ invariant mass distribution shown in Fig. 4.12. This distribution is fitted with a Breit-Wigner (BW) convoluted with a Crystall-Ball in the mass range 80-100 GeV for central events and in the mass range 75-105 GeV for forward events. The width of the BW is fixed to the PDG value of the Z width (2.49 GeV) and the resolution is the sigma of

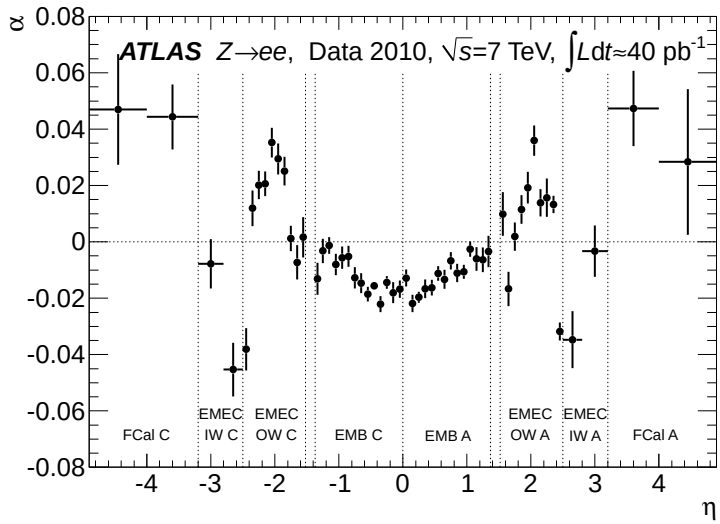

Figure 4.11: The energy-scale correction factor α as a function of the pseudorapidity η of the electron cluster derived from fits to Zee data [144].

the Crystal Ball function. The resolution parameters are extracted from the fit under the assumption that the sampling term, which dominates the electron energy resolution at low energies, is well described by the simulation. The latter assumption is justified by the good agreement in J/ψ M_{ee} distribution between data and MC. The results for the effective constant terms obtained by comparing data and MC resolutions are shown in table 4.3. They were obtained using the formula:

$$c_{data} = \sqrt{2\left(\left(\frac{\sigma}{M_Z}\right)^2_{data} - \left(\frac{\sigma}{M_Z}\right)^2_{MC}\right) + c^2_{MC}} \tag{4.27}$$

where c_{MC} is the residual constant term in the MC of about 0.5%, M_Z denotes the Z mass and σ the gaussian component of the experimental resolution. The main source of systematic uncertainties is coming from uncertainty on the sampling term (taken as 10%). Other sources coming from changing the fit range and from pileup effect are found to be small.

These effective constant terms, estimated from 2010 data, were updated for 2011 data in 2012 with a further split into η bins. It was noticed that the largest effective constant term ($\sim 2.5\%$) is localized in the region $1.5 < |\eta| < 1.8$, probably due to the additional material in front of the detector. In the remaining part of the detector the constant term is of the order of 1%, see [159]. Fig. 4.13 shows the new estimated constant term as a function of η. The same procedure was applied to estimate the constant terms from 2012 data.

η range	Effective constant term
$\eta < 1.37$	1.2% $\pm$0.1% (stat) $^{+0.5\%}_{-0.6\%}$ (syst)
$1.52 < \eta < 2.47$	1.8% $\pm$0.4% (stat) $\pm$0.4% (syst)
$2.5 < \eta < 3.2$	3.3% $\pm$0.2% (stat) $\pm$1.1% (syst)
$3.2 < \eta < 4.9$	2.5% $\pm$0.4% (stat) $^{+1.0\%}_{-1.5\%}$ (syst)

Table 4.3: Measured effective constant term c_{data} from the observed width of the Zee peak for different calorimeter regions.

Note that several stability tests were done in 2011 and 2012. The energy response stability with pile-up is shown in Fig. 4.14 for 1.7 fb^{-1} of 2012 data with $\sqrt{s}$ = 8 TeV [160]. The energy response stability with time is shown for the full 2011 dataset in Fig. 4.15 [161]. In both cases, one note that the energy response is rather very stable. In addition, plots with reconstructed ee mass from Z decays were recently updated for 2011 data and are shown in Fig. 4.16 [162]. A good agreement with 2010 results is seen with a better statistical uncertainty.

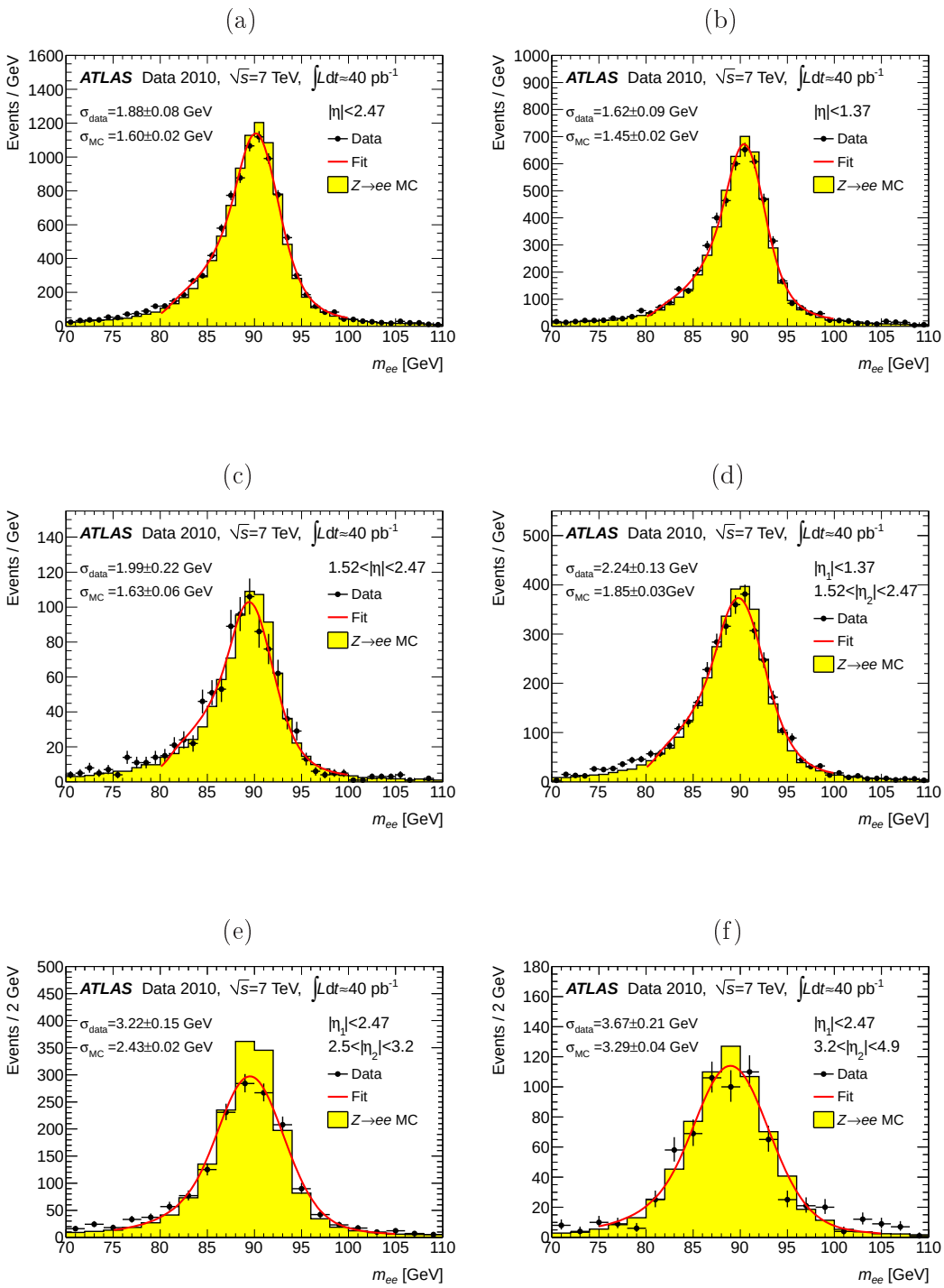

Figure 4.12: Reconstructed M_{ee} for Zee decays (2010 data) for different pseudorapidity regions after applying the baseline Zee calibration. The transition region 1.37<|eta|<1.52 is excluded. The data (full circles with statistical error bars) are compared to the signal MC expectation (filled histogram). The fits of a Breit-Wigner convolved with a Crystal Ball function are shown (full lines). The Gaussian width (sigma) of the Crystal Ball function is given both for data and MC simulation. Note that the additional constant term of 0.7% that is often added to the Monte Carlo is not taken into account in the Zee Monte Carlo shown in this figure [144].

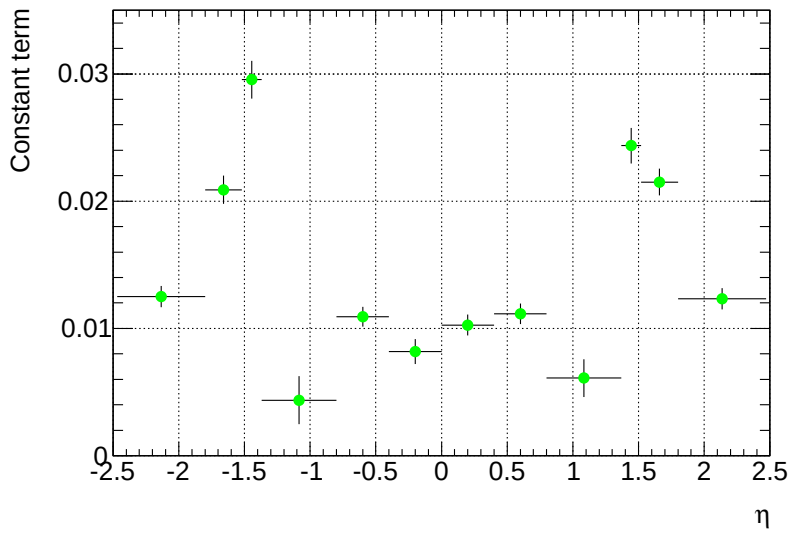

Figure 4.13: Effective constant terms as a function of η estimated from the full 2011 dataset [159].

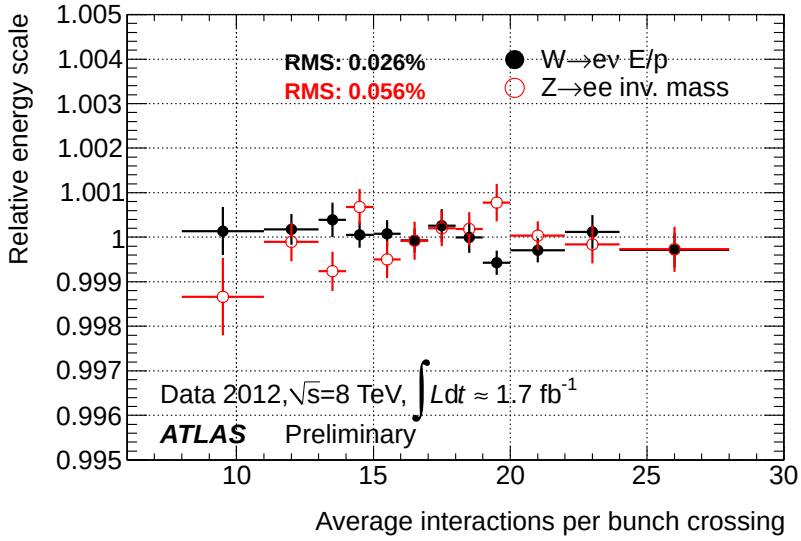

Figure 4.14: Relative fitted peak value of the $Z \to e^+e^-$ invariant mass and the most probable relative value of the E/p distribution for electrons coming from $W \to e\nu$ decays as a function of $\langle\mu\rangle$ for 1.7 fb^{-1} of 2012 data [160].

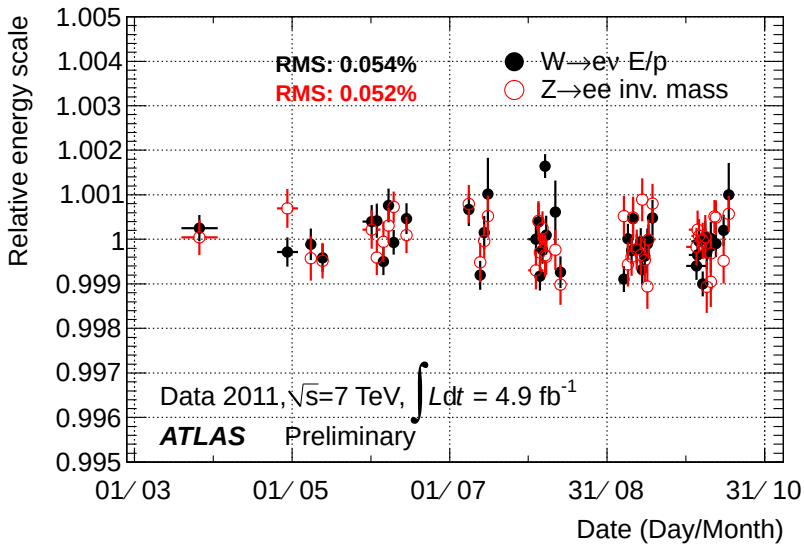

Figure 4.15: Relative fitted peak value of the $Z \to e^+e^-$ invariant mass and the most probable relative value of the E/p distribution for electrons coming from $W \to e\nu$ decays as a function of time for 4.9 fb^{-1} of 2011 data (each bin representing an amount of 100 pb^{-1} of data) [161].

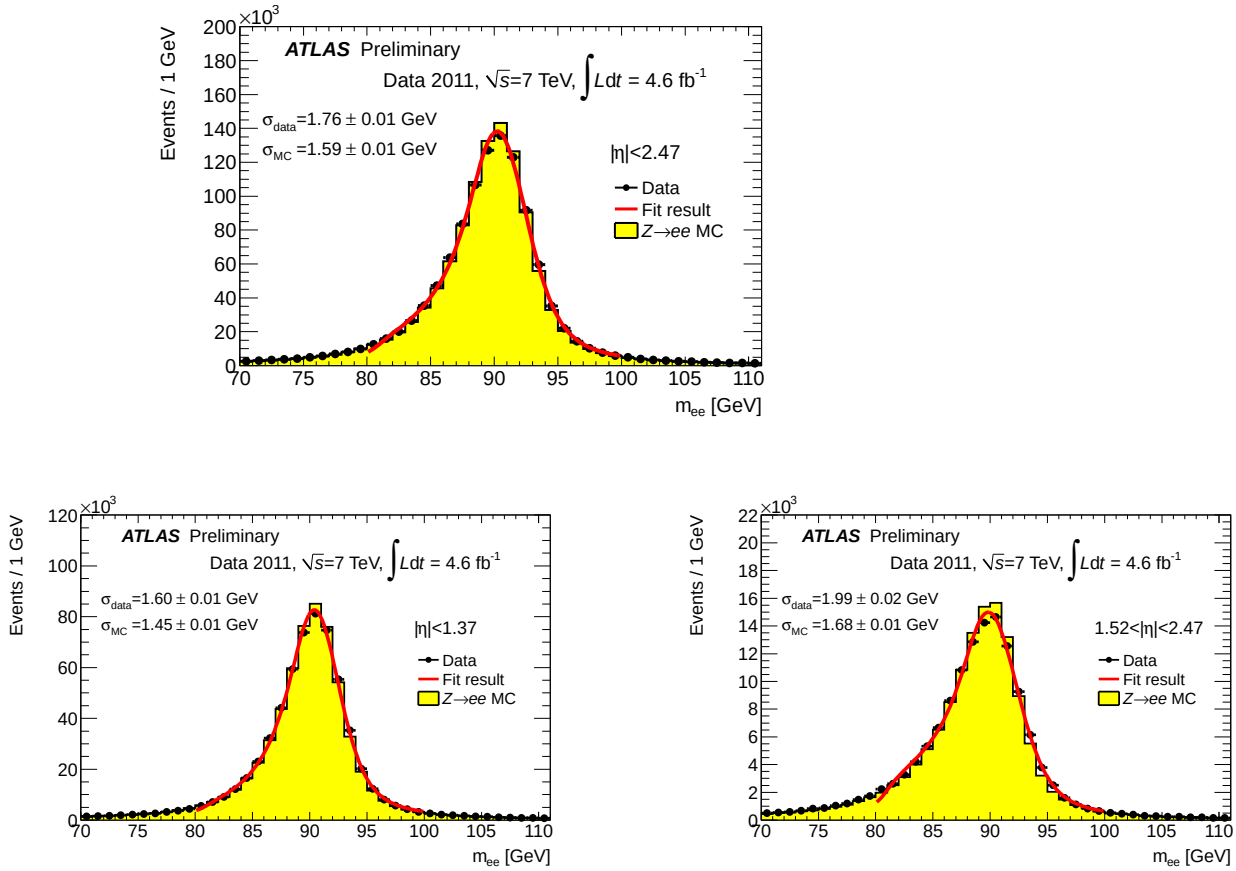

Figure 4.16: Reconstructed M_{ee} for Zee decays (2011 data) after applying the baseline Zee calibration for all pairs (top), for pairs in the barrel $|\eta| < 1.37$ (bottom left) and for pairs in the EC $1.52 < |\eta| < 2.47$ [162].

Chapter 5

Photon Performance

Contents

5.1 Photon Reconstruction **101**
5.2 Photon Identification **102**
5.2.1 Discriminating variables 102
5.2.2 Loose and Tight Selections 106
5.3 Photon Isolation **107**
5.4 Purity of single prompt photons **112**
5.5 Purity of single converted photons **114**
5.6 Purity in $H \to \gamma\gamma$ **117**
5.7 Photon efficiency **119**
5.7.1 Fudge Factors 119
5.7.2 Photon efficiency and uncertainty 120

5.1 Photon Reconstruction

Electromagnetic clusters are reconstructed using the "sliding window" algorithm. They are seeded with transverse energies > 2.5 GeV measured in projective towers of 3×5 cells (in $\eta \times \phi$) in the second layer of the calorimeter. The size of these towers is extended to 3×7 cells in the second layer for converted photons in the barrel to take into account the opening angle between the e^+ and e^- in the ϕ direction induced by the magnetic field. In the EC, the towers are extended to cover 5×5 cells in the second layer for all photons. The larger numbers of cells in η is chosen in order to compensate for the smaller transverse (to the direction of the incident particle) size of the cells (in cm) in the EC than in the barrel.
Clusters without matching tracks are classified as unconverted photons. However if at least one track matches the cluster it will be classified as a converted photon and/or an electron. A track is considered as matched to an EM cluster if its impact point after extrapolation from its last measurement to the second sampling of the calorimeter is within a certain range in (η, ϕ) from the cluster center. The reconstruction of converted photons includes the reconstruction of conversion vertices by the ID which are classified depending on the number

of electron-tracks assigned to them (single or double-track conversion vertices). Single-track conversions occur typically when one of the two produced electron-tracks failed to be reconstructed either if it is very soft ($p_T < 0.5$ GeV) or when the two tracks are very close to each others so they cannot be adequately separated. Double-track (single-track) conversions are efficiently reconstructed at low (large) values of the conversion radius. More details on photon reconstruction can be found in [163, 164, 165]. In [163], the overall reconstruction efficiency for 2011, estimated from Monte Carlo simulations, was found to be about 97.82 $\pm$ 0.03% (94.33 $\pm$ 0.09% for converted photons and 99.83 $\pm$ 0.01% for unconverted photons). From the remaining unreconstructed photons, 2.11 $\pm$ 0.03% are not recovered from the electron container and 0.06 $\pm$ 0.01% of the photons are not reconstructed at all. In 2012, the photon reconstruction was improved especially for converted photons: more stringent cuts on TRT tracks and an improvement of the cluster-track matching. A much more robust converted photon reconstruction with respect to pile-up was achieved before the 2012 data taking. Fig. 5.1 shows the photon reconstruction efficiency (computed from 2012 Monte Carlo mc12) as a function of η, μ (average number of interaction per beam crossing) and p_T for converted and unconverted photons. Fig. 5.2 shows the stability of the fraction of reconstructed photons (converted and unconverted) with respect to pile-up [167]. A migration of $\sim 3\%$ from double to single track conversions is observed while the fractions of converted and unconverted photons are stable within 1% between the two extreme pile-up conditions.

5.2 Photon Identification

5.2.1 Discriminating variables

It is particularly crucial to discriminate between real and fake (coming from jets) photons. For this purpose, cuts on calorimetric discriminating variables have been optimized to provide the best possible pair of high efficiency of real photons - high rejection of fake photons. A brief description of these variables is given in the following.

Variables using the first layer of the EM calorimeter

The fine granularity provided in the first layer for η measurements is used to distinguish between single photons and pairs of photons (mainly originating from π^0 decays) efficiently.

- Front side energy ratio

$$f_{side} = \frac{E(\pm 3) - E(\pm 1)}{E(\pm 1)} \tag{5.1}$$

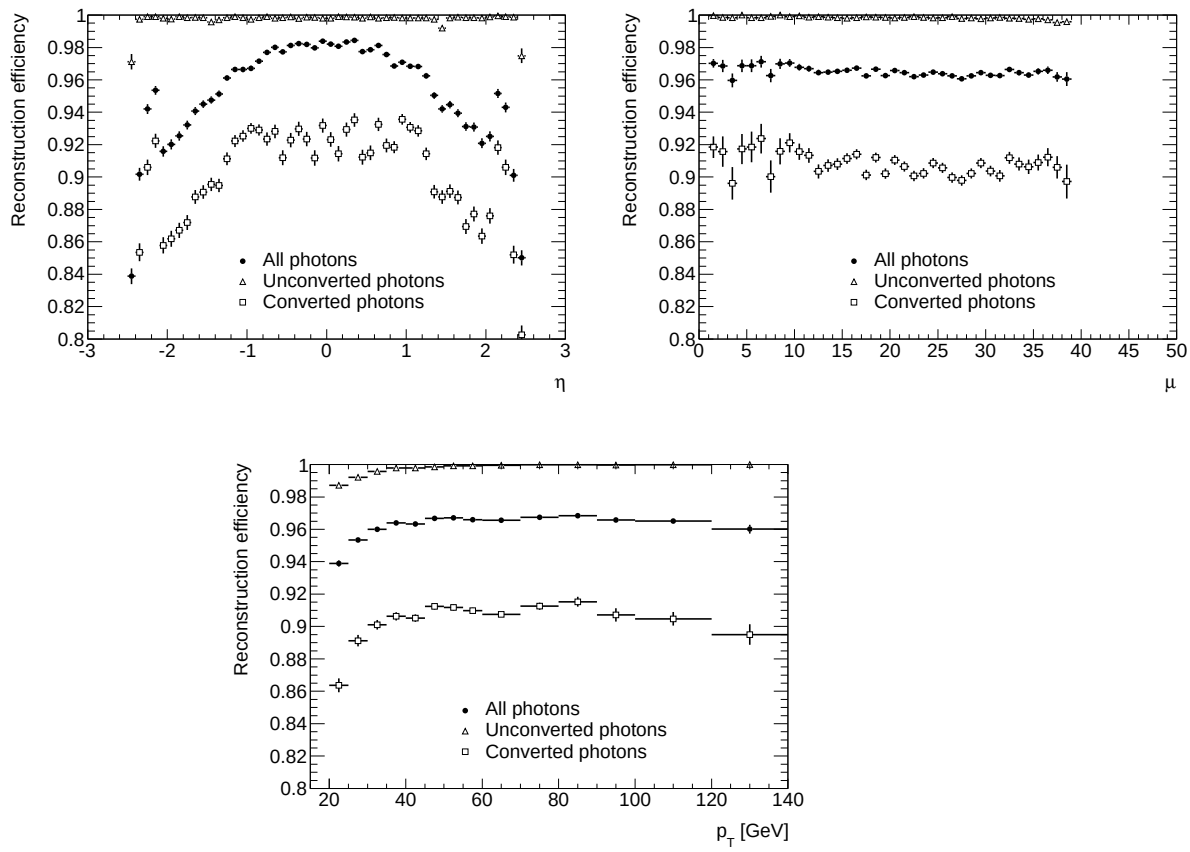

Figure 5.1: Photon reconstruction efficiency as a function of η, μ and p_T estimated from mc12 for converted and unconverted photon candidates [166].

is the fraction of energy deposited in three central strips outside the shower core. $E(\pm n)$ is the energy measured in the first layer of the EM calorimeter in $\pm n$ strip cells around the strip with the highest energy;

- Front lateral width (3 strips)

$$w_{s3} = \sqrt{\frac{\sum E_i (i - i_{max})^2}{\sum E_i}} \tag{5.2}$$

measures the shower width in the layer 1 of the EM calorimeter using three strip cells: the most energetic strip and 2 strip cells around it. The index i is the strip identification number, i_{max} identifies the strip with the maximum energy deposit, E_i is the energy deposit in each strip cell;

- Front lateral width (total) w_{tot} measures the shower width in the layer 1 of the EM calorimeter using all cells in a window $\Delta\eta \times \Delta\phi = 0.075 \times 0.2$,

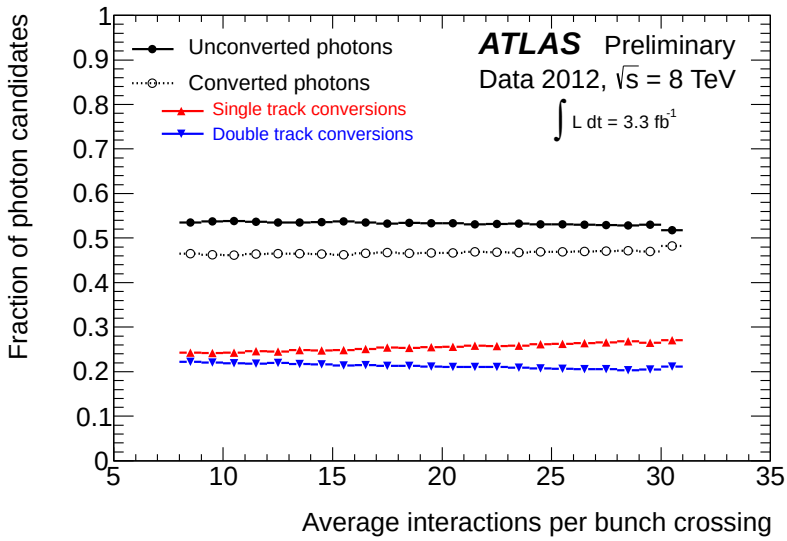

Figure 5.2: Fraction of unconverted and converted (single and double-track conversions) photon candidates as a function of the average number of interactions per beam crossing [167].

corresponding approximately to 24 strip cells in η and 2 in ϕ in the barrel and it is computed as w_{s3};

- Front second maximum difference

$$\Delta E = E_{2^{nd}max} - E_{min} \tag{5.3}$$

is the difference between the energy of the strip cells with the second maximum energy, $E_{2^{nd}max}$, and E_{min}, the energy reconstructed in the strip with the minimum value found in between the first and the second maxima. This variable quantifies the presence of two peaks in the energy profile;

- Front maxima relative ratio

$$E_{ratio} = \frac{E_{1^{st}max} - E_{2^{nd}max}}{E_{1^{st}max} + E_{2^{nd}max}} \tag{5.4}$$

measures the relative difference between the energy of the strip cell with the maximum energy $E_{1^{st}max}$ and the one with the second most energetic strip cell $E_{2^{nd}max}$. It shows the size of the second maximum relative to the size of the first maximum.

Variables using the second layer of the EM calorimeter

EM showers deposit most of their energy in the second layer of the EM calorimeter. They are typically narrower than hadronic showers, therefore the lateral spread of the shower allows a good discrimination between real and fake photons;

- Middle η energy ratio

$$R_\eta = \frac{E_{3\times7}}{E_{7\times7}} \tag{5.5}$$

where $E_{3\times7}$ is the reconstructed energy in 3×7 cells centered on the cluster in the second layer of the calorimeter and $E_{7\times7}$ that of 7×7 middle cells. It is used to measure the spread in η of the energy outside the cluster;

- Middle ϕ energy ratio

$$R_\phi = \frac{E_{3\times3}}{E_{3\times7}} \tag{5.6}$$

where $E_{3\times3}$ is the reconstructed energy in 3×3 cells in the second layer of the calorimeter and $E_{3\times7}$ that of 3×7 middle cells. R_ϕ measures the spread in ϕ of the energy within and outside the cluster. Note that R_ϕ is much less discriminating than R_η for converted photons because of their larger spread in ϕ caused by the magnetic field;

- Middle lateral width

$$w_{\eta_2} = \sqrt{\frac{\sum E_i \eta_i^2}{\sum E_i} - \left(\frac{\sum E_i \eta_i}{\sum E_i}\right)^2} \tag{5.7}$$

measures the shower lateral width in η over a window of 3×5 cells in $\Delta\eta \times \Delta\phi$ around the photon cluster. i is the cell index.

Variables using the hadronic calorimeter

Fake photons penetrate deeper in the calorimeter and deposit sizeable energy beyond the EM calorimeter since they are surrounded by hadronic activity while real photons deposit primarily their energies in the EM calorimeter;

- Normalized hadronic leakage

$$R_{had1} = \frac{E_T^{had1}}{E_T} \tag{5.8}$$

where E_T^{had1} is the transverse energy deposited in the first compartment of the hadronic calorimeter and E_T is the transverse energy computed as $E/cosh(\eta)$ with E the cluster energy and η the cluster pseudorapidity

reconstructed in the second sampling of the EM calorimeter. R_{had1} is used in the range $|\eta| < 0.8$ and $|\eta| > 1.37$, while for the rest the variable $R_{had} = \frac{E_T^{had}}{E_T}$ is used where E_T^{had} is the total transverse energy measured in all the hadronic calorimeter.

5.2.2 Loose and Tight Selections

The "loose" selection applies cuts only on the variables using the second layer of the calorimeter and the hadronic calorimeter. The cuts were optimized to have the highest background rejection for a photon efficiency at least of 97%. They are identical for converted and unconverted photon candidates. The "tight" selection applies cuts on all the above listed variables. They were optimized to have the highest rejection for an average efficiency e.g of about 85% for $p_T = 30$ GeV. Different cuts are used for converted and unconverted photons since the shower shapes are different for both types of photons [163] (especially for R_ϕ, which has not a discriminating power against background in the case of converted photons).

The tight cuts have improved progressively in the last years with the better understanding of data and Monte Carlo. In the Monte Carlo samples used for 2010 analysis (mc10), the EM calorimeter absorbers were described by a blended material and the GEANT4 version used at that time did not treat fully correctly energy loss in blended materials. This leads to too narrow shower shapes in the simulation. For the Monte Carlo samples used for 2011 analysis (mc11), the absorber description was made more accurate and at the same time the GEANT4 problem with blended material was fixed. It leads to an improvement in the comparison between data and MC in the shower shape variables, although some differences remain not completely understood. Besides the GEANT4 version used in mc11 had a bug in the electron multiple scattering description leading to a small excess of tails at very large scattering angles. This affected the photon identification efficiency prediction from the MC at the 1% level. This problem was fixed in the GEANT4 version for the MC samples used for the 2012 8 TeV analysis (mc12) [169]. Finally a re-optimization of some cuts has been done for 2012 data to take into account the change in the cross-talk induced by the updated OFCs in 2012 [170, 171].

Three sets of tight identification cuts were used for the 2011 and 2012 analysis:

- **Tight2011**: for the analysis of the $\sqrt{s} = 7$ TeV 2011 data published in [172, 173], a cut-based selection is used. The photon reconstruction and identification efficiency ranges typically from 65% to 90% for $25 < p_T < 80$ GeV;

- **NN2011**: for the improved analysis of $\sqrt{s} = 7$ TeV 2011 data published in [174], a neural network based selection [175, 176] is used. It was tuned to achieve similar jet rejection as the cut based menu Tight2011. An increase of about 15% on the efficiency for $H \to \gamma\gamma$ events for a given rejection is obtained [176]. The photon efficiencies, averaged over eta, range between 85% and above 95% for the p_T range corresponding to a BEH boson with a mass of 120 GeV;
- **Tight2012**: for the analysis of $\sqrt{s} = 8$ TeV 2012 data published in [174], a cut-based selection [171], tuned for robustness against high pileup effects (by relaxing some cuts on pileup-sensitive shower shape variables and tightening others), is used. In addition, a change in the loose 2012 is made to correct for pileup effects on photon efficiencies (loosening in particular the cuts on the hadronic leakage).

5.3 Photon Isolation

In order to further separate prompt photons from their background of fake photons (mainly light mesons), photon candidates are required to be isolated from nearby hadronic activity characteristic of a jet with a leading light meson. However, direct photons at LO are produced back-to-back in ϕ and are therefore considered isolated. This is not perfectly true for fragmentation photons which are accompanied by hadronic activity, and thus an isolation cut will remove in addition to the background some fraction of these fragmentation photons. The situation gets further complicated at NLO with the presence of soft gluons since the isolation cut restricts the allowable phase space for soft gluon emission. An optimization of the isolation cut has been performed, while measuring the first inclusive isolated prompt photon cross section [177], taking into account the theoretical restrictions and providing the best possible prompt photon efficiency and background rejection. The activity surrounding the photon cluster can either be measured by the ID, the so-called track isolation, or by the calorimeter, calorimetric isolation.

Track Isolation

In this case, the photon is considered isolated if the sum of p_T of the tracks, $\sum_{p_T}^{Tracks}$, surrounding it in a cone of $\Delta R = 0.3$ is less than 4 GeV. The value of the cut has been optimized on Monte Carlo in the CSC note [102] to get the best background rejection for a given signal efficiency. In addition the tracks have to satisfy the following conditions:

- have a transverse momentum $p_T > 1$ GeV;
- leave at least one B-layer hit and 7 silicon hits (Pixel+SCT);

- have an impact parameter $d_0 < 1$ mm.

In the smaller cone, $\Delta R = 0.1$, the tracks from conversions are excluded.
Fig. 5.3 (top) shows the rejection factor as a function of the signal efficiency using Pythia di-jets background samples (JF17) with no pileup, where the rejection factor is given by:

$$R = \frac{N_{jets}}{N_{fake\gamma}}, \tag{5.9}$$

with N_{jets} the number of jets passing the photon tight identification criteria and $N_{fake\gamma}$ the number of jets passing both the photon tight identification and track isolation criteria, and the signal efficiency is given by:

$$\varepsilon = \frac{N_{\gamma}^{reco\ after\ cut}}{N_{\gamma}^{truth,tight}}, \tag{5.10}$$

with $N_{\gamma}^{reco\ after\ cut}$ the number of reconstructed photons passing the photon tight identification and track isolation cut selections and $N_{\gamma}^{truth,tight}$ the true number of photons passing the tight identification criteria. Both true and fake photons are asked to have a $p_T > 25$ GeV and to pass the fiducial area selections ($|\eta| < 1.37$ or ($|\eta| > 1.52$ and $|\eta| < 2.37$)).
In addition, I excluded the Bremsstrahlung photons to avoid the double counting in the rejection computation of reducible background. The different points on the curves correspond to different cuts on $\sum_{p_T}^{Tracks}$. The red curve corresponds to the inclusive case while the green and blue curves correspond to the rejections of jets originating from gluons or quarks respectively. As expected the gluon rejection is higher than the quark rejection for a given efficiency (for more details see [178, 179]). The gluon has a lower probability to be fragmented into a π_0 with a large z ($p_T^{\pi_0}/p_T^{parton}$). Also, we have observed that this fake rate depends on event generators and processes. A comparison between Pythia and Herwig [180], in Fig. 5.3 (bottom) shows the better rejection provided by Pythia for a given signal efficiency. For instance for the cut used $\sum_{p_T}^{Tracks} < 4$ GeV, shown as a black dot on the figure, a signal efficiency of 99.22 $\pm$ 0.04% (99.23 $\pm$ 0.04%) and a rejection factor of 1.57 $\pm$ 0.01 (1.36 $\pm$ 0.01) is obtained in the Pythia (Herwig) samples (the fact that the rejection in Pythia is higher than in Herwig was already studied in [181]). In green is shown the rejection vs efficiency for γ + jet Pythia sample. The γ + jet rejection is equivalent to the dijets one for the cut we used at 4 GeV.

However despite these studies, the track isolation is not yet used in the photon analysis mainly for two reasons:

- in the $H \rightarrow \gamma\gamma$ searches because of the non ability to reconstruct correctly the unconverted photon vertices which will lead to a non-robustness of the isolation with the increasing pileup;

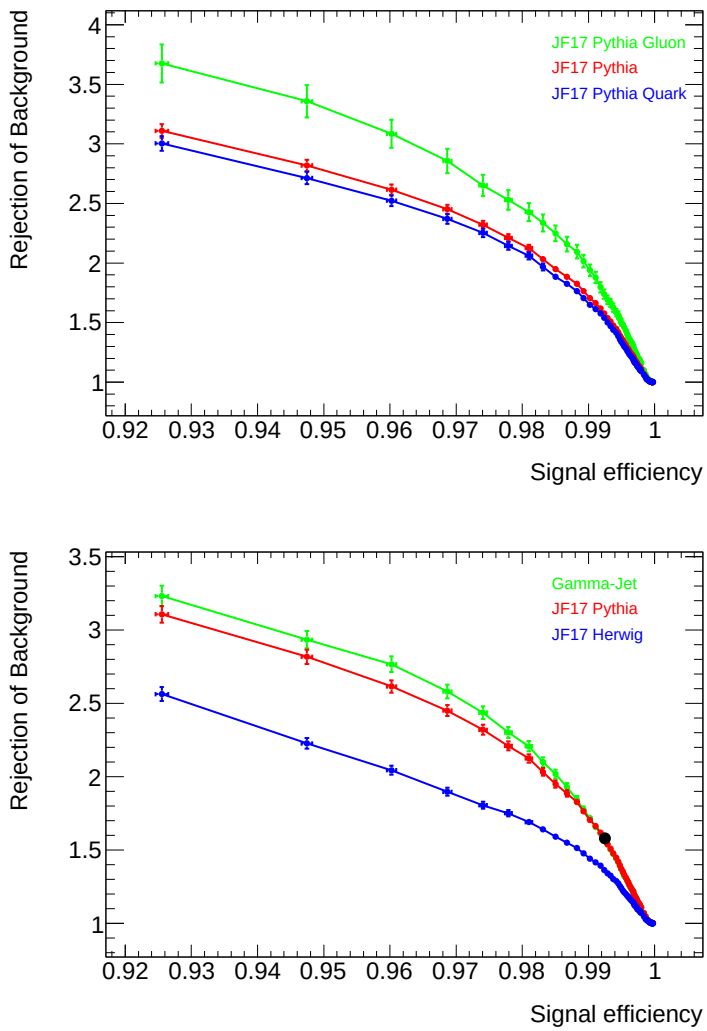

Figure 5.3: Background rejection versus signal efficiency for different cuts on $\sum_{p_T}^{Tracks}$ for (top) Pythia di-jets samples with a subdivision into jets coming from quarks and those coming from gluons and for (bottom) Pythia di-jets, Pythia γ-jet and Herwig di-jets. The black dot indicates the CSC note cut of $\sum_{p_T}^{Tracks} < 4$ GeV.

- in the single photon inclusive cross section measurements because of the non-trivial correspondence with the partonic isolation.

An alternative is the isolation based on the calorimeter detailed in the following.

Calorimetric Isolation

The calorimetric isolation variable, EtConeX, is computed as the scalar

sum of the transverse energy deposited in all the calorimetric cells (electromagnetic and hadronic) within a cone of radius $\Delta R = X/100$ around the photon axis (typically $\Delta R = 0.4$). The energy of the photon is excluded from the sum by substracting the energy in 5×7 rectangular core centered on the photon *i.e* the equivalent of $\sim 95\%$ of its energy. In the ATLAS analysis of 2010 (2011), a photon candidate is considered isolated if EtCone40$<$ 3 (5) GeV. This variable is corrected [140] based on [182, 183] for:

- the energy from underlying event (UE) and pileup (both in-time and out-of-time pileup). This correction is computed by multiplying the ambient transverse energy density by the active area of the isolation cone. The procedure used to estimate the ambient transverse energy density is made on an event-by-event basis, it is given by the median of the jet transverse energy divided by the jet area. The reconstruction of jets in a given event is done according to the k_T algorithm which is run on three-dimensional noise suppressed topological clusters outside the cone called "topoclusters" required to have one cell with a threshold of 4σ deviation from the baseline noise rate (for a detailed definition of the topoclusters see [184];
- the energy leakage from the photon outside the substracted rectangular core of 5×7. The leakage is estimated to be between 2 and 5% of the photon transverse energy (depending on η). After this correction, the mean of the photon isolation distribution is independent of the true photon transverse energy.

However, the isolation variable EtCone40 includes all the cells without any noise suppression (only used in the correction for UE and pileup). In addition, the correction of UE and pileup based on topoclusters leaves a residual dependence on the pileup due to low energy cells below the topocluster noise cut. An improvement was made in the beginning of 2012 using only topoclusters inside the cone for the isolation itself, the resulting variable is called topoPosEMEtCone40 [185]. The difference in computation of the isolation in both cases is sketched in Fig. 5.4, where EtCone40 corresponds to all the cells in the cone and topoPosEMEtCone40 corresponds to the "orange" topological clusters only. topoPosEMEtCone40 is also corrected for lateral leakage under the assumption of the correction linearity as a function of p_T for the sake of simplicity (the non-linearity effect was shown to be very small). It is further corrected the same way as for EtCone40 for the pileup and UE effects. Using the improved isolation reduces as well the global averaged shift over the leading and sub-leading candidate isolation distributions between data and MC from 800 MeV for EtCone40 to 100 MeV. The robustness of the new isolation variable at high pileup was tested up to an average number of interactions per beam crossing of $\mu = 40$. The new isolation is shown to be independent

of the bunch crossing ID (BCID). Fig. 5.5 shows the evolution of μ_{CB}, the mean of the Crystal-Ball used to fit the isolation distribution, as a function of BCID. The MC mean has been corrected with the shift described above. The large variation in the left plot shows that the pile-up corrections applied to EtCone40 are not efficient. The right plot shows a very nice stability with respect to pile-up. topoPosEMEtCone40 is used in the improved analysis of the 2011 data and in the 2012 data analysis, with photon candidate considered isolated if topoPosEMEtCone40<4 GeV.

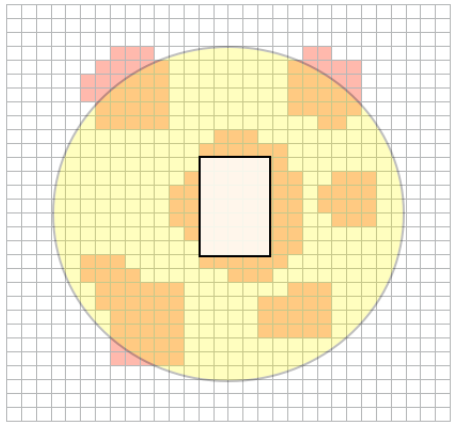

Figure 5.4: Illustration of the isolation computation. The photon candidate energy is mostly contained in the central white rectangle $\Delta\eta \times \Delta\phi = 5 \times 7$. The yellow cone of $\Delta R = 0.4$ is drawn around the candidate. All the cells inside the cone are used in the computation of EtCone40 whereas in the topoPosEMEtCone40 only cells belonging to 420 topological clusters shown in orange are used.

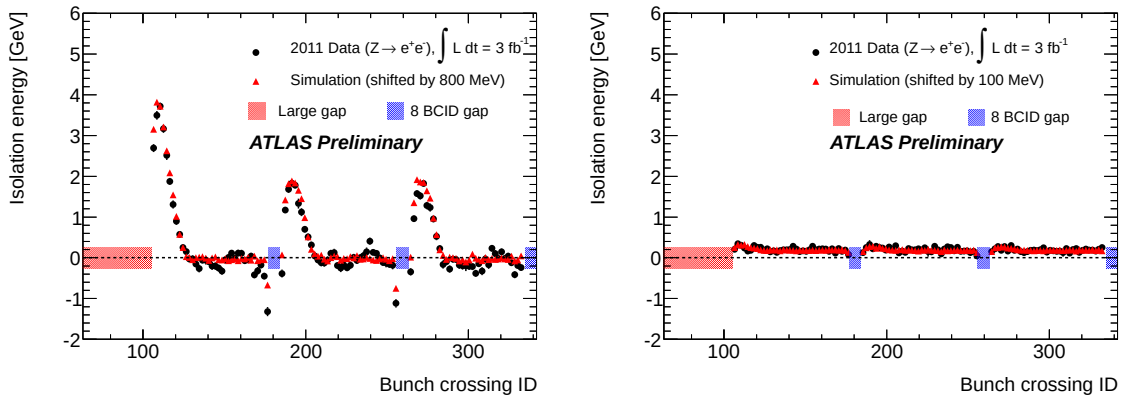

Figure 5.5: Evolution of μ_{CB} as a function of BCID for EtCone40 (left) and topoPosEMEtCone40 (right). Only the first three sub-trains of the first train are shown. The MC BCID have been shifted (by 104) to match the data [185].

5.4 Purity of single prompt photons

A data-driven method was used to estimate the background and to extract the prompt photon signal first in [186]. This method, so-called 2D method, relies on the use of two dimensions: the isolation variable and the "tightness" identification criteria (see Fig. 5.6). The signal region is defined as the region with isolated candidates (here EtCone40<3 GeV) passing the tight identification criteria, N^A. Two of the background enriched regions are formed with non-isolated candidates (here EtCone40>5 GeV) either passing (N^B) or failing (M^B) the tight identification criteria and one of the background enriched region with isolated candidates and failing the shower shape requirements (M^A). In addition this method relies on two assumptions:

- the signal contribution in the three background enriched regions is neglected;
- for the background, the isolation is independent of the shape of the energy deposit in the cells of the first layer. The ratios M^B_{bkg}/M^A_{bkg} and N^B_{bkg}/N^A_{bkg} are equal.

The signal yield and the purity are therefore given by:

$$N^A_{sig} = N^A - N^A_{bkg} = N^A - N^B \frac{M^A}{M^B} \tag{5.11}$$

$$P = N^A_{sig}/N^A = 1 - \frac{N^B}{N^A}\frac{M^A}{M^B} \tag{5.12}$$

These equations are corrected for the inaccuracy of the above assumptions. The first assumption is checked using prompt photons Monte Carlo sample. The fractions of signal leaking into the three background regions, $c_1 = \frac{N^B_{sig}}{N^A_{sig}}$, $c_2 = \frac{M^A_{sig}}{N^A_{sig}}$ and $c_3 = \frac{M^B_{sig}}{N^A_{sig}}$ are given in Table 5.1. It was found that the control region the most affected by the signal is the one with isolated candidates failing the shower shape requirements, with a fraction of signal events falling into this region varying from 18% to 5% depending on E_T. It follows the following corrections to equation 5.11:

- $N^B \rightarrow N^B - c_1 N^A_{sig}$;
- $M^A \rightarrow M^A - c_2 N^A_{sig}$;
- $M^B \rightarrow M^B - c_3 N^A_{sig}$.

The second assumption requires a minimum correlation between the isolation and the first layer variables. In order to minimize this correlation, one would prefer to revert cuts on a small subset of shower shape variables that are less correlated with isolation in the background enriched samples. The natural

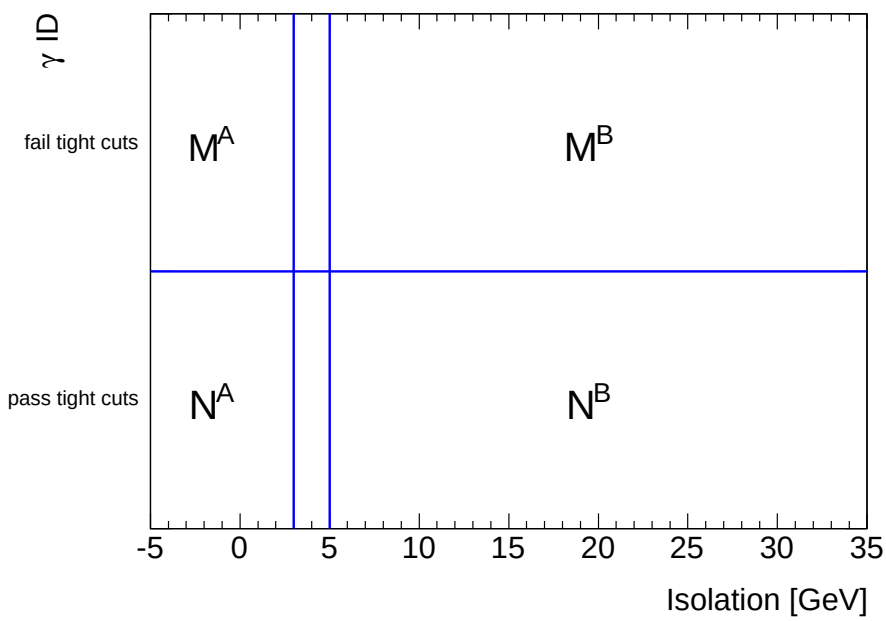

Figure 5.6: Illustration of the two-dimensional plane, defined by means of the isolation and a subset of the photon identification (ID) variables. N^B, M^A and M^B are the observed yields in the three control regions and N^A is the total yield in the signal region.

choice is to revert the cuts on f_{side} and w_{s3} which are variables using fewer cells. Another choice is to revert the cuts on the five strip variables, this corresponds to the Loose' in the Table 5.2. However due to the lack of Monte Carlo statistics, we reverted the requirements on four of the five variables (all but w_{tot}).

E_T interval [GeV]	$10 \leq E_T < 15$	$15 \leq E_T < 20$	$E_T \geq 20$
R	1.10 ± 0.03	0.91 ± 0.05	1.02 ± 0.02
c_1	$(1.8 \pm 0.2) \times 10^{-2}$	$(3.1 \pm 0.5) \times 10^{-2}$	$(5.3 \pm 0.3) \times 10^{-2}$
c_2	$(18.0 \pm 0.6) \times 10^{-2}$	$(11.3 \pm 0.7) \times 10^{-2}$	$(6.6 \pm 0.2) \times 10^{-2}$
c_3	$(5.3 \pm 1.1) \times 10^{-3}$	$(2.5 \pm 1.3) \times 10^{-3}$	$(6.9 \pm 1.0) \times 10^{-3}$

Table 5.1: Background pseudo-correlation factor R and fractions of signal leakage c_i into the three control regions for different bins of reconstructed transverse energy E_T.

With this configuration, the correlation is computed in the background Monte Carlo sample and found to be less than 15%. The values of the correlation ratio $R = \frac{N^A_{bkg} M^B_{bkg}}{N^B_{bkg} M^A_{bkg}}$ for photon candidates with $p_T > 10$ GeV are shown

in Table 5.1. One sees in particular that R is close to 1 when relaxing f_{side} and w_{s3}. The correlations between the isolation and the shower shape variables are taken into account by correcting the estimated background yield in the signal region by the correlation ratio estimated from simulated background events. Taking into account these corrections, the signal yield and the purity

Cut	EtCone40<5 GeV	EtCone40>5 GeV	Correlation
Tight	6518	2716	1.00
Loose - Tight	26040	13772	1.2692 ± 0.032
Loose' - Tight	8988	4430	1.1828 ± 0.035
ERatio - Tight	801	418	1.2523 ± 0.081
w_{s3} - Tight	502	170	0.8126 ± 0.074
f_{side} - Tight	874	406	1.1148 ± 0.072
w_{tot} - Tight	132	76	1.3817 ± 0.201
ΔE - Tight	348	188	1.2964 ± 0.121
w_η - Tight	353	121	0.8226 ± 0.089
R_ϕ - Tight	926	351	0.9097 ± 0.061
R_η - Tight	1639	1046	1.5316 ± 0.070
Hadronic leakage - Tight	294	187	1.5264 ± 0.147
f_{side} + w_{s3} - Tight	1708	693	0.9737 ± 0.049

Table 5.2: Values of the correlation ratio computed for single photons with $p_T > 10$ GeV. The convention Variable - Tight means relaxing cuts on this particular variable and requiring not to pass the tight identificiation criteria.

are given by:

$$N^A_{sig} = N^A - \left[(N^B - c_1 N^A_{sig})\frac{M^A - c_2 N^A_{sig}}{M^B - c_3 N^A_{sig}}\right]\left(\frac{N^A_{bkg}}{N^B_{bkg}}\frac{M^B_{bkg}}{M^A_{bkg}}\right) \quad (5.13)$$

$$P = \frac{N^A_{sig}}{N^A} \quad (5.14)$$

The number of photon candidates in the signal region in 15.8 nb^{-1} of 2010 data, together with the estimated purity, are summarized in Table 5.3 for three different transverse energy E_T bins. The total systematic uncertainties on the signal yield and on the purity are also quoted. For more details on the sources of systematic uncertainties, see [186]. These numbers were update later, see for instance [177].

5.5 Purity of single converted photons

Another method of qualitative purity estimation was used at the time of ICHEP 2010 applied on single converted photons. The converted photons

E_T interval [GeV]	$10 \leq E_T < 15$	$15 \leq E_T < 20$	$E_T \geq 20$
Number of candidates	5271	1213	864
Estimated purity P [%]	24 ± 5	58 ± 5	72 ± 3
Systematic uncertainty on P [%]	24	8	6
Estimated signal yield N_{sig}^{A}	1289 ± 297	706 ± 69	618 ± 42
Systematic uncertainty on N_{sig}^{A}	1362	86	59

Table 5.3: Number of candidates in data, estimated signal purity and signal yield in the signal region, and corresponding systematic uncertainties, in three intervals of the photon transverse energy.

were asked to have $p_T > 20$ GeV, to pass tight identification criteria, isolation requirements (EtCone40 (Corrected for pileup and UE) < 3 GeV) and to be associated with two tracks. Both tracks are required to leave hits in the silicon detector (pixel + SCT) in order to have a better measurement of their transverse momentum. The discriminating variable used is the p_T/E_T where p_T is the transverse momentum of the associated two tracks and E_T is the transverse energy of the photon candidate. p_T/E_T is expected to be roughly equal to 1 for prompt photons, in the absence of the bremsstrahlung of an electron or positron, and to be roughly flat between 0 and 1 for the dominant background coming from π^0. The comparison I made in Fig. 5.7 of [187, 188] was done for 2010 data with an integrated luminosity of 62 nb^{-1} and Monte Carlo simulation (photons selected from GJ17 and JF17 samples). The MC and data are normalized to unity. The signal from MC is obtained by selecting photons coming from hard process scattering or a bremsstrahlung process (radiations from quarks) while the background is anything else. One sees the compatibility between data and prompt photons looking to the peak $p_T/E_T = 1$. This analysis was not used in the determination of the purity but gave us more confidence in our first purity measurements. Fig. 5.8 shows an update of this study with an integrated luminosity of ~ 1 pb^{-1}.

In addition, another very preliminary study was made at that time looking at p_T/E_T for non isolated converted photon candidates for 2010 data with a luminosity of 20 pb^{-1}. Same selections were applied as above except for isolation: EtCone40 (corrected) > 5 GeV. Furthermore, both tracks are required to leave no hit in the B-layer in order to reduce the electron contamination. Fig. 5.9 shows the distributions of p_T/E_T for these non-isolated candidates in four different p_T ranges. One sees a peak of p_T/E_T at 1 in data, probably due to a bremsstrahlung component. This method (with further studies) could be a possible way to measure brem in data.

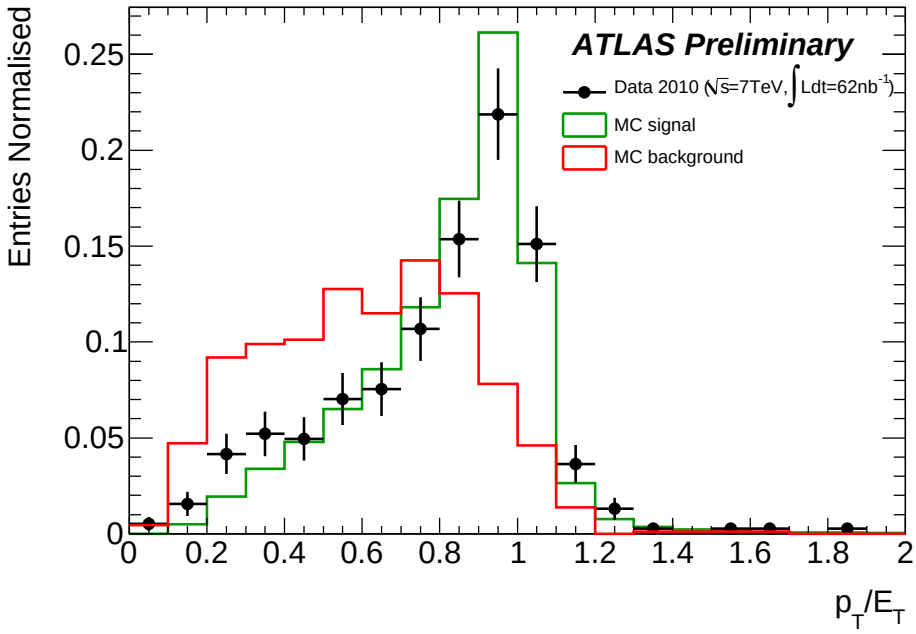

Figure 5.7: p_T/E_T for converted photons with 62 nb^{-1} of $\sqrt{s} = 7$ TeV 2010 data.

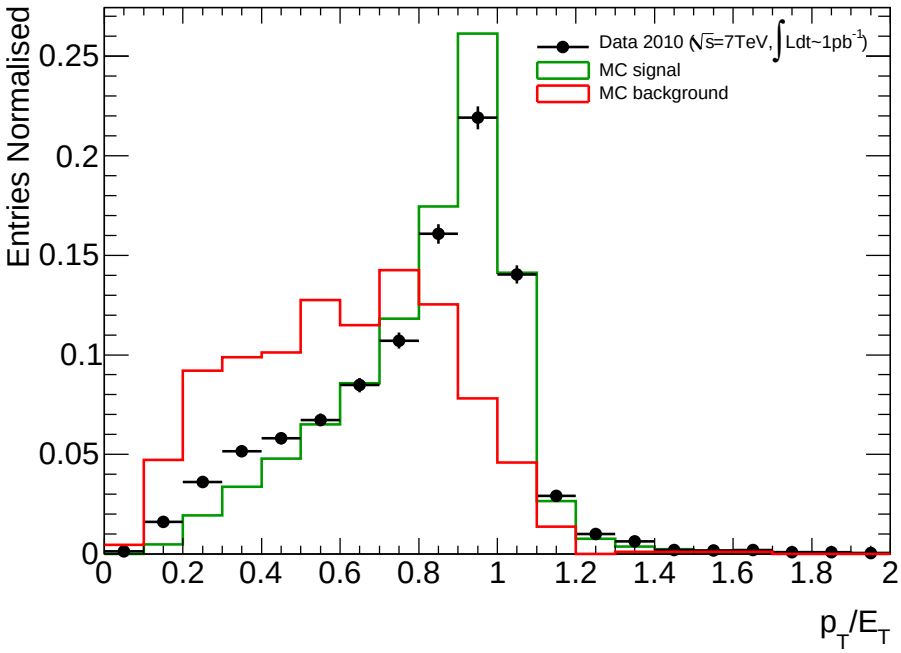

Figure 5.8: p_T/E_T for converted photons with ~ 1 pb^{-1} of $\sqrt{s} = 7$ TeV 2010 data.

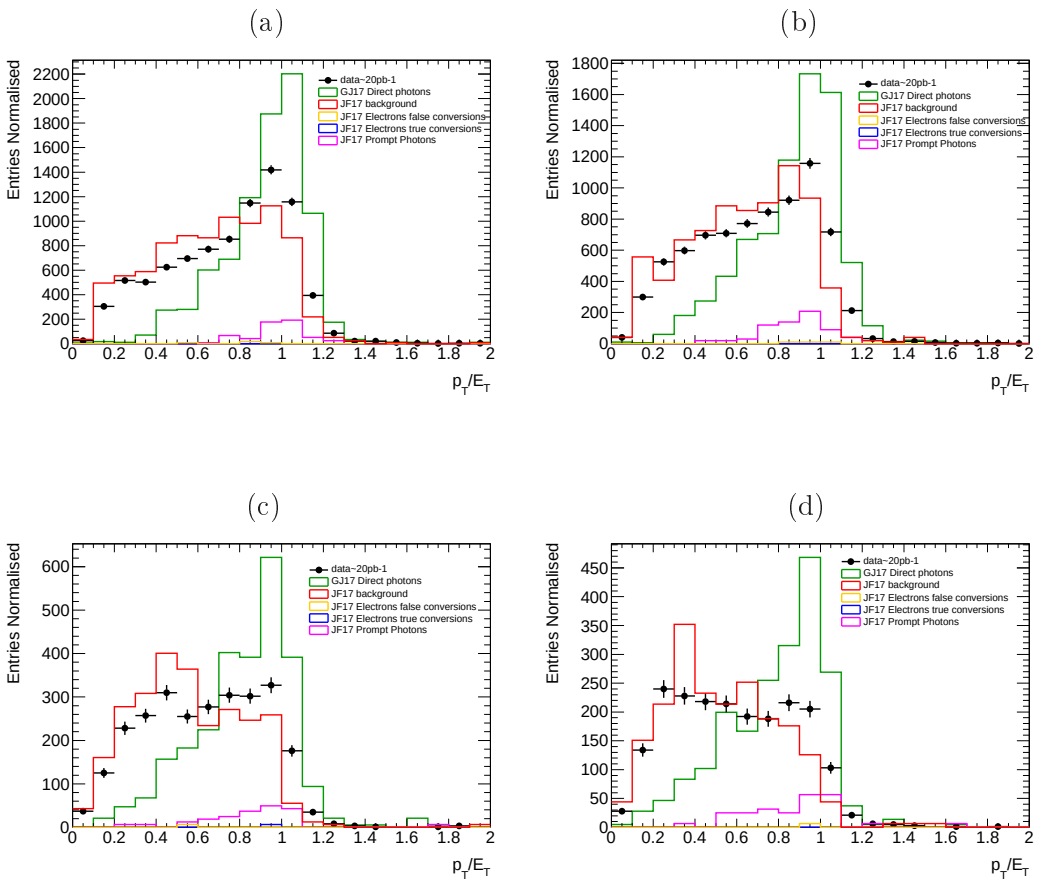

Figure 5.9: p_T/E_T distributions for non isolated converted photon candidates (2-tracks conversion with no B-layer hit) in different p_T ranges: (a) $20 < p_T < 25$ GeV (b) $25 < p_T < 35$ GeV (c) $35 < p_T < 45$ GeV (d) $45 < p_T < 100$ GeV. The comparison is made between 20 pb^{-1} of data 2010 with $\sqrt{s} = 7$ TeV and di-jet Monte Carlo (JF17) for background sample, gamma-jet (GJ17) for signal sample. The electrons contribution is shown to be negligible.

5.6 Purity in $H \to \gamma\gamma$

The same principle of the method described in section 5.4 is generalized to diphoton events [189, 190]. The so-called "$2 \times 2D$" method is used to estimate the purity of the diphoton events to the $H \to \gamma\gamma$ background (several methods were actually checked and gave consistent results, see for more details [191, 192]). This latter mainly consists of an irreducible background of QCD diphoton production and a reducible background of photon-jet and dijets final states (*i.e* when one or two jets fragmenting into neutral mesons (mainly π^0) are misidentified as prompt photons). Understanding the composition of the selected sample serves as a monitoring of the performance of the photon

identification, as well as a validation of the description of the backgrounds to the $H \to \gamma\gamma$ search in the simulation.

I quote in the next the results published in [174] where a comparison between the full 2011 dataset with $\sqrt{s} = 7$ TeV and 5.9 fb^{-1} of 2012 data with $\sqrt{s} = 8$ TeV is shown. The analysis details will be discussed in chapter 6. The fraction of diphoton events has been estimated to be $(80 \pm 4)\%$ in the $\sqrt{s} = 7$ TeV full 2011 dataset and $(75 +3 -2)\%$ in the $\sqrt{s} = 8$ TeV dataset. The better purity in 2011 is thanks to the better rejection provided by NN2011 compared to tight2012 for a given efficiency. The fraction of $\gamma-$jet and jet-jet events has been found to be $(19 \pm 3)\%$ ($(22 \pm 2)\%$) and $(1.8 \pm 0.5)\%$ ($(2.6 \pm 0.5)\%$) in the $\sqrt{s} = 7(8)$ TeV data sample. The Drell-Yan background, which is due to mis-reconstruction of electrons as photons (mostly converted photons), integrated in the mass region 100 - 160 GeV is estimated to be $(1.4 \pm 0.1)\%$ for $\sqrt{s} = 7$ TeV and $(0.8 \pm 0.1)\%$ for $\sqrt{s} = 8$ TeV data. The lower level of Drell-Yan background in the $\sqrt{s} = 8$ TeV data is due to the improvements in the reconstruction of converted photons for 2012 analysis. Fig. 5.10 shows the composition of the diphoton invariant mass spectrum, presented in bins of 1 GeV for the considered 2011 and 2012 datasets.

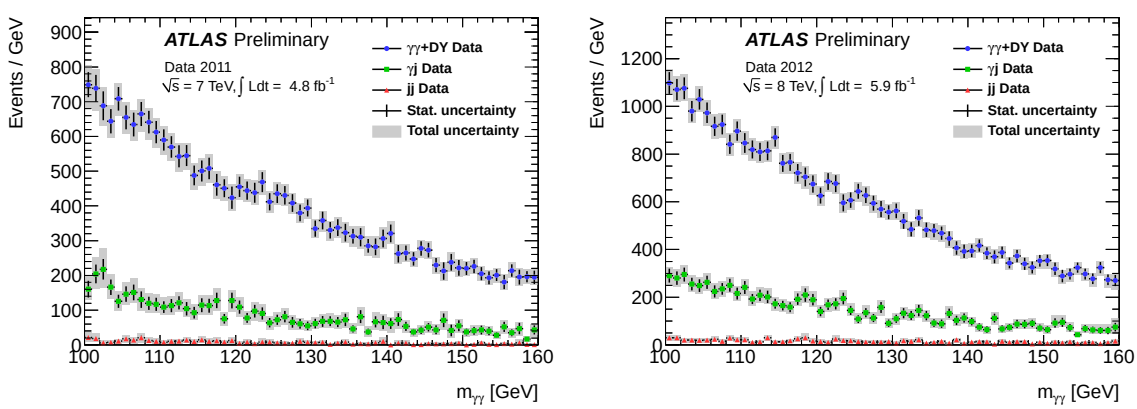

Figure 5.10: Diphoton sample composition as a function of the invariant mass for the $\sqrt{s} = 7$ TeV (left) and the $\sqrt{s} = 8$ TeV (right) dataset. The small contribution from Drell-Yan events is included in the diphoton component [174].

5.7 Photon efficiency

5.7.1 Fudge Factors

Since the beginning of the ATLAS data taking, discrepancies between data and Monte Carlo simulations in the distributions of the discriminating variables, listed in section 5.2.1, have been observed. These discrepancies are particularly pronounced for the variables describing the lateral electromagnetic shower shape variables (R_η, w_{η_2}, f_{side}). The sources of discrepancies are most probably due to an imperfect simulation of the shower's lateral development in the Monte Carlo. The baseline method used to account for these differences in the analysis of 2010 and 2011 data is based on an approximative approach: the applied correction on the Monte Carlo distributions is a small shift evaluated as the difference between the means of the distributions in data and Monte Carlo. This shift can be described by the following equation:

$$\Delta\mu_{DV} =< DV_{data} > - < DV_{MC} >, \tag{5.15}$$

and it is commonly called "fudge factor" (FF).

In the following, I quote only the latest results I have obtained when estimating the FF for 2011 data, these are the ones used for the analysis (for the improved analysis as well) of the full 2011 dataset. In order to quantitatively estimate the FF, single photon candidates are selected in data and MC with the following requirements:

- the event (for data only) passes the e/γ Good Runs List (GRL) i.e good inner detector and calorimeter data quality;
- the event contains at least one primary vertex with at least three associated tracks;
- the event passes the g20_loose trigger for $25 < p_T < 45$ GeV, g40_loose trigger for $45 < p_T < 65$ GeV, g60_loose trigger for $65 < p_T < 85$ GeV and g80_loose trigger for $p_T > 85$ GeV;
- the photon cluster containing a bad channel or overlapping with regions affected by a dead front-end board are rejected;
- the photon candidate has a reconstructed transverse energy $E_T > 25$ GeV and pseudorapidity in the fiducial region: $|\eta_{S_2}| < 1.37$ or $1.52 < |\eta_{S_2}| < 2.37$;
- the photon candidate is isolated: EtCone40 (corrected) < 5 GeV;
- the photon candidate satisfies the tight identification criteria.

The distributions of discriminating variables are compared between data and MC in four different pseudorapidity bins:

$$\eta \in [0, 0.6[\ , \quad \eta \in [0.6, 1.37[\ , \quad \eta \in [1.52, 1.81[\quad \text{and} \quad \eta \in [1.81, 2.37[$$

and in several p_T (GeV) bins:

$$p_T \in [25, 30[\ , \quad p_T \in [30, 35[\ , \quad p_T \in [35, 40[\ , \quad p_T \in [40, 45[\ ,$$
$$p_T \in [45, 50[\ , \quad p_T \in [50, 60[\ , \quad p_T \in [60, 85[\quad \text{and} \quad p_T > 85 \text{ GeV}.$$

In addition, photon candidates were splitted to converted and unconverted.

Fig. 5.11 top (bottom) shows the R_η distributions for unconverted (converted) single photons with $25 < p_T < 30$ GeV, in the central barrel $\eta < 0.6$ (left) and in the end-cap $1.81 < \eta < 2.37$ (right). Fig. 5.12 shows the FF computed for the R_η (top) and w_{η_2} (bottom) variables as a function of η separately for unconverted (left) and converted (right) single photons. The comparison is made between the latest FF (with mc11a) and the previous ones used in 2011 (FF 2011) and 2010 (FF 2010). It shows that the FF are smaller with the new MC (mc11a) after corrections were applied in order to have a better description of the absorber, as discussed above in section 5.2.2.

Fig. 5.13 shows the w_{η_2} distributions for different pile-up configurations. Period B-I of 2011 data is characterized by a $< \mu >$ of about 5.6, for Period L, it increased to $< \mu >= 10.8$. Fig. 5.14 shows the FF computed as a function of η for these different pile-up configurations separately for unconverted (left) and converted (right) single photons. R_η (top) and w_{η_2} (bottom) are the discriminating variables used for this comparison. The impact of pile-up is small on the FF. The FF have been recomputed for the 2012 analysis, see for instance [171].

5.7.2 Photon efficiency and uncertainty

The offline photon selection efficiency is defined as the efficiency for reconstructed prompt photons, with a reconstructed isolation energy ($E^{Iso}_{T,reco}$) lower than $E^{Iso}_{T,reco}|_{cut}$, to pass the tight identification criteria (tight-ID) in a given E_T, η region. In a pseudorapidity bin k, it is given by the equation:

$$\varepsilon^k_{ID}(E^\gamma_{T,reco}) \equiv \frac{dN^\gamma(\eta_{k,1} \leq |\eta^k_{reco}| < \eta_{k,2}, E^{Iso}_{T,reco} < E^{Iso}_{T,reco}|_{cut}, tight-ID)/dE^\gamma_{T,reco}}{dN^\gamma(\eta_{k,1} \leq |\eta^k_{reco}| < \eta_{k,2}, E^{Iso}_{T,reco} < E^{Iso}_{T,reco}|_{cut})/dE^\gamma_{T,reco}} \tag{5.16}$$

where $E^{Iso}_{T,reco}$ = EtCone40 (corrected) and $E^{Iso}_{T,reco}|_{cut}$ was taken 3 GeV for 2010 analysis, 5 GeV for 2011 analysis. In 2012 (for 2011 improved analysis and 2012 analysis), the isolation variable has been updated as described in section 5.3, $E^{Iso}_{T,reco}$ = topoPosEMEtCone40 and $E^{Iso}_{T,reco}|_{cut}$ is set to 4 GeV. In addition,

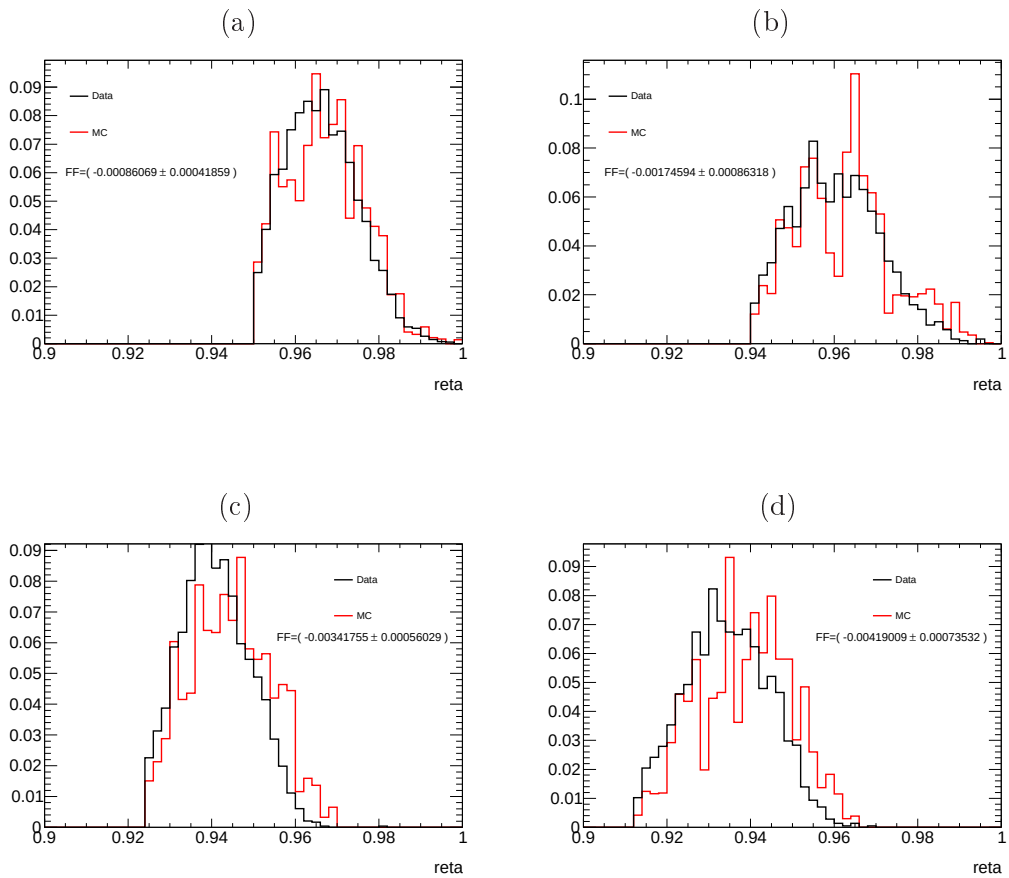

Figure 5.11: R_η distributions for single photons with $25 < p_T < 32$ GeV selected from 2011 data and Pythia MC ($\sqrt{s} = 7$ TeV): (a) unconverted photons in the central barrel $\eta < 0.6$, (b) converted photons in the central barrel $\eta < 0.6$, (c) unconverted photons in the EC $1.81 < \eta < 2.37$, (d) converted photons in the EC $1.81 < \eta < 2.37$.

tight-ID is set to Tight2011 for 2011 analysis, NN2011 for the improved 2011 analysis and Tight2012 for the 2012 analysis. $\eta_{k,1}$ and $\eta_{k,2}$ are the lower and upper η values in the pseudorapidity bin k.

The photon identification efficiency is determined using MC simulated sample, corrected for the differences in the electromagnetic shower shapes between data and MC with the FF-method described above. The uncertainties on these MC-based ε_{ID} values are mainly due to the correction technique, that had to account for the imperfect knowledge of the material in front of the electromagnetic calorimeter, the uncertainty on the photon candidate purity, and the accuracy of the data/MC discrepancy parametrizations used to correct the MC. These MC-based values have been validated with preliminary results from data-driven methods based on 2011 data [193]. Three different methods

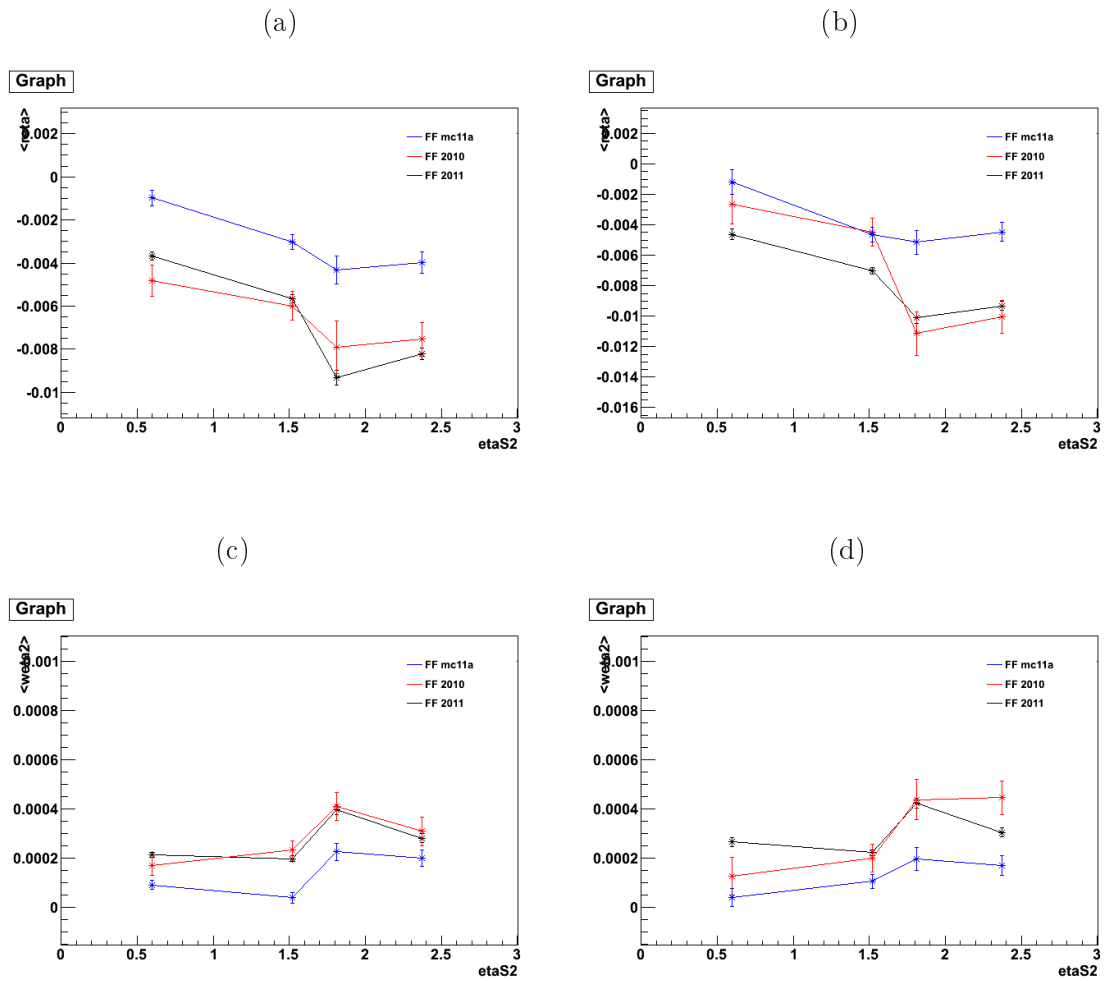

Figure 5.12: FF as a function of η for single photons with $25 < p_T < 32$ GeV selected from 2011 data and Pythia MC ($\sqrt{s} = 7$ TeV): (a) R_η for unconverted photons, (b) R_η for converted photons, (c) w_{η_2} for unconverted photons, (d) w_{η_2} for converted photons.

have been used in different photon E_T ranges:

- isolated prompt photons selected from the radiative decays of the Z boson: $Z \to ll\gamma$ [194];
- extrapolation from pure electrons, obtained from $Z \to e^+e^-$ sample, to photons [195];
- isolated prompt photons selected using a "matrix method" which relies on track isolation as a discriminating variable between prompt and fake photons [196].

The three measurements agree within their uncertainies in the overlapping

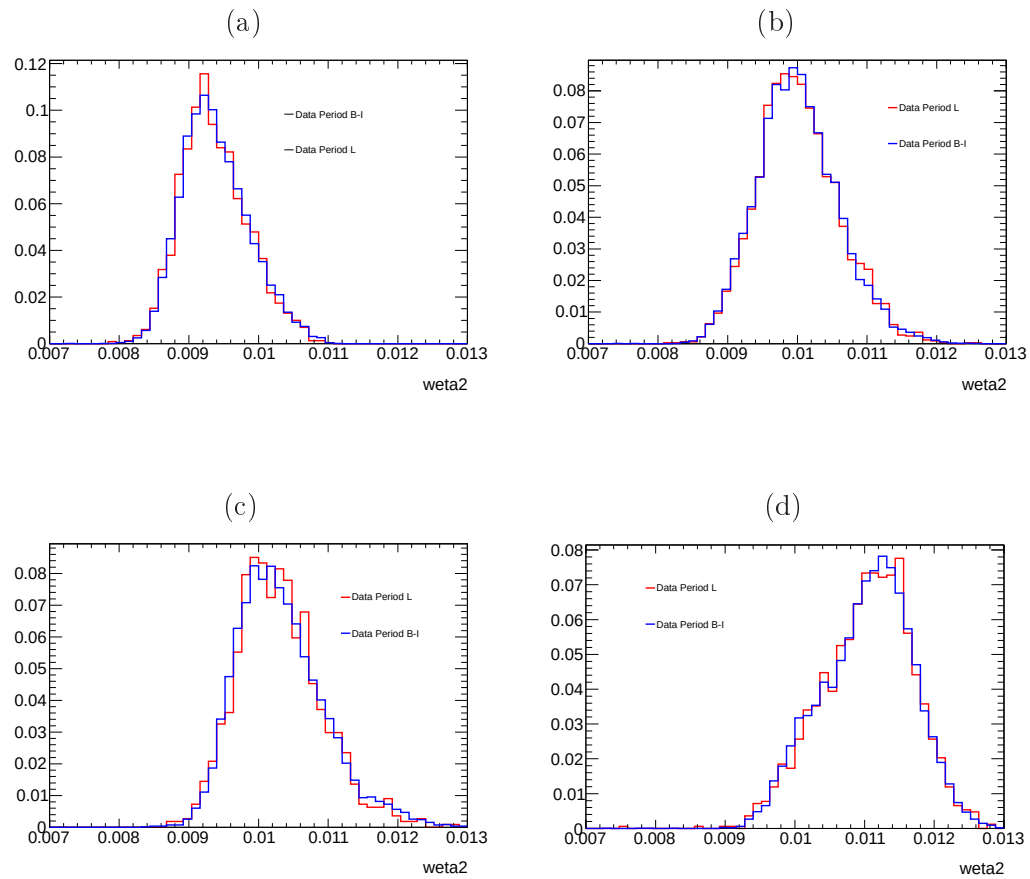

Figure 5.13: w_{η_2} distributions for single photons with $25 < p_T < 32$ GeV selected from 2011 data ($\sqrt{s} = 7$ TeV): (a) unconverted photons in the central barrel $\eta < 0.6$, (b) converted photons in the central barrel $\eta < 0.6$, (c) unconverted photons in the EC $1.81 < \eta < 2.37$, (d) converted photons in the EC $1.81 < \eta < 2.37$. Two pile-up configurations are shown: Period B-I $< \mu > \sim 5.6$ (red) and Period L $< \mu > \sim 10.8$ (black).

E_T ranges and are combined together. The values of photon identification efficiency obtained from FF-corrected MC samples were found to be consistent with the data-driven values within 5%.

Photon efficiency in 2011

As discussed in section 5.2.2, a neural network based selection is used in the improved 2011 analysis. The neural net photon efficiencies are shown in Fig. 5.15 for different η bins as a function of E_T. The efficiencies shown are normalized to the isolated photons in the photon "container". The comparison is shown between Monte Carlo and the three data-driven methods

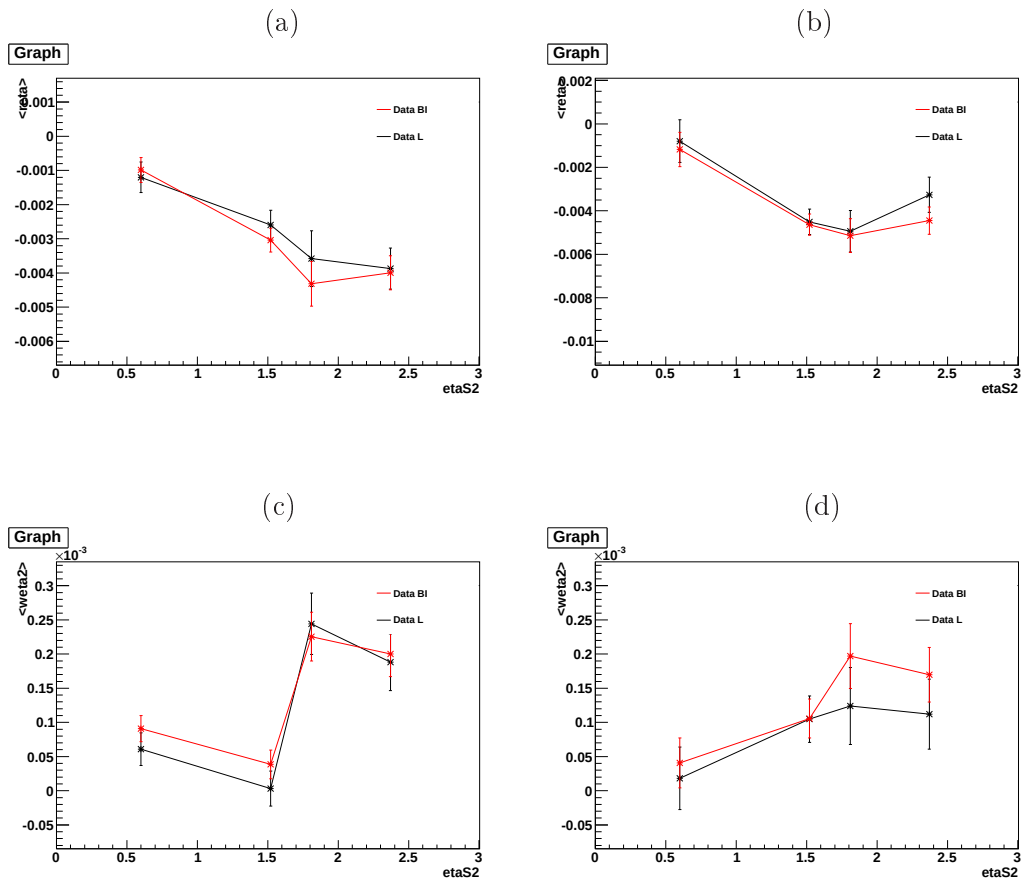

Figure 5.14: FF as a function of η for single photons with $25 < p_T < 32$ GeV selected from 2011 data and Pythia MC ($\sqrt{s} = 7$ TeV): (a) R_η for unconverted photons, (b) R_η for converted photons, (c) w_{η_2} for unconverted photons, (d) w_{η_2} for converted photons. Two pile-up configurations are shown: Period B-I $< \mu > \sim 5.6$ (red) and Period L $< \mu > \sim 10.8$ (black).

(briefly described above) separately for converted and unconverted photons. The dots marked "data 2011" in this figure correspond to the combined weighted measurements of these data-driven methods. The differences are larger for unconverted photons than for the converted photons because the extrapolation from electrons is less straightforward. The gain in efficiency compared to the cut-based tight selection previously used (Tight2011) vary by bin; it is larger at low p_T and high η. The average gain in efficiency per photon is about 8% with a gain of $\sim$ 3% in purity of the diphoton events selected for $H \to \gamma\gamma$ analysis.

Uncertainty on the 2011 photon efficiency

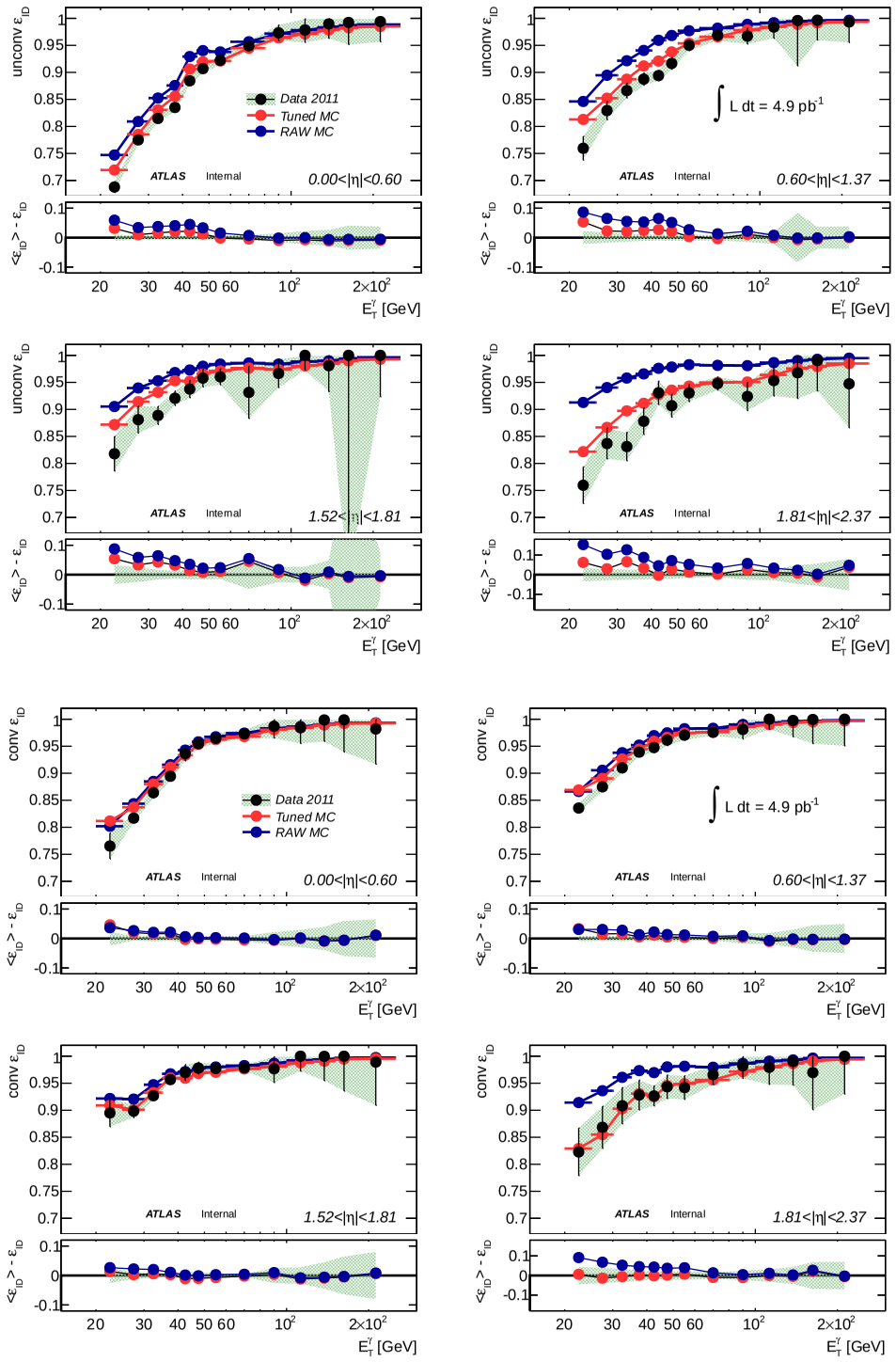

Figure 5.15: Neural Net photon efficiencies for different η bins used in 2011 improved analysis [175].

The primary systematic on the neural net efficiency comes from the difference between the measurements in MC and data shown in Fig. 5.15. The total recommended uncertainty is taken in a conservative way as the sum of these differences with other small potential factors discussed in [175] (mainly pile-up). For $p_T > 30$ GeV, the uncertainties are:

- 5% for unconverted photons in the pseudorapidity bin $1.52 < |\eta| < 1.81$;
- 7% for unconverted photons in the pseudorapidity bin $1.81 < |\eta| < 2.37$;
- 4% otherwise.

The effect of these uncertainties on the signal yields of $H \to \gamma\gamma$ was estimated by reweighting the leading and subleading photons with the uncertainties quoted above. This effect is found to be of the order of $^{+8.6}_{-8.2}$%. In the improved 2011 analysis, the average i.e 8.4% was taken as a total systematic uncertainty on the signal yield. For the previous 2011 analysis [172, 173], it was taken conservatively as ±10%.

Photon efficiency in 2012

For the $\sqrt{s} = 8$ TeV 2012 data, a cut-based selection was used (Tight2012) and the efficiency compared to preliminary data-driven methods [197, 198]. The obtained efficiencies are similar to those shown in Fig. 5.15 for NN2011. However the background rejection with NN2011 is higher than the one with Tight2012 by about 10%, which leads to a worse purity in 2012 (by about 5%).

Uncertainty on the 2012 photon efficiency

The uncertainty is computed as for 2011 [199]. The recommendation for photons is to take:

- 5% for $|\eta| < 1.52$;
- 7% otherwise.

The effect of these uncertainties on the signal yields of $H \to \gamma\gamma$ was estimated to be ±10.8%.

Chapter 6

$H \to \gamma\gamma$ Analysis

Contents

6.1 Analysis of 2010 data 127
6.1.1 Aspen 2011 127
6.1.2 Moriond 2011 131
6.2 Analysis of 2011 data 136
6.2.1 PLHC 2011 136
6.2.2 EPS 2011 142
6.2.3 Council 2011 152
6.3 Improved Analysis of 2011 data 156
6.3.1 Improved selections and corrections 157
6.3.2 Event categorization 158
6.4 Analysis of 2012 data 165
6.5 Conclusion 168

In the following chapter, I will summarize the evolution of the $H \to \gamma\gamma$ analysis from 2010 to 2012. This chapter is based on results published and presented at various conferences from Aspen 2011 to ICHEP 2012. I will focus here on the signal and systematics studies to which I contributed. The statistical treatment of these results will be discussed in the next chapter.

6.1 Analysis of 2010 data

6.1.1 Aspen 2011

The ATLAS collaboration has published first results for $H \to \gamma\gamma$ search in [200, 201], presented at Aspen 2011 based on 37 pb^{-1} of $\sqrt{s} = 7$ TeV 2010 data. A measurement of the background to $H \to \gamma\gamma$ was performed and a projection of the sensitivity to 1 fb^{-1} has been studied. In the following, I will briefly recall this analysis.

Event Selection

Events are required to fulfill the following criteria:

- The run and luminosity block need to be contained in the good run list (GRL) to ensure good quality data from inner detector, electromagnetic and hadronic calorimeter;
- The events are required to be triggered by the `2g15_loose` trigger chain (except for the first 1 pb^{-1} where a `L1_EM14` trigger was used). The efficiency of this trigger with respect to the $H \to \gamma\gamma$ selection was measured and found to be $\sim 100\%$;
- In order to reject candidates from non-collision backgrounds, the events are required to have at least one reconstructed primary vertex with at least three associated tracks;
- Photon candidates with a cluster containing a bad channel or overlapping with regions affected by a dead front-end board in the calorimeter are rejected;
- Only photon candidates reconstructed in the fiducial region of the calorimeter, $|\eta| < 1.37$ or $1.52 < |\eta| < 2.37$, are considered. The barrel-endcap transition region, $1.37 < |\eta| < 1.52$ is excluded. Photons in this region suffer from a worse reconstruction quality and a large amount of material in front of the calorimeter;
- The photon candidates are required to pass the loose identification criteria, and to have a transverse energy of at least 25 GeV.

Diphoton candidates are selected from events passing the event selection by imposing the following criteria on the two most energetic photon candidates:

- The leading photon candidate is required to have $E_T > 40$ GeV, and the subleading photon candidate $E_T > 25$ GeV;
- Both photon candidates are required to pass the tight identification criteria (Tight2010). In the MC, the cuts are applied after the correction of the shower shape using the FF method;
- Both photon candidates are required to be isolated in the calorimeter, EtCone40 (corrected) < 3 GeV.

With these selections, 83 diphoton candidates are observed in the invariant mass range between 100 and 150 GeV.

The invariant mass of the photon candidate pair is estimated using the photon energies as measured in the calorimeter, ϕ as determined from the second calorimeter layer, and η as measured from the first layer in the calorimeter. The direction of the photon is measured using the first sampling

of the EM calorimeter and the position of the primary vertex. For events with more than one reconstructed vertex, the vertex associated with tracks having the highest sum of p_T is used.

Furthermore, the photon energy is corrected in data (not Monte Carlo) with very preliminary scaling factors derived from $Z \to e^+e^-$ decays. These are two-binned corrections: -0.96% ($+1.9\%$) for photons in the barrel (EC) with a $\pm 1\%$ ($\pm 3\%$) systematic uncertainty. However, in this analysis the MC events are not smeared to take into account for differences between the $Z \to e^+e^-$ resolution in data and MC. The MC used has the nominal constant term of 0.7%. Large pessimistic uncertainties of 100% in the barrel and 400% in the EC were assigned and their impact on the projected sensitivity was studied.

The measurement of the inclusive distribution of diphoton events is used to estimate the sensitivity with an integrated luminosity of 1 fb^{-1}. The extrapolation of the background from data is done taking into account the expected increase of pileup in the coming 2011 data. While the mean number of interactions per beam crossing was on average $< \mu >= 2.3$ in the 2010 data, a $< \mu >$ of 5 was considered as expected pileup for the coming 1 fb^{-1}. The increase of pileup reduces the number of selected events by a factor of 0.86, estimated from MC $H \to \gamma\gamma$ samples with $< \mu >= 2$ and $< \mu >= 5$ (considering only in-time pileup). On the other hand, an increase of the number of events by a factor of 1/0.85 was expected in 2011 after repairing the faulty optical links in the LAr readout system; this factor was estimated from MC using true photons.

These corrections were also applied on the expected signal events. Besides, one additional correction was applied to take into account the difference of the isolation cut efficiency between data and MC estimated from $Z \to e^+e^-$ samples. This leads to a reduction by 0.84 of the signal yields. Table 6.1 summarizes the expected yields and efficiencies after the application of the selection and corrections specified above. These signal yields are normalized to an integrated luminosity of 1 fb^{-1}.

The probability density function (PDF) used for the signal parametrization is modeled by the sum of a *Crystal Ball* function (CB) (for the bulk of events which have a narrow Gaussian spectrum in the peak region and a non-Gaussian tail towards lower reconstructed mass values) and a small, wider Gaussian component (to model the far outliers in the distribution). The CB function is defined as:

$$N \cdot \begin{cases} e^{-t^2/2} & \text{if } t > -\alpha \\ (\frac{n}{|\alpha|})^n \cdot e^{-|\alpha|^2/2} \cdot (\frac{n}{|\alpha|} - |\alpha| - t)^{-n} & \text{otherwise} \end{cases} \tag{6.1}$$

Mode	110 GeV		115 GeV		120 GeV		130 GeV		140 GeV	
	ε (%)	N_{ev}	ε (%)	N_{ev}	ε (%)	N_{ev}	ε (%)	N_{ev}	ε (%)	N_{ev}
ggH	24.8	9.72	25.2	9.75	26.5	9.92	28.2	9.00	28.9	6.82
VBF	25.0	0.69	25.8	0.74	26.5	0.76	27.7	0.73	28.9	0.59
Total		11.0		11.1		11.2		10.2		7.7

Table 6.1: Selection efficiencies on signal, and expected yield for an integrated luminosity of 1 fb^{-1} computed from gluon-gluon fusion and VBF MC samples with $<\mu>= 5$. The total expected number of events is corrected for the small contributions of the remaining production modes (WH, ZH, $t\bar{t}H$).

where $t = (M_{\gamma\gamma} - M_H)/\sigma$, N is a normalization parameter, M_H is the hypothesized BEH boson mass, σ represents the diphoton invariant mass resolution, and n and α parametrize the non-Gaussian tail. The non-Gaussian contributions to the mass resolution arise mostly from converted photons with at least one electron losing a significant fraction of its energy through bremsstrahlung in the inner detector material.

A comparison between the invariant mass distributions for signal MC samples $H \to \gamma\gamma$ with $M_H = 120$ GeV between $<\mu>= 0$ (no pileup) and $<\mu>= 5$ is shown in Fig. 6.1. The fitted values of the parameters of the resolution function are shown in the inset. The worse resolution in the sample with $<\mu>= 5$ is partly due to a bad selection of the primary vertex reconstructed with the $\sum p_T^2$ method.

The background modeling is a fit to the invariant mass spectrum obtained from data. The analytic function used for the fit is a simple falling exponential.

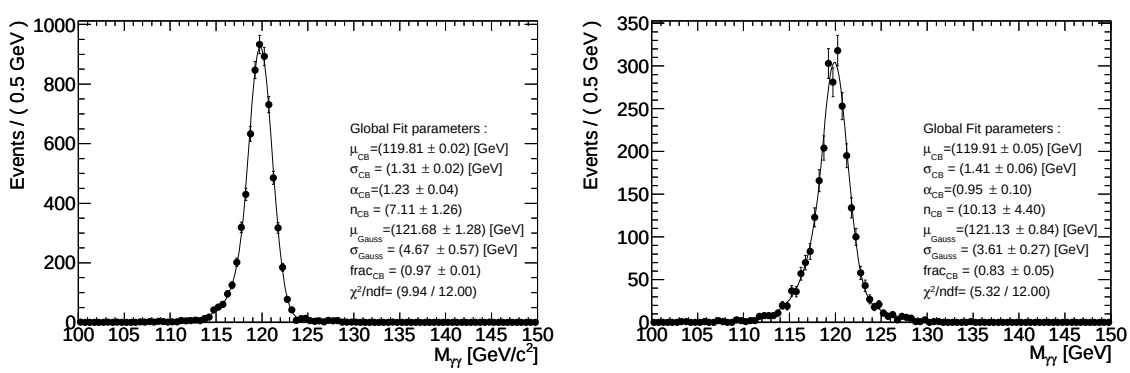

Figure 6.1: Invariant mass distributions for a BEH boson with $M_H = 120$ GeV, with $<\mu>= 0$ (left) and $<\mu>= 5$ (right). The MC samples used have the nominal constant term of 0.7%.

The systematic uncertainties were not used in the sensitivity projection results, however their impact on the sensitivity was quoted. I will briefly summarize them in the following:

- Luminosity: the uncertainty on the integrated luminosity was $\pm 11\%$;
- Trigger efficiency: the uncertainty on the trigger efficiency was found to be $\pm 1\%$ per event;
- Photon identification: the uncertainty from the photon reconstruction and identification was assumed to be $\pm 5\%$ per photon. Treating the uncertainty as fully correlated between the two photons, this translates in a relative uncertainty of $\pm 10\%$ per event. This number is very conservative and based on the 2010 prompt photon cross section measurements and differences in the shower shape variables between data and MC.

6.1.2 Moriond 2011

In comparison to the previous analysis, several improvements were made at the time of Moriond 2011 [202, 203]:

- a recovered detector problem in the tile calorimeter leading to an additional 2 pb^{-1} of data;
- an improved measurement of the luminosity decreasing its central value by 3.6% and its uncertainty from 11% to 3.4%;
- an improved photon identification (slightly looser) minimizing the effect of the discrepancies in the shower shape variables between data and MC, essentially in the EC ($1.8 < |\eta| < 2.37$);
- a finer grained offline energy calibration using $Z \to e^+e^-$ events (50 η bins) see Fig. 4.11, which improves the photon energy resolution and the corresponding uncertainties;
- an improvement of the object quality efficiency increasing the number of selected events by $3 - 4\%$;
- new MC samples are used with $< \mu >= 2.2$ to take into account the out-of-time pileup and the correct bunch train structure.

The selections and the way to compute the invariant mass remain unchanged with regards to Aspen. However, the photon energy in the MC is now smeared by default to take into account for differences in resolution between data and simulation. The constant terms used are of $(1.1 \pm 0.1 \pm 0.2)\%$ for $|\eta| < 1.37$ and $(1.8 \pm 0.4 \pm 0.2)\%$ for $1.52 < |\eta| < 2.47$. After these selections

and corrections, 99 events have a diphoton invariant mass between 100 and 150 GeV.

Table 6.2 summarizes the expected signal events from MC $H \to \gamma\gamma$ samples for different BEH masses normalized to an integrated luminosity of 38 pb^{-1} with $< \mu >= 2.2$. These numbers were corrected for the difference of the isolation cut efficiency by a factor of 0.95; the improvement with regards to Aspen (it was 0.84) is due to an additional lateral leakage correction applied on the isolation.

BEH boson mass [GeV]	110	115	120	130	140
Number of signal events	$0.43^{+0.11}_{-0.09}$	$0.45^{+0.11}_{-0.10}$	$0.45^{+0.11}_{-0.10}$	$0.41^{+0.10}_{-0.08}$	0.31 ± 0.08

Table 6.2: The expected BEH signal yields for an integrated luminosity of 38 pb^{-1} estimated using $H \to \gamma\gamma$ MC samples with $< \mu >= 2.2$. The error combines the experimental systematic uncertainties and the theoretical uncertainty on the SM BEH boson production cross section.

The modeling used for signal and background are the same as for Aspen. Fig. 6.2 illustrates the signal PDF and the corresponding shape parameters for different BEH masses. Fig. 6.3 shows again the resolution function for 120 GeV BEH where the FWHM [1] was found to be equal to 4.4 GeV.

The systematic uncertainties applied on the expected signal yields are given in the following:

- Luminosity: the uncertainty on the integrated luminosity was taken as $\pm 3.4\%$;
- Trigger efficiency: the uncertainty on the trigger efficiency was taken conservatively to be as $^{+1.1}_{-3.7}\%$ per event;
- Photon Identification: the uncertainty from the photon reconstruction and identification was assumed to be $\pm 5\%$ per photon for $|\eta| < 1.81$ and $\pm 10\%$ for $|\eta| > 1.81$. This uncertainty leads to an overall $10.7 \pm 0.6\%$ reduction on the offline efficiency. In addition 2% of difference on this efficiency is obtained when applying FF to MC events. An overall $\pm 11\%$ uncertainty is assigned to the photon ID systematic;
- Isolation cut efficiency: the difference in the isolation cut efficiency of EtCone40 (corrected) < 3 GeV between data and MC estimated on $Z \to e^+e^-$ sample was taken as a $\pm 10\%$ uncertainty per event;

[1] Full width at half maximum

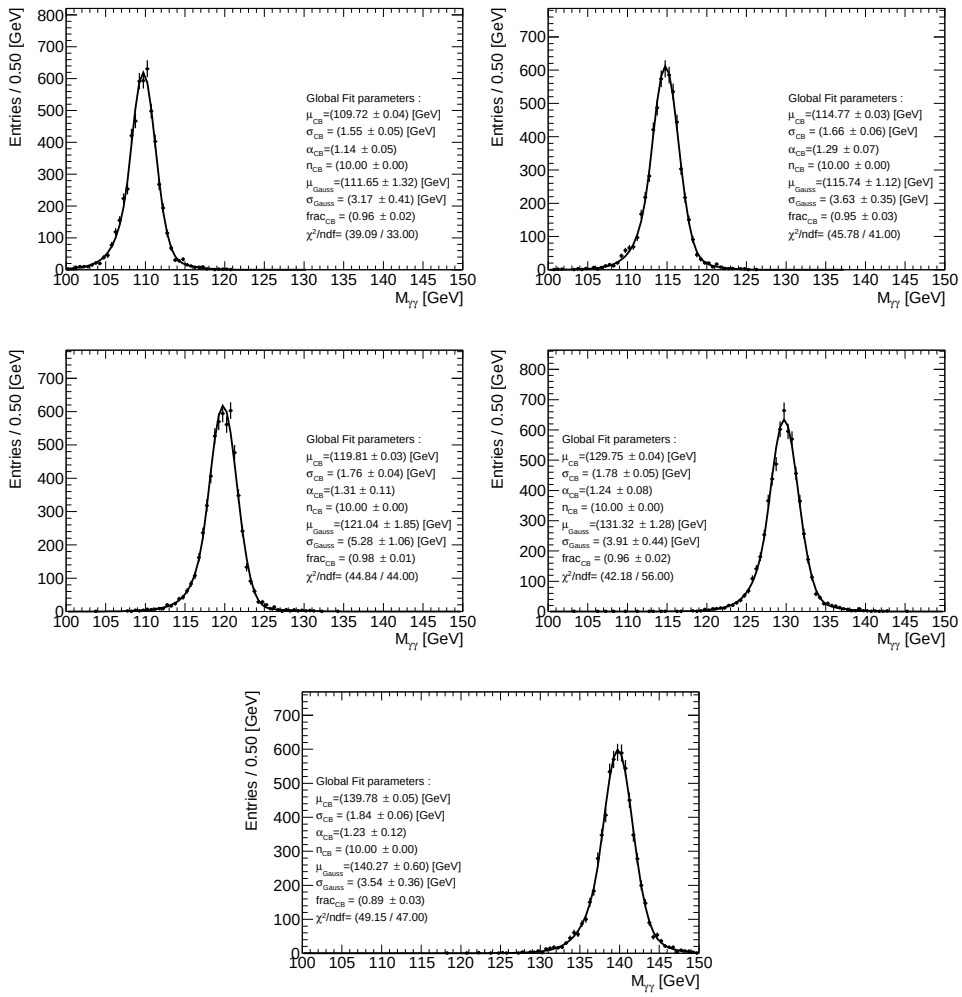

Figure 6.2: Signal PDFs and shape parameters used for fitting for five different BEH masses.

- Pile-up: the effect of the pileup on the number of events has been studied comparing the percentage of events in a window of 117−123 GeV between two MC $H \to \gamma\gamma$ samples: without pileup and with pileup $< \mu >= 2.2$. The difference is found to be $\sim 2\%$ and was considered as negligible;

- Theory: the uncertainty is taken as $^{+20}_{-15}\%$ on the computation of the production cross section.

The systematic uncertainties on the mass resolution originate from different sources:

- Uncertainty on the constant term. The effect of the smearing can be seen on Fig. 6.4 where the nominal (with a constant term of 0.7%) and the

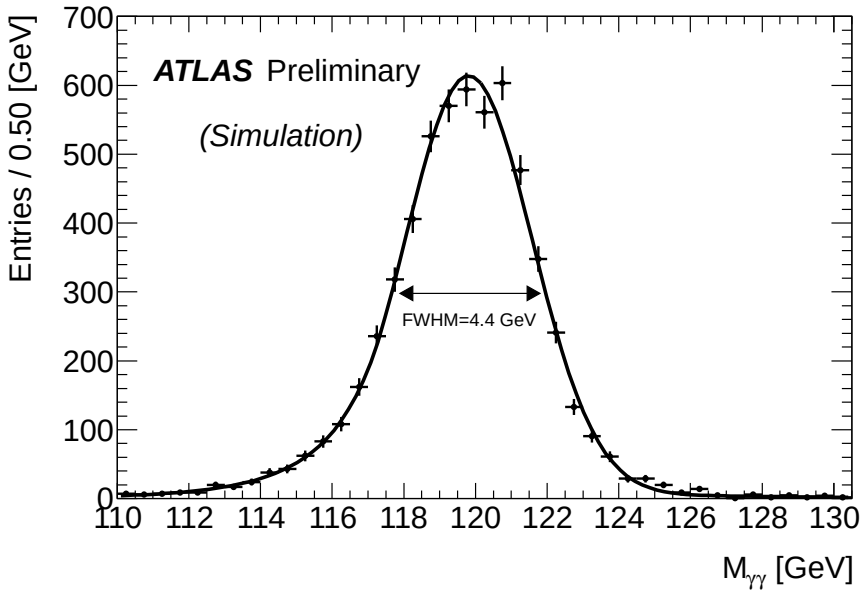

Figure 6.3: The distribution of the diphoton invariant mass for simulated events with a 120 GeV BEH boson decaying into two photons. The FWHM of the distribution is 4.4 GeV. The MC events have been smeared to take into account the differences in resolution between data and MC estimated from $Z \to e^+e^-$ events.

smeared MC (with constant terms of $(1.1 \pm 0.1 \pm 0.2)\%$ for $|\eta| < 1.37$ and $(1.8 \pm 0.4 \pm 0.2)\%$ for $1.52 < |\eta| < 2.47$) are compared. A remaining $\sim$ 15% improvement on the mass resolution can be obtained when reaching the nominal constant term. To estimate the uncertainty on the mass resolution due to the uncertainty on the constant term, we choose to smear our MC samples with: 0.74% in the barrel and 1.35% in the EC. These numbers represent the additional smearing due to the uncertainty on the constant term computed as: $1.1 + (0.1 \oplus 0.2) = 1.1 + 0.22 = 1.1 \oplus 0.74$ in the barrel and $1.8 + (0.4 \oplus 0.2) = 1.8 + 0.45 = 1.8 \oplus 1.35$ in the EC. The RMS of the relative difference of the invariant mass between the sample smeared (with 0.74% in the barrel and 1.35% in the EC) and the nominal sample is taken as an uncertainty. The uncertainty is found to be 0.63% on the mass resolution;

- Uncertainty due to the electron to photon extrapolation. The energy scale corrections derived from $Z \to e^+e^-$ events are used to correct both electrons and photons in data (since there is not a large statistics photon sample available to estimate proper corrections to photon energies). These electron energy scale corrections overcorrect the photon energies

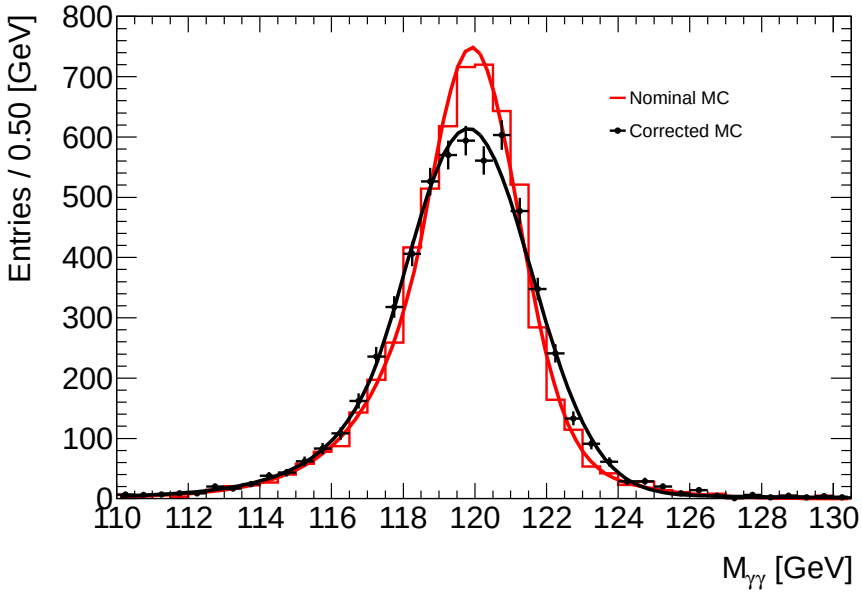

Figure 6.4: The distribution of the diphoton invariant mass for simulated events with a 120 GeV BEH boson decaying into two photons. The solid red histogram is the output of the nominal MC simulation, and the red curve is the corresponding PDF fitted to this distribution. The histogram with black dots is the distribution of the same simulated sample, where the photon energies are corrected with the offline smearing procedure. The black curve is the PDFs describing the nominal invariant mass resolution. The fitted width of the CB core before (after) smearing is 1.55 (1.75) GeV.

if these are due to the material in front of the calorimeter. A systematic uncertainty is needed to take into account the electron to photon extrapolation. For this purpose, a study was made in [204, 205] using MC $Z \to e^+e^-$ sample with a distorted geometry [2]. New electron energy scale corrections are obtained from the comparison of the MC $Z \to e^+e^-$ sample with distorted geometry and the MC $Z \to e^+e^-$ sample with nominal geometry (instead of the comparison between data and MC $Z \to e^+e^-$ sample with nominal geometry). These "distorted" energy scale corrections translate the effect of the material on the electron energy. If the electrons and photons behave identically in the material, applying these "distorted" corrections to the energy of a photon from a distorted $H \to \gamma\gamma$ sample will give exactly the energy of the photon of the corresponding nominal sample. However since this assumption is

[2] Additional material

not correct, the difference of photon energies will give an estimation of the electron to photon extrapolation uncertainty. Therefore, the relative difference of RMS between the invariant mass distributions of a $H \to \gamma\gamma$ nominal sample and a $H \to \gamma\gamma$ distorted sample corrected with these distorted electron energy scale corrections is taken as an uncertainty due to the electron to photon extrapolation. It was found to be 0.4% on the mass resolutio;

- Pileup. This was estimated from the comparison of the invariant mass distributions between MC $H \to \gamma\gamma$ samples ($M_H = 120$ GeV): $< \mu >= 0$ and $< \mu >= 2.2$. Half of the RMS difference (for $117 < M_{\gamma\gamma} < 123$ GeV) was taken as an uncertainty i.e 0.16% on the mass resolution.

Adding up quadratically these uncertainties give a total of 0.76% on the mass resolution. This can be written explicitly as $(\sigma_M/M \oplus 0.76)\%$ where $\sigma_M = \sigma_{CB} \sim 1.76$ GeV. Taking $M = 120$ GeV, this translates to $(1.76/120 \oplus 0.76)\% = (1.47 \oplus 0.76)\% = 1.126 \times 1.47$. The total relative uncertainty on the mass resolution is therefore $\sim 13\%$.

Table 6.3 summarizes the systematic uncertainties on the signal normalization and invariant mass resolution used in this analysis.

	Source	Uncertainty
	Luminosity	$\pm 3.4\%$
Theory	Cross-section	$^{+20}_{-15}\%$
Efficiency	Photon identification	$\pm 11\%$
	Photon isolation	$\pm 10\%$
	Trigger	$^{+1.1}_{-3.7}\%$
Resolution	Calibration	
	$e \to \gamma$ extrapolation	$\pm 13\%$
	Pile-up	

Table 6.3: Relative systematic uncertainties associated to the signal normalization and invariant mass resolution. For the resolution, the quoted uncertainty is relative to the width of the invariant mass.

6.2 Analysis of 2011 data

6.2.1 PLHC 2011

The first analysis of 2011 data was presented at PLHC 2011 [206, 207]. The updated search used an integrated luminosity of 209 pb^{-1} of $\sqrt{s} = 7$ TeV data. A maximum average number of interactions per bunch crossing of ~ 8 was

reached. The MC samples were simulated with a varied μ and a reweighting procedure is applied to match the μ distribution of the MC to that of the data. The kinematic cuts are unchanged with respect to Moriond 2011. A LAr error bit is defined to reject events when there is an indication of data integrity errors in the LAr calorimeter or noise bursts. The trigger has been changed to `2g20_loose`, its efficiency for events passing all selection criteria is found to be $99 \pm 1\%$. In addition, two major improvements were made to cope with higher pileup environment:

- The isolation cut on EtCone40 (corrected) was relaxed from 3 GeV to 5 GeV. This modification resulted in an increase of $\sim 12\%$ in isolation efficiency per photon and a small reduction in the purity of diphoton sample from about 76% to 70%;

- The reconstruction of the primary vertex is very crucial for a precise reconstruction of the invariant mass. With the increasing pileup a more robust method to reconstruct the photon direction has been used based on the longitudinal segmentation of the LAr electromagnetic calorimeter and the fine granularity of its first sampling layer [208]. For unconverted photons, the vertex position is estimated from the shower position measurements in the first and second layers of the calorimeter which can be used to calculate the photon direction. The independent vertex position measurements from both photons are combined also taking into account the average beam spot position in z. If one or both photons are converted with tracks leaving silicon hits, the vertex position is estimated from the intercept of the line joining the reconstructed conversion position and the calorimeter impact point with the beam line. The improvement on the invariant mass resolution using this new method amounts to $\sim 5\%$. Fig. 6.5 shows the comparison of the invariant mass distributions between the new method of PV reconstruction and the one used in the previous analyses for a MC $H \to \gamma\gamma$ sample with $M_H = 120$ GeV. The FWHM of the diphoton mass distribution used for this analysis is 4.1 GeV.

Fig. 6.6 shows the comparison of the invariant mass resolution computed using the "pointing" method and the true vertex for MC $H \to \gamma\gamma$ sample with $M_H = 120$ GeV. The smearing of the MC events is not applied in these distributions to better visualize the impact of the PV selection. The resolution obtained using the "pointing" is not far from the one we could have if we would truly know the vertex, especially when both photons are in the barrel.

After all selections are applied, 926 photon candidates are selected with an invariant mass between 100 and 150 GeV.

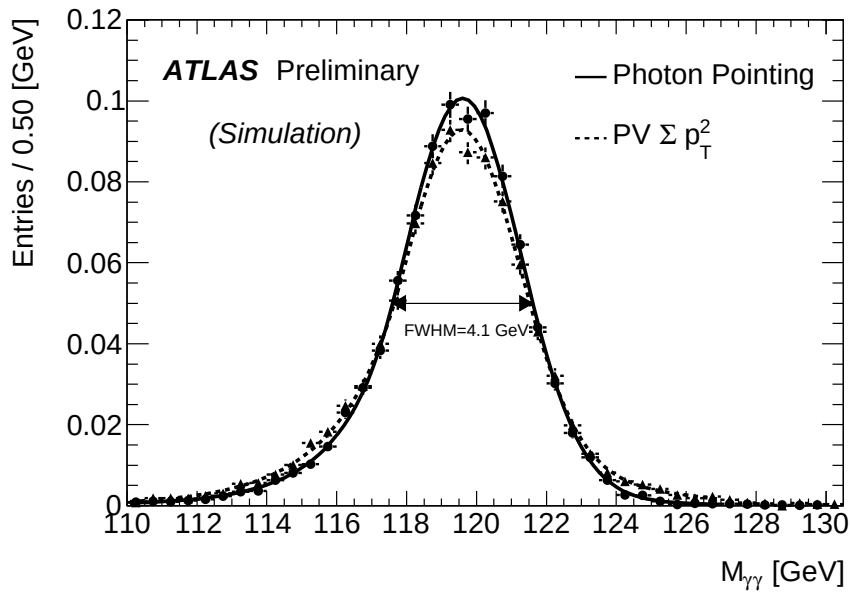

Figure 6.5: Distribution of the reconstructed diphoton invariant mass of a simulated 120 GeV BEH boson signal. The points and solid fit function correspond to the photon direction or conversion-based PV reconstruction. The triangles and dashed fit function represent the method using the PV with the highest sum of transverse momentum squared. The FWHM of the invariant mass distribution is 4.1 GeV with the method using photon directions and conversion tracks.

Table 6.4 summarizes the expected signal yield from the MC $H \to \gamma\gamma$ samples for different BEH masses normalized to an integrated luminosity of 209 pb^{-1}. These numbers were corrected for the difference of the isolation cut efficiency by a factor of 0.97; the improvement with regards to Moriond (it was 0.95) is due to the relaxed cut on isolation (5 GeV instead of 3 GeV).

	M_H=110 GeV	M_H=115 GeV	M_H=120 GeV	M_H=130 GeV	M_H=140 GeV
ggF	3.06	3.18	3.15	2.84	2.17
VBF	0.23	0.24	0.25	0.24	0.20
WH	0.12	0.12	0.11	0.09	0.06
ZH	0.07	0.06	0.06	0.05	0.04
ttH	0.01	0.01	0.01	0.01	0.01
Total	3.49	3.61	3.58	3.23	2.48

Table 6.4: Expected signal yield in the 2011 data sample corresponding to an integrated luminosity of 209 pb^{-1}.

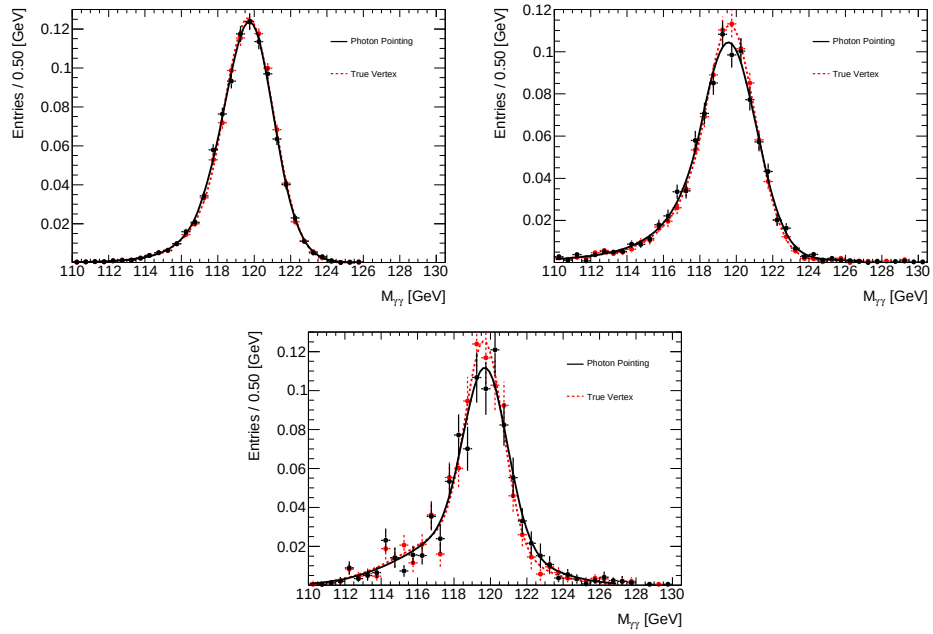

Figure 6.6: Comparison of the invariant mass resolution for a $H \to \gamma\gamma$ sample with $M_H = 120$ GeV when both photons are in the barrel, one of the photon is in the barrel and the other in the EC and when both photons are in the EC. No smearing correction is applied.

The modelings used for signal and background are the same as for 2010 analyses. Fig. 6.7 illustrates the signal PDF and the corresponding shape parameters for different BEH masses. For other masses, a linear interpolation of the fit parameters determined from the simulated samples is done.

The systematic uncertainties on the signal yield are summarized in the following:

- Luminosity: the uncertainty on the integrated luminosity for this 2011 dataset was taken as $\pm 4.5\%$;
- Trigger efficiency: the uncertainty on the trigger efficiency was taken to be $\pm 1\%$ per event;
- Photon Identification: the uncertainty from the photon reconstruction and identification was assumed to be $\pm 5\%$ per photon. Treating the uncertainty as fully correlated between the two photons, this translates in a relative uncertainty of $\pm 10\%$ per event;
- Pileup: the effect of the pile-up on the expected signal yield was estimated from the variation of the tight identification efficiency as a function of $< \mu >$ (the average interactions per beam crossing). The differ-

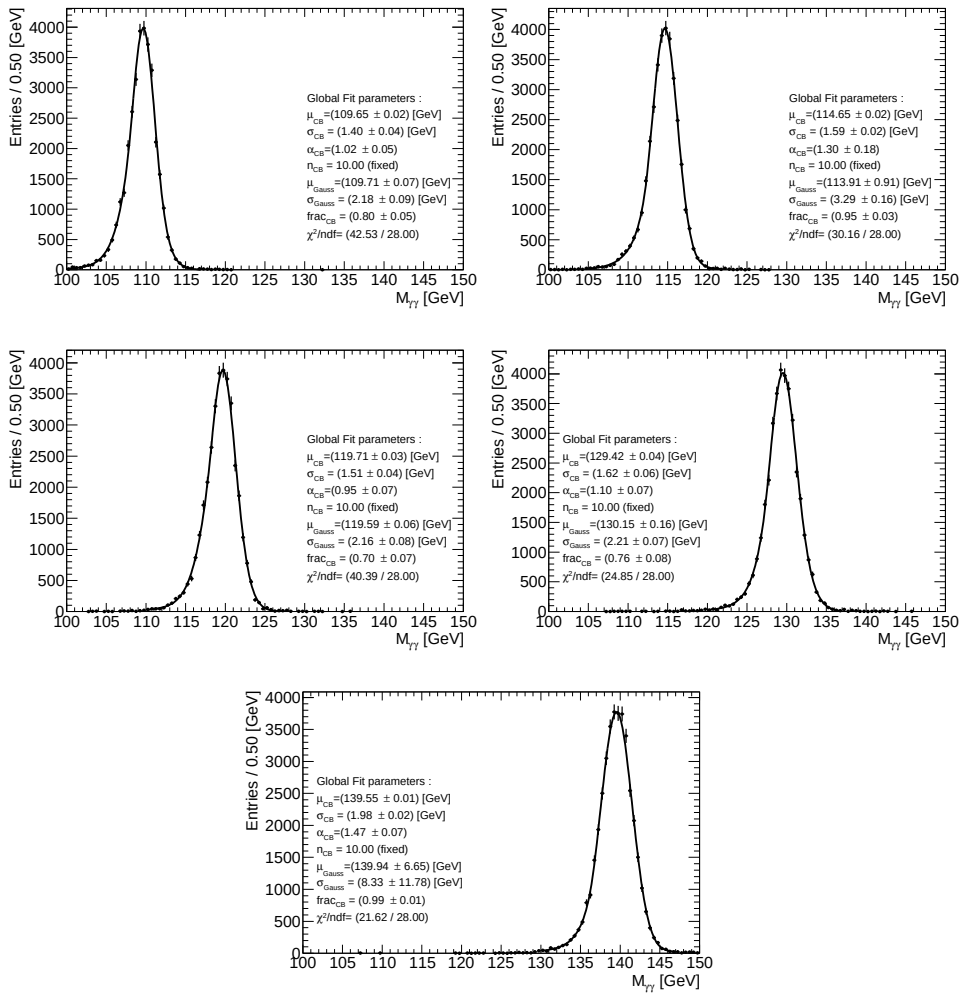

Figure 6.7: Signal PDFs and shape parameters used for fitting for five different BEH masses.

ence in this efficiency between $< \mu >= 6$ (at that time in 2011 data) and $< \mu >= 0$ was estimated to be about 4% per photon. The assigned systematic uncertainty was taken as $\sim$ the half of this effect, i.e $\pm 2\%$ per photon. This translates into $\pm 4\%$ per event;

- Isolation cut efficiency: the difference in the isolation cut efficiency of EtCone40 (corrected) < 5 GeV between data and MC estimated on $Z \to e^+e^-$ sample was taken as a $\pm 3\%$ uncertainty per event;

- Theory: the uncertainty is taken as $^{+20}_{-15}\%$ on the computation of the production cross section.

The total experimental uncertainty on the overall signal event yield amounts to ±12%.

The systematic uncertainties on the invariant mass resolution are due to:

- Uncertainty on the constant term. This uncertainty remains unchanged with regards to Moriond. It amounts to an ±11% relative uncertainty on the diphoton invariant mass resolution;

- Uncertainty due to the electron to photon extrapolation. This uncertainty is also unchanged with regards to Moriond. It is ±6% relative uncertainty on the mass resolution;

- Pileup. To check the impact of the pileup noise on the photon energy resolution, a comparison of tranverse energies in random clusters (centered around a given η and ϕ with a size of 3×5 cells in the barrel and 5×5 in the EC) was made between data and MC [209]. Zero bias data events are compared to single muon simulated events with the same pileup configuration (muon are used since they give rise to similar response in the calorimeter as the zero bias events). Fig. 6.8 shows the RMS of the transverse energy in these random clusters (describing the noise) as a function of the average number of interactions per beam crossing, μ. A fair agreement is observed between data and MC (slightly worse in the EC) for two different values of μ. The uncertainty on the pileup noise can be bound to be < 200 MeV on the E_T noise, the difference in quadrature between data and MC. Smearing the transverse energy of the photons from a $H \to \gamma\gamma$ sample by $E_T \to E_T + \alpha \times 200$ MeV where α is a gaussian centered on 0 with a σ of 1, leads to a variation by 3% of the invariant mass resolution. 3% is the resulting uncertainty on the mass resolution;

- PV location. This uncertainty arises from the differences between data and MC in the calorimeter photon direction reconstruction. It was estimated from a comparison of the pointing resolution between data and MC for $Z \to e^+e^-$ events shown in Fig. 6.9. The agreement between data and MC is good in the barrel, however a worse resolution is observed in the EC arising from a periodic bias in the second layer position measurement, see for more details [210]. Applying the difference between data and Monte Carlo as an extra smearing to the photon direction measurement in the EC leads to a relative change in the mass resolution of ±2.0% which is taken as an estimate for the systematic uncertainty.

  The total relative uncertainty on the mass resolution is ±13%.

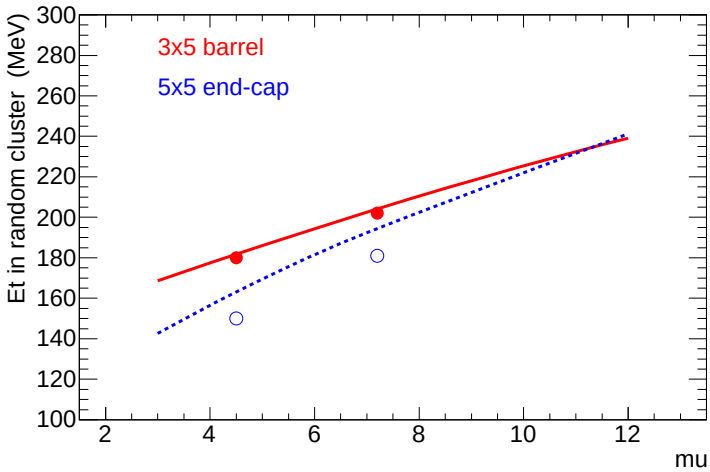

Figure 6.8: The RMS of the transverse energy observed in random clusters of size 3×5 in the barrel and 5×5 in the end-cap as a function of μ. The lines show the behaviour of mc10b Monte Carlo samples (single muon events) and the circles that of two data periods having different average value of μ (beginning of run 180701 and end of run 180636) [209].

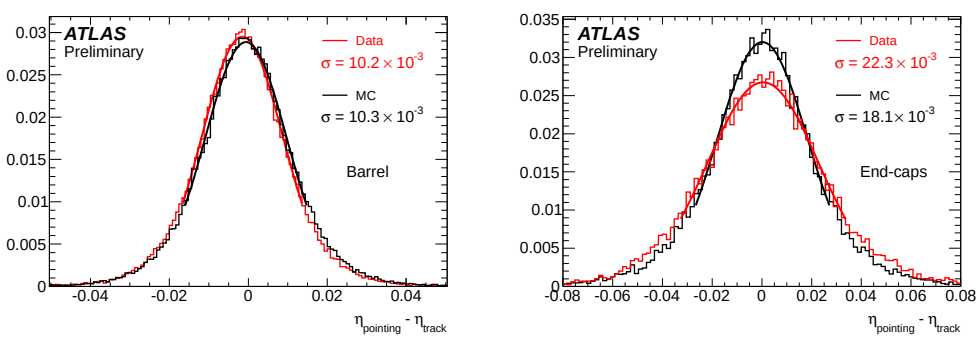

Figure 6.9: Comparison between data and Monte Carlo of the pointing resolution for electrons from $Z \to e^+e^-$ decays in the barrel (right) and in the EC (left) [207].

6.2.2 EPS 2011

The analysis of 2011 data has been updated for EPS 2011 with an integrated luminosity of $\sim$ 1 fb^{-1} [211]. The event selections, the computation of the diphoton invariant mass are the same as in PLHC 2011. The photon energy in data is futher corrected by residual correction factors (in 26 η bins) determined from 2011 $Z \to e^+e^-$ events. 5063 diphoton candidates are selected in the invariant mass range (which is extended wrt to previous analyses from 150 to 160) between 100 and 160 GeV.

In the analysis of the Monte Carlo events, the following corrections are applied:

- To correct for discrepancies between data and MC, fudge factors are applied to the shower shape variables according to the measurements from 2010 data (FF 2010). A cross check was made using the FF updated with 2011 data (FF 2011) and an overall correction of 0.7% is applied to the final signal yields;
- The photon energy is smeared to account for differences in resolution between data and simulation. The constant terms used are of $1.1^{+0.5}_{-0.6}\%$ in the barrel and $1.8 \pm 0.6\%$ in the EC;
- The MC samples are reweighted according to the average number of interactions per bunch crossing to match the distribution in data;
- The MC signal yields are rescaled by the ratio of the isolation cut efficiency in data and MC. The EtCone40 (corrected) distribution is compared in Fig. 6.10 for data and Monte Carlo (after pileup reweighting) for $Z \to e^+e^-$ events. The isolation cut (at 5 GeV) efficiency is different by 3% per event between data and Monte Carlo. Table 6.5 shows the comparison with a 120 GeV $H \to \gamma\gamma$ sample. Under the hypothesis of similar behaviour of electrons and photons in data, the difference is considered to be as well of the order of 3% per BEH event. The MC signal yields are therefore reduced by 3%. As a cross check, the isolation of the photons is shifted by 850 MeV (the difference between mean values of isolation for $Z \to e^+e^-$ in MC and data), which leads to a difference of cut isolation efficiency of about 4% (comparing the first two columns in Table 6.5).

	$H \to \gamma\gamma$	$H \to \gamma\gamma$ corrected by 850 MeV	$Z \to e^+e^-$ MC	$Z \to e^+e^-$ data
5 GeV cut	93.30%	89.60%	93.19%	90.50%

Table 6.5: Comparison of isolation cut efficiency

The main change with regards to the previous analyses is the classification of events into subsamples with different signal-to-background ratios and different invariant mass resolutions in order to improve the sensitivity of the search. The categorization is made following the photon positions in the calorimeter (η) and their conversion status:

- Unconverted central: Both photon candidates are reconstructed as unconverted photons and have $|\eta| < 0.75$;

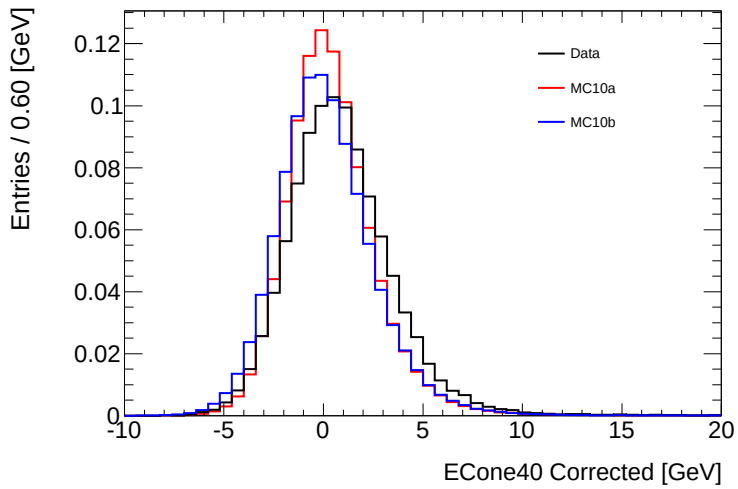

Figure 6.10: Corrected isolation distribution for data, mc10a and mc10b samples after pile-up reweighting

- Unconverted rest: Both photon candidates are reconstructed as unconverted photons and at least one candidate has $|\eta| > 0.75$;
- Converted central: At least one photon candidate is reconstructed as a converted photon and both photon candidates have $|\eta| < 0.75$;
- Converted rest: At least one photon candidate is reconstructed as a converted photon and both photon candidates have $|\eta| < 1.30$ or $|\eta| > 1.75$, but at least one photon candidate has $|\eta| > 0.75$;
- Converted transition: At least one photon candidate is reconstructed as a converted photon and at least one photon candidate is in the range $1.3 < |\eta| < 1.37$ or $1.52 < |\eta| < 1.75$.

This categorization leads to an improvement on the sensitivity of about 15%.

Table 6.6 shows the effects of the different event and photon selection cuts used for the inclusive analysis of data. The mass window cut applied in the one before last line is $100 - 160$ GeV. Table 6.7 shows the number of events passing all the analysis cuts in each category for data.

The cut flow is given in table 6.8 for a MC $H \to \gamma\gamma$ 120 GeV PowHeg [212] sample gluon gluon fusion production process. The acceptance of the kinematic cuts is $\sim$ 60%. The overall event selection efficiency, when both reconstructed

Cut	Number of events
No cut	1046434
Trigger	923766
GoodRunList	801482
Primary Vertex requirement ($\geq$ 3tracks)	801461
Loose - Loose	267242
p_T cuts	137852
Tight-Tight	29896
Isolation	16963
$M_{\gamma\gamma}$ window	5063
LAr quality	5063

Table 6.6: Effects of the different analysis cuts applied on data from period B-H4 (1.08 fb^{-1}). The mass window cut applied in the one before last line is 100-160 GeV.

Category	Unconverted central	Unconverted rest	Converted central	Converted rest	Converted transition
Number of events	400	1431	364	2068	800

Table 6.7: Number of events passing the analysis cuts in each diphoton category using the data from period B-H4 (1.08 fb^{-1})

photons pass the kinematical cuts and tight identification criteria, is 43%, which corresponds typically to an average efficiency per photon of $\sim$ 85%. The isolation cut requirement in the MC decreases this number further by $\sim$ 8% and the acceptance loss from the dead FEBs leads to another loss of $\sim$ 3%. After taking into account the correction for the isolation cut efficiency (-3%) and the difference of shower shape fudge factors between 2010 and 2011 ($+0.7\%$), the final acceptance times efficiency for the gluon gluon fusion process for a 120 GeV BEH mass is thus 38.5%.

Table 6.9 summarizes the expected signal yields from the signal MC samples after the application of the selection and corrections specified above. These signal yields are normalized for an integrated luminosity of 1.08 fb^{-1} and are given in step of 5 GeV of the BEH mass for the five different production mechanisms. In addition, the expected signal efficiency is quoted. Table 6.10 displays the expected signal yields in the different categories used for the fit of the different BEH boson masses.

Same signal and background models are used as in the previous analyses. Fig. 6.11 shows the expected mass resolution for a BEH boson of 120 GeV. For

Cut	Number of events
No cut	99974
Trigger	70786
Primary Vertex requirement (≥ 3 tracks)	70780
Preselection cuts	54513
p_T cuts	52610
Tight-Tight	42652
Isolation	39388
$M_{\gamma\gamma}$ window	39377
LAr quality	39377

Table 6.8: Effects of the different analysis cuts applied on ggH 120 GeV MC sample

m_H [GeV]	$gg \to H$		VBF		WH		ZH		ttH		
	$\varepsilon(\%)$	N_{evt}	$\varepsilon(\%)$	N_{evt}	$\varepsilon(\%)$	N_{evt}	$\varepsilon(\%)$	N_{evt}	$\varepsilon(\%)$	N_{evt}	N_{evt} total
100	31.96	13.13	34.43	0.91	29.22	0.59	29.16	0.31	26.12	0.07	15.02
105	34.29	14.30	36.09	1.02	30.73	0.60	30.77	0.32	26.98	0.07	16.31
110	35.56	14.95	36.75	1.09	32.02	0.59	31.99	0.32	28.49	0.08	17.03
115	36.46	15.14	38.75	1.18	33.16	0.57	33.20	0.31	29.26	0.07	17.29
120	38.46	15.48	39.66	1.22	33.82	0.54	34.59	0.30	30.46	0.07	17.61
125	39.37	14.91	40.40	1.21	35.40	0.50	36.46	0.28	30.86	0.07	16.98
130	40.41	13.87	42.93	1.20	36.92	0.45	36.73	0.25	31.85	0.06	15.83
135	41.29	12.43	43.14	1.09	38.03	0.38	37.59	0.21	31.45	0.05	14.17
140	42.04	10.64	44.08	0.97	37.93	0.31	39.82	0.18	32.87	0.04	12.14
145	43.18	8.79	45.31	0.82	39.48	0.24	39.70	0.14	34.32	0.03	10.03
150	43.25	6.69	45.95	0.65	39.92	0.18	40.45	0.10	34.02	0.02	7.65

Table 6.9: Expected signal efficiency and yields assuming a luminosity of 1.08 fb^{-1}. Results are given for the five different production mechanisms.

M_H [GeV]	100	105	110	115	120	125	130	135	140	145	150
Unconverted central	2.52	2.56	2.55	2.47	2.64	2.37	2.30	2.03	1.71	1.39	1.11
Unconverted rest	3.89	4.31	4.55	4.71	4.74	4.52	4.18	3.94	3.38	2.74	2.08
Converted central	1.77	1.87	1.98	1.94	1.96	1.95	1.71	1.54	1.34	1.08	0.82
Converted rest	4.89	5.56	5.62	5.97	6.04	5.94	5.56	4.82	4.19	3.49	2.67
Converted transition	1.95	2.01	2.32	2.21	2.23	2.20	2.09	1.83	1.52	1.33	0.97

Table 6.10: Expected signal yields in the different categories for an integrated luminosity of 1.08 fb^{-1}

the five categories, the resolutions are shown separately in Fig. 6.12. The core component of the mass resolution, σ_{CB} ranges from 1.4 GeV in the "Unconverted central" category to 2.1 GeV in the "Converted transition" category.

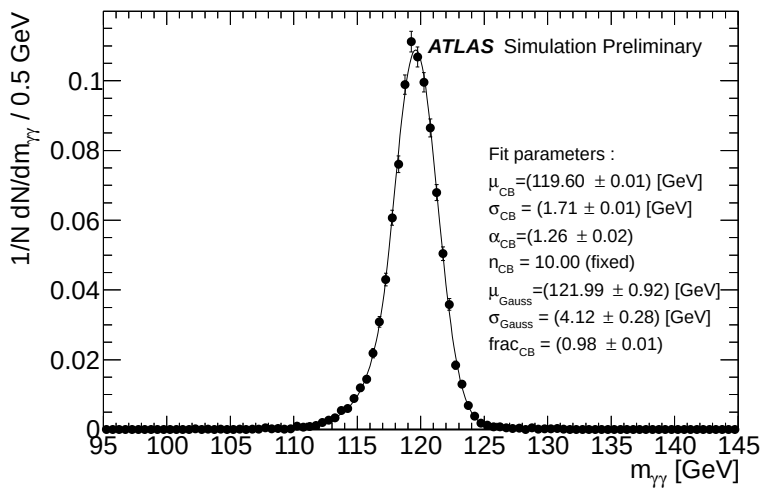

Figure 6.11: Invariant mass distribution for a BEH boson with $M_H = 120$ GeV [213].

The systematic uncertainties considered for the calculation of the expected signal yields with MC are given in the following:

- Luminosity: the uncertainty on the integrated luminosity was taken as $\pm 3.7\%$;
- Trigger efficiency: the uncertainty on the trigger efficiency was found to be $\pm 1\%$ per event;
- Photon Identification: unchanged wrt to PLHC i.e $\pm 10\%$ per event;
- Isolation cut efficiency: unchanged wrt to PLHC i.e $\pm 3\%$ per event;
- Event pile-up effect: unchanged wrt to PLHC i.e $\pm 4\%$ per event;
- Photon energy scale: the variation of the photon energy by 1% leads to less than 0.5% of variation in the $H \to \gamma\gamma$ yield. Therefore this uncertainty was neglected;
- BEH p_T modeling: the uncertainty on the kinematic cut acceptance from the modeling of the BEH boson p_T distribution was estimated to be $\pm 1\%$, in particular looking at the difference in acceptance when reweighting with HqT [214].

Adding in quadrature these uncertainties, the overall uncertainty on the signal yield is $\pm 12\%$ per event. Table 6.11 summarizes these uncertainties.

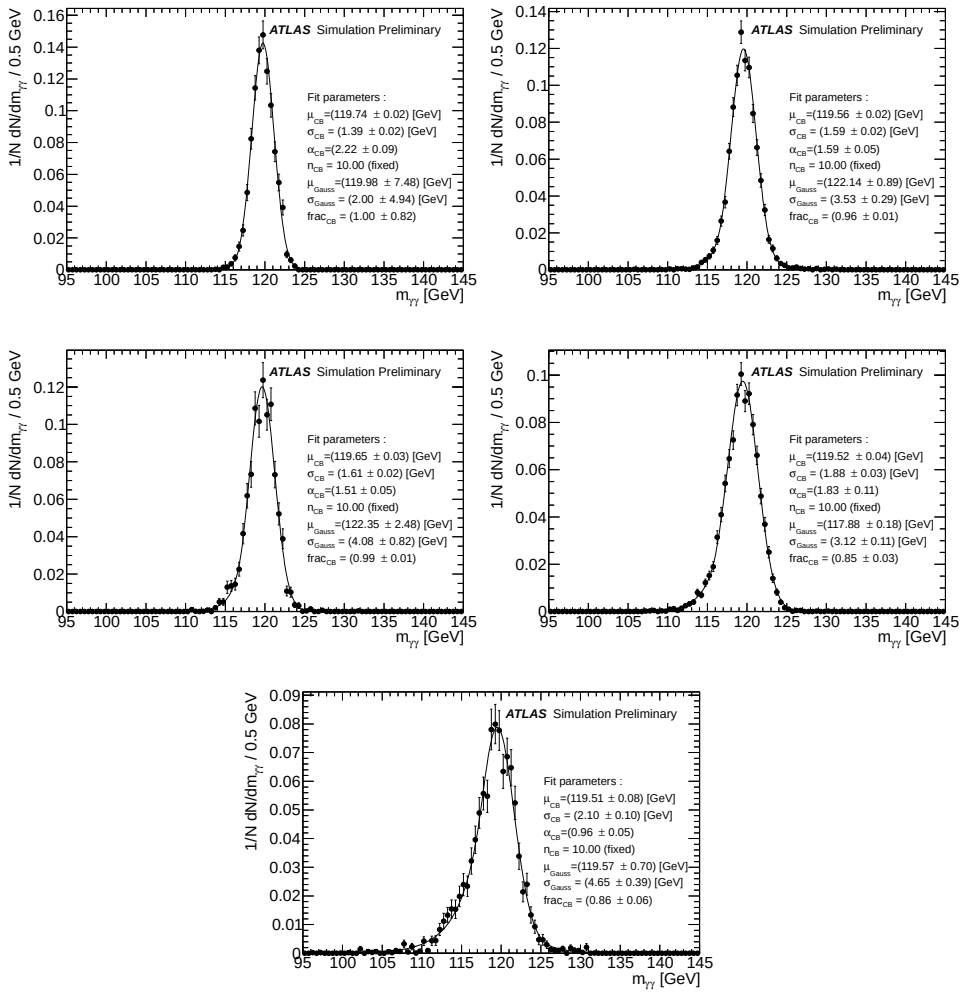

Figure 6.12: Invariant mass distribution for a BEH boson with $M_H = 120$ GeV in the five different categories [213].

The systematics on the mass resolution originate from the:

- Uncertainty on the constant term: Although the central values of the constant terms are similar to those used in the 2010 analyses, the assigned uncertainties are larger because of the consideration of the uncertainty on the sampling term. Therefore a more robust treatment of these uncertainties is needed to estimate the systematics from the constant term. For recalling, the constant term is estimated using the equation 4.27. To estimate the uncertainties on the constant term for PLHC (c_{up} and c_{down}), the sampling term was scaled by $\pm 10\%$. In order to minimize the impact of the larger uncertainties on the

Source	Systematic
Photon Identification	$\pm$ 10.0%
Pile-Up	$\pm$ 4.0%
Isolation	$\pm$ 3.0%
Kinematic	$\pm$ 1.0%
Trigger	$\pm$ 1.0%
Luminosity	$\pm$ 3.7%
Total	$\pm$ 12.0%

Table 6.11: Summary of systematic uncertainties applied on signal yields (per event)

mass resolution, the uncertainties on the constant term have been divided for EPS into statistical and systematic uncertainties correlated and uncorrelated with the sampling term as shown in table 6.12;

	Stat	Syst uncorrelated	Syst correlated
Barrel	± 0.1	± 0.3	$^{+0.4}_{-0.5}$
EC	± 0.4	± 0.2	$^{+0.3}_{-0.4}$

Table 6.12: Statistical and systematic uncertainties (correlated and uncorrelated with the sampling term) for the barrel and the EC.

We thus define two terms: $c1_{up}$ ($c1_{down}$) and $c2_{up}$ ($c2_{down}$) as the uncertainty on the constant term uncorrelated and correlated to the sampling term respectively. The statistical uncertainty is considered as uncorrelated to the sampling term and thus the total uncorrelated term is the quadratical sum of the first two columns of table 6.12.

The central values and the corresponding errors $c1_{up}$ ($c1_{down}$) and $c2_{up}$ ($c2_{down}$) are given in table 6.13 for different η bins. These numbers do not include the nominal constant term 0.7%. I give in the following an example of how we compute the term $c1_{up}$ in the barrel. The statistical and the uncorrelated systematic uncertainty of the first two columns in table 6.12 in the barrel sum up quadratically to $0.1 \oplus 0.3 = 0.32\%$. The constant term obtained adding up this error is $1.1 + 0.32 = 1.42\%$. Removing the nominal constant term, we obtain $1.42 \ominus 0.7 = 1.24\%$ which can be written as $(1.1 \ominus 0.7) + 0.39\%$. This is the so-called $c1_{up}$ term which has a value of 0.39% in the barrel.

The resolutions obtained from a gaussian fit to the core of the invariant mass distributions from $H \to \gamma\gamma$ MC samples with $M_H = 120$ GeV are

listed in table 6.14 for different treatment of the constant term. For these numbers, the vertex is determined using its true position in z instead of the "pointing", which has a minor impact on the mass resolution. The Nominal MC corresponds to the nominal constant term 0.7% wihout any extra smearing and the Smeared MC corresponds to a smearing with the central values $c_{central}$ of table 6.13. Smeared+$c1_{up}$ ($c1_{down}$) corresponds to the invariant mass distributions smeared with $c_{central} + c1_{up}$ ($c_{central} - c1_{down}$). For $c2_{up}$ ($c2_{down}$), the constant term is changed into $c_{central} + c2_{up}$ ($c_{central} - c2_{down}$) with a scaling of the sampling term into -10% ($+10\%$) to take into account the correlation between $c2$ and the sampling term. Practically, the scaling of the sampling term by $\pm 10\%$ is done by scaling the nominal MC resolution (1.52 GeV) by $\pm 8\%$: the sampling term contributes to ~ 1.4 GeV of the MC resolution ($1.52 = 1.4 \oplus 0.59$), $\pm 10\%$ uncertainty on the sampling term i.e on 1.4 GeV translates into $(0.9 \times 1.4) \oplus 0.59 = 0.92 \times 1.52$ i.e $\pm 8\%$ on a resolution of 1.52 GeV. In conclusion, in the spectific case of $c2$, the mass is obtained by the following equation:

$$M_{c2_{up}} = 120 + 0.92 * (M_{nominal} - 120) + (M_{c2_{up}} - M_{nominal}) \tag{6.2}$$

and

$$M_{c2_{down}} = 120 + 1.08 * (M_{nominal} - 120) + (M_{c2_{down}} - M_{nominal}) \tag{6.3}$$

where $M_{nominal}$ is the mass obtained from a nominal MC without any extra smearing.

The total relative uncertainty due to the uncorrelated part ($c1$) is $+11 - 9\%$ and $+8 - 5\%$ for the correlated one ($c2$). Adding up these errors quadratically gives $+14 - 10\%$ i.e $\sim 12\%$ on the mass resolution.

	$0 < \|\eta\| < 0.6$	$0.6 < \|\eta\| < 1.37$	$1.37 < \|\eta\| < 1.52$	$1.52 < \|\eta\| < 2.47$	$2.47 < \|\eta\| < 3.2$	$3.2 < \|\eta\| < 4.9$
$c_{central}$	0.0085	0.0085	0.0165	0.0165	0.04	0.02
$c1_{up}$	0.0039	0.0039	0.0047	0.0047	0.02	0.006
$c1_{down}$	0.0051	0.0051	0.0048	0.0048	0.02	0.006
$c2_{up}$	0.0047	0.0047	0.0032	0.0032	0.011	0.010
$c2_{down}$	0.0085	0.0085	0.0044	0.0044	0.011	0.016

Table 6.13: Constant term values used: central values and errors (correlated and uncorrelated) removing 0.7% of constant term.

- Uncertainty on the photon pointing: $\pm 1\%$ of relative uncertainty on the mass resolution,
- Uncertainty due to the electron to photon extrapolation: same as for PLHC. The relative uncertainty on the mass resolution is 6%. This difference has been checked again here in Table 6.14. The difference between distorted smeared MC (corrected by distorted energy scale corrections estimated from a distorted

	Resolution
Nominal MC	1.52 GeV
Smeared MC	1.75 GeV
Smeared+$c1_{up}$	1.95 GeV
Smeared+$c1_{down}$	1.61 GeV
Smeared+$c2_{up}$	1.89 GeV
Smeared+$c2_{down}$	1.67 GeV
Distorted smeared MC	1.80 GeV

Table 6.14: Resolutions obtained with a gaussian fit to the core of the distribution.

$Z \to e^+e^-$ MC) and the smeared MC is about 3% from the gaussian fit to the core and about 6% from the RMS difference;

- Pileup: same as for PLHC, i.e ±3% relative uncertainty on the mass resolution.

Table 6.15 summarizes the relative uncertainties applied on the mass resolution. The overall relative uncertainty on the mass resolution is ±14% which is applied to both crystal-ball sigma and the wide gaussian sigma in a correlated way. Furthermore,

Source	Systematic
Constant term	± 12.0%
Pile-Up	± 3.0%
e^-/γ extrapolation	± 6.0%
Pointing	± 1.0%
Total	± 14.0%

Table 6.15: Summary of systematic uncertainties applied on mass resolution.

a study of the material impact on the mass peak has been done in [213]. Table 6.16 shows a comparison of the reconstructed mass value, obtained from a gaussian fit to the core of the invariant mass distributions, between a MC with a nominal geometry and a MC with a distorted geometry (corrected by the distorted energy scale corrections computed from the distorted MC $Z \to e^+e^-$ sample). This is done as well for the five different categories. In the last two columns are shown the values of the reconstructed mass when changing the photon energy scale by +0.5%, −0.5% in the barrel, EC and by +0%, −1% respectively in the nominal MC sample. The percentage quoted between brackets is the relative change wrt to the nominal inclusive number. For example, for the unconverted central category with the distorted geometry, the relative change is computed as $(120.2 \times 119.7)/(120.1 \times 119.9) = -0.1\%$. The difference is found to be small in all the categories (about 0.2%) and is therefore neglected in the current analysis.

An exponential function is used as a model for the background in all the categories. The uncertainty from this background modeling was estimated from the

$M_H = 120$ GeV	nominal	distorted	+0.5% barrel,-0.5% EC	+0% barrel, -1% EC
Inclusive	119.7	120.1	120.1	119.5
Unconverted central	119.9	120.2(-0.1%)	120.4(+0.1%)	119.9(+0.2%)
Unconverted rest	119.7	120.3(+0.2%)	120.0(-0.1%)	119.6(+0%)
Converted central	119.6	119.8(-0.2%)	120.2(+0.2%)	119.6(+0.2%)
Converted rest	119.7	120.0(-0.1%)	120.0(-0.1%)	119.4(-0.1%)
Converted transition	119.6	120.0(0%)	119.8(-0.2%)	119.2(-0.2%)

Table 6.16: Mass peak for each of the diphoton categories for Monte Carlo simulated with nominal and distorted geometry. Between brackets is given the relative difference wrt the nominal sample.

inclusive sample and checked in each category. It is taken as the maximum potential difference integrated over a window of 4 GeV between the true background shape (using DIPHOX [215]) and the single exponential function which could fake a signal-like signature. The resulting uncertainty was found to be between ± 5 events at 110 GeV and ± 3 events at 150 GeV. This uncertainty is propagated linearly as a function of the BEH mass and it is scaled by the fraction of events in each category. Other functional forms, including 2nd order polynomial, exponential of a second order polynomial, double exponential, exponential times a power law functions, were fitted to the data and compared to the exponential fit. The uncertainties arising from these comparisons were found to be in a fair agreement with the MC-based estimate.

6.2.3 Council 2011

The analysis of the full 2011 dataset, corresponding to an integrated luminosity of 4.9 fb^{-1}, has been presented at Council 2011 and published in [216, 173]. For this analysis, slight differences in the selections and corrections with regards to EPS have been done and are summarized in the following:

- Photon candidates are required to pass the Ambiguity Resolver bit (AR bit). This bit assures the rejection of the converted candidate if its associated track has not a hit in the B-layer but rather in the next layer and if the B-layer is not working properly. This affects only converted photons and strongly decreases the misidentification of electrons as photons;

- Photon candidates are rejected if they are badly timed (photon cleaning);

- The LAr error bit definition has been updated to include a time veto cut allowing the recovery of the previously rejected lumiblock;

- In case of gluon fusion production, the MC events are reweighted in order that the distribution of the BEH boson p_T matches the one obtained from the HqT package;

- A correction to the z coordinate of the vertex position is applied for photons reconstructed in the EC in order to compensate for an oscillation structure in the second layer position measurement observed only in data [210];
- The shower shape variables in the MC are corrected with FF2011;
- The MC signal samples are reweighted to correct for the spread in z of the beam spot: the MC samples were generated with a width $\sigma_z \sim 7.5$ cm which is larger than that observed in data $\sigma_z \sim 6$ cm.

22489 diphoton candidates are selected in the invariant mass range between 100 and 160 GeV.

The main change with regards to EPS is the further splitting into categories in order to increase the sensitivity to a possible BEH boson signal. A new diphoton observable is introduced, p_{Tt}, which is defined as the component of the diphoton transverse momentum $p_T^{\gamma\gamma}$ orthogonal to the thrust axis, as shown in Fig. 6.13. The

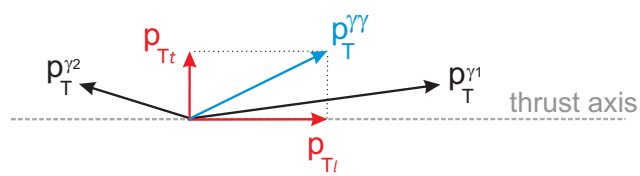

Figure 6.13: Sketch of the p_{Tt} definition.

diphoton thrust axis, $\widehat{t}$, is defined as:

$$\widehat{t} = \frac{\vec{p}_{\mathrm{T}}^{\gamma 1} - \vec{p}_{\mathrm{T}}^{\gamma 2}}{|\vec{p}_{\mathrm{T}}^{\gamma 1} - \vec{p}_{\mathrm{T}}^{\gamma 2}|},$$

where the $\vec{p}_{\mathrm{T}}^{\gamma 1}$ and $\vec{p}_{\mathrm{T}}^{\gamma 2}$ are the transverse momenta of the two selected photons. The transverse momentum of the diphoton system, $p_T^{\gamma\gamma}$, is given by:

$$\vec{p}_{\mathrm{T}}^{\gamma\gamma} = \vec{p}_{\mathrm{T}}^{\gamma 1} + \vec{p}_{\mathrm{T}}^{\gamma 2}.$$

The p_{Tt} is then calculated as follows:

$$\begin{aligned} \vec{p}_{\mathrm{Tt}} &= \vec{p}_{\mathrm{T}}^{\gamma\gamma} - (\vec{p}_{\mathrm{T}}^{\gamma\gamma} \cdot \widehat{t}) \cdot \widehat{t}, \\ p_{\mathrm{Tt}} &= |\vec{p}_{\mathrm{T}}^{\gamma\gamma} \times \widehat{t}|. \end{aligned}$$

The p_{Tt} is strongly correlated with the diphoton transverse momentum, but it has a better detector resolution and retains a monotically falling diphoton invariant mass distribution. Fig. 6.14 displays the distributions of p_{Tt} for data and Monte Carlo signal processes for the inclusive event selection. The gluon-gluon fusion p_{Tt} distribution is very similar to the one of the background. The other signal processes show on average larger p_{Tt} values than the data. Four of the five categories used

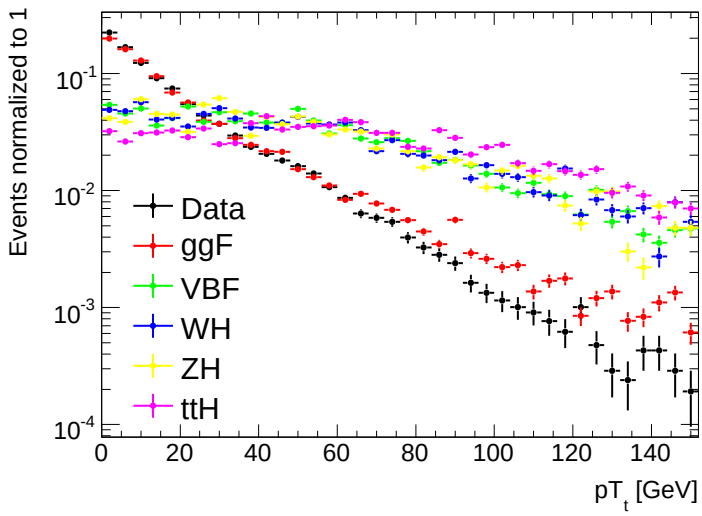

Figure 6.14: Distributions of p_{Tt} normalized to unity for 4.9 fb^{-1} of data and the signal processes for a BEH boson mass of 120 GeV. The p_T reweighting is applied [217].

for the EPS analysis (except the "Converted transition") are divided by a cut at $p_{\mathrm{Tt}} = 40$ GeV into two categories, low p_{Tt} and high p_{Tt}. Events are therefore classified into 9 categories.

The expected signal yields are shown in Table 6.17 together with the corresponding efficiencies for different BEH mass hypothesis. These numbers are normalized to 4.9 fb^{-1} and are summed up over all the categories. The numbers are corrected for the difference in the isolation cut efficiency between data and MC by a factor of 0.956 estimated from $Z \to e^+e^-$ events. Moreover, the number of signal events produced by gluon fusion is rescaled to take into account the expected destructive interference between the $gg \to \gamma\gamma$ and the $gg \to H \to \gamma\gamma$ process [218], leading to a reduction of the production rate by $2 - 5\%$ depending on the BEH mass and the category [219]. A small change wrt to EPS is that the signal yields, in each category, for a given mass are derived from a 3rd order polynomial fit to the yields extracted from the simulated samples. This reduces the statistical fluctuations in particular due to large pileup weights.

The signal and background modeling remain almost unchanged compared to the previous analyses. A small difference wrt to EPS for the signal modeling is that a global fit is done for the crystal ball and the gaussian component. For a $M_H = 120$ GeV, the FWHM was found to be 4.1 GeV and $\sigma_{CB} = 1.7$ GeV for the inclusive dataset. The FWHM varies between categories from 3.3 GeV ("Unconverted Central, High p_{Tt}") to 5.9 GeV ("Converted transition") and the σ_{CB}

M_H [GeV]	110	115	120	125	130	135	140	145	150
$\sigma \times BR$ [fb]	45	44	43	40	36	32	27	22	16
Signal events	69	72	72	69	65	58	50	41	31
Efficiency [%]	31	33	34	35	37	37	38	38	39

Table 6.17: BEH boson production cross section multiplied by the branching ratio into two photons, expected number of signal events summed over all categories for 4.9 fb^{-1} and selection efficiencies for various BEH boson masses.

from 1.4 to 2.3 GeV (for the same categories). The invariant mass distribution of the selected candidates in the inclusive sample is shown in Fig. 6.15. The sum of the background-only fits to the invariant mass in each of the categories is overlaid. The signal expectation for a SM BEH boson with $M_H = 120$ GeV and the residual of the data with respect to the total background as a function of $M_{\gamma\gamma}$ are also shown.

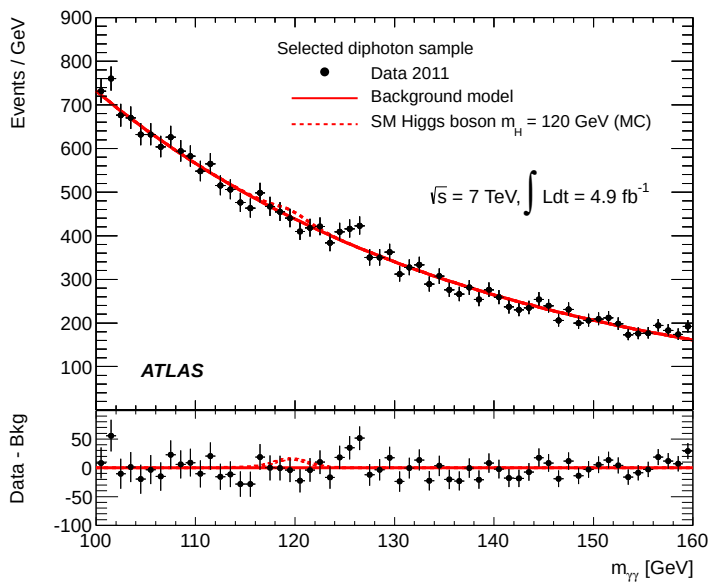

Figure 6.15: Invariant mass distribution for the selected data sample, overlaid with the total background. The bottom inset displays the residual of the data with respect to the total background. The BEH boson expectation for a mass hypothesis of 120 GeV corresponding to the SM cross section is also shown [173].

The systematic uncertainties for the signal yield and the invariant mass resolution are essentially the same than those used for EPS. However some of them are modified and some additional systematics were introduced. I will summarize these in the following:

- Luminosity: the overall uncertainty on the total integrated luminosity was found to be $\pm 3.9\%$;
- Theory: the theoretical uncertainties are divided into uncertainties on the QCD renormalization and factorization scales $^{+12}_{-8}\%$ and on the PDF+α_s $\pm 8\%$;
- Isolation cut efficiency: a 5% uncertainty is assigned to take into account for the difference in the isolation cut efficiency between data and MC,
- Migration of events from the high p_{Tt} to the low p_{Tt} categories: this arises from the modeling of the BEH boson p_T. It was estimated by varying scale choices and PDFs in HqT on the BEH signal MC events. It was found to be $\pm 8\%$;
- Migration of events from the unconverted categories to the converted categories: it arises from the impact of pileup on the photon reconstruction and from the limited knowledge of the material in front of the calorimeter. It was estimated by comparing category fractions between a sample without pileup and with an average number of interactions between 8 and 12, and by comparing the category fractions between MC signal sample with the nominal geometry and another one with a distorted geometry. Both differences are added up quadratically and the uncertainty is taken as 4.5%.

The systematic uncertainty from the background modeling is estimated in the same way as for EPS. The values of this uncertainty depend on the analysis category, it ranges between ± 0.1 and ± 5.6 events (normalized to 4.9 fb^{-1}). These uncertainties are treated as uncorrelated between the various categories except those that share the same η and p_{Tt} classification but different conversion status. In addition, they are taken conservatively to be independent of the BEH mass.

The uncertainty on the mass peak position was studied and found to be ± 0.7 GeV. It is estimated by comparing the peak positions of the invariant mass distributions between a nominal MC $H \to \gamma\gamma$ sample and a similar sample with a distorted geometry, after applying the distorted energy scale corrections from $Z \to e^+e^-$ events [220].

Table 6.18 summarizes the systematic uncertainties on the expected signal yield, on the mass resolution and from the background modeling.

6.3 Improved Analysis of 2011 data

The re-analysis of the full 2011 dataset has been presented first at the CERN seminar of July 4th 2012 [221] and a few days later at ICHEP 2012 [174]. The analysis and the results have been published in [222]. This analysis follows closely the Council's analysis. However major improvements were done and I will

Signal event yield	
Photon reconstruction and identification	$\pm 11\%$
Effect of pileup on photon identification	$\pm 4\%$
Isolation cut efficiency	$\pm 5\%$
Trigger efficiency	$\pm 1\%$
BEH boson cross section (scales)	$^{+12}_{-8}\%$
BEH boson cross section (PDF+α_s)	$\pm 8\%$
BEH boson p_T modeling	$\pm 1\%$
Luminosity	$\pm 3.9\%$
Signal mass resolution	
Calorimeter energy resolution	$\pm 12\%$
Photon to electron extrapolation	$\pm 6\%$
Effect of pileup on energy resolution	$\pm 3\%$
Photon angular resolution	$\pm 1\%$
Signal mass position	
Photon energy scale	± 0.7 GeV
Signal category migration	
BEH boson p_{T} modeling	$\pm 8\%$
Conversion rate	$\pm 4.5\%$
Background model	$\pm\,(0.1 - 7.9)$ events

Table 6.18: The relative variations of the signal yield, mass resolution, mass position and amount of signal events in the categories for various sources of uncertainties are shown. The uncertainty from the background modeling depends on the analysis category and is given as a number of events corresponding to an integrated luminosity of 4.9 fb^{-1}.

summarize them in the following.

6.3.1 Improved selections and corrections

Several improvements to the photon selection procedure were made:

- Increasing the transverse momentum cut on the subleading photon. Several configurations were tested and the best compromise in terms of expected sensitivity, robustness and performance was chosen. The cut on the subleading photon was increased from 25 to 30 GeV;
- An improved photon identification. A neural network based selection (NN2011), tuned to achieve similar jet rejection as the cut-based menu (Tight2011) but with higher efficiency, is used (already discussed in section 5.2.2);

- An improved isolation, described in section 5.3. Photon candidates are isolated if topoPosEMEtCone40 < 4 GeV;
- An improvement on the primary vertex selection. The PV of the hard interaction is identified by combining the following elements in a global likelihood [223]: the "pointing" direction of the photons, the average beam spot position, and the $\sum p_T^2$ of the tracks associated with each reconstructed vertex. The conversion vertex is used in the likelihood for converted photons with tracks containing silicon hits.

An improvement of the luminosity measurement leads to a decrease of the central value from 4.9 to 4.8 fb^{-1}, moreover its assigned systematic uncertainty decreases to 1.8%.
On the other hand, the MC samples are reweighted for pileup and the spread of the beam spot position to match the corresponding distributions in data, as described above. The BEH p_T spectrum is reweighted to match the spectrum given by HqT for events produced by gluon-gluon fusion. The shower shape variables are corrected with FF2011 for differences with data. Finally, the photon energy in MC is smeared to take into account for differences in resolution between data and MC estimated from $Z \to e^+e^-$ events. These corrections have been updated since Council 2011 and are splitted into finer bins as described in section 4.3 for what was published in [222], however old corrections were used in [174]. Differences between [174] and [222] are shown in [224].

With this selection, 23788 diphoton candidates are observed in the invariant mass range between 100 and 160 GeV.

6.3.2 Event categorization

The events are classified to similar categories as those used for the Council's analysis. However the p_{Tt} cut has been increased to 60 GeV. Fig. 6.16 shows the difference in p_{Tt} distribution for different BEH boson production processes. In addition, one of the major improvement is the further split into a $2-jet$ category with a VBF-like signature i.e two forward jets (with little QCD radiation in the central region from the hard interaction). In total, 10 categories are used for the analysis.
In the following are described the cuts used to select events in the 10th category i.e the $2-jet$ category:

- At least two hadronic jets in $|\eta^{jet}| < 4.5$ with $p_T^{jet} > 25$ GeV. Jets in the tracker acceptance range ($|\eta| < 2.5$) are required to have a jet-vertex-fraction [3] of at least 0.75. The jets are required to pass quality jet cuts and to have

[3] The fraction of the sum of p_T carried by tracks in the jet and associated to the PV selected with the likelihood method wrt to the total p_T carried by all the tracks associated to the jet.

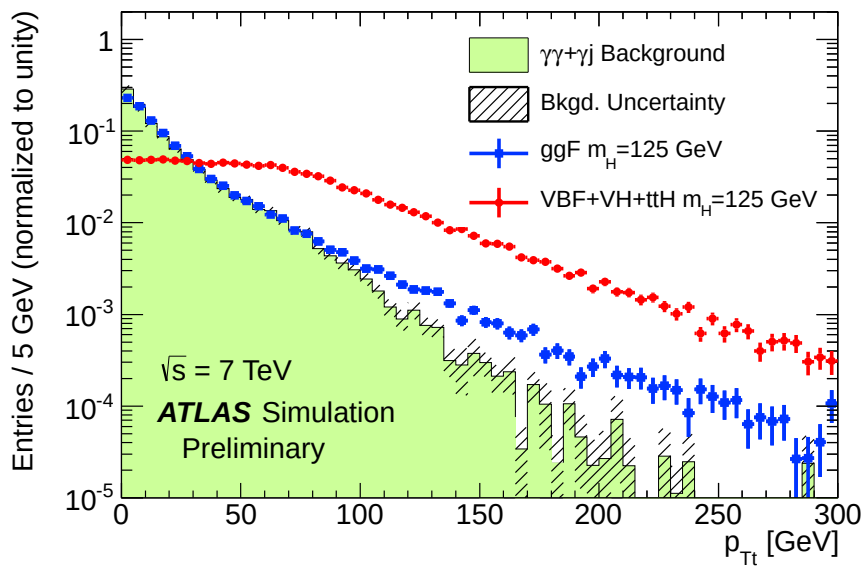

Figure 6.16: Comparison of the p_{Tt} distribution between simulated events with BEH boson production and background events. The signal distribution is shown separately for gluon fusion (blue), and vector-boson fusion together with associated production (red) for $M_H = 125$ GeV. The background MC and the two signal distributions are normalized to unit area [174].

a minimum distance $\Delta R = 0.4$ to any of the selected photons. Among the selected jets, the two jets with the highest p_T are considered as the tagging jets;

- A large pseudorapidity gap between the tagging jets $\Delta\eta_{jj} > 2.8$;
- A large invariant mass of the tagging jets $M_{jj} > 400$ GeV;
- $\Delta\phi$ between the di-jet and the di-photon system larger than 2.6.

29% (1%) of the selected VBF (gluon-gluon fusion) events are classified into the $2-jet$ category. The jet multiplicity in the $\sqrt{s} = 7$ TeV data is compared to the simulation in Fig. 6.17.

The expected BEH boson signal efficiency and yields are summarized in Table 6.19 for an integrated luminosity of 4.8 fb^{-1}. The numbers are given for different BEH masses and for different production processes, the last column shows the total number of expected events summed up over all the processes. The signal yields for events produced by gluon-gluon fusion are corrected to take into account the destructive interference with the $gg \to \gamma\gamma$, leading to a reduction of the production

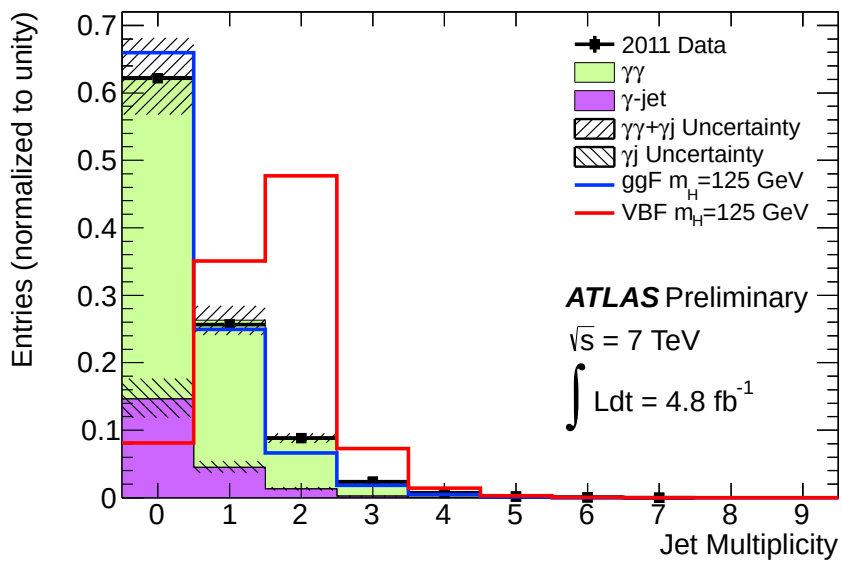

Figure 6.17: Jet multiplicity in the $\sqrt{s} = 7$ TeV data compared to simulation. The $\gamma\gamma$ component is simulated with SHERPA, while the γ-jet component is simulated with ALPGEN, and the small jet-jet and Drell-Yan components are neglected. The two components are normalized such that the final sample has a diphoton purity of 80% as measured on data. The uncertainties on the background components take both the statistical uncertainties of the simulation samples and the uncertainties from the data-driven background decomposition into account. The distributions are normalized to unit area to allow for a comparison of the shapes of data and background simulation, and of background and signal simulation. Events from data and background simulation are taken from the mass range between 100 and 160 GeV [174].

rate by $2 - 5\%$ depending on the BEH mass and the category (as done for the Council's analysis).

Table 6.20 shows the expected signal events per category, for $M_H = 126.5$ GeV. The percentage of events produced by $gg \to H$, VBF, WH, ZH and ttH are also given for each category.

The signal modeling is similar to the one used for the Council 2011. However several studies were made to chose the optimal background modeling. Different parametrizations are chosen for the different categories in a way to achieve a compromise between limiting the size of a potential bias introduced by the chosen parametrization and retaining good statistical power. More details will be given in chapter 7. Table 6.21 list the different analytic functions used depending on the category: an exponential function in the low statistics categories, a fourth-order

M_H [GeV]	$gg \to H$		VBF		WH		ZH		ttH		Total
	ε(%)	$N_{\rm evt}$	ε(%)	$N_{\rm evt}$	ε(%)	$N_{\rm evt}$	ε(%)	$N_{\rm evt}$	ε(%)	$N_{\rm evt}$	$N_{\rm evt}$
110	37.3	71.7	37.9	5.2	33.5	2.8	33.6	1.5	33.7	0.4	81.6
115	39.5	73.8	40.1	5.5	34.9	2.8	35.5	1.5	34.9	0.3	83.9
120	40.9	73.5	42.1	5.8	37.0	2.6	37.0	1.4	35.9	0.3	83.7
125	42.0	70.9	43.8	5.8	38.1	2.4	38.4	1.3	37.2	0.3	80.7
130	43.1	66.3	44.8	5.7	39.3	2.1	39.9	1.2	37.8	0.3	75.6
135	43.1	59.8	46.9	5.3	40.7	1.8	40.8	1.0	38.7	0.2	68.3
140	45.2	51.7	48.7	4.8	41.9	1.5	42.3	0.9	39.5	0.2	59.1
145	45.8	42.3	49.8	4.1	42.5	1.2	43.6	0.7	40.5	0.2	48.4
150	45.8	31.6	49.7	3.1	44.1	0.9	44.7	0.5	40.7	0.1	36.2

Table 6.19: Expected BEH boson signal efficiency (for the gluon-gluon fusion process, the numbers include the effect of the destructive interference with the background $gg \to \gamma\gamma$) and event yield assuming a luminosity of 4.8 fb^{-1} for the $\sqrt{s} = 7$ TeV data. Results are given for different production processes.

Category	$N_{\rm evt}$	$gg \to H$ [%]	VBF [%]	WH [%]	ZH [%]	ttH [%]
Inclusive	79.4	87.8	7.3	2.9	1.6	0.4
Unconverted central, low $p_{\rm Tt}$	10.5	92.9	4.0	1.8	1.0	0.2
Unconverted central, high $p_{\rm Tt}$	1.5	66.5	15.7	9.9	5.7	2.4
Unconverted rest, low $p_{\rm Tt}$	21.6	92.8	3.9	2.0	1.1	0.2
Unconverted rest, high $p_{\rm Tt}$	2.8	65.4	16.1	10.8	6.0	1.8
Converted central, low $p_{\rm Tt}$	6.7	92.8	4.0	1.9	1.0	0.2
Converted central, high $p_{\rm Tt}$	1.0	66.6	15.3	10.0	5.7	2.5
Converted rest, low $p_{\rm Tt}$	21.1	92.8	3.8	2.0	1.1	0.2
Converted rest, high $p_{\rm Tt}$	2.7	65.3	15.9	11.0	5.9	1.8
Converted transition	9.5	89.4	5.2	3.3	1.7	0.3
2-jet	2.2	22.5	76.7	0.4	0.2	0.1

Table 6.20: Number of expected signal events for $\sqrt{s} = 7$ TeV obtained from simulation with $M_H = 126.5$ GeV. The numbers are normalized for 4.8 fb^{-1}. The percentage of events in each production process is also given.

Bernstein polynomial or an exponential function of a second-order polynomial otherwise. The systematic uncertainty due to the choice of the parametrization is also given, it is estimated from the comparison between the given function and the background model based on SHERPA for the diphoton component. The largest difference observed over the full mass range is taken as a systematic uncertainty. This uncertainty is equally applied to all the BEH mass hypothesis. Table 6.22 summarizes the number of fitted background events (using a background-only fit) and the number of observed events in a window containing 90% of the expected signal yields around $M_H = 126.5$ GeV. It also gives the values of the parameters characterizing the signal resolution function: σ_{CB} and FWHM. The numbers are given for the inclusive sample and the different categories. The 2-jet category has the better ratio of S/B and the category "Unconverted central, high $p_{\rm Tt}$" gives the

best FWHM.

Category	Parametrization	Uncertainty [N_{evt}]
Inclusive	4th order pol.	7.3
Unconverted central, low p_{Tt}	Exp. of 2nd order pol.	2.1
Unconverted central, high p_{Tt}	Exponential	0.2
Unconverted rest, low p_{Tt}	4th order pol.	2.2
Unconverted rest, high p_{Tt}	Exponential	0.5
Converted central, low p_{Tt}	Exp. of 2nd order pol.	1.6
Converted central, high p_{Tt}	Exponential	0.3
Converted rest, low p_{Tt}	4th order pol.	4.6
Converted rest, high p_{Tt}	Exponential	0.5
Converted transition	Exp. of 2nd order pol.	3.2
2-jet	Exponential	0.4

Table 6.21: Systematic uncertainty on the number of signal events fitted due to the background parametrization, given in number of events for 4.8 fb^{-1} of $\sqrt{s} = 7$ TeV data. Three different background parametrizations are used depending on the category, an exponential function, a fourth-order Bernstein polynomial and the exponential of a second-order polynomial.

Category	σ_{CB}	FWHM	Window [GeV]	Observed	S	B	S/B
Inclusive	1.63	3.84	122.94 - 129.28	2653	71.5	2557.6	0.028
Unconverted central, low p_{Tt}	1.45	3.41	123.8 - 128.61	161	9.4	154.9	0.061
Unconverted central, high p_{Tt}	1.37	3.22	123.96 - 128.48	7	1.3	7.2	0.181
Unconverted rest, low p_{Tt}	1.57	3.71	123.36 - 128.85	700	19.5	669.7	0.029
Unconverted rest, high p_{Tt}	1.43	3.36	123.68 - 128.65	57	2.5	37.7	0.066
Converted central, low p_{Tt}	1.63	3.84	123.12 - 128.83	166	6	136.4	0.044
Converted central, high p_{Tt}	1.48	3.48	123.58 - 128.66	2	0.9	6.4	0.141
Converted rest, low p_{Tt}	1.79	4.23	122.53 - 129.43	986	18.9	967.3	0.02
Converted rest, high p_{Tt}	1.61	3.8	123.12 - 129.11	48	2.5	51.2	0.049
Converted transition	2.27	5.52	120.24 - 131.55	709	8.5	703.9	0.012
2-jet	1.52	3.59	123.26 - 129.03	12	2	8.7	0.23

Table 6.22: Number of fitted background events (using a background-only fit) (B) and the number of observed events (Observed) in a window containing 90% of the expected signal yields (S) around $M_H = 126.5$ GeV for $\sqrt{s} = 7$ TeV data. The values of the parameters characterizing the signal resolution function are given by σ_{CB} and FWHM. The numbers are given for the inclusive sample and the different categories.

The uncertainty on the invariant mass peak position is shown in Table 6.23. These are due to the uncertainty on the presampler scale (5% in the barrel, 10% in the EC) and to the material effects when extrapolating the electron energy scale to photons. The first column shows the impact of the multiple small uncertainties

generated specifically from the in-situ calibration method.

Category	Method [%]	Mat ($\|\eta\| < 1.8$ [%])	Mat ($\|\eta\| > 1.8$) [%]	PS Barrel [%]	PS EC [%]
Unconverted central, low p_{Tt}	±0.30	±0.30	0	±0.10	0
Unconverted central, high p_{Tt}	±0.30	±0.30	0	±0.10	0
Unconverted rest, low p_{Tt}	±0.30	±0.50	0.10	±0.20	0
Unconverted rest, high p_{Tt}	±0.30	±0.50	0.10	±0.30	0
Converted central, low p_{Tt}	±0.30	±0.10	0	0	0
Converted central, high p_{Tt}	±0.30	±0.10	0	0	0
Converted rest, low p_{Tt}	±0.30	±0.20	0.10	±0.10	0
Converted rest, high p_{Tt}	±0.30	±0.20	0.10	±0.10	0
Converted transition	±0.40	±0.60	0	0	±0.10
2-jet	±0.30	±0.30	0	±0.10	0

Table 6.23: Systematic uncertainties due to the energy scale effect on the invariant mass peak position [175].

The systematic uncertainties on the expected signal yields are summarized in the following, for more details see [174]:

- Luminosity: The uncertainty on the integrated luminosity has decreased to ±1.8%;
- Trigger: The uncertainty on the trigger efficiency is ±1% per event;
- Photon Identification: The uncertainty of the neural net photon identification is ±8.4% per event;
- Isolation cut efficiency: The difference of the isolation cut efficiency between data and MC for $Z \to e^+e^-$ events is taken as an uncertainty and found to be ±0.4%;
- Pileup: The impact of the pileup has been evaluated by comparing a sample with $< \mu > \; < \; 10$ and $< \mu > \; > \; 10$ and is found to be ±4%;
- Photon energy scale: the uncertainty on the photon energy scale leads to a ±0.3% uncertainty on the $H \to \gamma\gamma$ yield;
- Theory: The theoretical uncertainties on the BEH production cross section are taken per production process from [73, 77]. The uncertainty on the branching ratio is taken as ±5% per event.

Other systematic uncertainties on the expected signal yields are due to migration of signal events between categories:

- BEH kinematics: this uncertainty is estimated by varying the scales and PDFs used in HqT, it leads to an uncertainty on the population of the different categories: 1.1% in the low-p_T categories, 12.5% in the high-p_T categories and 9% in the 2-jet category;

- Pileup: The impact of the pileup on the population of the converted and unconverted categories is estimated by comparing a sample with $< \mu > \; < 10$ and $< \mu > \; > 10$. The difference in population between these two samples is found to be 3% for categories with unconverted photons, 2% for categories with converted photons and 2% for the 2-jet category;

- Material description: The fraction of events in the different categories has been compared between a nominal MC and a MC with a distorted geometry. The assigned systematic amounts to 4% for categories with unconverted photons and 3.5% for categories with converted photons;

- PV selection: The quantity $\sum p_T^2$ has been varied by an amount larger than the difference between data and MC: the effect on the signal yield is found to be less than 0.1% and it is therefore neglected;

- Jet energy scale and resolution: it is estimated by varying the jet energy scales within their uncertainties. The uncertainty is estimated for the different production processes and different categories, it is up to 19% in the 2-jet category and 4% otherwise. The effect on the expected signal yield of the uncertainty on the jet energy resolution was found to be negligible;

- Jet binning: The perturbative uncertainty on the gluon-gluon fusion contribution to the 2-jet category is treated independently from the total cross section uncertainty following the idea of I. Stewart and F. Tackmann [225]: it is found to be 25% [226] from the gluon-gluon fusion process in the 2-jet category by varying the renormalization and factorization scales in MCFM [227] between $M_H/2$ and $2M_H$;

- Underlying event: It is estimated by comparing different UE tunes in the simulation, it was taken as 30% in the 2-jet category for events produced by gluon-gluon fusion and 6% for those produced by VBF.

The systematic uncertainties on the mass resolution are briefly summarized in the following:

- Uncertainty on the constant term: It is taken conservatively equal to the one used in the previous analyses as ±12%;

- Electron to photon extrapolation: It is also taken as in the previous analyses as ±6%;

- Pileup: It is evaluated by comparing the FWHM of the signal peak for events with a $< \mu > \; < 10$ and others with $< \mu > \; > 10$ and it is was taken as ±4%;

- PV selection: The quantity $\sum p_T^2$ has been varied by an amount larger than the difference between data and MC: the effect on the resolution is found to be less than 0.2% and it is therefore neglected.

Table 6.24 shows a summary of all the considered systematic uncertainties on the expected signal yields, mass resolution, and from the background modeling. For more details, see [174].

6.4 Analysis of 2012 data

The analysis presented at the CERN seminar of July 4th 2012 [221] and later at ICHEP 2012 [174], published in [222], is based on the 2012 data taking, with a center-of-mass energy of 8 TeV and a total integrated luminosity of 5.9 fb^{-1}. The gluon-gluon fusion cross section increases by about 27% and the VBF cross section by about 31% going from $\sqrt{s} = 7$ TeV to $\sqrt{s} = 8$ TeV. The analysis strategy is the same as the one used for the improved 2011 analysis described above, since it was fixed before unblinding the data. However some of the selection cuts and systematics are different. I will summarize them briefly in the following:

- Trigger: the threshold on the transverse energy is raised from 20 to 35 GeV for the leading photon and to 25 GeV for the subleading photon;
- PV selection: The selection of the PV is done almost like for the 2011 re-analysis. However the conversion vertex is not used in the likelihood for the converted photons since there was a small bug in the 2012 final processed dataset. In addition, there is a small difference wrt to the PV selection between what was presented at ICHEP [174] and what was published afterwards in [222]. In [174], the error from the conversion vertex has been introduced in the likelihood biasing the selection of the PV. This was corrected for the paper [222] (see also [224]). Fig. 6.18 shows the comparison of the invariant mass distrubutions for different algorithms used to determine the longitudinal vertex position of the hard-scattering event. Fig. 6.19 shows the efficiency of finding a reconstructed primary vertex within 0.2 mm of the true hard interaction vertex as a function of the number of reconstructed vertices;
- Jet selection: the jet selection is described above however the cut on p_T^{jet} is raised from 25 to 30 GeV in the pseudorapidity range $2.5 < |\eta^{jet}| < 4.5$. 25% (1%) of the selected VBF (gluon-gluon fusion) events are classified into the $2 - jet$ category;
- Photon energy scale: the photon energy is corrected in data by a set of energy scales computed from the 2012 data as discussed in section 4.3;
- Photon Identification: a cut-based selection, tuned against pileup effects, is used (Tight2012);
- The dead FEBs have been repaired in 2012.

After this selection, 35251 diphoton candidates are observed in the invariant mass between 100 and 160 GeV. The expected signal efficiency and event yields are

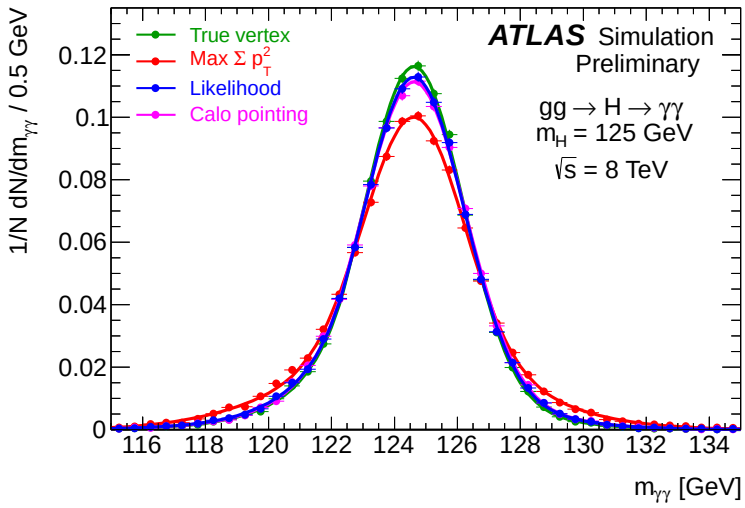

Figure 6.18: Distribution of the expected diphoton invariant mass for $H \to \gamma\gamma$ signal events as a function of the algorithm used to determine the longitudinal vertex position of the hard-scattering event. The use of the calorimeter information, labelled as "Calo pointing" is fully adequate to reach the optimal achievable mass resolution labelled as "True vertex". The likelihood, combining this information with the primary vertex information from the tracking, provides similar mass resolution [174].

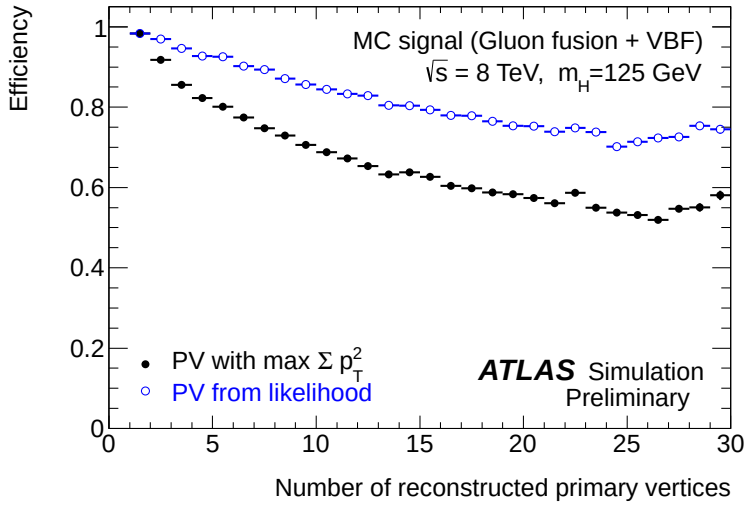

Figure 6.19: The dependence of the efficiency for selecting a reconstructed primary vertex within $\Delta z = 0.2$ mm of the true hard interaction vertex using two different methods: the highest $\sum p_T^2$ of all tracks assigned to a vertex (black) and from the likelihood method (blue) [174].

given in Table 6.25 for different production processes and normalized to 5.9 fb^{-1}. Table 6.26 shows the expected signal events per category, for $M_H = 126.5$ GeV. The percentage of events produced by $gg \to H$, VBF, WH, ZH and ttH are also given for each category.

The modeling for signal is the same as for previous analyses. The FWHM of the BEH mass distribution at $M_H = 126.5$ GeV in the inclusive sample is 3.88 GeV and it varies between the various categories from 3.24 ("Unconverted central, high p_{Tt}") to 6.10 ("Converted transition"). The robustness of the invariant mass resolution against pileup is shown in Fig. 6.20 for μ up to 20. The background modeling is the one used for the 2011 improved analysis. The corresponding systematic uncertainties are the ones listed in Table 6.21 rescaled by the ratio of luminosities (5.9/4.8) and by a factor of 1.2 to take into account the increasing background between 7 and 8 TeV. Table 6.27 summarizes the number of fitted background events (using a background-only fit) and the number of observed events in a window containing 90% of the expected signal yields around $M_H = 126.5$ GeV. It also gives the values of the parameters characterizing the signal resolution function: σ_{CB} and FWHM. The numbers are given for the inclusive sample and the different categories. The 2-jet category has the better ratio of S/B and the category "Unconverted central, high p_{Tt}" gives the best FWHM.

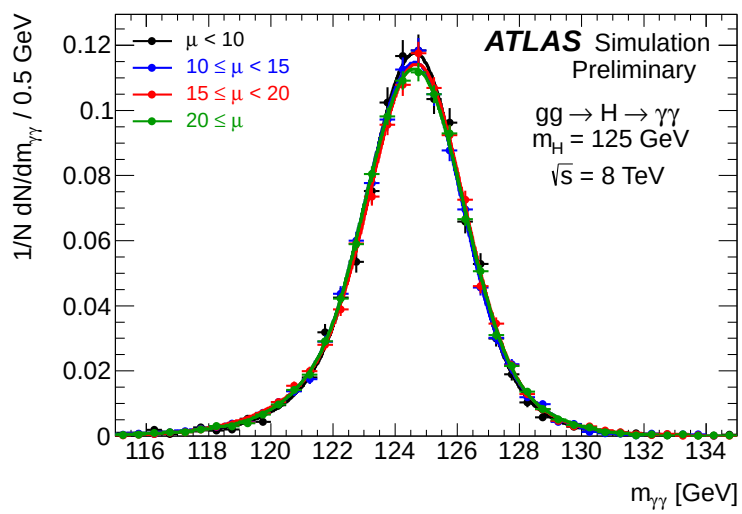

Figure 6.20: Stability of the invariant mass resolution with pileup [174].

The systematic uncertainties on the expected signal yields and the mass resolution are evaluated the same way as dicussed above for 2011 data. However, because of the larger pileup in 2012, the systematics due to pileup are estimated comparing samples with $<\mu> \; < 18$ and $<\mu> \; > 18$. An additional systematic on the expected signal yields is considered, it is due to the choice of the JVF and it

has an impact on the migration of events between categories. This was estimated comparing JVF efficiencies between data and MC on Z+2jets events. It was taken as 13% in the 2-jet category and as 0.3% otherwise.
Table 6.28 shows a summary of all the considered systematic uncertainties on the expected signal yields, mass resolution, and from the background modeling. When combining 2011 and 2012, the systematic uncertainties are treated as fully correlated except for the uncertainty on the luminosity.

6.5 Conclusion

In conclusion, the analysis used in the search of the $H \to \gamma\gamma$ has undergone major improvements during the data taking between 2010 and 2012. Several studies were made to improve the expected sensitivity to a potential BEH signal with a split of the dataset into categories, going from 5 categories at the time of EPS 2011 to 9 for Council 2011 and finally to 10 categories for ICHEP 2012. In addition, the higher statistics accumulated for ICHEP 2012 has lead to the introduction of the 2-jet category which has a VBF-like signature. Another important improvement was the neural-network based photon identification used for the analysis of the 2011 dataset and the tuned, against pileup, cut-based selection used for the analysis of the 2012 data. Many studies were done as well on the background modeling in order to have a good compromise between a better expected sensitivity and a less possible introduced bias. This was optimized using the full 2011 dataset and different analytic functions were used for ICHEP 2012 depending on the categories. The systematics studies on the signal yields and on the mass resolution were taken conservatively in all the published analyses. The PV selection based on the pointing and later on the combined likelihood has shown a very good robustness against pileup. Finally, the energy scales calibration has been evolving since 2010, finer bins are used and a better understanding is achieved for ICHEP 2012. These improvements (and others) in the analysis yield to a remarkable progress in the search for the $H \to \gamma\gamma$ through these years. These results will be the subject of the next chapter.

Source	Value [%]
Signal event yield	
Photon identification	± 8.4
Effect of pileup on photon rec/ID	± 4
Photon energy scale	± 0.3
Photon Isolation	± 0.4
Trigger	± 1
BEH boson cross section (perturbative)	$gg \to H$: $^{+12}_{-8}$, VBF: ± 0.3,
	WH: $^{+0.2}_{-0.8}$, ZH: $^{+1.4}_{-1.6}$, ttH: $^{+3}_{-9}$
	$gg \to H + 2$ jets: ± 25
BEH boson cross section (PDF+α_s)	$gg \to H$: $^{+8}_{-7}$, VBF: $^{+2.5}_{-2.1}$,
	VH: ± 3.5, ttH: ± 9
BEH boson branching ratio	± 5
BEH boson p_T modeling	low p_{Tt}: ± 1.1, high p_{Tt}: ∓ 12.5, 2-jets: ∓ 9
Underlying Event (2-jet)	VBF: ± 6, Others: ± 30
Luminosity	± 1.8
Signal category migration	
Material	Unconv: ± 4, Conv: ∓ 3.5
Effect of pileup on photon rec/ID	Unconv: ± 3, Conv: ∓ 2,
	2-jets: ± 2
Jet energy scale	low p_{Tt}
	$gg \to H$: ± 0.1, VBF: ± 2.6,
	Others: ± 0.1
	high p_{Tt}
	$gg \to H$: ± 0.1, VBF: ± 4,
	Others: ± 0.1
	2-jets
	$gg \to H$: ∓ 19, VBF: ∓ 8,
	Others: ∓ 15
Jet-vertex-fraction	-
Primary vertex selection	negligible
Signal mass resolution	
Calorimeter energy resolution	± 12
Electron to photon extrapolation	± 6
Effect of pileup on energy resolution	± 4
Primary vertex selection	negligible
Signal mass position	
Photon energy scale	see Table 6.23
Background modeling	see Table 6.21

Table 6.24: Summary of systematic uncertainties on the expected signal and the invariant mass resolution used for the analysis of $\sqrt{s} = 7$ TeV data. The values given are the relative uncertainties on these quantities from the various sources investigated for a BEH boson mass of 125 GeV, except for the case of background modeling, where the uncertainties are provided in Table 6.21 in terms of the number of events. The sign in the front of values for each systematic uncertainty shows correlations among categories and processes.

M_H [GeV]	$gg \to H$		VBF		WH		ZH		ttH		Total
	ε(%)	N_{evt}	ε(%)	N_{evt}	ε(%)	N_{evt}	ε(%)	N_{evt}	ε(%)	N_{evt}	N_{evt}
110	33.7	100.3	34.4	7.3	29.8	3.7	29.4	2.1	27.2	0.6	114.0
115	35.5	103.5	36.1	7.9	30.5	3.6	32.3	2.0	27.8	0.6	117.6
120	37.1	103.3	38.0	8.2	32.5	3.4	32.8	2.0	29.3	0.6	117.4
125	38.2	100.0	39.5	8.2	33.8	3.1	34.1	1.8	29.7	0.5	113.7
130	39.0	93.8	41.1	8.0	35.1	2.8	35.8	1.6	31.0	0.5	106.7
135	40.4	84.9	42.2	7.5	35.6	2.4	36.6	1.4	32.1	0.4	96.7
140	40.9	73.7	42.9	6.8	36.8	1.2	36.7	1.2	32.3	0.3	84.0
145	41.5	60.4	43.2	5.7	37.8	1.6	38.3	0.9	33.5	0.3	68.8
150	41.6	45.1	44.6	4.4	38.1	1.1	39.0	0.7	34.0	0.2	51.6

Table 6.25: Expected BEH boson signal efficiency and event yield assuming a luminosity of 5.9 fb^{-1} for the $\sqrt{s} = 8$ TeV data. Results are given for different production processes.

Category	N_{evt}	$gg \to H$ [%]	VBF [%]	WH [%]	ZH [%]	ttH [%]
Inclusive	111.9	87.9	7.3	2.7	1.6	0.5
Unconverted central, low p_{Tt}	14.2	94.0	4.3	1.7	1.0	0.3
Unconverted central, high p_{Tt}	2.5	73.5	14.3	7.0	4.3	2.4
Unconverted rest, low p_{Tt}	30.9	93.7	4.2	2.0	1.1	0.2
Unconverted rest, high p_{Tt}	5.2	72.9	14.0	7.9	4.7	1.7
Converted central, low p_{Tt}	8.9	94.0	4.3	1.7	1.0	0.3
Converted central, high p_{Tt}	1.6	73.8	13.6	7.2	4.2	2.3
Converted rest, low p_{Tt}	26.9	93.8	4.2	2.0	1.1	0.2
Converted rest, high p_{Tt}	4.5	72.1	14.1	8.5	4.8	1.8
Converted transition	12.8	90.1	5.9	3.1	1.8	0.4
2-jet	3.0	30.8	69.3	0.4	0.2	0.2

Table 6.26: Number of expected signal events for $\sqrt{s} = 8$ TeV obtained from simulation with $M_H = 126.5$ GeV. The numbers are normalized for 5.9 fb^{-1}. The percentage of events in each production process is also given.

Category	σ_{CB}	FWHM	Window [GeV]	Observed	S	B	S/B
Inclusive	1.64	3.88	123.14 - 129.12	3649	100.7	3584.8	0.028
Unconverted central, low p_{Tt}	1.46	3.44	123.78 - 128.68	237	12.7	224.7	0.057
Unconverted central, high p_{Tt}	1.37	3.24	123.98 - 128.59	16	2.3	13.6	0.169
Unconverted rest, low p_{Tt}	1.58	3.73	123.42 - 128.8	1141	27.8	1122.5	0.025
Unconverted rest, high p_{Tt}	1.52	3.57	123.66 - 128.76	75	4.7	68.3	0.069
Converted central, low p_{Tt}	1.64	3.86	123.16 - 128.95	207	8	186.6	0.043
Converted central, high p_{Tt}	1.5	3.53	123.61 - 128.74	13	1.5	9.7	0.155
Converted rest, low p_{Tt}	1.89	4.45	122.57 - 129.36	1311	24.2	1299.9	0.019
Converted rest, high p_{Tt}	1.65	3.9	123.18 - 129.09	71	4	71.3	0.056
Converted transition	2.59	6.1	121.36 - 130.88	849	11.5	821.2	0.014
2-jet	1.59	3.74	123.38 - 129.01	19	2.7	13.3	0.203

Table 6.27: Number of fitted background events (using a background-only fit) (B) and the number of observed events (Observed) in a window containing 90% of the expected signal yields (S) around $M_H = 126.5$ GeV for $\sqrt{s} = 8$ TeV data. The values of the parameters characterizing the signal resolution function are given by σ_{CB} and FWHM. The numbers are given for the inclusive sample and the different categories.

Source	Value [%]
Signal event yield	
Photon identification	± 10.8
Effect of pileup on photon rec/ID	± 4
Photon energy scale	± 0.3
Photon Isolation	± 0.5
Trigger	± 1
BEH boson cross section (perturbative)	$gg \to H$: $^{+7}_{-8}$, VBF: ± 0.2, WH: $^{+0.2}_{-0.6}$, ZH: $^{+1.6}_{-1.5}$, ttH: $^{+4}_{-9}$ $gg \to H + 2$ jets: ± 25
BEH boson cross section (PDF+α_s)	$gg \to H$: $^{+8}_{-7}$, VBF: $^{+2.6}_{-2.8}$, VH: ± 3.5, ttH: ± 8
BEH boson branching ratio	± 5
BEH boson p_T modeling	low p_{Tt}: ± 1.1, high p_{Tt}: ∓ 12.5, 2-jet: ∓ 9
Underlying Event (2-jet)	VBF: ± 6, Others: ± 30
Luminosity	± 3.6
Signal category migration	
Material	Unconv: ± 4, Conv: ∓ 3.5
Effect of pileup on photon rec/ID	Unconv: ± 2, Conv: ∓ 2, 2-jet: ± 12
Jet energy scale	low p_{Tt} $gg \to H$: ± 0.1, VBF: ± 2.3, Others: ± 0.1 high p_{Tt} $gg \to H$: ± 0.1, VBF: ± 4, Others: ± 0.1 2-jet $gg \to H$: ∓ 18, VBF: ∓ 9, Others: ∓ 13
Jet-vertex-fraction	2-jet: ± 12, Others:∓ 0.3
Primary vertex selection	negligible
Signal mass resolution	
Calorimeter energy resolution	± 12
Electron to photon extrapolation	± 6
Effect of pileup on energy resolution	± 4
Primary vertex selection	negligible
Signal mass position	
Photon energy scale	see Table 6.23
Background modeling	see Table 6.21 ($\times(5.9/4.8) \times 1.2$)

Table 6.28: Summary of systematic uncertainties on the expected signal yields and invariant mass resolution for the analysis of $\sqrt{s} = 8$ TeV data. The values given are the relative uncertainties on these quantities from the various sources investigated for a BEH boson mass of 125 GeV, except for the case of background modeling, where the uncertainties are provided in Table 6.21 in terms of the number of events (to be rescaled by the quoted ratio). The sign in the front of values for each systematic uncertainty shows correlations among categories and processes.

Chapter 7

Observation of a BEH-like particle

Contents

7.1 Evolution of the $H \to \gamma\gamma$ search 173

7.2 BEH-like particle decaying to a pair of photons 178

7.2.1 Statistical procedure 178

7.2.2 Background modeling 184

7.2.3 Observation Results 185

7.3 BEH-like particle in the combined channels 198

During the seminar on July 4th 2012, CERN has announced the discovery of a new particle that is compatible with the production and decay of the long-searched SM BEH boson. The discovery of this new particle within the ATLAS detector was based on the analysis of the full 2011 dataset, corresponding to an integrated luminosity of 4.8 fb^{-1} with $\sqrt{s} = 7$ TeV, and a dataset collected in 2012, with an integrated luminosity of 5.9 fb^{-1} with $\sqrt{s} = 8$ TeV [222]. This analysis combined individual searches in the channels $H \to \gamma\gamma$, $H \to ZZ^{(*)} \to 4l$ and $H \to WW^{(*)} \to e\nu\mu\nu$ from $\sqrt{s} = 8$ TeV data; previously published results of searches in the channels $H \to ZZ^{(*)}$, $WW^{(*)}$, $b\bar{b}$ and $\tau^+\tau^-$ for the 7 TeV data; and the improved analyses of the $H \to \gamma\gamma$ and $H \to ZZ^{(*)} \to 4l$ for the 7 TeV data. The results show an excess of events with a significance of 5.9σ and provide a conclusive evidence for the discovery of a new particle with a mass of 126.0 $\pm$0.4 (stat) $\pm$0.4 (sys) GeV. This excess is driven by the two channels with the highest mass resolution $H \to \gamma\gamma$ and $H \to ZZ^{(*)} \to 4l$, and the equally sensitive but low-resolution channel $H \to WW^{(*)} \to l\nu l\nu$.

In the following chapter, I will focus on the observation of the new particle in the search for $H \to \gamma\gamma$. First, I will recall the path of previously published results based on the analysis of 2010 and 2011 data. In the second part, I will present the latest $H \to \gamma\gamma$ results and finally the results for the combined channels.

7.1 Evolution of the $H \to \gamma\gamma$ search

At the time of Aspen 2011, the thoughts were oriented towards a projection into a 1 fb^{-1} of data. Fig. 7.1 shows the exclusion sensitivity as a function of the BEH mass for 1 fb^{-1} based on the analysis described in section 6.1.1. No systematic uncertainties on the signal yields or mass resolution are included in the likelihood.

The normalization and the shape of the background are considered as the only nuisance parameters. The CL_{s+b} method was used to set these exclusion limits. The dashed line shows the deterioration of the sensitivity if one smears the photon energy to take into account very pessimistic uncertainties on the constant term. The expected sensitivity ranges between 3.2 and 4.2 times the SM cross section in the $110 - 140$ GeV mass range.

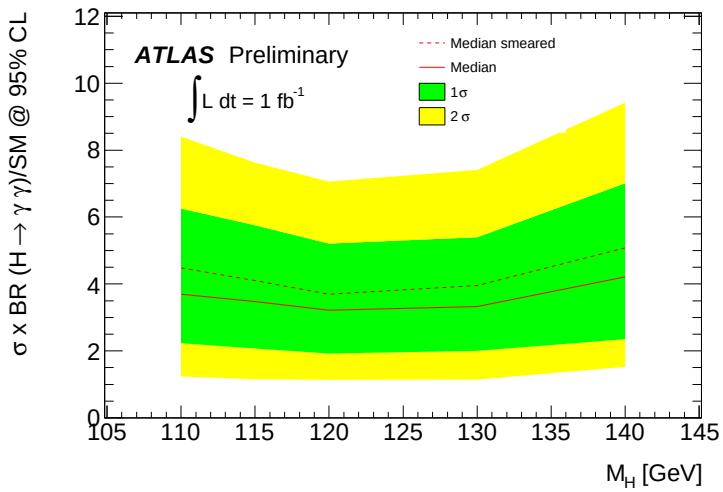

Figure 7.1: The estimated limit, using the CL_{s+b} method, on the SM signal cross section at 95% C.L. as a function of the BEH mass by projecting to 1 fb^{-1}. The dashed curve corresponds to the exclusion after degrading the photon energy resolution with pessimistic assumptions on the constant term. The green (yellow) bands correspond to the expected exclusion in the case of a 1σ (2σ) fluctuation of the background.

In Moriond 2011, observed exclusion limits were published for the first time based on the analysis of the full 2010 dataset corresponding to an integrated luminosity of 38 pb^{-1}. Fig. 7.2 shows the upper bound on the exclusion limit at the 95% C.L., in units of the SM BEH boson cross section, as a function of the BEH mass. The statistical method shown here is the CL_s, although the baseline at that time up to PLHC was the PCL method (modified CL_{s+b}). In the mass range $110 < M_H < 140$ GeV, the expected upper limit is about 25 times the SM cross section. The observed exclusions range from ~ 15 times the SM prediction at 127 GeV to ~ 40 times at 116 GeV. The systematic uncertainties are taken into account and degrade the exclusion limit by about 10%.

The first analysis of the 2011 dataset was published at PLHC 2011 using a dataset with an integrated luminosity of 209 pb^{-1}. Fig. 7.3 shows the exclusion limits, using the CL_s method, in units of SM signal cross section, as a function of the BEH mass. The expected exclusion limits at 95% C.L. range between 7 to 8 times the SM cross section in the mass range $110 - 140$ GeV. The observed excluded cross section ranges between 6 and 16 times the SM cross section. A slight excess

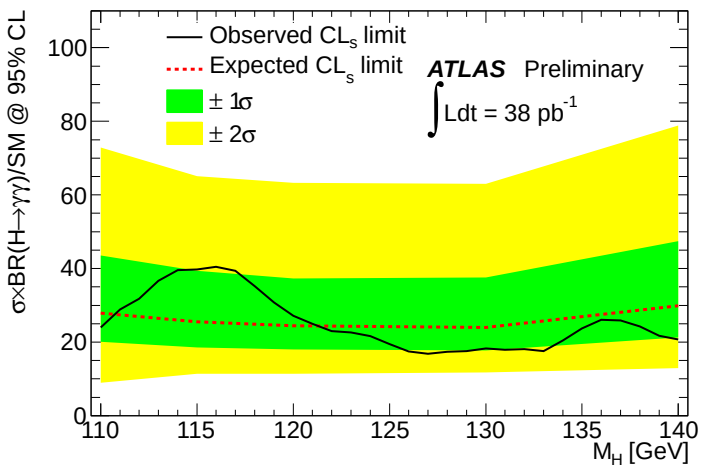

Figure 7.2: Exclusion limits, using the CL_s method, on the production cross section relative to the SM cross section as a function of the BEH mass hypothesis corresponding to the analysis of 38 pb^{-1} of 2010 data.

was observed at 127 GeV corresponding to a 2% p-value ($1-CL_b$) i.e $\sim 2\sigma$, while the expected significance was of the order of 0.3σ. The probability for such an excess to occur anywhere in the $110-140$ GeV mass range was estimated to be approximately 30%.

At the time of EPS 2011, the analysis of 2011 data with an integrated luminosity of 1.08 fb^{-1} was performed. Fig. 7.4 shows the expected and observed exclusion limits as a function of the BEH mass hypothesis using the CL_s method. The expected median limit in the case of no signal varies from 3.3 to 5.8 as a function of the BEH boson mass. The variations of the observed limit between 2.0 and 5.8, are consistent with expected statistical fluctuations around the median limit. A small excess is observed around 128 GeV corresponding to a p-value (p_0) of $\sim 5\%$ i.e $\sim 1.65\sigma$ while the expected significance was about 0.65σ. The probability of such an excess to appear anywhere in the investigated mass range of $110-150$ GeV is around 40%.

At the time of Council 2011, the picture becomes clearer. The results of the analysis corresponding to the full 2011 dataset with an integrated luminosity of 4.9 fb^{-1} are shown in Fig. 7.5. The median expected upper limits on the SM BEH boson production cross section in the absence of a signal, at 95% C.L., vary between 1.6 and 2.7 times the SM cross section in the mass range $110-150$ GeV. The observed 95% C.L. upper limit on the cross section relative to the SM cross section is between 0.86 and 3.6 over the full mass range. A SM BEH boson is excluded at 95% C.L. in the mass ranges of $113-115$ GeV and $134.5-136$ GeV. Fig. 7.6 shows the probability of the background-only hypothesis, p_0, used to quantify discovery significance. Before considering the energy scale uncertainty on the mass peak position, the minimun

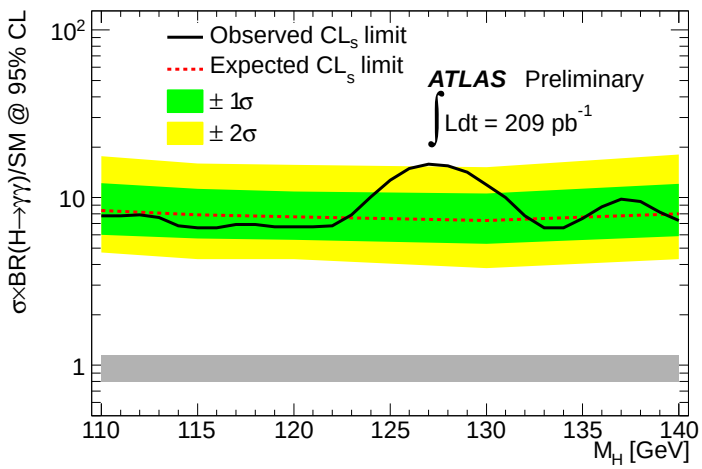

Figure 7.3: Exclusion limits, using the CL_s method, on the production cross section relative to the SM cross section as a function of the BEH mass hypothesis. The band around 1 shows the theoretical uncertainty on the predicted SM cross section. These results correspond to the analysis of a 2011 dataset with an integrated luminosity of 209 pb^{-1} [206].

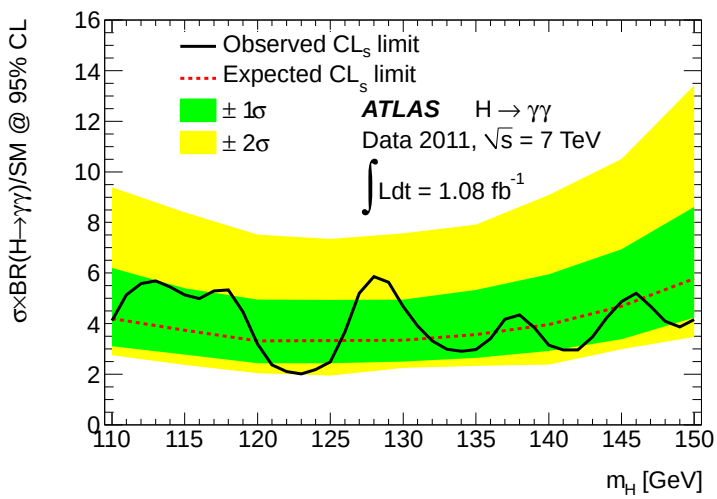

Figure 7.4: 95% C.L. upper limits on a SM BEH boson production cross section as a function of the BEH boson mass hypothesis for the analysis of a 2011 dataset with an integrated luminosity of 1.08 fb^{-1} [211].

local p_0 is obtained at 126.5 GeV corresponding to a local significance of 2.9σ. When this uncertainty is taken into account using pseudo-experiments, the local significance at 126.5 GeV becomes 2.8σ. When considering the look-elsewhere effect

for the mass range $110 - 150$ GeV, this significance becomes 1.5σ. These results provide an indication of a new particle around a mass of 126.5 GeV.

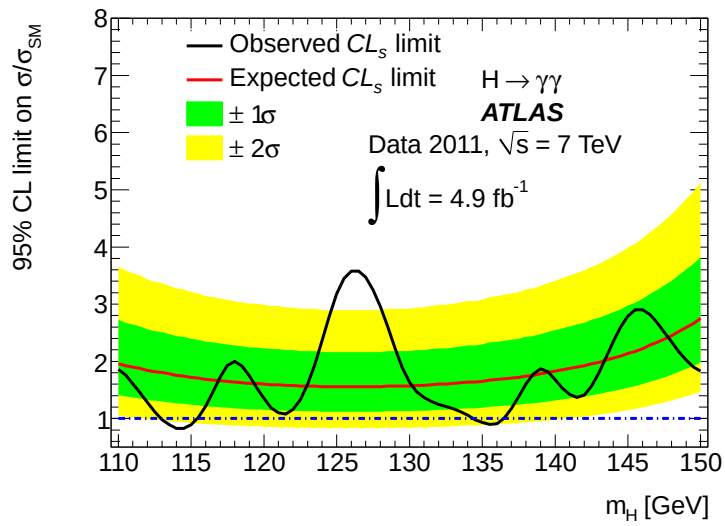

Figure 7.5: Observed and expected 95% C.L. exclusion limits on the SM BEH boson production cross section normalized to the predicted cross section as a function of the BEH mass. These results correspond to the analysis of the full 2011 dataset with an integrated luminosity of 4.9 fb^{-1} [173].

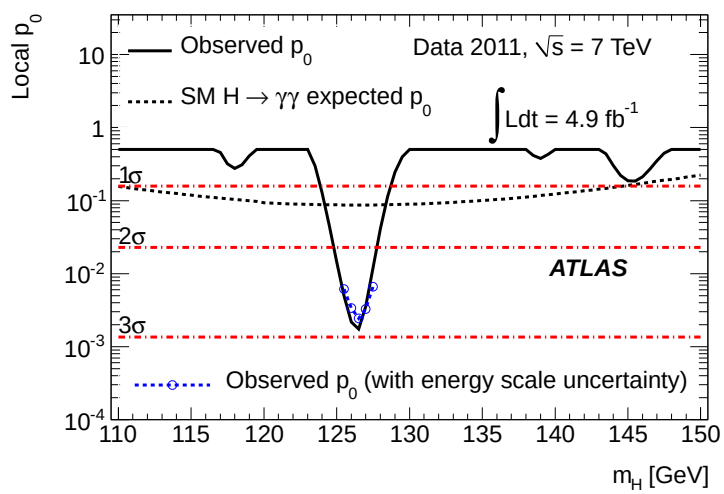

Figure 7.6: The observed and the expected local p_0 as a function of the BEH mass. The open points indicate the observed local p_0 values computed using pseudo-experiments when energy scale uncertainties are taken into account [173].

7.2 BEH-like particle decaying to a pair of photons

The picture has been completed at the time of ICHEP 2012, when the analysis combined the 2012 dataset corresponding to an integrated luminosity of 5.9 fb^{-1} and the full 2011 dataset. The analyses were described separately in sections 6.3 and 6.4.
The invariant mass distribution of the combined 2011 and 2012 datasets summed overall the categories is shown in Fig. 7.7 for the mass range $100 - 160$ GeV (The plots per year and per category can be found in the appendix). The result of a signal+ background (S+B) fit is superimposed. The signal component is fixed to $M_H = 126.5$ GeV and the background component (dashed line) is described by a fourth-order Bernstein polynomial. In order to quantify the significance of the visible excess, a statistical procedure is needed. This is described in the following.

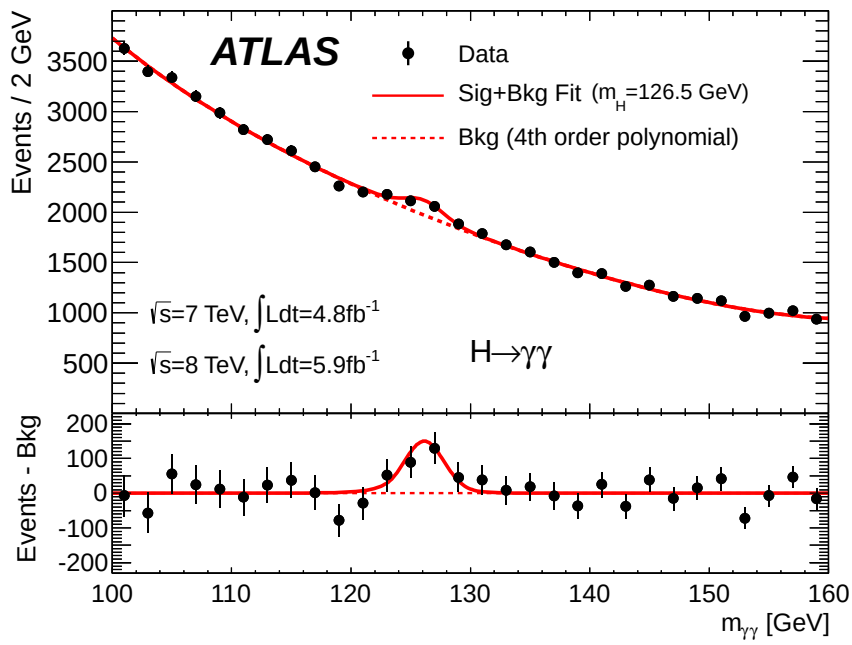

Figure 7.7: The diphoton invariant mass distribution for the combined 7 and 8 TeV data inclusive samples. The result of a fit to the data, including a signal component fixed to $M_H = 126.5$ GeV and a background component (dashed line) described by a fourth-order Bernstein polynomial, is superimposed. The residuals of the data with respect to the fitted background component is displayed in the bottom inset [222].

7.2.1 Statistical procedure

The statistical analysis of the data is based on an unbinned maximum likelihood using the diphoton mass $M_{\gamma\gamma}$ as a single dependent variable. The test statistic used is the profile likelihood ratio. The parameter of interest is the overall

signal strength factor μ. The nuisance parameters include the background contribution and the systematic uncertainties. Furthermore, the different categories are treated independently, a simultaneous fit is then performed to extract the results.

The full likelihood is therefore written as:

$$L\left(\mu, \boldsymbol{\theta}\right) = \prod_{c=1}^{n_{cat}} L_c(\mu, \boldsymbol{\theta}_c) \tag{7.1}$$

where n_{cat} is the number of categories and $\boldsymbol{\theta}_c$ are the nuisance parameters used to describe the model in category c. L_c is the likelihood for category c given by:

$$L_c(\mu, \boldsymbol{\theta}_c) = e^{-(\mu N_{\mathrm{sig,c}} + N_{\mathrm{bkg,c}})} \prod_{k=1}^{N_c} \mathcal{L}_c(M_{\gamma\gamma}(k); \mu, \boldsymbol{\theta}_c) \tag{7.2}$$

where $N_{\mathrm{sig,c}}$ and $N_{\mathrm{bkg,c}}$ are the fitted numbers of signal and background events in category c and N_c is the total number of events in category c. The index k runs over the events, and $M_{\gamma\gamma}(k)$ is the invariant mass value for event k. $\mathcal{L}_c$ is the per-event likelihood given by:

$$\mathcal{L}_c(M_{\gamma\gamma}; \mu, \boldsymbol{\theta}_c) = N_{\mathrm{sig,c}}(\mu, \boldsymbol{\theta}_c^{\mathrm{norm}})\, f_{\mathrm{sig,c}}(M_{\gamma\gamma}; \boldsymbol{\theta}_c^{\mathrm{shape}}) + N_{\mathrm{bkg,c}}\, f_{\mathrm{bkg,c}}(M_{\gamma\gamma}; \boldsymbol{\theta}_c^{\mathrm{bkg}}) \tag{7.3}$$

with $f_{\mathrm{sig,c}}$ and $f_{\mathrm{bkg,c}}$ the signal and background probability density functions (PDFs) for category c; and $\boldsymbol{\theta}_c^{\mathrm{norm}}$, $\boldsymbol{\theta}_c^{\mathrm{shape}}$ and $\boldsymbol{\theta}_c^{\mathrm{bkg}}$ are the nuisance parameters associated to the signal normalization, the signal shape and the background parametrization. $\boldsymbol{\theta}_c$ is therefore $\boldsymbol{\theta}_c^{\mathrm{norm}} \cup \boldsymbol{\theta}_c^{\mathrm{shape}} \cup \boldsymbol{\theta}_c^{\mathrm{bkg}} \cup \{N_{bkg,c}\}$.
In the following, I will define first the terms of the likelihood for the 2011 analysis, then I will recall the differences for the 2012 analysis.

The signal normalization can be written as:

$$\begin{aligned}
N_{\mathrm{sig,c}}\left(\mu, \boldsymbol{\theta}_c^{\mathrm{norm}}\right) &= \mu \left[N_c^{\mathrm{ggH}}(\boldsymbol{\theta}^{\mathrm{ggH}}) + N_c^{\mathrm{VBF}}(\boldsymbol{\theta}^{\mathrm{VBF}}) + N_c^{\mathrm{WH}}(\boldsymbol{\theta}^{\mathrm{WH}}) + N_c^{\mathrm{ZH}}(\boldsymbol{\theta}^{\mathrm{ZH}}) + N_c^{\mathrm{t\bar{t}H}}(\boldsymbol{\theta}^{\mathrm{t\bar{t}H}})\right] \\
&\times \exp\left(\sqrt{\log(1+\sigma_{\mathrm{BR}}^2)}\,\theta_{\mathrm{BR}}\right) \exp\left(\sqrt{\log(1+\sigma_{\mathrm{lumi}}^2)}\theta_{\mathrm{lumi}}\right) \\
&\quad \exp\left(\sqrt{\log(1+\sigma_{\mathrm{eff}}^2)}\,\theta_{\mathrm{eff}}\right) \exp\left(\sqrt{\log(1+\sigma_{\mathrm{iso}}^2)}\theta_{\mathrm{iso}}\right) \\
&\quad \exp\left(\sqrt{\log(1+\sigma_{\mathrm{pileup}}^2)}\theta_{\mathrm{pileup}}\right) (1+\sigma_{\mathrm{pileup_mig,c}}\,\theta_{\mathrm{pileup}}) \\
&\quad (1+\sigma_{\mathrm{mat_mig,c}}\,\theta_{\mathrm{mat_mig}}) \exp\left(\sqrt{\log(1+\sigma_{\mathrm{PES}}^2)}\,\theta_{\mathrm{PES}}\right) \\
&+ \sigma_{\mathrm{SS,c}}\,\theta_{\mathrm{SS,c}}
\end{aligned}$$

with

$$
\begin{aligned}
N_c^{\mathrm{ggH}}\left(\boldsymbol{\theta}^{\mathrm{ggH}}\right) &= N_c^{\mathrm{ggH,SM}} \exp\left(\sqrt{\log(1+\sigma^2_{\mathrm{ggH\,scale}})}\,\theta_{\mathrm{ggH\,scale}}\right)\,(1+\sigma_{\mathrm{gg\,PDF_ggH}}\,\theta_{\mathrm{gg\,PDF}}) \\
&\quad (1+\sigma_{p_T^{\mathrm{model}},c}\,\theta_{p_T^{\mathrm{model}}})\,(1+\sigma_{\mathrm{ggH\,JES_mig,c}}\,\theta_{\mathrm{JES_mig}}) \\
N_c^{\mathrm{VBF}}\left(\boldsymbol{\theta}^{\mathrm{VBF}}\right) &= N_c^{\mathrm{VBF,SM}} \exp\left(\sqrt{\log(1+\sigma^2_{\mathrm{VBF\,scale}})}\,\theta_{\mathrm{VBF\,scale}}\right)\,(1+\sigma_{\mathrm{q\bar{q}\,PDF_VBF}}\,\theta_{\mathrm{q\bar{q}\,PDF}}) \\
&\quad (1+\sigma_{\mathrm{VBF\,JES_mig,c}}\,\theta_{\mathrm{JES_mig}}) \\
N_c^{\mathrm{WH}}\left(\boldsymbol{\theta}^{\mathrm{WH}}\right) &= N_c^{\mathrm{WH,SM}} \exp\left(\sqrt{\log(1+\sigma^2_{\mathrm{WH\,scale}})}\,\theta_{\mathrm{VH\,scale}}\right)\,(1+\sigma_{\mathrm{q\bar{q}\,PDF_WH}}\,\theta_{\mathrm{q\bar{q}\,PDF}}) \\
&\quad (1+\sigma_{\mathrm{XH\,JES_mig,c}}\,\theta_{\mathrm{JES_mig}}) \\
N_c^{\mathrm{ZH}}\left(\boldsymbol{\theta}^{\mathrm{ZH}}\right) &= N_c^{\mathrm{ZH,SM}} \exp\left(\sqrt{\log(1+\sigma^2_{\mathrm{ZH\,scale}})}\,\theta_{\mathrm{VH\,scale}}\right)\,(1+\sigma_{\mathrm{q\bar{q}\,PDF_ZH}}\,\theta_{\mathrm{q\bar{q}\,PDF}}) \\
&\quad (1+\sigma_{\mathrm{XH\,JES_mig,c}}\,\theta_{\mathrm{JES_mig}}) \\
N_c^{\mathrm{t\bar{t}H}}\left(\boldsymbol{\theta}^{\mathrm{t\bar{t}H}}\right) &= N_c^{\mathrm{t\bar{t}H,SM}} \exp\left(\sqrt{\log(1+\sigma^2_{\mathrm{t\bar{t}H\,scale}})}\,\theta_{\mathrm{t\bar{t}H\,scale}}\right)\,(1+\sigma_{\mathrm{gg\,PDF_t\bar{t}H}}\,\theta_{\mathrm{gg\,PDF}}) \\
&\quad (1+\sigma_{\mathrm{XH\,JES_mig,c}}\,\theta_{\mathrm{JES_mig}})
\end{aligned}
$$

for categories $c = 1...9$, and

$$
\begin{aligned}
N_{2-\mathrm{jet}}^{\mathrm{ggH}}\left(\boldsymbol{\theta}^{\mathrm{ggH}}\right) &= N_{2-\mathrm{jet}}^{\mathrm{ggH,SM}} \exp\left(\sqrt{\log(1+\sigma^2_{\mathrm{ggH,\,2-jet}})}\,\theta_{\mathrm{ggH,\,2-jet}}\right) \\
&\quad (1+\sigma_{\mathrm{gg\,PDF_ggH}}\,\theta_{\mathrm{gg\,PDF}})\,\exp\left(\sqrt{\log(1+\sigma^2_{\mathrm{XH\,UE}})}\,\theta_{\mathrm{UE}}\right) \\
&\quad (1+\sigma_{p_T^{\mathrm{model}},\,2-\mathrm{jet}}\,\theta_{p_T^{\mathrm{model}}})\,(1+\sigma_{\mathrm{ggH\,JES_mig}}\,\theta_{\mathrm{JES_mig}}) \\
N_{2-\mathrm{jet}}^{\mathrm{VBF}}\left(\boldsymbol{\theta}^{\mathrm{VBF}}\right) &= N_{2-\mathrm{jet}}^{\mathrm{VBF,SM}} \exp\left(\sqrt{\log(1+\sigma^2_{\mathrm{VBF\,scale}})}\,\theta_{\mathrm{VBF\,scale}}\right) \\
&\quad (1+\sigma_{\mathrm{q\bar{q}\,PDF_VBF}}\,\theta_{\mathrm{q\bar{q}\,PDF}})\,\exp\left(\sqrt{\log(1+\sigma^2_{\mathrm{VBF\,UE}})}\,\theta_{\mathrm{UE}}\right) \\
&\quad (1+\sigma_{\mathrm{VBF\,JES_mig}}\,\theta_{\mathrm{JES_mig}}) \\
N_{2-\mathrm{jet}}^{\mathrm{WH}}\left(\boldsymbol{\theta}^{\mathrm{WH}}\right) &= N_{2-\mathrm{jet}}^{\mathrm{WH,SM}} \exp\left(\sqrt{\log(1+\sigma^2_{\mathrm{WH\,scale}})}\,\theta_{\mathrm{VH\,scale}}\right) \\
&\quad (1+\sigma_{\mathrm{q\bar{q}\,PDF_WH}}\,\theta_{\mathrm{q\bar{q}\,PDF}})\,\exp\left(\sqrt{\log(1+\sigma^2_{\mathrm{XH\,UE}})}\,\theta_{\mathrm{UE}}\right) \\
&\quad (1+\sigma_{\mathrm{XH\,JES_mig}}\,\theta_{\mathrm{JES_mig}}) \\
N_{2-\mathrm{jet}}^{\mathrm{ZH}}\left(\boldsymbol{\theta}^{\mathrm{ZH}}\right) &= N_{2-\mathrm{jet}}^{\mathrm{ZH,SM}} \exp\left(\sqrt{\log(1+\sigma^2_{\mathrm{ZH\,scale}})}\,\theta_{\mathrm{VH\,scale}}\right) \\
&\quad (1+\sigma_{\mathrm{q\bar{q}\,PDF_ZH}}\,\theta_{\mathrm{q\bar{q}\,PDF}})\,\exp\left(\sqrt{\log(1+\sigma^2_{\mathrm{XH\,UE}})}\,\theta_{\mathrm{UE}}\right) \\
&\quad (1+\sigma_{\mathrm{XH\,JES_mig}}\,\theta_{\mathrm{JES_mig}})
\end{aligned}
$$

$$
\begin{aligned}
N_{2-\mathrm{jet}}^{\mathrm{t\bar{t}H}}\left(\boldsymbol{\theta}^{\mathrm{t\bar{t}H}}\right) &= N_{2-\mathrm{jet}}^{\mathrm{t\bar{t}H,SM}} \exp\left(\sqrt{\log(1+\sigma^2_{\mathrm{t\bar{t}H\,scale}})}\,\theta_{\mathrm{t\bar{t}H\,scale}}\right) \\
&\quad (1+\sigma_{\mathrm{gg\,PDF_t\bar{t}H}}\,\theta_{\mathrm{gg\,PDF}})\ \exp\left(\sqrt{\log(1+\sigma^2_{\mathrm{XH\,UE}})}\,\theta_{\mathrm{UE}}\right) \\
&\quad (1+\sigma_{\mathrm{XH\,JES_mig}}\,\theta_{\mathrm{JES_mig}})
\end{aligned}
$$

for the 2-jet category ($c = 10$).

$N_c^{X,SM}$ are the expected number of events in the SM for production process X in category c (given in Table 6.19 for 7 TeV data and in Table 6.25 for 8 TeV data), σ accounts for the values of the systematic uncertainties (given in Table 6.24 for 7 TeV data and in Table 6.28 for 8 TeV data) and θ represents the corresponding nuisance parameter. The systematic uncertainties follow a gaussian $(1+\sigma\theta)$ or a log normal $\exp\left(\sqrt{\log(1+\sigma^2)}\theta\right)$ depending on their sources. If the systematic uncertainty represents an effect on the expected signal yield, a log normal is used to avoid negative tails and if it represents a migration between categories it is modelized by a gaussian.

In the following, I recall briefly the meaning of these uncertainties:

- σ_{BR}: uncertainty on the $H \to \gamma\gamma$ branching ratio (1 nuisance parameter $\boldsymbol{\theta}_{\mathrm{BR}}$);
- σ_{lumi}: uncertainty on the integrated luminosity (1 nuisance parameter $\boldsymbol{\theta}_{\mathrm{lumi}}$);
- σ_{eff}: uncertainty on the signal efficiency, including trigger efficiency (1 nuisance parameter $\boldsymbol{\theta}_{\mathrm{eff}}$);
- σ_{iso}: uncertainty on the efficiency of the isolation cut (1 nuisance parameter $\boldsymbol{\theta}_{\mathrm{iso}}$);
- σ_{pileup}: uncertainty due to pileup effect on the signal yields (1 nuisance parameter $\boldsymbol{\theta}_{\mathrm{pileup}}$);
- $\sigma_{\mathrm{pileup_mig,c}}$: uncertainty due to pileup effect on the migration of events between categories, it takes different values depending on the category (the same nuisance parameter $\boldsymbol{\theta}_{\mathrm{pileup}}$);
- $\sigma_{\mathrm{mat_mig,c}}$: uncertainty due to the amount of material in front of the calorimeter on the migration between different categories, it is not applied in the 2-jet category (1 nuisance parameter $\boldsymbol{\theta}_{\mathrm{mat_mig}}$);
- σ_{PES}: uncertainty due the photon energy scale on the expected signal yields (1 nuisance parameter $\boldsymbol{\theta}_{\mathrm{PES}}$);
- $\sigma_{\mathrm{SS,c}}$: uncertainty due to the choice of background modeling representing the spurious signal term, it is estimated per category and the values are given in

Table 6.21 for 7 TeV data and must be scaled by $\times(5.9/4.8) \times 1.2$ for 8 TeV data (10 nuisance parameters $\boldsymbol{\theta}_{\mathrm{SS,c}}$);

- $\sigma_{\mathrm{X\,scale}}$, for $X = ggH$, VBF, WH, ZH and $t\bar{t}H$: systematic uncertainty on the production cross-section evaluated from scale variations (4 nuisance parameters $\theta_{\mathrm{X'\,scale}}$ with $X' = ggH$, VBF, VH and $t\bar{t}H$);

- $\sigma_{\mathrm{ggH,\,2-jet}}$: systematic uncertainty on the signal yields due to the fraction of ggH production in the 2-jet bin. Similar effects in the other production modes are neglected (1 nuisance parameter $\theta_{\mathrm{ggH,\,2-jet}}$);

- $\sigma_{\mathrm{gg\,PDF_ggH,t\bar{t}H}}$ and $\sigma_{\mathrm{q\bar{q}\,PDF_VBF,WH,ZH}}$: systematic uncertainties on the production cross-section due to gg and $q\bar{q}$ PDF uncertainties respectively (2 nuisance parameters $\theta_{\mathrm{gg\,PDF}}$ and $\theta_{\mathrm{q\bar{q}\,PDF}}$);

- $\sigma_{\mathrm{XH,\,VBF,\,UE}}$: uncertainty due to the underlying event activity in the 2-jet category, it has different values for the VBF production mode and for the others (1 nuisance parameter θ_{UE});

- $\sigma_{p_T^{\mathrm{model}},c}$: uncertainty on the diphoton p_T spectrum in the ggH production mode (1 nuisance parameter $\theta_{p_T^{\mathrm{model}}}$);

- $\sigma_{\mathrm{X\,JES_mig}}$: jet energy scale uncertainty applied in the 2-jet category and has different values depending on the production process (1 nuisance parameter $\theta_{\mathrm{JES_mig}}$).

The signal PDF is represented as a sum of a Crystal Ball (CB) lineshape describing the core of the $M_{\gamma\gamma}$ distribution (see equation 6.1) and a Gaussian (G) describing the outlier component,

$$\begin{aligned} f_{\mathrm{sig,c}}\left(M_{\gamma\gamma};\boldsymbol{\theta}^{\mathrm{shape}}\right) &= \phi_{\mathrm{CB}}\mathrm{CB}(\mathrm{M}_{\gamma\gamma},\mathrm{M}_{\mathrm{peak,c}}, \\ &\quad \sigma_{\mathrm{CB,c}}\exp\left(\sqrt{\log(1+\sigma_{\mathrm{res}}^2)}\,\theta_{\mathrm{res}}\right),\alpha_c,n) \\ &+ (1-\phi_{\mathrm{CB}})\,\mathrm{G}(\mathrm{M}_{\gamma\gamma},\mathrm{M}_{\mathrm{peak,c}},\mathrm{R_c}\,\sigma_{\mathrm{CB,c}}\exp\left(\sqrt{\log(1+\sigma_{\mathrm{res}}^2)}\,\theta_{\mathrm{res}}\right)). \end{aligned}$$

The parameter $M_{\mathrm{peak,c}}$ is the common peak position of the Crystal Ball and the Gaussian shapes. R_c is the ratio of the Gaussian width to the core width $\sigma_{\mathrm{CB,c}}$ of the Crystal Ball. n is fixed to 10 for all categories. σ_{res} is the systematic uncertainty on the photon energy resolution applied to both the CB and the Gaussian widths. θ_{res} is the corresponding nuisance parameter (1 nuisance parameter).
If taking into account the energy scale uncertainties, the signal PDF is expressed by:

$$
\begin{aligned}
f_{\mathrm{sig,c}}\left(M_{\gamma\gamma};\boldsymbol{\theta}^{\mathrm{shape}}\right) &= \phi_{\mathrm{CB}}\mathrm{CB}(\mathrm{M}_{\gamma\gamma},\mathrm{M}_{\mathrm{peak,c}}(1+\sigma_{\mathrm{escale,c}}\,\theta_{\mathrm{escale}}) \\
&\quad (1+\sigma_{\mathrm{MAT_LOW,c}}\,\theta_{\mathrm{MAT_LOW}})(1+\sigma_{\mathrm{MAT_HIGH,c}}\,\theta_{\mathrm{MAT_HIGH}}) \\
&\quad (1+\sigma_{\mathrm{PS_B,c}}\,\theta_{\mathrm{PS_B}})(1+\sigma_{\mathrm{PS_EC,c}}\,\theta_{\mathrm{PS_EC}}), \\
&\quad \sigma_{\mathrm{CB,c}}\exp\left(\sqrt{\log(1+\sigma_{\mathrm{res}}^2)}\,\theta_{\mathrm{res}}\right),\alpha_c,n) \\
&+ (1-\phi_{\mathrm{CB}})\mathrm{G}(\mathrm{M}_{\gamma\gamma},\mathrm{M}_{\mathrm{peak,c}}(1+\sigma_{\mathrm{escale,c}}\,\theta_{\mathrm{escale}}) \\
&\quad (1+\sigma_{\mathrm{MAT_LOW,c}}\,\theta_{\mathrm{MAT_LOW}})(1+\sigma_{\mathrm{MAT_HIGH,c}}\,\theta_{\mathrm{MAT_HIGH}}) \\
&\quad (1+\sigma_{\mathrm{PS_B,c}}\,\theta_{\mathrm{PS_B}})(1+\sigma_{\mathrm{PS_EC,c}}\,\theta_{\mathrm{PS_EC}}), \\
&\quad R_c\sigma_{\mathrm{CB,c}}\exp\left(\sqrt{\log(1+\sigma_{\mathrm{res}}^2)}\,\theta_{\mathrm{res}}\right)).
\end{aligned}
$$

where $\sigma_{\mathrm{escale,c}}$, $\sigma_{\mathrm{MAT_LOW,c}}$, $\sigma_{\mathrm{MAT_HIGH,c}}$, $\sigma_{\mathrm{PS_B,c}}$, $\sigma_{\mathrm{PS_EC,c}}$ are the systematic uncertainties due to the effect of the photon energy scale on the mass peak position, their values were given in Table 6.23. θ_{escale}, $\theta_{\mathrm{MAT_LOW}}$, $\theta_{\mathrm{MAT_HIGH}}$, $\theta_{\mathrm{PS_B}}$, $\theta_{\mathrm{PS_EC}}$ are the corresponding nuisance parameters (5 nuisance parameters)

For the background, the normalization terms $N_{\mathrm{bkg,c}}$ in the likelihood are treated as nuisance parameters (10 nuisance parameters). The background PDFs in each category are taken to be as follows (the justification for the choice of these PDFs is detailed in the next section):

- categories 2, 4, 6, 8, 10: an exponential form
  $f_{\mathrm{bkg,c}}\left(M_{\gamma\gamma};\boldsymbol{\theta}_c^{\mathrm{bkg}}=\{\xi_c\}\right)=Ae^{-\xi_c M_{\gamma\gamma}}$;
- categories 1, 5, 9: the exponential of a quadratic polynomial
  $f_{\mathrm{bkg,c}}\left(M_{\gamma\gamma};\boldsymbol{\theta}_c^{\mathrm{bkg}}=\{a_{1,c},a_{2,c}\}\right)=Ae^{a_{1,c}\,((M_{\gamma\gamma}-100)/100)+a_{2,c}\,((M_{\gamma\gamma}-100)/100)^2}$;
- categories 3, 7 : a fourth-order Bernstein polynomial
  $f_{\mathrm{bkg,c}}\left(M_{\gamma\gamma};\boldsymbol{\theta}_c^{\mathrm{bkg}}=\{B_{i,c}\}_{1\leq i\leq 4}\right)=A\left(1+\sum_{i=1}^{4}B_{i,c}b_{i,n}(u)\right)$
  with $b_{i,n}(u)=C_n^i u^i(1-u)^{n-i}$ and $u=(M_{\gamma\gamma}-M_{\gamma\gamma}^{\min})/(M_{\gamma\gamma}^{\max}-M_{\gamma\gamma}^{\min})$.

where A is a normalization constant. The slopes ξ_c (5 nuisance parameters), the coefficients $a_{i,c}$ (6 nuisance parameters) and $B_{i,c}$ (8 nuisance parameters) are varied freely in the fit.

In total, we count for 2011 statistical analysis 57 nuisance parameters and 62 nuisance parameters if we take into account the photon energy scale systematic (ESS) uncertainties on the mass peak position.
In 2012, an additional term is added to $N_{\mathrm{sig,c}}\left(\mu,\boldsymbol{\theta}_c^{\mathrm{norm}}\right)$ to take into account the uncertainty on the jet vertex fraction i.e $\exp\left(\sqrt{\log(1+\sigma_{\mathrm{JVF_mig,c}}^2)}\,\theta_{\mathrm{JVF_mig,c}}\right)$

leading to 58 nuisance parameters (or 63 if ESS is taken into account).
When combining 2011 and 2012 datasets, the systematic uncertainties on the expected signal yields and on the mass resolution are taken as fully correlated, except for the luminosity. However the shape of the background is taken as uncorrelated. The total number of nuisance parameters is therefore 78 (or 83 if taken into account the ESS).

Among these nuisance parameters, those related to the background shape are unconstrained parameters. However the remaining nuisance parameters are constrained with a Gaussian distribution except for the 4 nuisance parameters $\theta_{\mathrm{X'\,scale}}$ for which the assigned $\sigma_{\mathrm{X\,scale}}$ take asymmetric values, these are constrained by bifurcated gaussians.

7.2.2 Background modeling

The choice of the background modeling has been examined carefully before unblinding the 2012 data. It has been made in a way to minimize a possible introduced bias while retaining good statistical power. The biases were estimated using three different sets of high statistics background-only MC models. The prompt diphoton background is obtained from the three generators RESBOS [228], DIPHOX and SHERPA [229], while the same reducible background is used for all three models, based on SHERPA for the gamma-jet component and on PYTHIA6 for the jet-jet background. The Drell-Yan component is also taken into account. Detector effects are included whenever possible. The proportions of the different MC background components are estimated from data and normalized to the total number of events observed in the data.

A variety of functional forms were considered for the background parametrization: single and double exponential, Bernstein polynomials up to seventh order, exponentials of second and third-order polynomials, and exponentials with modified turn-on behaviour. The potential bias for a given parametrization is estimated by performing a maximum likelihood fit in the mass range $100 - 160$ GeV using the sum of a signal (the signal shape is taken from the SM BEH parametrization and the normalization is floating) and the background parametrization to all three sets of background-only simulation models for each category. The categories mainly affected by background parametrization bias are the high statistics categories, which also have a lower signal to background ratio. Parametrizations that exhibit problems with fit convergence are discarded. Parametrizations for which the estimated potential bias is smaller than 20% of the uncertainty on the fitted signal yield or where the bias is smaller than 10% of the expected signal events for each of the background models are selected. Among these selected parametrizations, the one with the best expected sensitivity at $M_H = 125$ GeV is selected as the background parametrization. The largest bias in each category of the full mass range is taken as a systematic uncertainty, $\sigma_{SS,c}$.

Fig. 7.8 shows the comparison of different background parametrizations in terms of expected p_0 values. The double exponential function and the exponential of a third-order polynomial are excluded because of fit problems. Among the considered models, the model: exponential function for categories 2, 4, 6, 8, 10; exponential of a quadratic polynomial for categories 1,5,9; and a fourth order Bernstein polynomial for categories 3,7; denoted by "Exp/X2/B4", gives the best expected p_0 and is chosen as a reference model for the analysis.

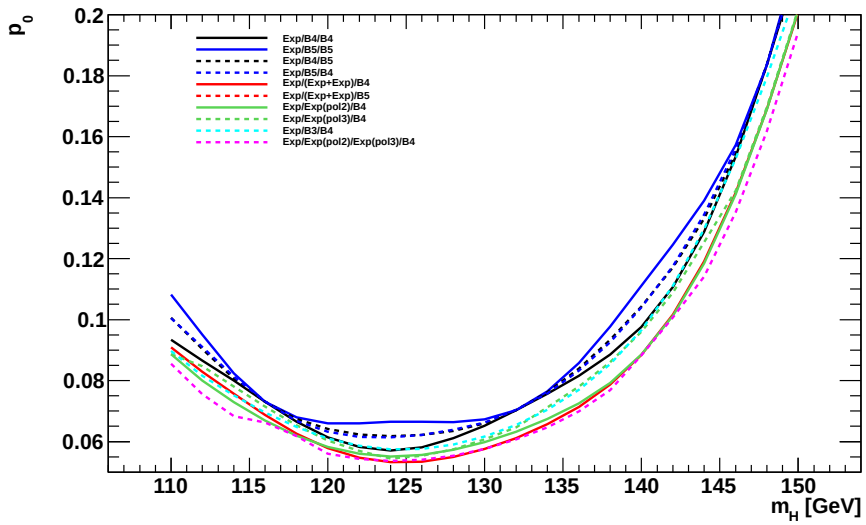

Figure 7.8: Expected local p_0 for various background parametrizations as a function of the BEH mass. Exp is for an exponential, Bn is for an n-th order Bernstein polynomial and poln for an n-th order polynomial. X/Y/Z translates the split into categories 2,4,6,8,10/1,5,9/3,7 and W/X/Y/Z for 2,4,6,8,10/1,5,9/3/7.

7.2.3 Observation Results

Based on the above described statistical procedure, results for $H \to \gamma\gamma$ search in the mass range $110 - 150$ GeV are discussed in the following.

As described in section 6.3, a re-analysis of the 2011 full dataset has been done. To quantify the improvement wrt to what was published at Council 2011, Fig. 7.9 shows the expected and observed local p_0 for both analyses. The improvement is of the order of 18% in terms of the expected significance for $M_H = 126.5$ GeV.

Results for 95% C.L. exclusion limits on the BEH boson production cross section are shown separately for 7 and 8 TeV data in Fig. 7.10 for the mass range

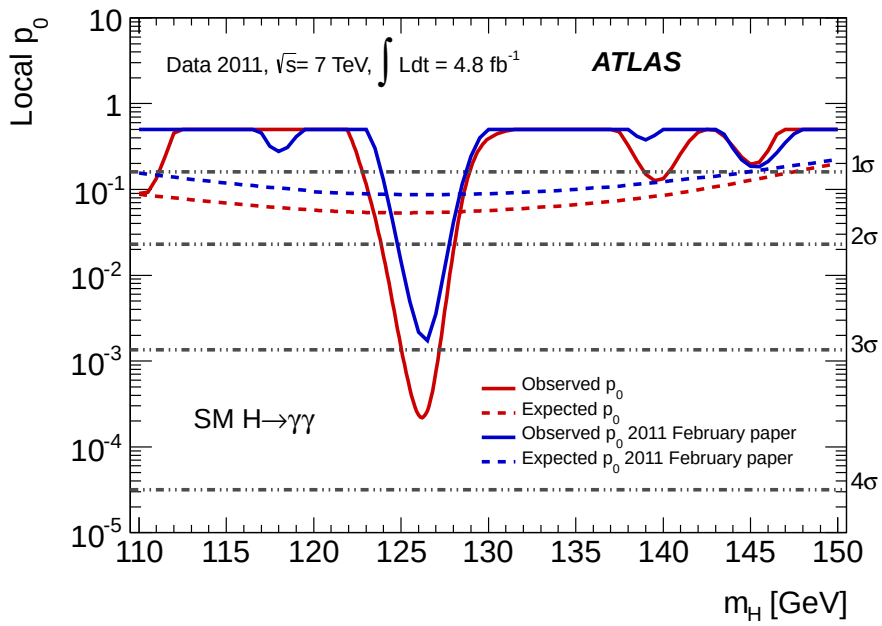

Figure 7.9: Comparison of the expected and observed capped local p_0 values obtained for the Council 2011 analysis and the improved analysis of the $\sqrt{s} = 7$ TeV data.

$110 - 150$ GeV. The expected CL_s limit in the absence of a SM BEH boson signal ranges from 1.3 to 2.5 times the SM expectation for 7 TeV data and from 1.1 to 2.1 times the SM expectation for 8 TeV data. A SM BEH boson is excluded in the mass range $113.0 - 121.3$ GeV in the 7 TeV data and from $117.5 - 123.2$ and $138 - 142.5$ GeV in the 8 TeV data. Fig. 7.11 shows the results for 95% C.L. exclusion limits on the BEH boson production cross section obtained in the mass range $110 - 150$ GeV for the combined 7 and 8 TeV data. The expected CL_s limit in the absence of a SM signal ranges from 0.8 to 1.6 times the SM expectation. The analysis is already sensitive to an exclusion of a SM BEH boson in the range $110.0 - 140.5$ GeV. The actual observed exclusion ranges between $112.0 - 123.0$ GeV and $132.0 - 143.5$ GeV. The non-excluded region between 123 and 132 GeV is due to an excess in this mass range.

To quantify its discovery significance, Fig. 7.12 shows the background-only p_0 for the combined 2011 and 2012 datasets, along with the p_0 for the $\sqrt{s} = 7$ TeV and $\sqrt{s} = 8$ TeV analyses. The minimal p_0-values observed in the mass range $110 - 150$ GeV for the $\sqrt{s} = 7$ TeV and the $\sqrt{s} = 8$ TeV data samples are 2.2×10^{-4} and 4.8×10^{-4}, respectively. They are found at $M_H = 126.2$ GeV and 127.1 GeV and correspond to local significances of 3.5σ and 3.3σ. For a SM BEH boson, the expected p_0 values would be 5.4×10^{-2} and 3×10^{-2} at these hypothesized mass values, corresponding to local significances of 1.6σ and 1.9σ, respectively.

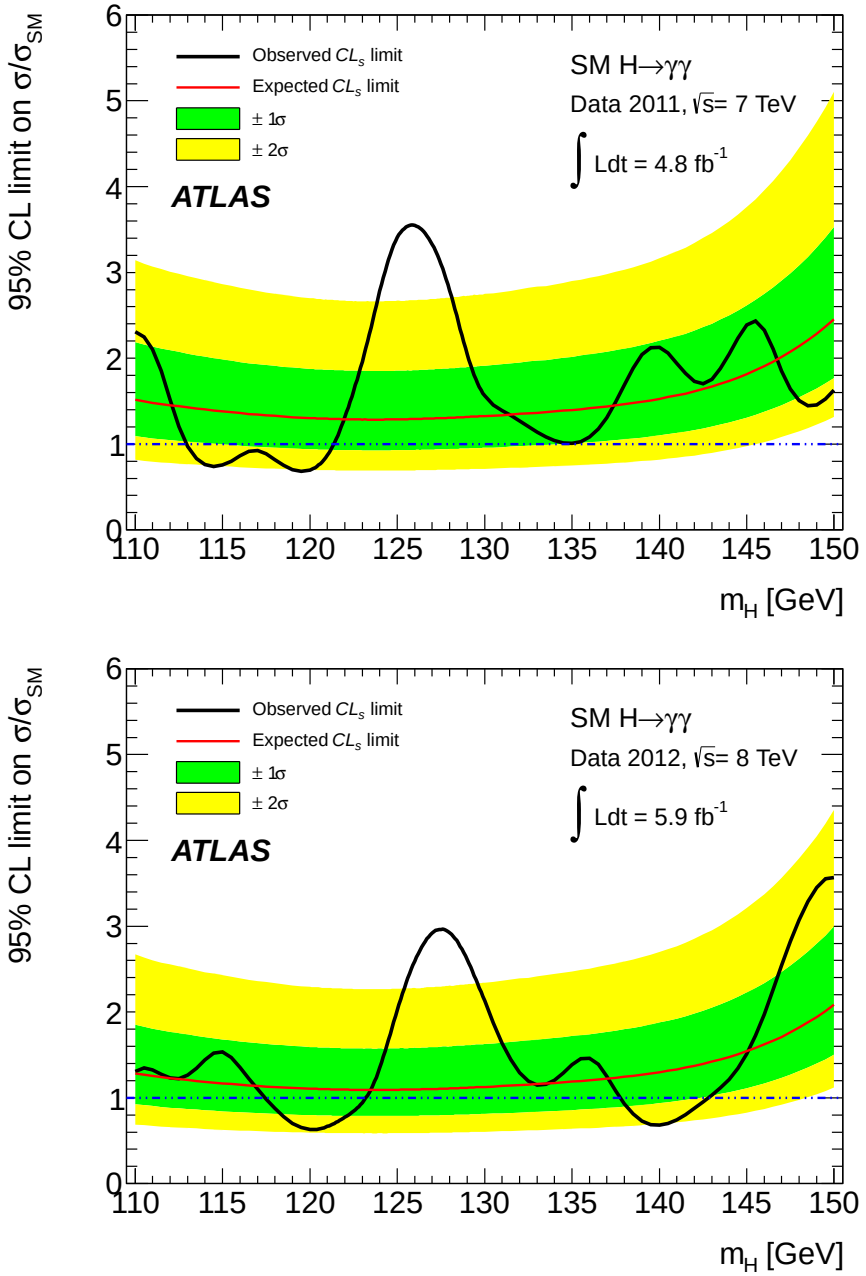

Figure 7.10: Observed and expected CL_s limit on the normalized signal strength as a function of the assumed BEH boson mass for the $\sqrt{s} = 7$ TeV (top) and $\sqrt{s} = 8$ TeV (bottom) analyses.

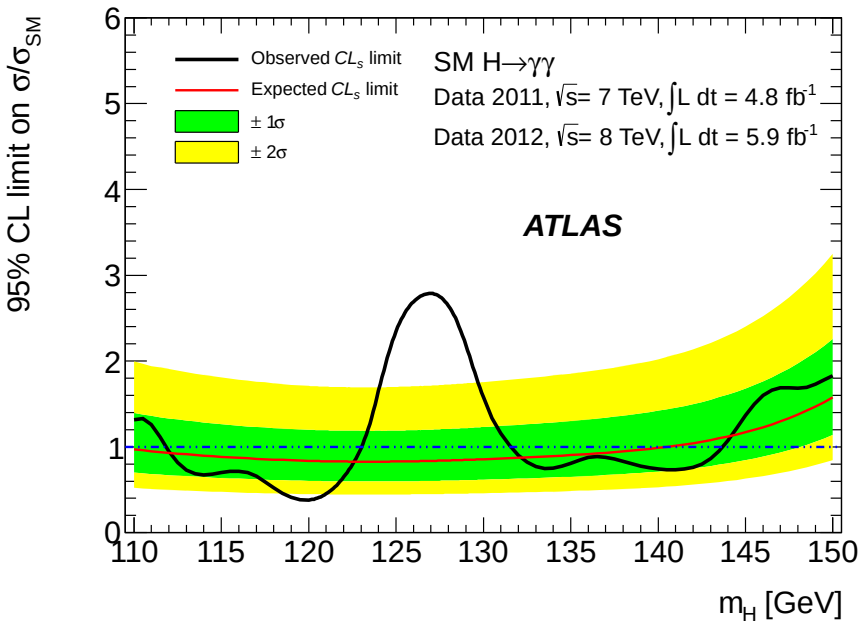

Figure 7.11: Expected and observed CL_s limit on the normalized signal strength as a function of the hypothesized BEH boson mass for the combined 2011 and 2012 datasets.

The positions of the two minima are compatible within their uncertainties. The minimal observed p_0-value of the combined datasets is 1.7×10^{-6} at $M_H = 126.5$ GeV corresponding to a local significance of 4.6σ. This is reduced to 4.5σ when including the energy scale systematic uncertainty using pseudo-experiments. The expected local significance at $M_H = 126.5$ GeV for a SM BEH boson is 2.5σ. After correction to the look-elsewhere effect, the observed global significance is 3.6σ in the mass range $110 - 150$ GeV.

Fig. 7.13 shows the expected and observed local p_0 comparing the analysis using 10 categories, an analysis using 9 categories (without the 2-jet category) and a fully inclusive analysis (without dividing the dataset into categories) for the combined 7 and 8 TeV data. The excess has a maximum local significance at $M_H = 126.5$ GeV for the inclusive analysis of 2.7σ (expected 1.2σ) for 7 TeV data, 2.2σ (expected 1.4σ) at $M_H = 127$ GeV for 8 TeV data and 3.3σ (expected 1.9σ) at $M_H = 126.5$ GeV for the combined 7 and 8 TeV data. For the 9 categories analysis, the excess has a maximum local significance at $M_H = 126$ GeV of 3.0σ (expected 1.5σ) for 7 TeV data, 2.9σ (expected 1.8σ) at $M_H = 127$ GeV for 8 TeV data and 4.1σ (expected 2.4σ) for the combined 7 and 8 TeV data. Therefore the analysis used, with 10 categories, improves the expected p_0 at $M_H = 126.5$ GeV by $\sim 30\%$ compared to the inclusive analysis, and by $\sim 4\%$ with respect to the 9 categories

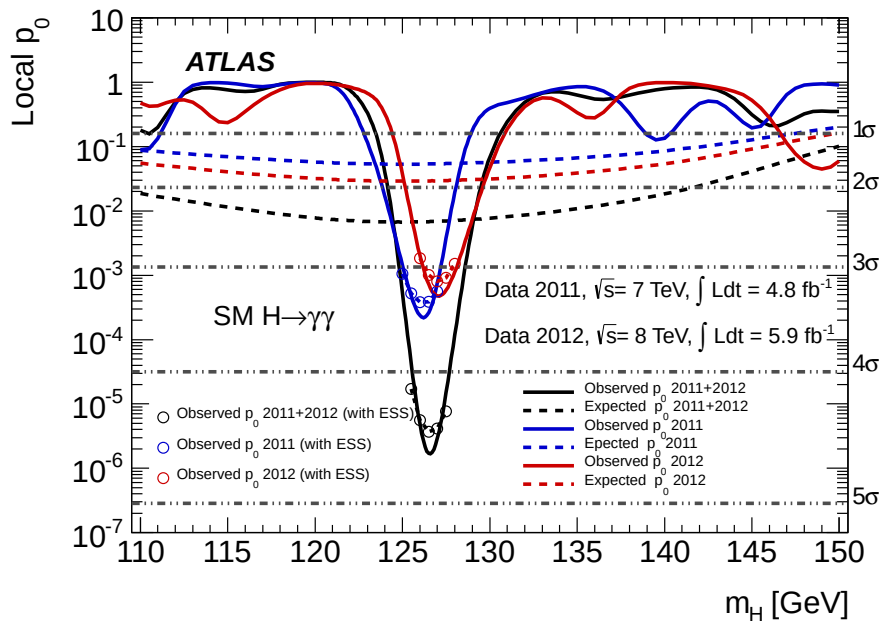

Figure 7.12: Expected and observed local p_0 values as a function of the hypothesized BEH boson mass for the combined analysis and for the $\sqrt{s} = 7$ TeV and $\sqrt{s} = 8$ TeV separately. The observed local p_0 including the effect of the energy scale systematic uncertainty on the mass position is computed using pseudo-experiments and shown as open circles.

analysis.

Fig. 7.14 (Fig. 7.15) shows the distributions of the local p_0 (significance) obtained from fits to individual categories for the 7 and 8 TeV data separately. The distributions show the behaviour of the excess in each category. The curves are dominated by statistical fluctuations. For instance, the largest fluctuation in 2011 correponds to the category "Unconverted rest, high p_{Tt}" while it is not the case for 2012 data.

In order to show the contribution of the excess in each category to the observed combined significance, a weight has been assigned to the observed significance in each category. The weight was defined following the procedure of combining uncorrelated channels described in [230] where one has the approximation:

$$\begin{aligned} \hat{\mu} &= \sum_i \frac{\hat{\mu}_i/\sigma_i^2}{1/\sigma^2} \\ &= \sum_i \frac{\hat{\mu}_i \sigma^2}{\sigma_i^2} \end{aligned}$$

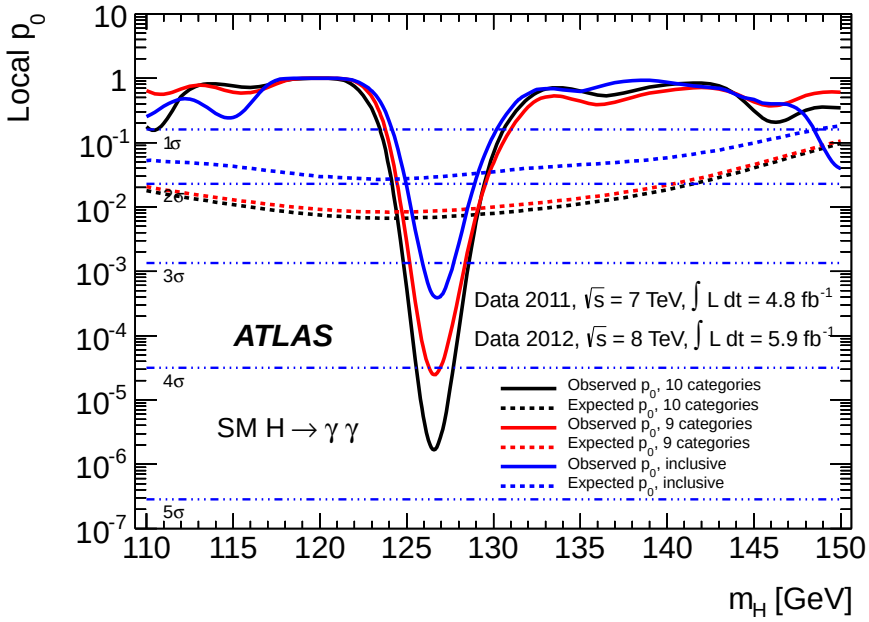

Figure 7.13: Expected and observed local p_0 for the analysis using 10 categories, compared to an analysis using 9 categories (without the 2-jet category) and a fully inclusive analysis for the combined $\sqrt{s} = 7$ TeV and $\sqrt{s} = 8$ TeV data [222].

where $\hat{\mu}$ is the fitted signal strength parameter and σ represents the error on $\hat{\mu}$. i runs overs all the categories (or channels).
Thus, the fitted signal strength $\hat{\mu}$ of the combined categories is given by the sum overall the categories of the fitted strength in each category weighted by σ^2/σ_i^2.
Since the significance is given by $Z = \hat{\mu}/\sigma$, one can write:

$$\begin{aligned} Z &= \sum_i \frac{\hat{\mu}_i \sigma}{\sigma_i^2} \\ &= \sum_i \frac{Z_i \sigma}{\sigma_i} \end{aligned}$$

The significance in the combined categories is given by the sum of significances in each category weighted by σ/σ_i. In addition, for $\hat{\mu}_i = 1$ (SM), $Z = \sum_i \sigma/\sigma_i^2$, thus the expected contribution from each category to the combined is propotional to the square of the considered weight σ/σ_i.
Moreover, from [230] we have:

$$\mu_{up}^{med} = \sigma \Phi^{-1}(1 - \alpha/2) \tag{7.4}$$

where μ_{up}^{med} is the upper expected limit, Φ is the normal cumulative distribution, and $1 - \alpha$ is the confidence level. $\Phi^{-1}(1 - \alpha/2)$ is considered as a factor of proportionality and therefore the weight of the significance can be rather written as $\mu_{up}^{med}/\mu_{up,i}^{med}$.

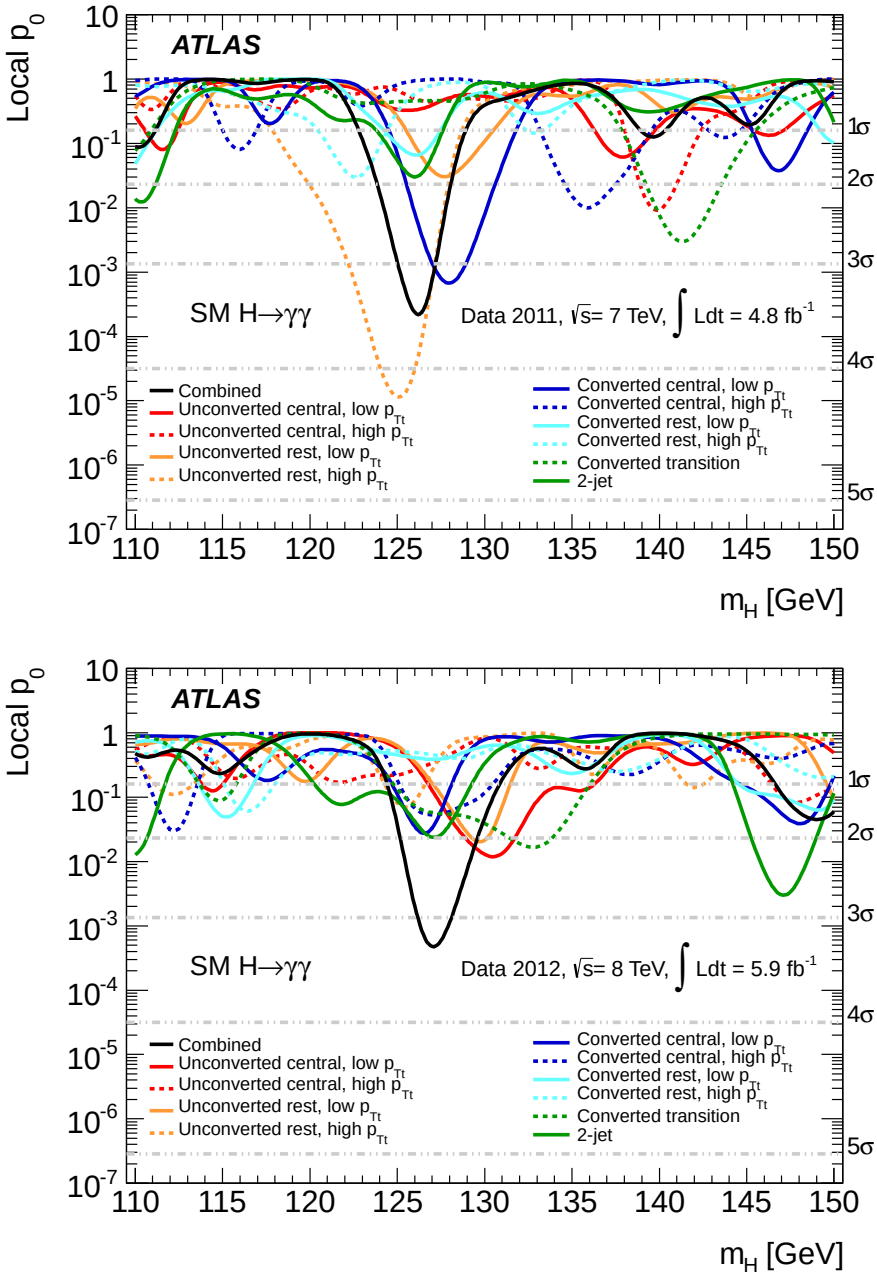

Figure 7.14: Distributions of p_0 obtained from fits to single categories for the $\sqrt{s} = 7$ TeV data (top) and the $\sqrt{s} = 8$ TeV (bottom), along with the result from the combined fit.

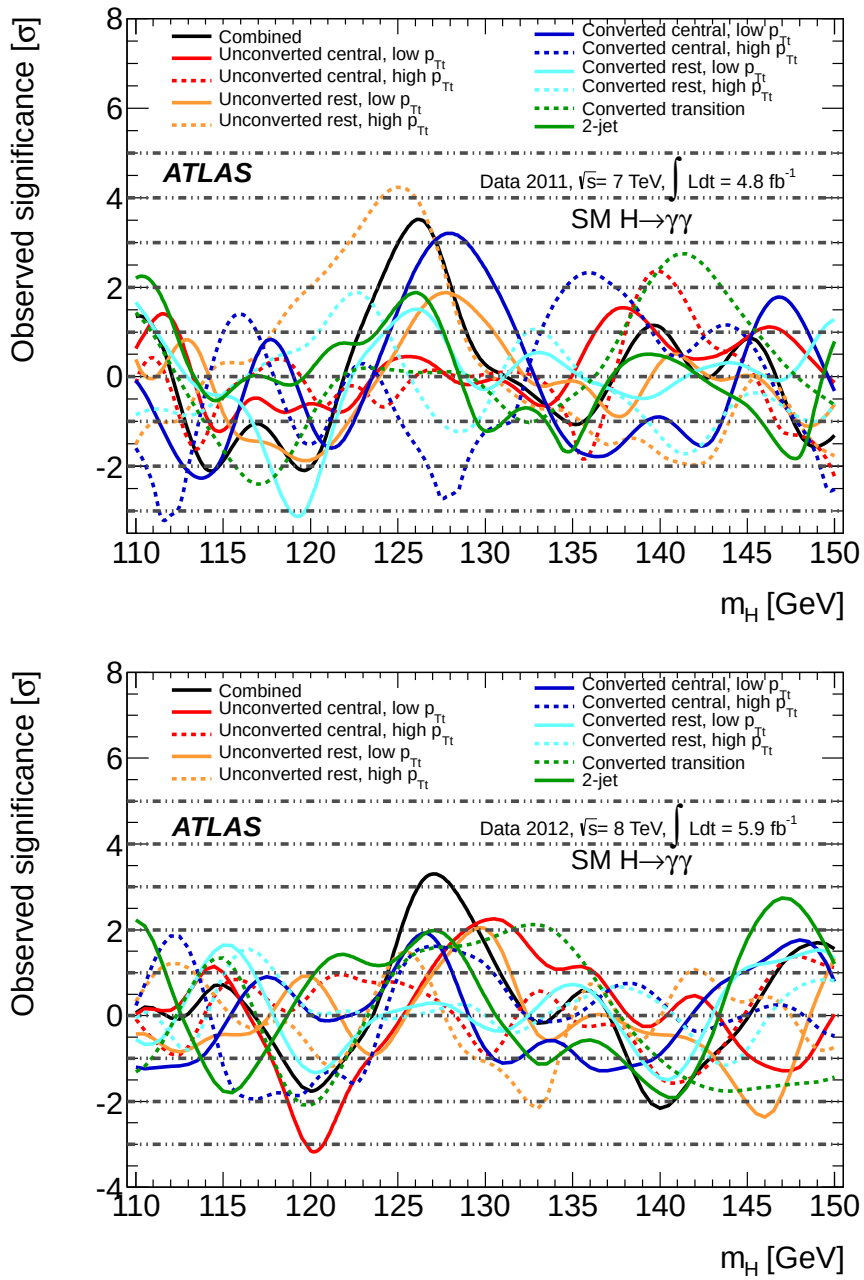

Figure 7.15: Distributions of the observed significance obtained from fits to single categories for the $\sqrt{s} = 7$ TeV (top) and the $\sqrt{s} = 8$ TeV (bottom) data, along with the result from the combined fit.

Fig. 7.16 (Fig. 7.17) shows the observed (zoomed) weighted significance for the 7 and 8 TeV analyses separately. Fig. 7.18 (Fig. 7.19) shows the observed (zoomed) weighted significance for the combined 7 and 8 TeV analyses. The weight is defined as the ratio of the expected upper median limit in the combined fit to this limit in each category. The right side bar in the figures displays the square of the weights which translates into the expected weight of each category under the SM assumption.

The best fit value of the signal strength μ is shown separately for 7 and 8 TeV data in Fig. 7.20 and for the combined datasets in Fig. 7.21. At $M_H = 126.5$ GeV, the best fit value is $\hat{\mu} = 2.1 \pm 0.7$ for 7 TeV analysis, $\hat{\mu} = 1.7 \pm 0.6$ for 8 TeV analysis, and $\hat{\mu} = 1.8 \pm 0.5$ for the combined analyses. This corresponds to about 350 signal events and deviates by 1.6σ from the SM hypothesis. The best fit values of μ at $M_H = 126.5$ GeV for the combined 7 and 8 TeV analyses obtained from fits to the individual categories is shown in Fig. 7.22. The $\hat{\mu}$ values are compatible among categories with the SM hypothesis within the statistical uncertainty.
Another explanation of the difference with respect to the SM hypothesis ($\mu = 1$) is a possible bias on $\hat{\mu}$ introduced by looking at the largest deviation from the background to estimate the best fit value of μ rather than to the true BEH boson mass [231]. It has been shown, using pseudo-experiments, that injecting a SM signal $\mu = 1$ at $M_H = 125$ GeV will induce a bias on the estimation of $\hat{\mu}$ at 126.5 GeV of about 8% [232].

Moreover, the contributions from the different production modes have been studied. A signal strength parameter μ_i is defined by production mode. μ_{ggH} and $\mu_{t\bar{t}H}$ have been grouped together as they scale with the $t\bar{t}H$ coupling in the SM and are denoted by $\mu_{ggH+t\bar{t}H}$. Similarly, μ_{VBF} and μ_{VH} have been grouped together as they scale with the WWH/ZZH coupling in the SM, and are denoted by μ_{VBF+VH}. In order to determine the values of $(\mu_{ggH+t\bar{t}H}, \mu_{VBF+VH})$ that are simultaneously consistent with the data, the following profile likelihood is used:

$$\lambda(\mu_i, \mu_j) = \frac{L(\mu_i, \mu_j, \hat{\hat{M}}_H(\mu_i, \mu_j), \hat{\hat{\boldsymbol{\theta}}}(\mu_i, \mu_j))}{L(\hat{\mu}_i, \hat{\mu}_j, \hat{M}_H, \hat{\boldsymbol{\theta}})} \tag{7.5}$$

where $\hat{\hat{M}}_H$ and $\hat{\hat{\boldsymbol{\theta}}}$ are the conditional maximum likelihood estimates of M_H and $\boldsymbol{\theta}$ with $\mu_i(\mu_{ggH+t\bar{t}H})$ and $\mu_j(\mu_{VBF+VH})$ fixed.
The resulting likelihood contours at 68% and 95% C.L. are shown in Fig. 7.23 for $M_H = 126$ GeV, along with the best fit to the data $(\hat{\mu}_{ggH+t\bar{t}H}, \hat{\mu}_{VBF+VH})$ as well as the SM expectation. These include the theoretical uncertainties as well as the branching ratio factor BR/BR_{SM} where BR is the branching ratio for $H \to \gamma\gamma$. The data are compatible with the SM expectation at the 1.5σ level.

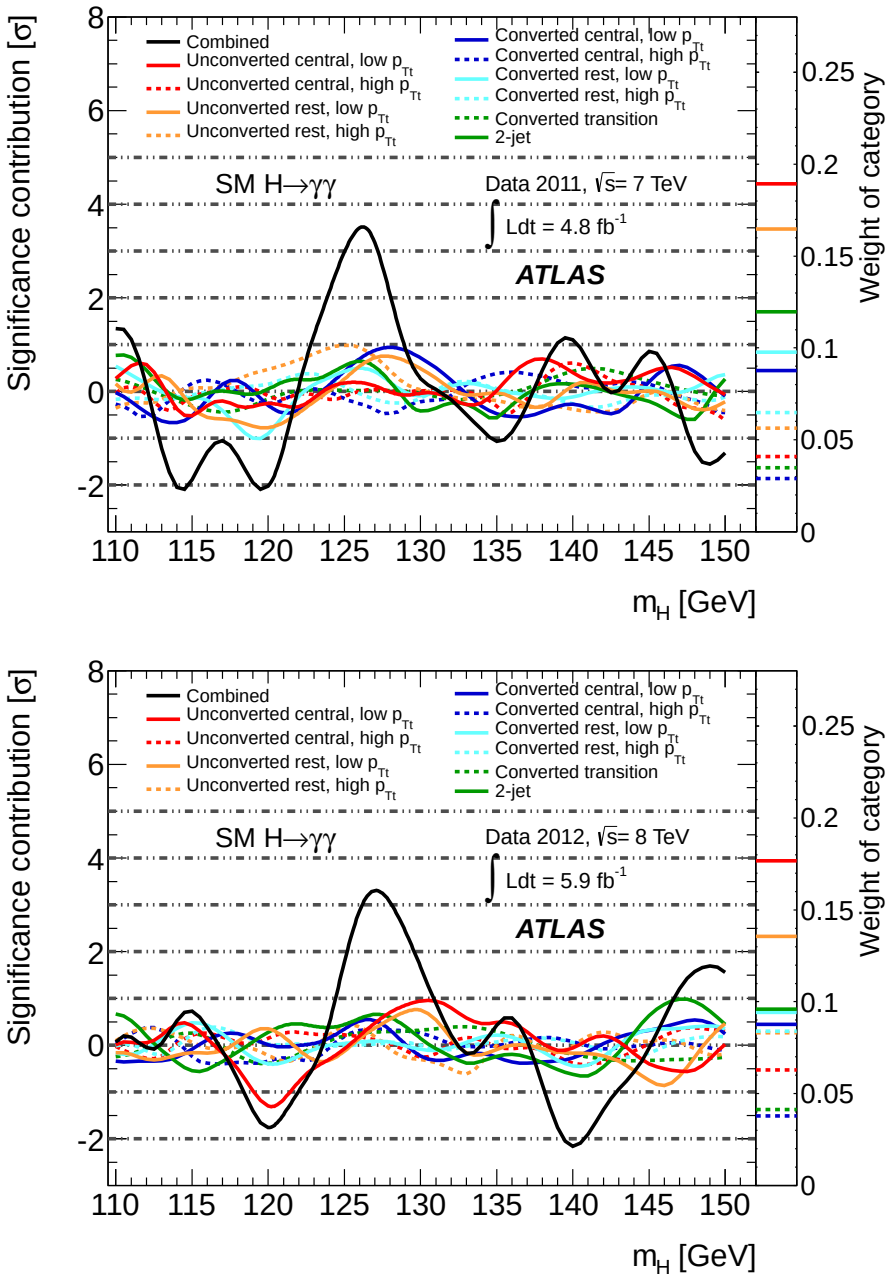

Figure 7.16: Weighted local significances observed for the $\sqrt{s} = 7$ TeV and $\sqrt{s} = 8$ TeV analysis separately as a function of the BEH boson mass. It shows the contribution of the individual categories (colored curves) to the combined result (black). The squared weights are shown in the right side bar.

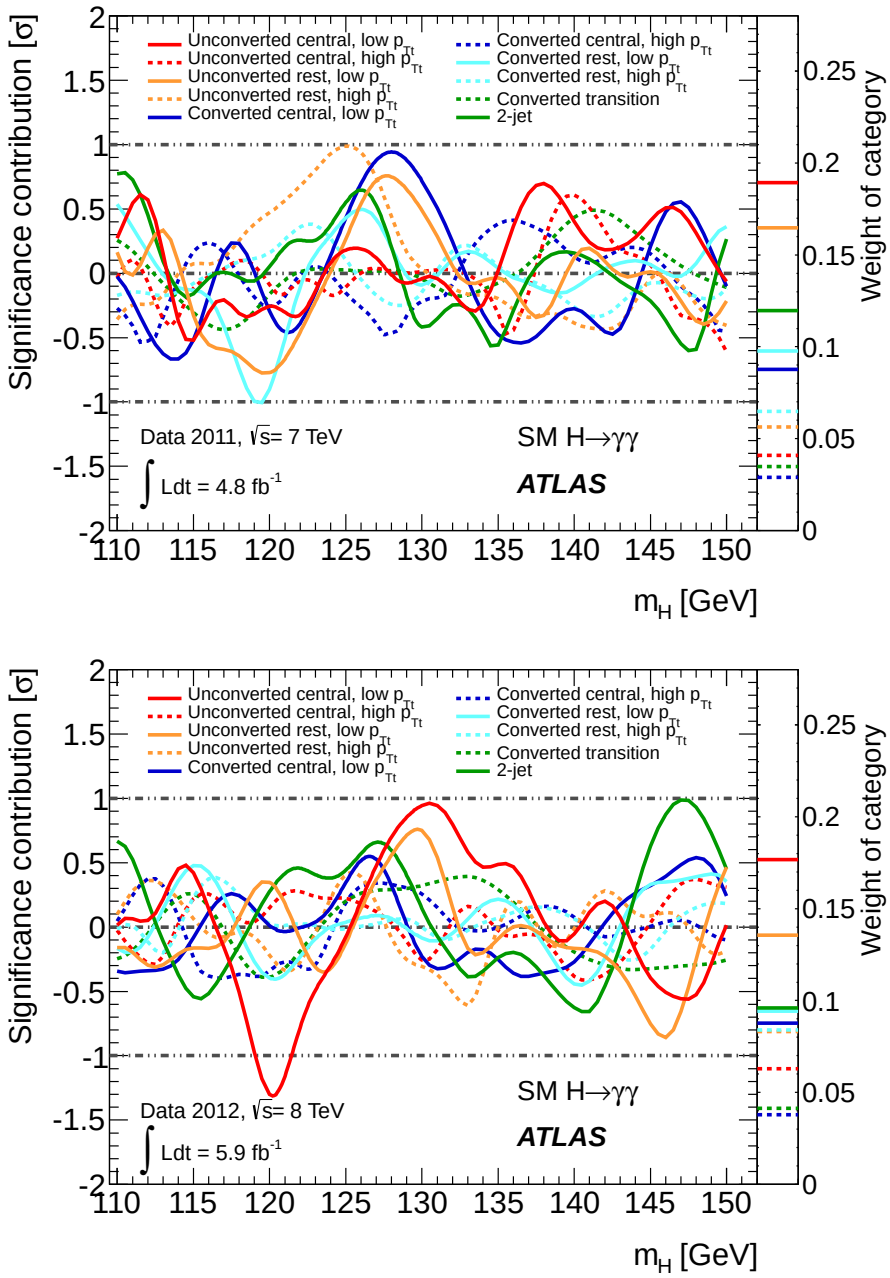

Figure 7.17: Weighted local significances observed for the $\sqrt{s} = 7$ TeV and $\sqrt{s} = 8$ TeV analysis separately as a function of the BEH boson mass. It shows the contribution of the individual categories (colored curves) to the combined result. The squared weights are shown in the right side bar.

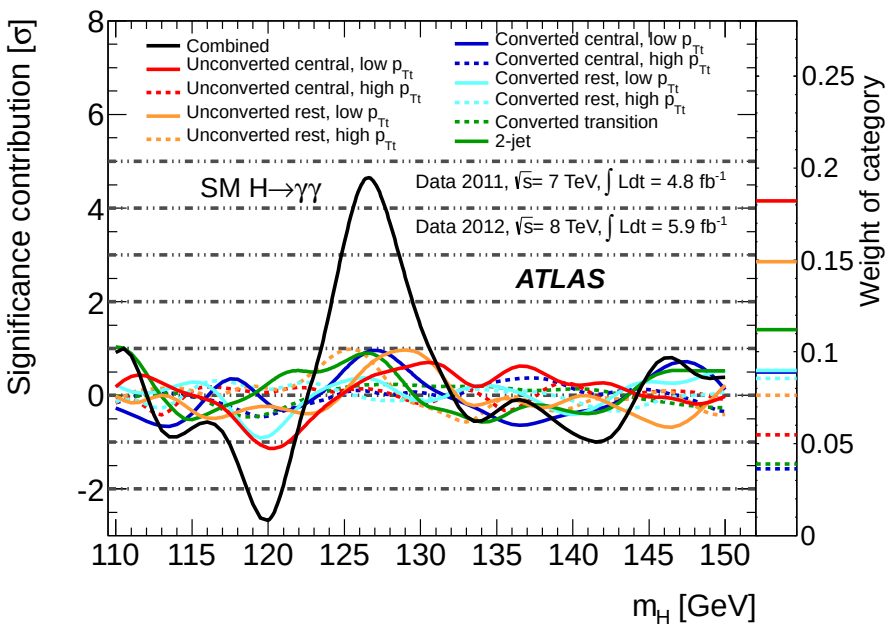

Figure 7.18: Weighted local significances observed for the combined analysis of the $\sqrt{s} = 7$ TeV and $\sqrt{s} = 8$ TeV data as a function of the BEH boson mass. It shows the contribution of the individual categories (colored curves) to the combined result (black). The squared weights are shown in the right side bar.

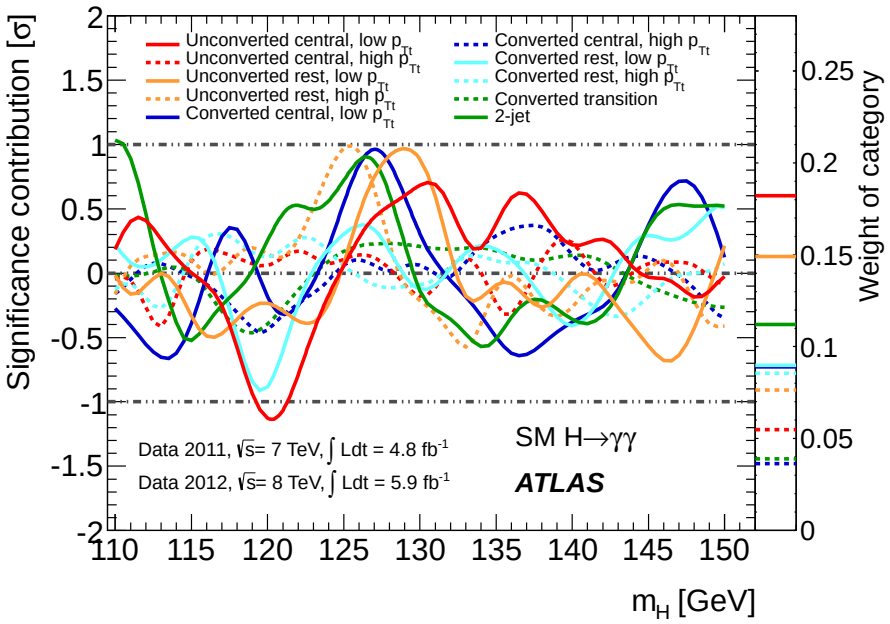

Figure 7.19: Weighted local significances observed for the combined analysis of the $\sqrt{s} = 7$ TeV and $\sqrt{s} = 8$ TeV data as a function of the BEH boson mass. It shows the contribution of the individual categories (colored curves) to the combined result. The squared weights are shown in the right side bar.

7.3 BEH-like particle in the combined channels

The discovery of the new particle is not limited to the $H \to \gamma\gamma$ channel. An excess of 3.6σ at $M_H = 125$ GeV is observed in the $H \to ZZ^{(*)} \to 4l$ search for the combined 7 (improved analysis) and 8 TeV data. This excess is confirmed as well in the highly sensitive but low-resolution channel $H \to WW^{(*)} \to l\nu l\nu$ in a combined analysis of 7 TeV data and of $H \to WW^{(*)} \to e\nu\mu\nu$ updated for 8 TeV data. It has a significance of 2.8σ at $M_H = 125$ GeV.
Fig. 7.24 shows the observed and expected local p_0 for the $H \to \gamma\gamma$, $H \to ZZ^{(*)} \to 4l$ and $H \to WW^{(*)} \to l\nu l\nu$ for the combined datasets.

The combination of individual searches in these three channels with previously published results of searches in the channels $H \to ZZ^{(*)}$, $WW^{(*)}$, $b\bar{b}$ and $\tau^+\tau^-$ for the 7 TeV data gives a maximum local observed significance of 6σ for a SM BEH boson mass hypothesis of $M_H = 126.5$ GeV. The expected local significance in the presence of a SM BEH boson signal is 4.9σ at this mass. This is shown in Fig. 7.25 for the low mass range $110 - 150$ GeV.
When including the uncertainties on the energy resolutions and energy scales for photons and electrons (the effect of the muon energy scale systematic uncertainties is neglected), the maximum local significance reduces to 5.9σ. The global significance in the mass range $110 - 600$ GeV is estimated to be 5.1σ, increasing to 5.3σ in the mass range $110 - 150$ GeV.

The best fit value of the strength parameter is $\hat{\mu} = 1.4 \pm 0.3$ for $M_H = 126$ GeV which is consistent with the SM BEH boson within 1.3σ. It is $\hat{\mu} = 1.4 \pm 0.6$ for $H \to ZZ^{(*)} \to 4l$ and $\hat{\mu} = 1.3 \pm 0.5$ for $H \to WW^{(*)} \to l\nu l\nu$ at $M_H = 126$ GeV. Fig. 7.26 shows the summary of the individual and combined best-fit values of the strength parameter for a SM BEH mass of 126 GeV.

Another important result to quote is the SM BEH exclusion at 95% C.L. for mass ranges $112 - 122$ GeV and $131 - 559$ GeV and at 99% C.L. for mass ranges $113 - 114$ GeV, $117 - 121$ GeV and $132 - 527$ GeV. The expected exclusion ranges from 110 to 582 GeV at 95% C.L. and from 113 to 532 GeV at 99% C.L..

More information about the three main channels is provided in Table 7.1.

In order to test which values of the strength parameter and mass of a signal hypothesis are simultaneously consistent with the data, the profile likelihood ratio

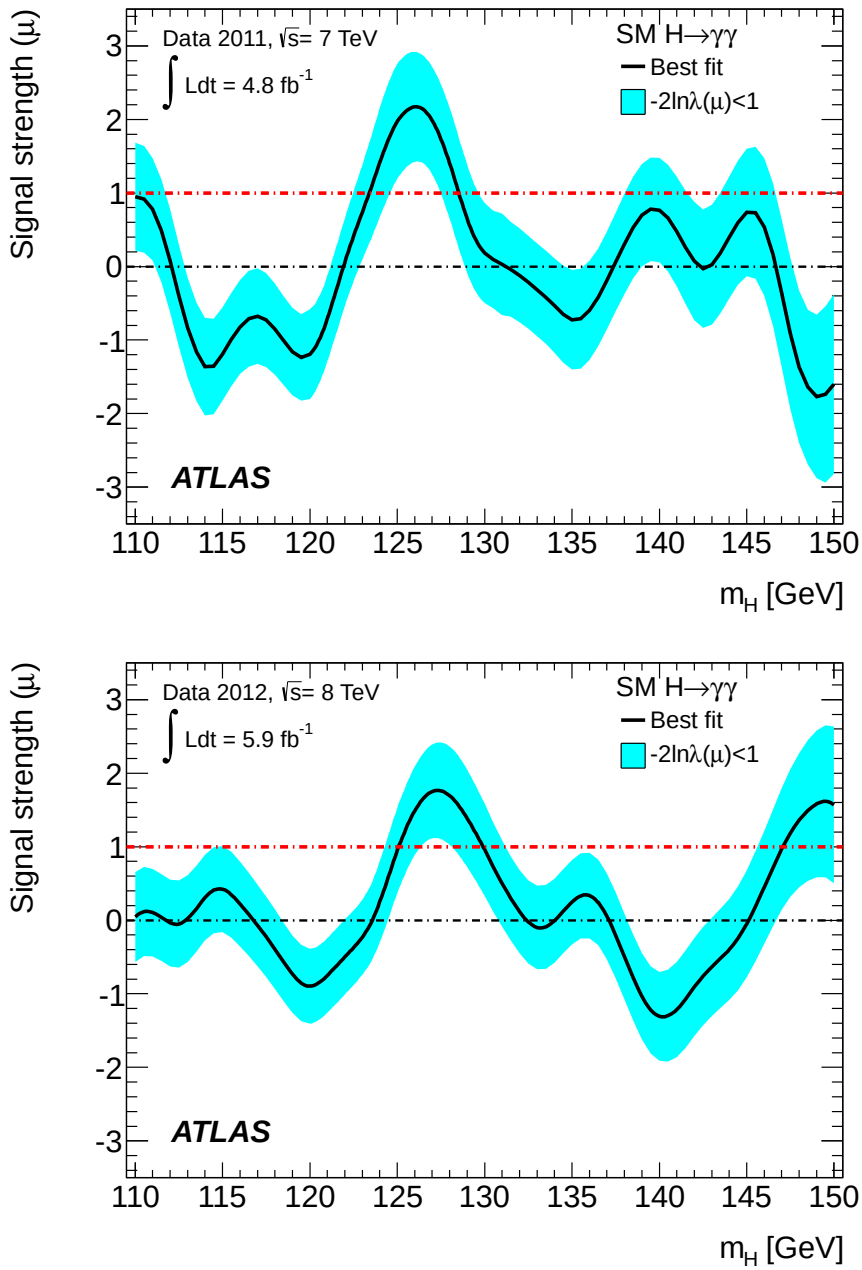

Figure 7.20: Best fit value for the signal strength as a function of the hypothesized BEH mass for the $\sqrt{s} = 7$ TeV and $\sqrt{s} = 8$ TeV analyses.

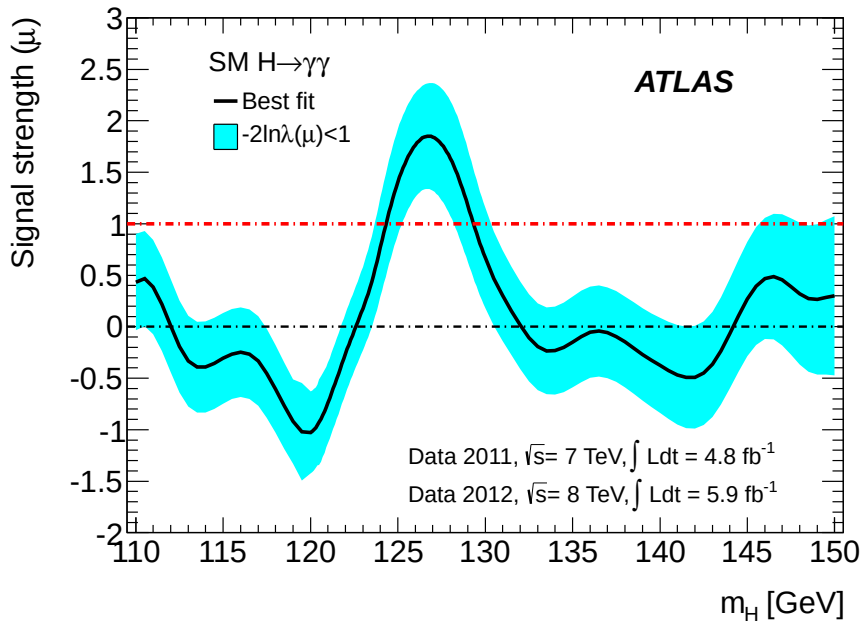

Figure 7.21: Best fit value for the signal strength as a function of the hypothesized BEH mass for the combined analysis of $\sqrt{s} = 7$ TeV and $\sqrt{s} = 8$ TeV data.

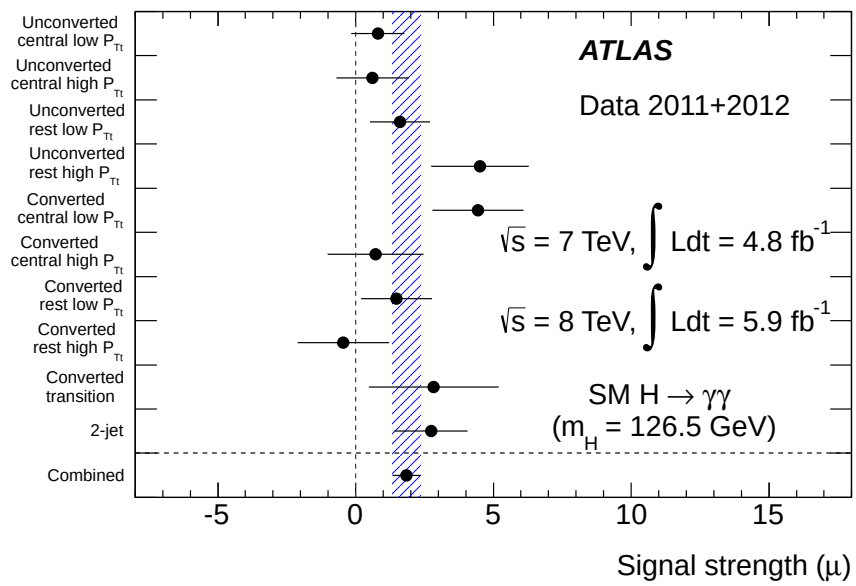

Figure 7.22: Best fit values for the strength parameter in the different categories for a BEH boson mass $M_H = 126.5$ GeV for the combined $\sqrt{s} = 7$ TeV and $\sqrt{s} = 8$ TeV data [222].

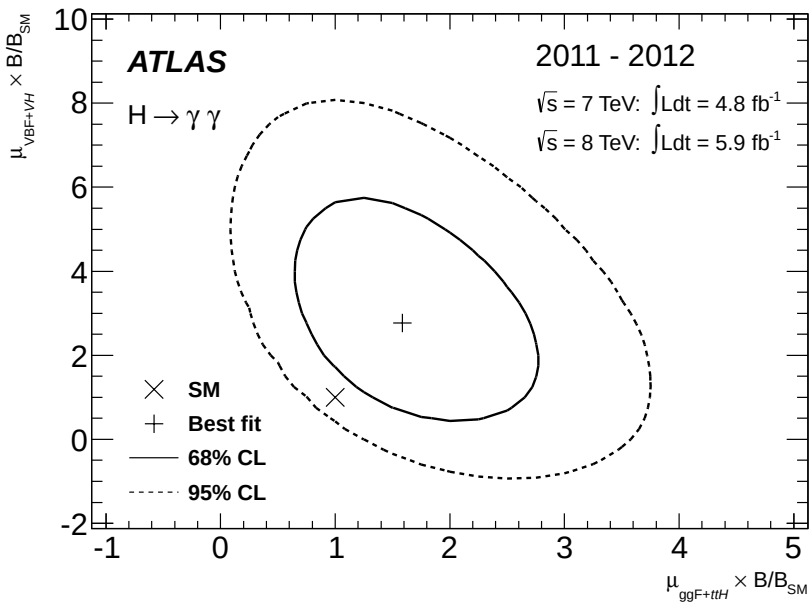

Figure 7.23: Likelihood contours for the $H \to \gamma\gamma$ channel in the $(\mu_{ggH+t\bar{t}H}, \mu_{VBF+VH})$ plane including the branching ratio factor (BR/BR_{SM}). The best fit to the data (+) and 68% (full) and 95% (dashed) C.L. contours are also indicated, as well as the SM expectation (×) [222].

Search channel	Dataset	$M_{\max}$ [GeV]	$Z_l\,[\sigma]$	$E(Z_l)\,[\sigma]$	$\hat{\mu}$ ($M_H = 126$ GeV)	Expected exclusion [GeV]	Observed exclusion [GeV]
$H \to ZZ^{(*)} \to 4l$	7 TeV	125.0	2.5	1.6	1.7 ± 1.1		
	8 TeV	125.5	2.6	2.1	1.3 ± 0.8		
	7 & 8 TeV	125.0	3.6	2.7	1.4 ± 0.6	124-164, 176-500	131-162, 170-460
$H \to \gamma\gamma$	7 TeV	126.0	3.4	1.6	2.2 ± 0.7		
	8 TeV	127.0	3.2	1.9	1.5 ± 0.6		
	7 & 8 TeV	126.5	4.5	2.5	1.8 ± 0.5	110-140	112-123, 132-143
$H \to WW^{(*)} \to l\nu l\nu$	7 TeV	135.0	1.1	3.4	0.5 ± 0.6		
	8 TeV	120.0	3.3	1.0	1.9 ± 0.7		
	7 & 8 TeV	125.0	2.8	2.3	1.3 ± 0.5	124-233	137-261
Combined	7 TeV	126.5	3.6	3.2	1.2 ± 0.4		
	8 TeV	126.5	4.9	3.8	1.5 ± 0.4		
	7 & 8 TeV	126.5	6.0	4.9	1.4 ± 0.3	110-582 113-532 (*)	111-122, 131-559 113-114, 117-121, 132-527 (*)

Table 7.1: Characterization of the excess in the $H \to \gamma\gamma$, $H \to ZZ^{(*)} \to 4l$ and $H \to WW^{(*)} \to l\nu l\nu$ channels and the combination of these channels with $H \to ZZ^{(*)}$, $WW^{(*)}$, $b\bar{b}$ and $\tau^+\tau^-$ channels from 7 TeV data. The mass value $M_{\max}$ for which the local significance is maximum, the maximum observed local significance Z_l and the expected local significance $E(Z_l)$ in the presence of a SM BEH boson signal at $M_{\max}$ are given. The best fit value of the signal strength parameter $\hat{\mu}$ at $M_H = 126$ GeV is shown with the total uncertainty. The expected and observed mass ranges excluded at 95% C.L. (99% C.L., indicated by a *) are also given, for the combined $\sqrt{s} = 7$ TeV and $\sqrt{s} = 8$ TeV data [222].

$\lambda(\mu, M_H)$ is used. It is given by:

$$\lambda(\mu, M_H) = \frac{L(\mu, M_H, \hat{\hat{\boldsymbol{\theta}}}(\mu, M_H))}{L(\hat{\mu}, \hat{M}_H, \hat{\boldsymbol{\theta}})} \tag{7.6}$$

where $\hat{\hat{\boldsymbol{\theta}}}(\mu, M_H)$ is the conditional maximum likelihood estimate with μ and M_H fixed.
In the presence of a strong signal, it will produce closed contours around the best-fit point $(\hat{\mu}, \hat{M}_H)$, while in the absence of a signal the contours will be upper limits on μ for all values of M_H. Asymptotically the test statistic $-2ln\lambda(\mu, M_H)$ is distributed as a χ^2 distribution with two degrees of freedom. The asymptoticity was explicitly validated using pseudo-experiments.
Fig. 7.27 shows the resulting 68% and 95% C.L. contours for the $H \to \gamma\gamma$, $H \to ZZ^{(*)} \to 4l$ and $H \to WW^* \to l\nu l\nu$ channels including uncertainties on the energy scale and resolution.

To assess the consistency in mass of the two narrow resonances observed in $H \to \gamma\gamma$ and $H \to ZZ^{(*)} \to 4l$, the profile likelihood ratio $-2ln\lambda(M_H^{\gamma\gamma}, M_H^{4l})$ is considered with $M_H^{\gamma\gamma}$ and M_H^{4l} varying indepently. $\lambda(M_H^{\gamma\gamma}, M_H^{4l})$ is given by:

$$\lambda(M_H^{\gamma\gamma}, M_H^{4l}) = \frac{L(M_H^{\gamma\gamma}, M_H^{4l}, \hat{\hat{\mu}}^{\gamma\gamma}, \hat{\hat{\mu}}^{4l}, \hat{\hat{\boldsymbol{\theta}}})}{L(\hat{M}_H^{\gamma\gamma}, \hat{M}_H^{4l}, \hat{\mu}^{\gamma\gamma}, \hat{\mu}^{4l}, \hat{\boldsymbol{\theta}})} \tag{7.7}$$

Then, the hypothesis $M_H^{\gamma\gamma} = M_H^{4l}$ is tested. This is done by replacing in the numerator of the above profile likelihood ratio $M_H^{\gamma\gamma}$ and M_H^{4l} by M_H. $\mu^{\gamma\gamma}$ and μ^{4l} are allowed to vary independently and are profiled in the numerator of the above profile likelihood ratio. The scan of this likelihood is performed as a function of M_H and the minimum is found to be at $\mu = 3.03$. This minimum follows a χ^2 distribution with one degree of freedom if repeating the same experiment an infinite number of times. The probability of a single BEH-like particle to produce resonant mass peaks in the $H \to \gamma\gamma$ and $H \to ZZ^{(*)} \to 4l$ channels separated by more than the observed mass difference, allowing signal strengths to vary independently, is about $\text{Prob}(3.03, 1) = 8\%$.

The mass of the observed new particle is estimated from the two channels with the highest mass resolution $H \to \gamma\gamma$ and $H \to ZZ^{(*)} \to 4l$ using the profile likelihood ratio $\lambda(M_H)$ given by:

$$\lambda(M_H) = \frac{L(\hat{\hat{\mu}}, M_H, \hat{\hat{\boldsymbol{\theta}}}(M_H))}{L(\hat{\mu}, \hat{M}_H, \hat{\boldsymbol{\theta}})} \tag{7.8}$$

where $\hat{\hat{\mu}}$ and $\hat{\hat{\boldsymbol{\theta}}}(M_H)$ are the conditional maximum likelihood estimates of μ and $\boldsymbol{\theta}$ with M_H fixed.
The signal strength is allowed to vary independently in the two channels, although the result is essentially unchanged when restricting to the SM hypothesis $\mu = 1$. The leading sources of systematic uncertainties come from the electron and photon energy scales and resolutions. The value of M_H maximizing the likelihood $\lambda(M_H)$ is the resulting mass estimate of the new particle. The uncertainties on the mass are determined from $-2ln\lambda(M_H) = 1$ for 1σ band and $-2ln\lambda(M_H) = 4$ for 2σ. The

resulting estimate for the mass of the new particle is:

$$126.0 \pm 0.4\,(\text{stat})\ \pm 0.4\,(\text{sys})\ \text{GeV} \tag{7.9}$$

The mass estimate from the $H \to \gamma\gamma$ channel alone is 126.65 ±0.39 (stat) ±0.52 (sys) GeV for the combined 7 and 8 TeV analyses. It was estimated to be 126.63 ±0.5 (stat) ±0.6 (sys) GeV for the 2011 dataset and 127.1 ±0.6 (stat) ±0.5 (sys) GeV for the 2012 dataset.

The discovery of a new particle with a mass of 126.0 ±0.4 (stat) ±0.4 (sys) GeV was presented. The new particle is compatible with the SM BEH boson. The signal strength parameter μ has a value of 1.4 ± 0.3 at the fitted mass consistent with $\mu = 1$. The new particle is a neutral boson since it decays to a pair of vector bosons whose net electric charge is zero (ZZ, $\gamma\gamma$). It is not a spin-1 particle since it decays into a pair of photons [233, 234]. It is more likely a spin-0 particle, since a spin-2 particle will obviously have different production rates than those of the SM. For what concerns the CP, more than 3σ separation per experiment between 0^+ and 0^- using $4l$ angular distributions is expected for 30 fb^{-1} at $\sqrt{s} = 8$ TeV (see [235, 236]), it will be hopefully reached by the end of this year. Preliminary studies of coupling properties of this new particle have already started, however solid results are expected for a longer time scale. More data is needed to assess the nature of this new particle in detail. The comparison between ATLAS and CMS results will be the subject of the next chapter.

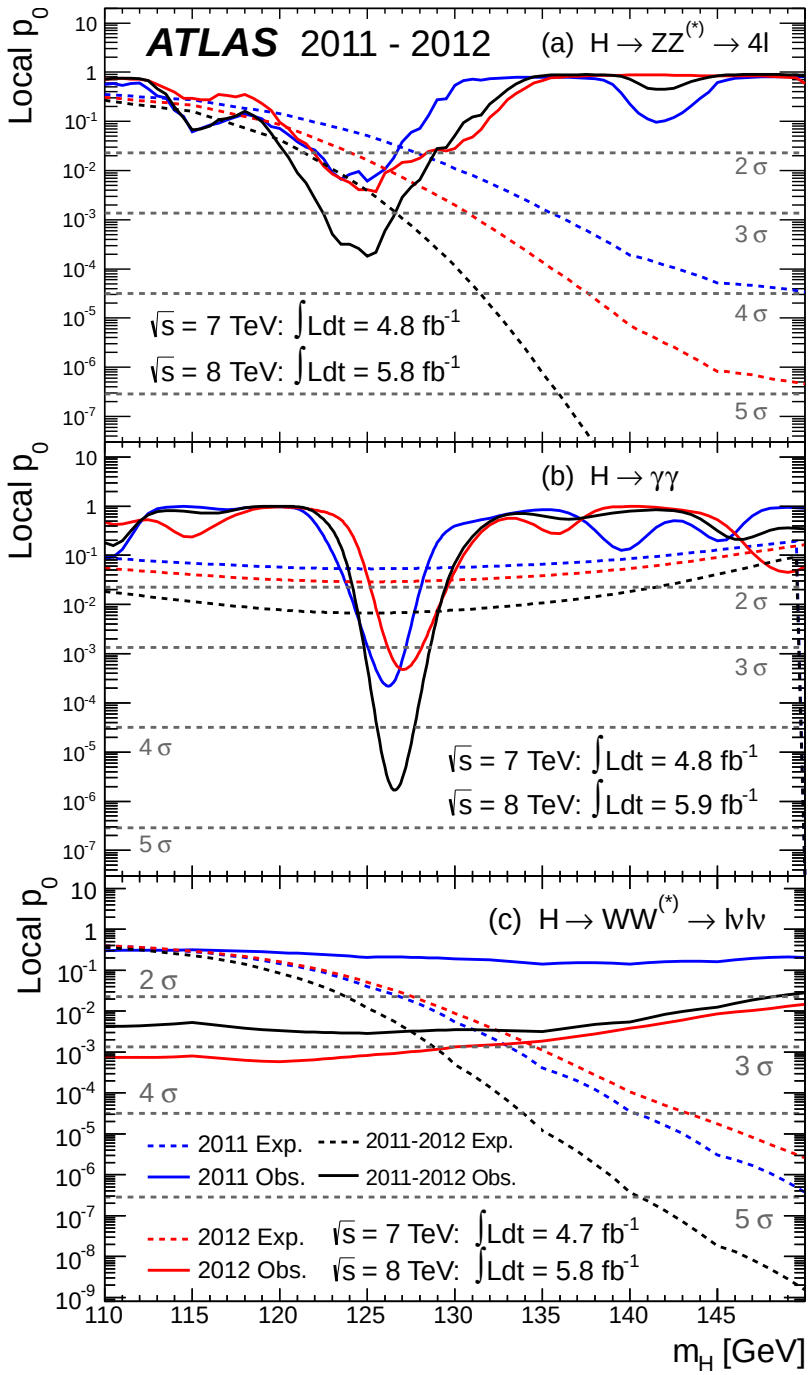

Figure 7.24: The observed local p_0 as a function of the hypothesized BEH boson mass for the $H \to ZZ^* \to 4l$, $H \to \gamma\gamma$ and $H \to WW^* \to l\nu l\nu$ channels. The dashed curves show the expected local p_0 under the hypothesis of a SM BEH boson signal at that mass. Results are shown separately for the $\sqrt{s} = 7$ TeV data (dark blue), the $\sqrt{s} = 8$ TeV (light, red) and their combination (black) [222].

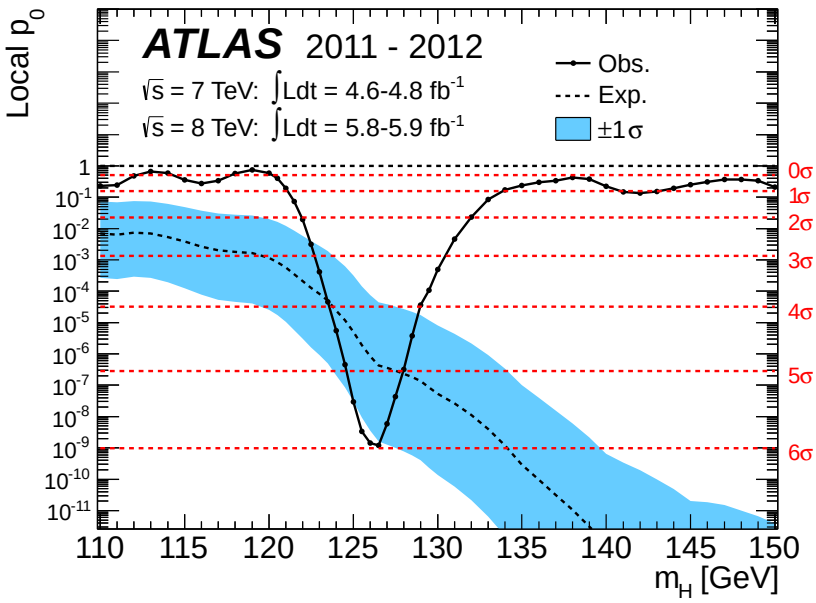

Figure 7.25: The observed (solid) local p_0 as a function of the hypothesized BEH boson mass in the low mass range $110 - 150$ GeV. The dashed curve shows the expected local p_0 under the hypothesis of a SM BEH boson signal with its $\pm 1\sigma$ band. The horizontal dashed lines indicate the p-values corresponding to significances up to 6σ [222].

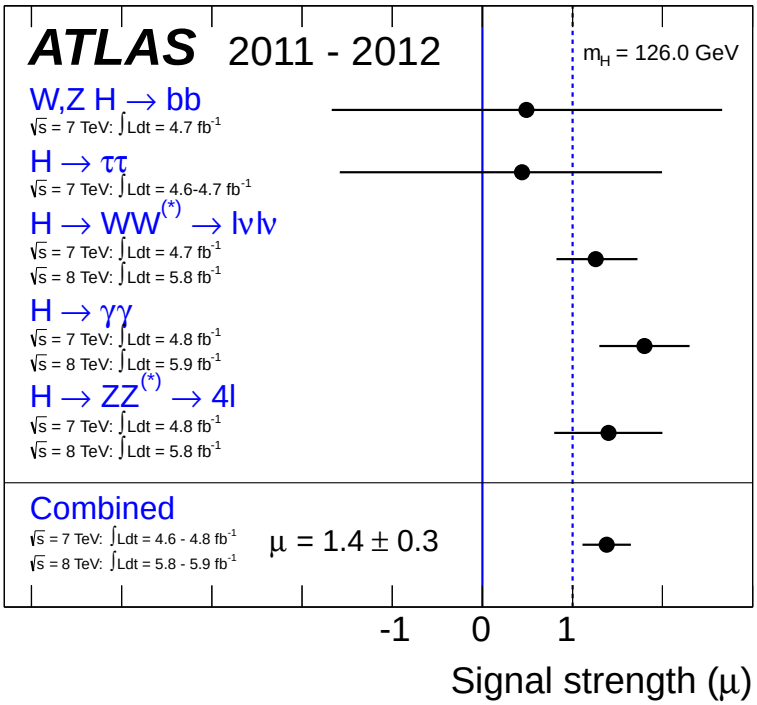

Figure 7.26: Best-fit values of the signal strength parameter for $M_H = 126$ GeV for the individual channels and their combination [222].

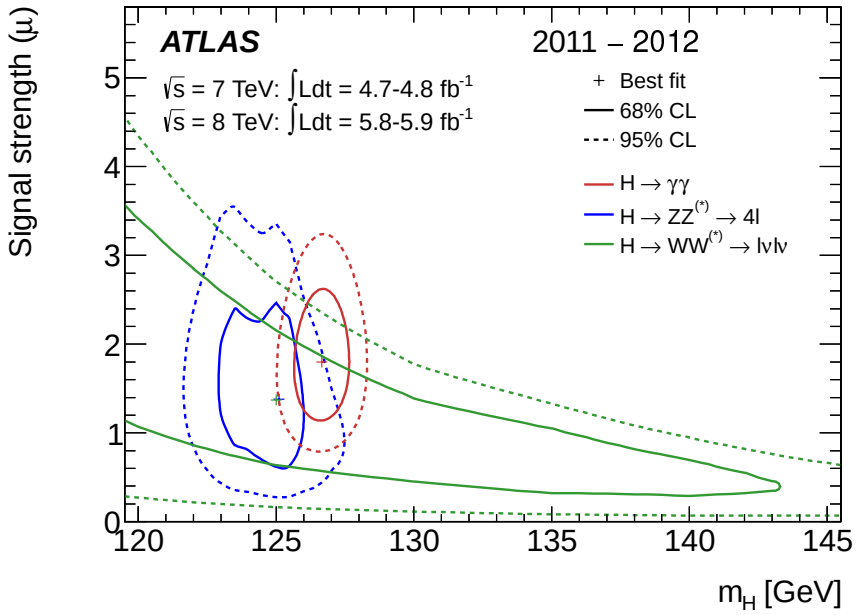

Figure 7.27: Confidence intervals in the (μ, M_H) plane for the $H \to \gamma\gamma$, $H \to ZZ^* \to 4l$ and $H \to WW^* \to l\nu l\nu$ channels, including all systematic uncertainties. The markers indicate the maximum likelihood estimates $(\hat{\mu}, \hat{M}_H)$ in the corresponding channels (the maximum likelihood estimates coincide for the $H \to ZZ^* \to 4l$ and $H \to WW^* \to l\nu l\nu$ channels) [222].

Chapter 8

ATLAS-CMS comparison

The announcement by CERN of a new particle discovery is based on the compatible results obtained by both ATLAS and CMS experiments. As for ATLAS, CMS observed an excess of events around 125 GeV. This excess was quantified by analyzing the full 2011 dataset corresponding to an integrated luminosity of 5.1 fb^{-1} and a 2012 dataset with an integrated luminosity of 5.3 fb^{-1} for the combined decay channels: $\gamma\gamma$, ZZ, WW, $b\bar{b}$, $\tau^+\tau^-$[237]. Its significance was found to be 5.0σ which permits a statement of discovery. The mass of the new particle as measured in CMS is 125.3 ± 0.4 (stat) ± 0.5 (sys) GeV. In this chapter, I will recall briefly the search of the $H \to \gamma\gamma$ in the CMS detector published in [238]. A comparison of $H \to \gamma\gamma$ search results between ATLAS and CMS is discussed in section 8.2. The CMS results for the combined channels [237] are compared to those of ATLAS [222] in section 8.3.

8.1 Observation of the BEH-like particle decaying into a pair of photons with the CMS detector

The search of the scalar boson decaying into two photons with the CMS detector was based on the analysis of the full 2011 dataset corresponding to an integrated luminosity of 5.1 fb^{-1} and a 2012 dataset with an integrated luminosity of 5.3 fb^{-1}. In CMS, photon candidates are reconstructed from clusters in the electromagnetic calorimeter channels around a significant energy deposit, these clusters are then merged to superclusters. In the barrel, five crystal-wide strips in η centered on the most energetic crystal are used to define the superclusters together with a variable extension in ϕ. In the EC, matrices of 5×5 in $x \times y$ crystals around the most energetic crystal are merged if they lie within a narrow road in η. The raw supercluster energy is added to the energy recorded in the preshower detector ($|\eta| > 1.65$). The energy is then corrected for the containment of the shower in the clustered crystals and for loss in the material upstream of the calorimeter. These corrections are computed using a multivariate regression technique based on the boosted decision tree (BDT) implementation in TMVA. The calibration of the CMS electromagnetic calorimeter uses $\pi^0 \to \gamma\gamma$, $W \to e\nu$ and $Z \to e^+e^-$ decays.

An important contribution to the invariant mass resolution comes from the knowledge of the primary vertex. The primary vertex location is determined from a BDT based on kinematic properties of the associated tracks and their correlation with the diphoton kinematic properties. The variables used are: $\sum_{\text{tracks}} p_T^2$; and

two variables quantifying the p_T balance with respect to the diphoton system: $-\sum(\vec{p}_T \cdot \frac{\vec{p}_T^{\gamma\gamma}}{|\vec{p}_T^{\gamma\gamma}|})$; $\left(|\sum \vec{p_T}| - p_T^{\gamma\gamma}\right) / \left(|\sum \vec{p_T}| + p_T^{\gamma\gamma}\right)$; where p_T is the transverse momentum of the associated track and $p_T^{\gamma\gamma}$ the transverse momentum of the diphoton system. In addition, the direction of the converted photon is determined by combining the conversion vertex position and the supercluster position in the electromagnetic calorimeter. In this case, an additional variable is added to the multivariate system estimated for each vertex $\frac{|z_{\text{conv}} - z_{\text{vtx}}|}{\sigma_{\text{conv}}}$.
The vertex-finding efficiency is defined as the efficiency to locate the vertex to within 10 mm of its true position and is measured with $Z \to \mu\mu$ events for the events with unconverted photons. The muon tracks are removed from the collection of tracks used in the vertex reconstruction algorithm to mimic the topology of a BEH boson decaying into two unconverted photons. For converted photons, γ+jet events are used. The ratio of the vertex identification efficiency between data and simulation is close to unity. The remaining difference is applied as a correction to the BEH boson signal model. The overall vertex-finding efficiency for $M_H = 120$ GeV, integrated over its p_T spectrum, is found from simulation to be $83.0 \pm 0.2(\text{stat}) \pm 0.4(\text{sys})\%$ in the 7 TeV sample and $79.0 \pm 0.2(\text{stat})\%$ in the 8 TeV sample. The systematic uncertainty comes from the statistical uncertainty on the efficiency measurement from $Z \to \mu\mu$ (0.2%) and the uncertainty on the BEH boson p_T spectrum (0.3%). The worse efficiency in the 8 TeV sample is due to the larger pile-up in 2012.

The diphoton candidates are triggered with asymmetric transverse energy thresholds (at least 10% lower than the final selections) and two different photon selections:

- loose shower-shape based identification and very loose isolation;
- high R_9, where R_9 is defined as the energy sum of 3×3 crystals centered on the most energetic crystal in the supercluster divided by the energy of the supercluster, used to identify the conversion status of the photon candidate (low R_9 values for converted photons).

The trigger efficiency is found to be 99.5% for all selected events.

The photon candidates have to pass the following selection criteria:

- Both photons have to lie within the electromagnetic calorimeter fiducial region $|\eta| < 2.5$, excluding the barrel-EC transition region $1.44 < |\eta| < 1.57$;
- $p_T^{\gamma_1} > M_{\gamma\gamma}/3$ and $p_T^{\gamma_2} > M_{\gamma\gamma}/4$, where $p_T^{\gamma_1}$ denotes the transverse momentum of the leading photon and $p_T^{\gamma_2}$ that of the subleading photon;
- BDT photon identification having the following variables as input:
  - Shower topology variables corrected for differences between simulation and data;

  - Isolation variables based on the particle flow algorithm;
  - Supercluster pseudorapidity η;
  - the event energy density per unit: to correct for pile-up dependence in the isolation variables.

  The photon identification BDT output retains more than 99% of the signal events and removes 27% of the data events in the range $100 < M_{\gamma\gamma} < 180$ GeV.

- A diphoton BDT is trained on Monte Carlo background and signal BEH events to give a high output value for signal-like events with good diphoton invariant mass resolution based on the following observables:

  - Kinematic characteristics: the relative transverse momenta of both photons: $p_T^{\gamma_{1,2}}/M_{\gamma\gamma}$, their pseudorapidities $\eta^{\gamma_{1,2}}$ and the diphoton opening angle $\cos(\phi^{\gamma_1} - \phi^{\gamma_2})$;
  - Photon identification BDT output value for both photons;
  - Relative diphoton mass resolution: $\sigma_M^{\text{right}}/M_{\gamma\gamma}$ assuming the knowledge of the correct primary vertex;
  - In addition, the relative diphoton mass resolution computed under the assumption of a wrong primary vertex is used since the correct primary vertex is not always selected. The signal events are weighted in the training based on signal-to-background ratio being inversely proportional to the mass resolution. This weight is related to the probability of finding the correct vertex within 10 mm from the true vertex.

Futhermore, to enhance the sensitivity of the analysis, the diphoton candidate events are separated into mutually exclusive categories of different expected signal-to-background ratios. The classification of the diphoton events not satisfying the dijet selection is based on the output of the BDT with category boundaries optimized for sensitivity to a SM BEH boson. Events in the category with the smallest expected signal-to-background ratio (lowest BDT output score) are rejected, leaving four categories of events. Dropping this category translates into a drop of 76% of diphoton data events in the mass range $100 < M_{\gamma\gamma} < 180$ GeV and 22% of the BEH boson events.
Events passing the dijet tag, selecting preferentially VBF production process, are analysed separately. The additional classification of events into dijet-tagged classes improves the sensitivity of the analysis by about 10%. One single class of dijet-tagged events is used for the $\sqrt{s} = 7$ TeV analysis and two classes defined using the dijet invariant mass in the $\sqrt{s} = 8$ TeV analysis. Dijet-tagged events with BDT scores smaller than the threshold for the fourth category are also rejected.

The diphoton candidates events for the dijet-tagged classes have the same selection requirements imposed on the photons as for the other classes with

the exception on the p_T threshold on the leading photon which is increased to $p_T^{\gamma 1} > M_{\gamma\gamma}/2$. The jets have to pass the following selection criteria:

- Two jets within the pseudorapidity region $|\eta| < 4.7$ and $p_T > 30$ GeV. For the loose dijet class used in the 8 TeV analysis, the p_T of the subleading jet is required to be greater than 20 GeV;
- Jet separation $\Delta\eta_{jj} > 3.0$;
- Dijet invariant mass $M_{jj} > 500$ GeV. For the loose dijet class used in the $\sqrt{s} = 8$ TeV analysis, this requirement is changed to $M_{jj} > 250$ GeV;
- $|(\eta^{jet_1} + \eta^{jet_2})/2 - \eta^{\gamma\gamma}| < 2.5$;
- $|\Delta\phi_{jj-\gamma\gamma}| > 2.6$.

Fig. 8.1 shows the number of expected signal events from a SM BEH boson with a mass $M_H = 125$ GeV as well as the estimated background for the different categories separately for the 7 and 8 TeV datasets. The fraction of each production process as well as the mass resolution, measured both by σ_{eff} [1] and by FWHM, are also shown.

Expected signal and estimated background										
Event classes		SM Higgs boson expected signal (m_H=125 GeV)							Background $m_{\gamma\gamma} = 125$ GeV (ev./GeV)	
		Total	ggH	VBF	VH	ttH	σ_{eff} (GeV)	FWHM/2.35 (GeV)		
7 TeV 5.1 fb^{-1}	Untagged 0	3.2	61%	17%	19%	3%	1.21	1.14	3.3	$\pm$ 0.4
	Untagged 1	16.3	88%	6%	6%	1%	1.26	1.08	37.5	$\pm$ 1.3
	Untagged 2	21.5	91%	4%	4%	–	1.59	1.32	74.8	$\pm$ 1.9
	Untagged 3	32.8	91%	4%	4%	–	2.47	2.07	193.6	$\pm$ 3.0
	Dijet tag	2.9	27%	73%	1%	–	1.73	1.37	1.7	$\pm$ 0.2
8 TeV 5.3 fb^{-1}	Untagged 0	6.1	68%	12%	16%	4%	1.38	1.23	7.4	$\pm$ 0.6
	Untagged 1	21.0	88%	6%	6%	1%	1.53	1.31	54.7	$\pm$ 1.5
	Untagged 2	30.2	92%	4%	3%	–	1.94	1.55	115.2	$\pm$ 2.3
	Untagged 3	40.0	92%	4%	4%	–	2.86	2.35	256.5	$\pm$ 3.4
	Dijet tight	2.6	23%	77%	–	–	2.06	1.57	1.3	$\pm$ 0.2
	Dijet loose	3.0	53%	45%	2%	–	1.95	1.48	3.7	$\pm$ 0.4

Figure 8.1: Expected number of SM BEH boson events ($M_H = 125$ GeV) and estimated background (at $M_H = 125$ GeV) for all the event classes of the 7 and 8 TeV datasets. The composition of the SM BEH boson signal in terms of the production process and its mass resolution is also given [238].

For the dominant gluon-gluon fusion process, the BEH boson transverse momentum has been reweighted to the NNLL + NLO distribution computed by the HqT program. The gluon-gluon fusion process cross-section is reduced by 2.5% for all values of M_H to take into account for the interference between the gluon fusion signal and the $gg \to \gamma\gamma$ background process [218]. The simulated events are

[1] Half the minimum width containing 68.3% of the signal events.

reweighted to match the distribution of the mean number of interactions in data. Fig. 8.2 summarizes the sources of systematic uncertainty on the signal considered in the analysis.

Sources of systematic uncertainty		**Uncertainty**	
Per photon		Barrel	Endcap
Photon selection efficiency		0.8%	2.2%
Energy resolution ($\Delta\sigma/E_{MC}$)	$R_9 > 0.94$ (low η, high η)	0.22%, 0.60%	0.90%, 0.34%
	$R_9 < 0.94$ (low η, high η)	0.24%, 0.59%	0.30%, 0.52%
Energy scale ($(E_{data} - E_{MC})/E_{MC}$)	$R_9 > 0.94$ (low η, high η)	0.19%, 0.71%	0.88%, 0.19%
	$R_9 < 0.94$ (low η, high η)	0.13%, 0.51%	0.18%, 0.28%
Photon identification BDT (Effect of up to 4.3% event class migration.)		±0.01 (shape shift)	
Photon energy resolution BDT (Effect of up to 8.1% event class migration.)		±10% (shape scaling)	
Per event			
Integrated luminosity		4.4%	
Vertex finding efficiency		0.2%	
Trigger efficiency	One or both photons $R_9 < 0.94$ in endcap	0.4%	
	Other events	0.1%	
Dijet selection			
Dijet-tagging efficiency	VBF process	10%	
	Gluon-gluon fusion process	50%	
(Effect of up to 15% event migration among dijet classes.)			
Production cross sections		Scale	PDF
Gluon-gluon fusion		+12.5% -8.2%	+7.9% -7.7%
Vector boson fusion		+0.5% -0.3%	+2.7% -2.1%
Associated production with W/Z		1.8%	4.2%
Associated production with $t\bar{t}$		+3.6% -9.5%	8.5%
Scale and PDF uncertainties (Effect of up to 12.5% event class migration.)		(y, p_T)-differential	

Figure 8.2: Sources of systematic uncertainties considered for the $\sqrt{s} = 8$ TeV analysis. The magnitude of the variation of the source that has been applied to the signal model is shown [238].

The background is estimated from data by fitting the diphoton invariant mass distribution in each of the categories in the range $100 < M_{\gamma\gamma} < 180$ GeV. The choice of the function used to model the background and of the fit range are made based on a study of the possible bias on the measured signal strength. An acceptable maximum bias on the fitted signal strength has been taken as five times smaller than the statistical accuracy. Polynomial functions are selected with a degree ranging from 3 to 5.

Fig. 8.3 shows the local p-value for the 7 and 8 TeV datasets separately as well as for the combined datasets. The local p_0 corresponding to the largest upward

fluctuation of the observed limit at 125 GeV has been computed to be 1.8×10^{-5} i.e 4.1σ. Taken into account the LEE, the probability under the background-only hypothesis of observing a similar or larger excess in the full analysis mass range $110 < M_H < 150$ GeV is 7.2×10^{-4} corresponding to a global significance of 3.2σ. The best fit signal strength is 1.56 ± 0.43 times the SM BEH boson cross section.

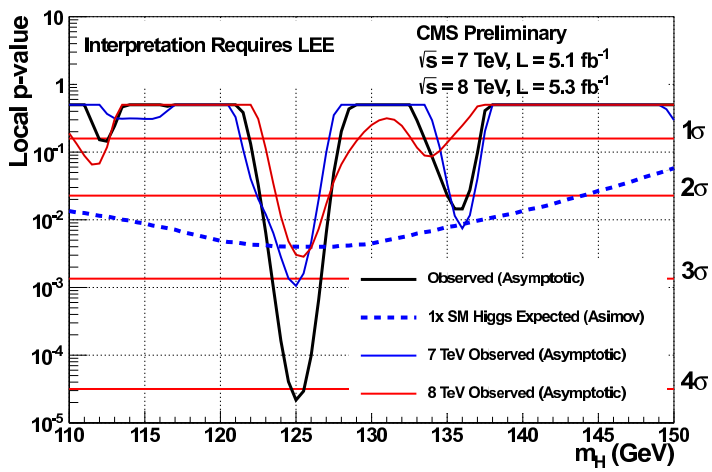

Figure 8.3: Observed local p_0 as a function of M_H for the combined 7 and 8 TeV analyses and for the $\sqrt{s} = 7$ TeV and $\sqrt{s} = 8$ TeV separately. The expected local p_0 is also shown in dashed line for the combined 7 and 8 TeV analyses [238].

8.2 ATLAS-CMS comparison in the $H \to \gamma\gamma$ channel

In the following, I will summarize the main differences between ATLAS and CMS $H \to \gamma\gamma$ analyses published respectively in [222] and [238, 237]. For more details, see [239, 240].

Table 8.1 shows the main differences in the analyses between ATLAS and CMS. CMS analysis is MVA-based (6 different MVA are used). The systematic uncertainty on the photon selection efficiency in CMS (0.8% in the barrel and 2.2% in the EC) is smaller than in ATLAS (around 5%).

Table 8.2 shows the comparison of the background modeling used to fit the invariant mass distribution in data.

Table 8.3 shows the comparison of the number of expected signal events, estimated background events, purity and mass resolution between ATLAS and CMS. The number of expected signal events is similar, the number of background events is smaller by $\sim 30\%$ in CMS thanks in particular to the diphoton BDT. The invariant mass resolutions are similar for the inclusive distributions. However, due to the better intrinsic energy resolution of the crystal calorimeter in CMS, the resolution in the best category is better in CMS. Taking into account the tails comparing σ_{eff},

ATLAS is slightly better due to the smaller constant terms and the more robust determination of the primary vertex.
Table 8.4 shows the comparison for the final results between ATLAS and CMS. The sensitivity is similar in both experiments (slightly better in CMS), the mass is slightly higher in ATLAS than in CMS but compatible within the statistical uncertainty. The observed significance and the fitted signal strength value are higher in ATLAS.

	ATLAS	CMS
Luminosity	4.8 fb^{-1} at 7 TeV 5.9 fb^{-1} at 8 TeV	5.1 fb^{-1} at 7 TeV 5.3 fb^{-1} at 8 TeV
Calibration	MC-based	MVA-based
Photon Kinematics	$p_T^{\gamma_1} > 40$ GeV $p_T^{\gamma_2} > 30$ GeV $\lvert\eta\rvert < 2.37$ (excluding $1.37 - 1.52$)	$p_T^{\gamma_1} > M_{\gamma\gamma}/3$ $p_T^{\gamma_2} > M_{\gamma\gamma}/4$ $\lvert\eta\rvert < 2.5$ (excluding $1.44 - 1.57$)
Jet Selection	$p_T^{jet} > 25$ GeV ($p_T^{jet} > 30$ GeV for $\lvert\eta\rvert > 2.5$ for 8 TeV) $JVF > 0.75$ $\lvert\eta\rvert < 4.5$ $\Delta\eta_{jj} > 2.8$ $M_{jj} > 400$ GeV $\lvert\Delta\phi_{jj-\gamma\gamma}\rvert > 2.6$	$p_T^{jet} > 30$ GeV ($p_T^{jet_2} > 20$ GeV for the loose dijet class) $\lvert(\eta^{jet_1} + \eta^{jet_2})/2 - \eta^{\gamma\gamma}\rvert < 2.5$ $\lvert\eta\rvert < 4.7$ $\Delta\eta_{jj} > 3.0$ $M_{jj} > 500$ GeV ($M_{jj} > 250$ GeV for the loose dijet class) $\lvert\Delta\phi_{jj-\gamma\gamma}\rvert > 2.6$
PV selection	Likelihood (calorimeter pointing + tracking + conversion)	MVA (tracking + p_T balance + conversion)
Identification	Neural network and cut based (NN2011 for 7 TeV and Tight2012 for 8 TeV)	MVA based
Isolation	Topocluster-based	Particle-flow (included in photon Id BDT)
Categorization	9 categories (conversion, η, p_{Tt}) 2-jet	4 categories (based on diphoton BDT) 2-jet (2 classes for 8 TeV tight and loose)

Table 8.1: Comparison between ATLAS and CMS analyses for the $H \to \gamma\gamma$ channel.

	ATLAS	CMS
Acceptance Criteria	Spurious signal $< 20\%$ of the fitted signal uncertainty Or spurious signal $< 10\%$ of the fitted signal yield	Bias $< 20\%$ of the fitted signal uncertainty
Parametrizations	Bernstein Polynomial 4th order Exponential of 2nd order polynomial Exponential	Polynomials 3rd - 5th order

Table 8.2: Comparison between ATLAS and CMS background modeling used to fit the diphoton invariant mass distributions.

	ATLAS	CMS
Expected signal events for $M_H = 125$ GeV (per fb^{-1})	17 (7 TeV) 19 (8 TeV)	15 (7 TeV) 19 (8 TeV)
Background events at a mass of 125 GeV (per GeV per fb^{-1})	100	70
Purity	$80 \pm 4\%$ (7 TeV) $75 + 3 - 2\%$ (8 TeV)	72%
Inclusive mass resolution at $M_H = 120$ GeV (FWHM/2.35)	1.61 GeV (7 TeV) 1.65 (8 TeV)	1.35 GeV (7 TeV) 1.57 GeV (8 TeV)
(FWHM/2.35) for the best category at 120 GeV	1.31 GeV (7 TeV) 1.32 (8 TeV)	1.07 GeV (7 TeV) 1.21 GeV (8 TeV)
Inclusive σ_{eff}	1.75 GeV (7 TeV) 1.73 (8 TeV)	1.76 GeV (7 TeV) 2.06 GeV (8 TeV)

Table 8.3: Comparison between ATLAS and CMS for the expected signal yields, observed background in data, purity and invariant mass resolution.

	ATLAS	CMS
Fitted signal strength ($\hat{\mu}$)	1.8 ± 0.5 at $M_H = 126.5$ GeV	1.6 ± 0.4 at $M_H = 125$ GeV
Expected median limit 95% C.L	0.8 SM at $M_H = 125$ GeV	0.76 SM at $M_H = 125$ GeV
Expected exclusion 95% C.L	$110 - 139.5$ GeV	$110 - 145$ GeV
Observed exclusion 95% C.L	$112 - 123$ GeV $132 - 143.5$ GeV	$114 - 121$ GeV $129 - 132$ GeV and $138 - 149$ GeV
Expected local significance	2.5σ at $M_H = 126.5$ GeV	2.7σ at $M_H = 125$ GeV
Observed local significance	4.5σ at $M_H = 126.5$ GeV	4.1σ at $M_H = 125$ GeV
Observed global significance	3.6σ for $110 < M_H < 150$ GeV	3.2σ for $110 < M_H < 150$ GeV
Mass measurement	126.7 ± 0.4 (stat) ± 0.5 (sys) GeV	125.1 ± 0.4 (stat) ± 0.6 (sys) GeV [241]

Table 8.4: Comparison between ATLAS and CMS for the characterization of the observed excess in the $H \to \gamma\gamma$ channel.

8.3 ATLAS-CMS comparison in the combined channels

The search for the SM scalar boson in CMS is performed in the five decay modes: $\gamma\gamma$, ZZ, WW, $\tau^+\tau^-$ and $b\bar{b}$. For all these channels, the full 2011 $\sqrt{s} = 7$ TeV dataset corresponding to a luminosity of 5.1 fb^{-1} and the 2012 $\sqrt{s} = 8$ TeV dataset with an integrated luminosity of 5.3 fb^{-1} are analyzed. The BEH boson is excluded at 95% C.L. in the mass ranges $110 - 121.5$ GeV and $127 - 600$ GeV. An excess has been observed with a local significance of 5.0σ at a mass around 125 GeV, indicating the presence of a new particle. The contribution to the excess originates mainly from the two decay modes with the best mass resolution $\gamma\gamma$ and ZZ. Fig. 8.4 shows the local p_0 values as a function of M_H for the five decay modes and the overall combination for the combined 2011 and 2012 datasets. Fig. 8.5 shows the best fit signal strength values at $M_H = 125.5$ GeV for the combined channels and for the five channels separately. The best fit values are compatible with the SM hypothesis $\mu = 1$ within the statistical uncertainties.

A comparison between ATLAS and CMS of the characteristics of the observed excess is shown in Table 8.5 for the decay modes ZZ, $\gamma\gamma$ and WW

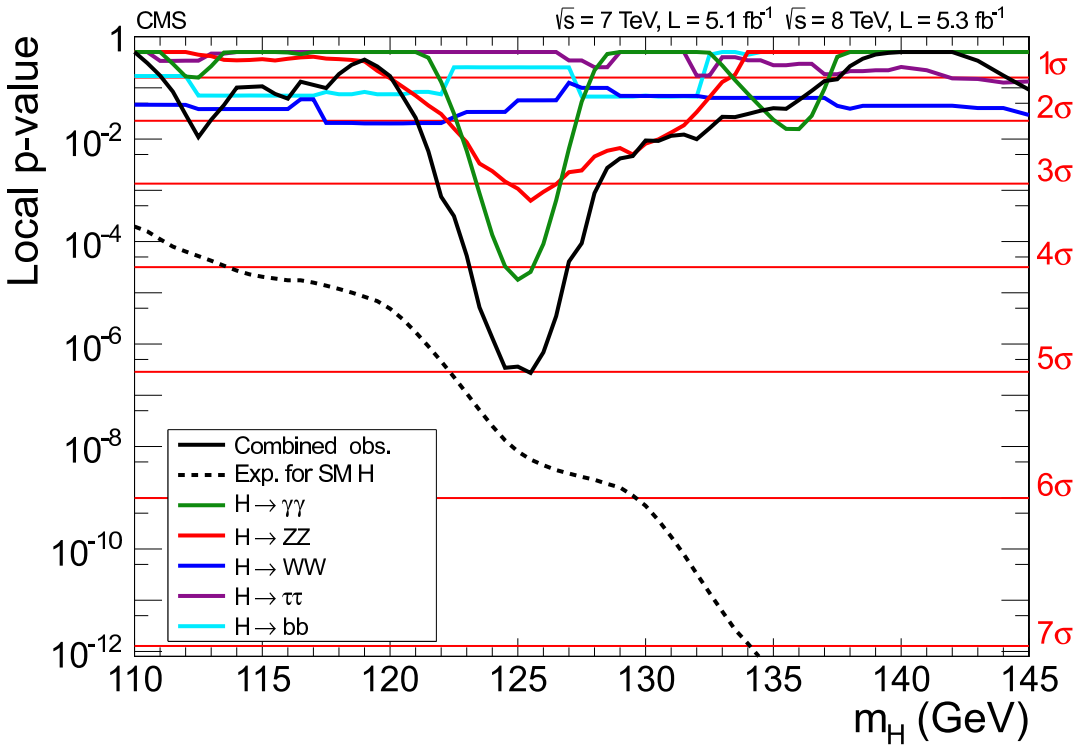

Figure 8.4: Observed local p_0 as a function of M_H for the five decay modes and the overall combination for the combined 7 and 8 TeV analyses in CMS. The dashed line shows the combined expected local p_0 for a SM BEH boson with a mass M_H [237].

separately along with the combined channels. The excess is compatible in terms of significance in the separate channels as well as for the combination between both experiments within the statistical uncertainties. The better combined expected significance in CMS originates from the better expected significance in the ZZ decay mode (due in particular to the use of the angular distributions) and to the update of the $b\bar{b}$ and $\tau^+\tau^-$ analyses with the $\sqrt{s} = 8$ TeV datasets.

The combined best-fit mass is 125.3 ± 0.4 (stat) ±0.5 (sys) GeV which is compatible with the mass quoted by ATLAS 126.0 ± 0.4 (stat) ±0.4 (sys) GeV. Again, the results are consistent with a SM BEH boson although more data is needed for confirmation.

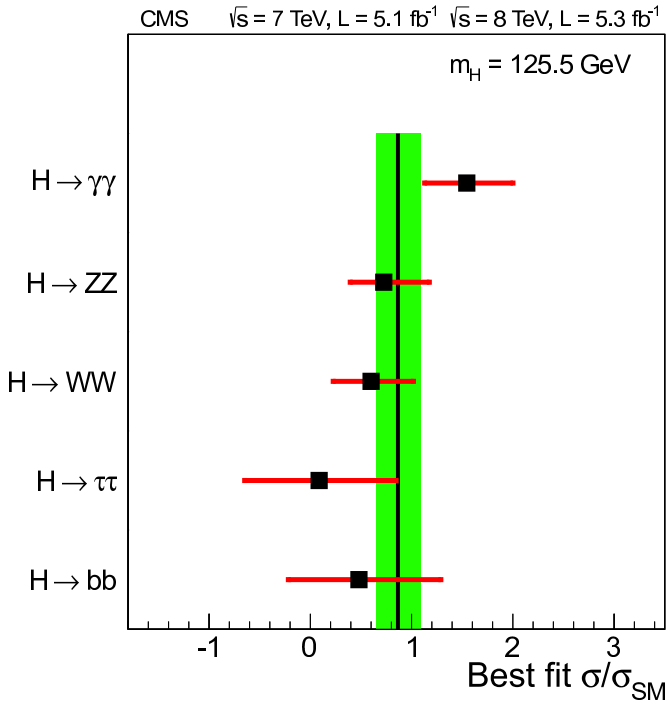

Figure 8.5: Best fit signal strength at $M_H = 125.5$ GeV for the combined channels (solid vertical line) and for individual channels. The vertical band shows the overall $\hat{\mu}$ value 0.87 ± 0.23. The horizontal bars indicate the $\pm 1\sigma$ uncertainty (including both statistical and systematic uncertainties) on the best fit values for individual modes [237].

Search channel	Collab	$M_{\max}$ [GeV]	$Z_l\,[\sigma]$	$E(Z_l)\,[\sigma]$	$\hat{\mu}$
$H \to ZZ^{(*)} \to 4l$	ATLAS	125.0	3.6	2.7	1.4 ± 0.6 for $M_H = 126$ GeV
	CMS	125.6	3.2	3.8	$0.7 + 0.4 - 0.3$ for $M_H = 125.6$ GeV
$H \to \gamma\gamma$	ATLAS	126.5	4.5	2.5	1.8 ± 0.5 for $M_H = 126$ GeV
	CMS	125.0	4.1	2.7	1.6 ± 0.4 for $M_H = 125$ GeV
$H \to WW^{(*)} \to l\nu l\nu$	ATLAS	125.0	2.8	2.3	1.3 ± 0.5 for $M_H = 126$ GeV
	CMS	125.0	1.6	2.4	0.6 ± 0.4 for $M_H = 125$ GeV
Combined	ATLAS	126.5	6.0	4.9	1.4 ± 0.3 for $M_H = 126$ GeV
	CMS	125.5	5.0	5.8	0.9 ± 0.2 for $M_H = 125.5$ GeV

Table 8.5: Characterization of the excess in the $H \to \gamma\gamma$, $H \to ZZ^{(*)} \to 4l$ and $H \to WW^{(*)} \to l\nu l\nu$ channels and the combination of these channels with $H \to ZZ^{(*)}$, $WW^{(*)}$, $b\bar{b}$ and $\tau^+\tau^-$ channels from $\sqrt{s} = 7$ TeV data for ATLAS and 7+8 TeV data for CMS. The mass value $M_{\max}$ for which the local significance is maximum, the maximum observed local significance Z_l and the expected local significance $E(Z_l)$ in the presence of a SM BEH boson signal at $M_{\max}$ are compared. The best fit value of the signal strength parameter $\hat{\mu}$ is shown with the total uncertainty for both ATLAS and CMS analyses.

Conclusion

During the last three years, the LHC has shown an outstanding performance. The energy has increased from $\sqrt{s} = 900$ GeV to $\sqrt{s} = 8$ TeV. The total integrated luminosity collected has reached ~ 10 fb^{-1} before the technical stop in June 2012. Both ATLAS and CMS experiments have analyzed and published historical results after the seminar of July 4th 2012 at CERN, thanks to the work of thousands of people for the last twenty years. Both detectors have shown very good performance and the analyses have undergone major improvements.

In particular, the $H \rightarrow \gamma\gamma$ analysis in ATLAS has remarkably evolved the last three years. With the data taking, we achieved a better understanding of the detector, in particular of the electromagnetic calorimeter. This allowed an amelioration of the photon reconstruction and identification. A neural network based identification was developed for the improved analysis of the full 2011 dataset. The energy calibration has also known important progress. The constant term as measured in the data is of the order of 1% except in the region $1.5 < |\eta| < 2.8$ where it is 2.5%. In addition, the energy response shows a remarkable stability with time and increasing pile-up.
The isolation method used to determine isolated photons is improved as well. Three dimensional noise suppressed topological clusters are used. The new isolation shows a very nice stability with respect to pile-up.
In addition, a very important improvement was implemented dealing with the algorithm used to locate the primary vertex. A global likelihood combines the "pointing" direction of the photons, the average beam spot position and the sum $\sum p_T^2$ of the tracks associated with each reconstructed vertex. The conversion vertex is also used in the likelihood for converted photons. This method shows a very good robustness with the increasing pile-up. The diphoton invariant mass resolution computed using the likelihood method for the primary vertex selection was compared using $H \rightarrow \gamma\gamma$ Monte Carlo samples to the case where the true vertex is used. Only a 3% room of improvement remains.
The comparison of shower shape variables between data and Monte Carlo simulation was subject of many discrepancies. The most important part of these differences was understood and corrected for in the simulation.
A much better understanding of the background has lead to a higher diphoton purity. This purity is estimated to be 80% $\pm$4% in the $\sqrt{s} = 7$ TeV dataset and $75 + 3 - 2$% in the $\sqrt{s} = 8$ TeV dataset.
Since an unbinned likelihood is used in the $H \rightarrow \gamma\gamma$ analysis, an analytic function is fitted on the data and taken as a background modeling. The choice of the analytic function was subject of different studies. It was decided to choose parametrizations

for which the estimated bias is smaller than 20% of the uncertainty on the fitted signal yield or where the bias is smaller than 10% of the expected signal events. The final choice between parametrizations was based on the expected p_0 values. Finally, a set of polynomials, exponentiated polynomials and exponential functions were selected.
The categorization of the analyses was also made more accurate. 10 categories were finally selected following the photon positions in the calorimeter, their conversion status, the value of p_{Tt}. The 10th category is a 2-jet category with a VBF-like signature.
The systematic uncertainties on the signal yields and on the mass resolution were accurately evaluated and pessimistic values were adopted in the analysis.

The analysis of the full 2011 dataset corresponding to an integrated luminosity of 4.8 fb^{-1} at $\sqrt{s} = 7$ TeV and of a 2012 dataset with an integrated luminosity of 5.9 fb^{-1} at $\sqrt{s} = 8$ TeV includes all these improvements. As a result, an excess of events over the background is observed at a mass of 126.5 GeV with a significance of 4.5σ. The fitted signal strength parameter is found to be 1.8 $\pm$0.5. This value exceeds the Standard Model hypothesis by less than 2σ. However since the error is dominated by the statistical uncertainty, more data is needed before making any assumption.

A combination of the analyses of individual searches in the channels $H \to \gamma\gamma$, $H \to ZZ^{(*)} \to 4l$ and $H \to WW^{(*)} \to e\nu\mu\nu$ from $\sqrt{s} = 8$ TeV data; previously published results of searches in the channels $H \to ZZ^{(*)}$, $WW^{(*)}$, $b\bar{b}$ and $\tau^+\tau^-$ for the 7 TeV data; and the improved analyses of the $H \to \gamma\gamma$ and $H \to ZZ^{(*)} \to 4l$ for the 7 TeV data is published. The results show an excess of events for a mass of 126.5 GeV with a significance of 5.9σ and provide a conclusive evidence for the discovery of a new particle. The mass of the new particle was measured from the two channels with the highest mass resolution, $H \to \gamma\gamma$ and $H \to ZZ^{(*)} \to 4l$, and is found to be: 126.0 $\pm$0.4 (stat) $\pm$0.4 (sys) GeV. If this particle is the Standard Model BEH boson with a mass of 126 GeV, it will be particular suited for studies at the LHC since it decays to many final states that can be experimentally reconstructed.

This discovery opens a new chapter in the history of Particle Physics. The major goal now is to establish the nature of this particle by determining its properties. These include the precise measurement of the mass, the width, the spin/CP quantum numbers, the cross-section, the branching ratio and the couplings to fermions and vector bosons.

Bibliography

[1] C-N. Yang and R. Mills, *Conservation of Isotopic Spin and Isotopic Gauge Invariance*, Phys.Rev.96:191-195, 1954. (Cited on page 2.)

[2] M. Baker and S.L. Glashow *Spontaneous Breakdown of Elementary Particle Symmetries*, Phys.Rev.128:2462-2471, 1962. (Cited on page 2.)

[3] W. Heisenberg, *Zur Theorie des Ferromagnetismus*, Z.Phys.49:619, 1928. (Cited on page 2.)

[4] V. L. Ginzburg, L. D. Landau, *On the Theory of superconductivity*, Zh.Eksp.Teor.Fiz.20:1064-1082, 1950. (Cited on page 2.)

[5] Y. Nambu, *Quasiparticles and Gauge Invariance in the Theory of Superconductivity*, Phys.Rev.117:648-663, 1960. (Cited on page 3.)

[6] Y. Nambu, *Axial vector current conservation in weak interactions*, Phys.Rev.Lett.4:380-382, 1960. (Cited on page 3.)

[7] Y. Nambu and G. Jona-Lasinio, *Dynamical Model of Elementary Particles Based on an Analogy with Superconductivity.I*, Phys.Rev.122:345-358, 1961. (Cited on page 3.)

[8] Y. Nambu and G. Jona-Lasinio, *Dynamical Model of Elementary Particles Based on an Analogy with Superconductivity.II*, Phys.Rev.124:246-254, 1961. (Cited on page 3.)

[9] J. Bardeen, L. N. Cooper, J. R. Schrieffer, *Theory of superconductivity*, Phys.Rev.108:1175-1204, 1957. (Cited on page 3.)

[10] J. Goldstone, *Field Theories with Superconductor Solutions*, Nuovo Cim.19:154-164, 1961. (Cited on page 3.)

[11] J. Goldstone, A. Salam and S. Weinberg, *Broken Symmetries*, Phys.Rev.127:965-970, 1962. (Cited on page 4.)

[12] F. Englert and R. Brout, *Broken Symmetry and the Mass of Gauge Vector Mesons*, Phys.Rev.Lett.13:321-323, 1964. (Cited on page 4.)

[13] P. Higgs, *Broken symmetries, massless particles and gauge fields*, Phys.Lett.12:132-133, 1964. (Cited on page 4.)

[14] P. Higgs, *Broken Symmetries and the Masses of Gauge Bosons*, Phys.Rev.Lett.13:508-509, 1964. (Cited on page 4.)

[15] G. S. Guralnik, C. R. Hagen and T. W. B. Kibble, *Global Conservation Laws and Massless Particles*, Phys.Rev.Lett.13:585-587, 1964. (Cited on page 4.)

[16] P. Anderson, *Plasmons, Gauge Invariance, and Mass*, Phys.Rev.130:439-442, 1963. (Cited on page 4.)

[17] J. Schwinger, *Gauge Invariance and Mass. 1*, Phys.Rev.125:397-398, 1962. (Cited on page 4.)

[18] J. Schwinger, *Gauge Invariance and Mass. 2*, Phys.Rev.128:2425-2429, 1962. (Cited on page 4.)

[19] P. Higgs, *Spontaneous Symmetry Breakdown without Massless Bosons*, Phys.Rev.145:1156-116, 1966. (Cited on page 4.)

[20] T. Kibble, *Symmetry breaking in nonAbelian gauge theories*, Phys.Rev.155:1554-1561, 1967. (Cited on page 4.)

[21] S. Weinberg, *A model of leptons*, Phys.Rev.Lett.19:1264-1266, 1967. (Cited on page 4.)

[22] A. Salam, *Weak and electromagnetic interactions*, "Elementary Particle Theory, Stockholm", Almquist and Wiksell, 1968. (Cited on page 4.)

[23] S.L. Glashow, *Partial Symmetries of Weak Interactions*, Nucl.Phys.22:579-588, 1961. (Cited on page 4.)

[24] A. Salam, J.C. Ward, *Electromagnetic and weak interactions*, Phys.Lett.13:168-171, 1964. (Cited on page 4.)

[25] L.D. Faddeev, V.N. Popov, *Feynman Diagrams for the Yang-Mills Field*, Phys.Lett.B25:29-30, 1967. (Cited on page 5.)

[26] G.'t Hooft, *Renormalization of Massless Yang-Mills Fields*, Nucl.Phys.B33:173-199, 1971. (Cited on page 5.)

[27] G.'t Hooft, *Renormalizable Lagrangians for Massive Yang-Mills Fields*, Nucl.Phys.B35:167-188, 1971. (Cited on page 5.)

[28] B. W. Lee and J. Zinn-Justin, *Spontaneously Broken Gauge Symmetries. 1. Preliminaries*, Phys.Rev.D5:3121-3137, 1972. (Cited on page 5.)

[29] B. W. Lee and J. Zinn-Justin, *Spontaneously broken gauge symmetries. 2. perturbation theory and renormalization*, Phys.Rev.D5:3137-3155, 1972, Erratum-ibid.D8:4654, 1973. (Cited on page 5.)

[30] B. W. Lee and J. Zinn-Justin, *Spontaneously broken gauge symmetries. 3. Equivalence*, Phys.Rev.D5:3155-3160, 1972. (Cited on page 5.)

[31] G.'t Hooft, M.J.G. Veltman, *Regularization and Renormalization of Gauge Fields*, Nucl.Phys.B44:189-213, 1972. (Cited on page 5.)

[32] C. Becchi, A. Rouet, R. Stora, *The abelian Higgs Kibble model, Unitarity of the S operator*, Phys.Lett.B52:344, 1974. (Cited on page 5.)

[33] C. Becchi, A. Rouet, R. Stora, *Renormalization of the Abelian Higgs-Kibble Model*, Commun.Math.Phys.42:127-162, 1975. (Cited on page 5.)

[34] C. Becchi, A. Rouet, R. Stora, *Renormalization of Gauge Theories*, Annals Phys.98:287-321, 1976. (Cited on page 5.)

[35] I.V. Tyutin, Lebedev Institute preprint N39, 1975. (Cited on page 5.)

[36] S. L. Glashow, J. Iliopoulos and L. Maiani, *Weak Interactions with Lepton-Hadron Symmetry*, Phys.Rev.D2:1285-1292, 1970. (Cited on page 5.)

[37] C. Bouchiat, J. Iliopoulos, P. Meyer, *An Anomaly Free Version of Weinberg's Model*, Phys.Lett.B38:519-523, 1972. (Cited on page 5.)

[38] F. J. Hasert et al. (Gargamelle Collaboration), *Search For Elastic Muon-Neutrino Electron Scattering*, Phys.Lett.B46:121-124, 1973. (Cited on page 5.)

[39] F. J. Hasert et al. (Gargamelle Collaboration), *Observation of Neutrino Like Interactions Without Muon Or Electron in the Gargamelle Neutrino Experiment*, Phys.Lett.B46:138-140, 1973. (Cited on page 5.)

[40] F. J. Hasert et al. (Gargamelle Collaboration), *Observation of Neutrino Like Interactions Without Muon Or Electron in the Gargamelle Neutrino Experiment*, Nucl.Phys.B73:1-22, 1974. (Cited on page 5.)

[41] C. Y. Prescott et al., *Parity Nonconservation in Inelastic Electron Scattering*, Phys.Lett.B77:347-352, 1978. (Cited on page 5.)

[42] UA1 Collaboration, *Experimental Observation of Isolated Large Transverse Energy Electrons with Associated Missing Energy at* $\sqrt{s} = 540\ GeV$, Phys.Lett.B122:103-116, 1983. (Cited on page 5.)

[43] UA2 Collaboration, *Observation of Single Isolated Electrons of High Transverse Momentum in Events with Missing Transverse Energy at the CERN* $\bar{p}p$ *Collider*, Phys.Lett.B122:476-485, 1983. (Cited on page 5.)

[44] UA1 Collaboration, *Experimental Observation of Lepton Pairs of Invariant Mass Around* 95 GeV/c^2 *at the CERN SPS Collider*, Phys.Lett.B126:398-410, 1983. (Cited on page 5.)

[45] UA2 Collaboration, *Evidence for* $Z^0 \to e^+e^-$ *at the CERN* $\bar{p}p$ *Collider*, Phys.Lett.B129:130-140, 1983. (Cited on page 5.)

[46] S. Weinberg, *The making of the Standard Model*, Eur.Phys.J.C34:5-13, 2004 hep-ph/0401010. (Cited on page 5.)

[47] F. Englert, *Broken symmetry and Yang-Mills theory*, hep-th/0406162. (Cited on page 5.)

[48] J. Zinn-Justin, *Higgs Hunting 2010*, http://indico2.lal.in2p3.fr/indico/getFile.py/access?contribId=65&sessionId=10&resId=0&materialId=slides&confId=1109 (Cited on page 5.)

[49] L. Alvarez-Gaume and J. Ellis, *Eyes on a prize particle*, Nature Physics 7:2-3, 2011. (Cited on page 5.)

[50] M. Gell-Mann and M. Levy, *The axial vector current in beta decay*, Nuovo Cim.16:705, 1960. (Cited on page 7.)

[51] S. Elitzur, *Impossibility of Spontaneously Breaking Local Symmetries*, Phys.Rev.D12:3978-3982, 1975. (Cited on page 7.)

[52] A. Djouadi, *The Anatomy of electro-weak symmetry breaking I: The Higgs boson in the standard model*, Phys.Rept.457:1-216, 2008, hep-ph/0503172. (Cited on pages 12, 15 and 16.)

[53] J. Baglio, *Phenomenology of the Higgs at the hadron colliders: from the Standard Model to Supersymmetry*, thesis (2011). (Cited on page 12.)

[54] B.Lee, C. Quigg and H. Thacker, *Weak Interactions at Very High-Energies: The Role of the Higgs Boson Mass*, Phys.Rev.D16:1519, 1977. (Cited on page 12.)

[55] B.Lee, C. Quigg and H. Thacker, *The Strength of Weak Interactions at Very High-Energies and the Higgs Boson Mass*, Phys.Rev.Lett.38:883-885, 1977. (Cited on page 12.)

[56] D. Dicus and V. Mathur, *Upper bounds on the values of masses in unified gauge theories*, Phys.Rev.D7:3111-3114, 1973. (Cited on page 12.)

[57] M. Einhorn(ed), *The Standard Model Higgs Boson*, North Holland (1991). (Cited on page 12.)

[58] T. Hambye, K. Riesselmann, *Matching conditions and Higgs mass upper bounds revisited*, Phys.Rev.D55:7255-7262, 1997, hep-ph/9610272. (Cited on page 15.)

[59] J. Ellis, M. K. Gaillard and D. Nanopoulos, *A Phenomenological Profile of the Higgs Boson*, Nucl.Phys.B106:292, 1976. (Cited on pages 15 and 27.)

[60] NA31 Collaboration, *Search For A Neutral Higgs Particle In The Decay Sequence $K_L \to \pi^0 H^0$ and $H^0 \to e^+e^-$*, Phys.Lett.B235:356, 1990. (Cited on page 15.)

[61] LEP Working Group for Higgs boson searches and ALEPH and DELPHI and L3 and OPAL Collaborations, *Search for the standard model Higgs boson at LEP*, Phys.Lett.B565:61-75, 2003, hep-ex/0306033. (Cited on pages 16 and 17.)

[62] ALEPH Collaboration, *Final results of the searches for neutral Higgs bosons in e^+e^- collisions at $\sqrt{s}$ up to 209 GeV*, Phys.Lett.B526:191-205, 2002, hep-ex/0201014. (Cited on page 16.)

[63] The CDF Collaboration, the D0 Collaboration, the Tevatron New Physics, Higgs Working Group, *Updated Combination of CDF and D0 Searches for Standard Model Higgs Boson Production with up to $10.0 fb^{-1}$ of Data*, arXiv:1207.0449. (Cited on pages 16 and 18.)

[64] ATLAS Collaboration, *Combined search for the Standard Model Higgs boson in pp collisions at $\sqrt{s} = 7$ TeV with the ATLAS detector*, Phys.Rev.D86:032003, 2012, arXiv:1207.0319. (Cited on pages 17 and 18.)

[65] CMS Collaboration, *Combination of SM, SM4, FP Higgs boson searches*, CMS-PAS-HIG-12-008. (Cited on pages 17, 19, 29 and 30.)

[66] LEP Electroweak Working Group, http://lepewwg.web.cern.ch/LEPEWWG/ (Cited on pages 19 and 21.)

[67] Gfitter Collaboration, http://gfitter.desy.de/ (Cited on page 20.)

[68] A. De Roeck, R.S. Thorne, *Structure Functions*, Prog.Part.Nucl.Phys.66:727-781, 2011, arXiv:1103.0555 [hep-ph]. (Cited on pages 20 and 23.)

[69] R. Harlander, W.B. Kilgore, *Next-to-next-to-leading order Higgs production at hadron colliders*, Phys.Rev.Lett.88:201801, 2002, hep-ph/0201206. (Cited on page 21.)

[70] C. Anastasiou, K. Melnikov, *Higgs boson production at hadron colliders in NNLO QCD*, Nucl.Phys.B646:220-256, 2002, hep-ph/0207004. (Cited on page 21.)

[71] V. Ravindran, J. Smith, W.L. van Neerven, *NNLO corrections to the total cross-section for Higgs boson production in hadron hadron collisions*, Nucl.Phys.B665:325-366, 2003, hep-ph/0302135. (Cited on page 21.)

[72] S. Catani, D. de Florian, M. Grazzini, P. Nason, *Soft gluon resummation for Higgs boson production at hadron colliders*, JHEP.0307:028, 2003, hep-ph/0306211. (Cited on page 21.)

[73] LHC Higgs Cross Section Working Group (S. Dittmaier et al.) *Handbook of LHC Higgs Cross Sections: 1. Inclusive Observables*, CERN-2011-002, arXiv:1101.0593 [hep-ph]. (Cited on pages 21, 24, 25, 26 and 163.)

[74] https://twiki.cern.ch/twiki/bin/view/LHCPhysics/CrossSections (Cited on page 22.)

[75] J. Baglio and A. Djouadi, *Higgs production at the LHC*, JHEP.1103:055, 2011, arXiv:1012.0530 [hep-ph]. (Cited on page 22.)

[76] J.M. Butterworth, A.R. Davison, M. Rubin, G.P. Salam, *Jet substructure as a new Higgs search channel at the LHC*, Phys.Rev.Lett.100:242001, 2008, arXiv:0802.2470 [hep-ph]. (Cited on pages 23 and 25.)

[77] S. Dittmaier et al (ed), *Handbook of LHC Higgs Cross Sections: 2. Differential Distributions*, arXiv:1201.3084 [hep-ph]. (Cited on pages 24, 26, 28, 29 and 163.)

[78] A. Djouadi, J. Kalinowski, M. Spira, *HDECAY: A Program for Higgs boson decays in the standard model and its supersymmetric extension*, Comput.Phys.Commun.108:56-74, 1998, hep-ph/9704448. (Cited on page 24.)

[79] A. Bredenstein, A. Denner, S. Dittmaier, M.M. Weber, *Radiative corrections to the semileptonic and hadronic Higgs-boson decays* $H \to WW/ZZ \to 4$ *fermions*, JHEP.0702:080, 2007, hep-ph/0611234. (Cited on page 24.)

[80] S. Actis et al., *NLO Electroweak Corrections to Higgs Boson Production at Hadron Colliders*, Phys.Lett.B670:12-17, 2008, arXiv:0809.1301 [hep-ph]. (Cited on page 24.)

[81] S. Actis et al., *NNLO Computational Techniques: The Cases* $H \to \gamma\gamma$ *and* $H \to gg$, Nucl.Phys.B811:182-273, 2009, arXiv:0809.3667 [hep-ph]. (Cited on page 24.)

[82] C. Seez and J. Virdee, *Photon decay modes of the intermediate masss Higgs*, Large Hadron Collider Workshop, Aachen October 1990 (ed by G. Jarlskog and D. Rein), vol 2 report CERN 90-10 ECFA 90-133 page 474 (Cited on page 27.)

[83] L. Fayard and G. Unal, *Search for Higgs decay into photons with EAGLE*, ATL-PHYS-92-001. (Cited on page 27.)

[84] M. Mangano, *Production of* $WH \to W\gamma\gamma$, SSC-SDC-90-00113. (Cited on page 27.)

[85] J. Gunion et al., *Searching For The Intermediate Mass Higgs Boson*, Phys.Rev.D34:101, 1986. (Cited on page 27.)

[86] J. Gunion, G. Kane and J. Wudka, *Search Techniques for Charged and Neutral Intermediate Mass Higgs Bosons*, Nucl.Phys.B299:231, 1988. (Cited on page 27.)

[87] C. Barter et al., *Detection of $H \to \gamma\gamma$ at the SSC*, Proceedings of the Summer Study on HEP in the 1990's, june 1988, Snowmass, Colorado. (Cited on page 27.)

[88] L. Resnick, M.K. Sundaresan and P.J.S. Watson, *Is there a light scalar boson*, Phys.Rev.D8:172-178, 1973. (Cited on page 27.)

[89] M. Shifman, A. Vainshtein, M. Voloshin, and V. Zakharov, *Low-energy theorems for Higgs boson couplings to photons*, Sov.J.Nucl.Phys.30:711-716, 1979 [Yad.Fiz.30:1368-1378, 1979] (Cited on page 27.)

[90] P. Fayet, *Spontaneously Broken Supersymmetric Theories of Weak, Electromagnetic and Strong Interactions* Phys.Lett.B69:489, 1977. (Cited on page 28.)

[91] G. Farrar and P. Fayet, *Phenomenology of the Production, Decay, and Detection of New Hadronic States Associated with Supersymmetry*, Phys.Lett.B76:575-579, 1978. (Cited on page 28.)

[92] S. Martin, *A Supersymmetry primer*, hep-ph/9709356. (Cited on pages 28 and 29.)

[93] S. Weinberg, *Implications of Dynamical Symmetry Breaking*, Phys.Rev.D13:974-996, 1976, Phys.Rev.D19:1277-1280, 1979. (Cited on page 29.)

[94] L. Susskind, *Dynamics of Spontaneous Symmetry Breaking in the Weinberg-Salam Theory*, Phys.Rev.D20:2619-2625, 1979. (Cited on page 29.)

[95] G. Kribs, T. Plehn, M. Spannowsky and T. Tait, *Four generations and Higgs physics*, Phys.Rev.D76:075016, 2007, arXiv:0706.3718 [hep-ph]. (Cited on page 29.)

[96] S. Mrenna and J. Wells, *Detecting a light Higgs boson at the Fermilab Tevatron through enhanced decays to photon pairs*, Phys.Rev.D63:015006, 2001, hep-ph/0001226. (Cited on page 29.)

[97] https://twiki.cern.ch/twiki/bin/view/LHCPhysics/Fermiophobic (Cited on page 29.)

[98] CMS Collaboration, *Search for a fermiophobic Higgs boson in pp collisions at $\sqrt(s) = 7$ TeV*, arXiv:1207.1130 [hep-ex]. (Cited on pages 29 and 31.)

[99] G. Cowan, *Statistical Data Analysis* Clarendon Press, Oxford (Cited on page 33.)

[100] ATLAS and CMS Collaboration, *Procedure for the LHC Higgs boson search combination in summer 2011*, ATL-PHYS-PUB-2011-11, CMS-NOTE-2011/005 (Cited on page 35.)

[101] Frequentist limit recommendation in ATLAS https://twiki.cern.ch/twiki/pub/AtlasProtected/StatisticsTools/Frequentist_Limit_Recommendation.pdf (Cited on page 35.)

[102] ATLAS Collaboration, *Expected Performance of the ATLAS Experiment - Detector, Trigger and Physics*, arXiv:0901.0512 [hep-ex]. (Cited on pages 35, 77 and 107.)

[103] G. Cowan, K. Cranmer, E. Gross and O. Vitells, *Asymptotic formulae for likelihood-based tests of new physics*, Eur.Phys.J.C71:1554, 2011. (Cited on pages 37 and 43.)

[104] A. Read, *Presentation of search results: The CL_s technique*, J.Phys.G28:2693-2704, 2002. (Cited on page 38.)

[105] T. Junk, *Confidence level computation for combining searches with small statistics*, Nucl.Instrum.Meth.A434:435-443, 1999. (Cited on page 38.)

[106] G. Cowan, K. Cranmer, E. Gross and O. Vitells, *Power-Constrained Limits*, arXiv:1105.3166. (Cited on page 39.)

[107] S. Wilks, *The large-sample distribution of the likelihood ratio for testing composite hyptheses* Ann.Math.Stat.9: 60-62, 1938. (Cited on page 39.)

[108] N. Andari, Y. Fang, L. Fayard, M. Kado, Y. Pan, F. Polci, H. Wang and S.L. Wu, *Exclusion limits and Systematics*, ATL-COM-PHYS-2010-844. (Cited on page 40.)

[109] A. Wald, *Tests of statistical hypotheses concerning several parameters when the number of observations is large*, Trans.Am.Math.Soc.54(3):426-482, 1943. (Cited on page 43.)

[110] E. Gross and O. Vitells, *Trial factors or the look elsewhere effect in high energy physics*, Eur.Phys.J.C70:525-530, 2010. (Cited on pages 48 and 49.)

[111] A. Read, https://indico.cern.ch/getFile.py/access?contribId=83&sessionId=18&resId=0&materialId=slides&confId=162621 (Cited on page 49.)

[112] A. Read, *Private Communication* (Cited on pages 49 and 50.)

[113] O. Vitells, *ATLAS Higgs combination meeting of February 10th 2012*, https://indico.cern.ch/conferenceDisplay.py?confId=168555 (Cited on page 50.)

[114] A. Read, *Physics plenary meeting of June 29th 2012*, https://indico.cern.ch/getFile.py/access?contribId=4&resId=0&materialId=2&confId=197335 (Cited on page 50.)

[115] ATLAS Collaboration, *Observation of an excess of events inthe search for the Standard Model Higgs boson with the ATLAS detector at the LHC*, ATLAS-CONF-2012-093. (Cited on page 50.)

[116] ATLAS Collaboration, *Properties of the excess observed in the search for the Standard Model Higgs Boson*, ATL-COM-PHYS-2012-1053. (Cited on page 50.)

[117] ATLAS Collaboration, *Combined search for the Standard Model Higgs boson in pp collisions at $\sqrt{s} = 7$ TeV with the ATLAS detector*, arXiv:1207.0319 [hep-ex]. (Cited on page 50.)

[118] L. Evans and P. Bryant (ed), *LHC machine*, JINST 3:S08001, 2008. (Cited on page 51.)

[119] L. Evans, *The Large Hadron Collider (LHC)*, New J.Phys.9:335, 2007. (Cited on page 51.)

[120] L. Evans, *The Large Hadron Collider from conception to commissioning: A personal recollection*, Rev.Accel.Sci.Tech.3:261-280, 2010. (Cited on page 51.)

[121] *Large Hadron Collider in the LEP tunnel , proceedings of the ECFA-CERN workshop , Lausanne and Geneva (March 1984)*, ECFA 84/85 CERN 84-10. (Cited on page 51.)

[122] ATLAS Collaboration, *The ATLAS Experiment at the CERN Large Hadron Collider*, JINST 3:S08003, 2008. (Cited on pages 52, 69 and 71.)

[123] CMS Collaboration, *The CMS experiment at the CERN LHC*, JINST 3:P10007, 2008. (Cited on pages 52 and 74.)

[124] LHCb Collaboration, *The LHCb Detector at the LHC*, JINST 3:S08005, 2008. (Cited on page 52.)

[125] ALICE Collaboration, *The ALICE experiment at the CERN LHC*, JINST 3:S08002, 2008. (Cited on page 52.)

[126] LHCf Collaboration, *The LHCf detector at the CERN Large Hadron Collider*, JINST 3:S08006, 2008. (Cited on page 52.)

[127] TOTEM Collaboration, *The TOTEM experiment at the CERN Large Hadron Collider*, JINST 3:S08007, 2008. (Cited on page 52.)

[128] *HL-LHC: High Luminosity - Large Hadron Collider*, `http://hilumilhc.web.cern.ch/HiLumiLHC/index.html` (Cited on page 53.)

[129] S. Bertolucci, *presented at HCP 2011, Paris*, `http://indico.in2p3.fr/conferenceOtherViews.py?view=cdsagenda&confId=6004` (Cited on page 53.)

[130] S. Van der Meer, *Calibration of the effective beam height at the ISR*, ISR-PO/68-31 (June 1968). (Cited on page 54.)

[131] M. Heller, *Mesure de la luminosité absolue et de la section efficace totale proton-proton dans l'expérience ATLAS au LHC*, thesis (Université Paris-Sud 11), LAL 10-21 (March 2010). (Cited on page 54.)

[132] S. White, *Determination of the absolute luminosity at the LHC*, thesis (Université Paris-Sud 11), LAL 10-154 (September 2010). (Cited on page 54.)

[133] ATLAS Collaboration, *Luminosity Determination in pp Collisions at $\sqrt{s} = 7$ TeV Using the ATLAS Detector at the LHC*, Eur.Phys.J.C71:1630, 2011, arXiv:1101.2185 [hep-ex]. (Cited on page 54.)

[134] ATLAS Collaboration, *Luminosity Determination in pp Collisions at $\sqrt{s} = 7$ TeV using the ATLAS Detector in 2011*, ATLAS-CONF-2011-116. (Cited on page 54.)

[135] ATLAS Collaboration, *Improved Luminosity Determination in pp Collisions at $\sqrt{s} = 7$ TeV using the ATLAS Detector at the LHC*, ATLAS-CONF-2012-080. (Cited on page 54.)

[136] ATLAS public plots, `https://twiki.cern.ch/twiki/bin/view/AtlasPublic/LuminosityPublicResults` (Cited on pages 56, 57 and 59.)

[137] ATLAS event displays from 2010 and 2011 collision data, `https://twiki.cern.ch/twiki/bin/view/AtlasPublic/EventDisplayPublicResults` (Cited on page 58.)

[138] ATLAS Collaboration, *Performance of the ATLAS Inner Detector Track and Vertex Reconstruction in the high pile-up LHC Environment*, ATLAS-CONF-2012-042. (Cited on pages 60 and 62.)

[139] A. Andreazza, *Private Communication*. (Cited on page 62.)

[140] M. Hance, *Measurement of Inclusive isolated prompt photon production in proton-proton collisions at $\sqrt{s} = 7$ TeV with the ATLAS detector*, CERN-THESIS-2011-044. (Cited on pages 63 and 110.)

[141] ATLAS Collaboration, *Particle Identification Performance of the ATLAS Transition Radiation Tracker*, ATLAS-CONF-2011-128. (Cited on page 64.)

[142] D. Fournier, *Liquid Argon Calorimetry*, Large Hadron Collider Workshop, Aachen, October 1990, vol 3, CERN-90-10, ECFA90-133 page 356. (Cited on page 67.)

[143] M. Agustoni et al., *Electron energy scale in-situ calibration and performance*, ATL-COM-PHYS-2011-263. (Cited on pages 68, 77 and 87.)

[144] ATLAS Collaboration, *Electron performance measurements with the ATLAS detector using the 2010 LHC proton-proton collision data*, Eur.Phys.J.C72:1909, 2012, arXiv:1110.3174 [hep-ex]. (Cited on pages 68, 77, 93, 94 and 96.)

[145] egamma public plots, https://atlas.web.cern.ch/Atlas/GROUPS/PHYSICS/EGAMMA/PublicPlots/20100721/display-photons, (Cited on page 69.)

[146] C. Guyot et al., *The alignment of the barrel part of the ATLAS muon spectrometer*, ATL-MUON-PUB-2008-007. (Cited on page 72.)

[147] T. Tabrelli de Fatis, *Presentation at CALOR 2012*, http://indico.ads.ttu.edu/getFile.py/access?contribId=82&sessionId=4&resId=0&materialId=slides&confId=3 (Cited on page 75.)

[148] D. Froidevaux and P. Sphicas, *General-purpose detectors for the Large Hadron Collider*, Ann.Rev.Nucl.Part.Sci.56:375-440, 2006. (Cited on page 75.)

[149] W. Cleland and E. Stern, *Signal processing considerations for liquid ionization calorimeters in a high rate environment*, Nucl.Inst.Meth.A338: 467-497, 1974. (Cited on pages 77 and 82.)

[150] D. Banfi, L. Carminati and L. Mandelli, *Calibration of the ATLAS electromagnetic calorimeter using calibration hits*, ATL-LARG-PUB-2007-012. (Cited on page 77.)

[151] J. Colas et al., *Electronics calibration board for the ATLAS liquid argon calorimeters*, Nucl.Inst.Meth.A.593: 269-291, 2008. (Cited on page 80.)

[152] W. Lampl et al., *Digitization of LAr calorimeter for CSC simulations*, ATL-LARG-PUB-2007-011. (Cited on page 82.)

[153] M. Lechowski, *Test of the 'Little Higgs' model in ATLAS at LHC, and simulation of the digitization of the electromagnetic calorimeter*, CERN-THESIS-2005-042, LAL-05-20. (Cited on page 82.)

[154] T. Sjostrand, S. Mrenna and P. Skands, *PYTHIA 6.4 Physics and Manual*, JHEP.0605:026, 2006. (Cited on page 88.)

[155] ATLAS Collaboration, *Electron and photon reconstruction and identification in ATLAS: expected performance at high energy and results at* 900 *GeV*, ATLAS-CONF-2010-005. (Cited on page 88.)

[156] J. Birks, *The theory and Practice of Scintillation Counting*, Pergamon, 1964. (Cited on page 89.)

[157] J. Apostolakis et al., *Private Communication.* (Cited on page 92.)

[158] ICARUS Collaboration, *Study of electron recombination in liquid argon with the ICARUS TPC*, Nucl.Inst.Meth.A.523: 275-286, 2004. (Cited on page 92.)

[159] L. Carminati, *egamma meeting of may 24th 2012*, https://indico.cern.ch/getFile.py/access?contribId=3&resId=1&materialId=slides&confId=163471 (Cited on pages 94 and 97.)

[160] egamma public plot, https://atlas.web.cern.ch/Atlas/GROUPS/PHYSICS/EGAMMA/PublicPlots/20120611/StabilityPlots/ATL-COM-PHYS-2012-782/index.html (Cited on pages 95 and 97.)

[161] egamma public plot, https://atlas.web.cern.ch/Atlas/GROUPS/PHYSICS/EGAMMA/PublicPlots/20121403/StabilityPlots/ATL-COM-PHYS-2012-259/index.html (Cited on pages 95 and 98.)

[162] egamma public plot, https://atlas.web.cern.ch/Atlas/GROUPS/PHYSICS/EGAMMA/PublicPlots/20110512/CalibratedZee/ATL-COM-PHYS-2011-1637/index.html (Cited on pages 95 and 99.)

[163] ATLAS Collaboration, *Expected photon performance in the ATLAS experiment*, ATL-PHYS-PUB-2011-007. (Cited on pages 102 and 106.)

[164] L. Carminati et al., *Reconstruction and Identification Efficiency of Inclusive Isolated Photons*, ATL-PHYS-INT-2011-014. (Cited on page 102.)

[165] J-F. Marchand, *Etude de la recherche du boson de higgs en deux photons dans l'expérience atlas au LHC et calibration du calorimètre à argon liquide*, CERN-THESIS-2009-127, LAPP-T-2009-001. (Cited on page 102.)

[166] J-F. Marchand, *Private Communication* (Cited on page 103.)

[167] egamma public plot, https://atlas.web.cern.ch/Atlas/GROUPS/PHYSICS/EGAMMA/PublicPlots/20120620/PhotonRecoStability/ATL-COM-PHYS-2012-823/index.html (Cited on pages 102 and 104.)

[168] H. Abreu, *Measurement of the inclusive prompt photon cross section and preparation of the search of the Higgs boson decaying into two photons with the ATLAS detector at the LHC*, CERN-THESIS-2011-157. (Not cited.)

[169] G. Unal, *egamma meeting of march 28th 2012* https://indico.cern.ch/getFile.py/access?contribId=1&resId=0&materialId=slides&confId=163462 (Cited on page 106.)

[170] G. Unal, *egamma meeting of may 8th 2012* https://indico.cern.ch/getFile.py/access?contribId=5&resId=0&materialId=slides&confId=163468 (Cited on page 106.)

[171] J. Saxon, *egamma meeting of may 16th 2012* https://indico.cern.ch/getFile.py/access?contribId=5&resId=0&materialId=slides&confId=163469 (Cited on pages 106, 107 and 120.)

[172] ATLAS Collaboration, *Search for the Standard Model Higgs boson in the two photon decay channel with the ATLAS detector at the LHC*, Phys.Lett.B705:452-470, 2011, arXiv:1108.5895 [hep-ex]. (Cited on pages 106 and 126.)

[173] ATLAS Collaboration, *Search for the Standard Model Higgs boson in the diphoton decay channel with 4.9 fb^{-1} of pp collisions at $\sqrt{s} = 7$ TeV with ATLAS*, Phys.Rev.Lett.108:111803, 2012, arXiv:1202.1414 [hep-ex]. (Cited on pages 106, 126, 152, 155 and 177.)

[174] ATLAS Collaboration, *Observation of an excess of events in the search for the Standard Model Higgs Boson in the gamma gamma channel with the ATLAS detector*, ATLAS-CONF-2012-091. (Cited on pages 107, 118, 156, 158, 159, 160, 163, 165, 166 and 167.)

[175] ATLAS Collaboration, *Signal studies for $H \to \gamma\gamma$*, ATL-COM-PHYS-2012-501. (Cited on pages 107, 125, 126 and 163.)

[176] J. Saxon, *HSG1 workshop of november 24th 2011*, https://indico.cern.ch/getFile.py/access?contribId=26&sessionId=1&resId=0&materialId=2&confId=153698 (Cited on page 107.)

[177] ATLAS Collaboration, *Measurement of the inclusive isolated prompt photon cross section in pp collisions at $\sqrt{s} = 7$ TeV with the ATLAS detector*, Phys.Rev.D83:052005, 2011, arXiv:1012.4389 [hep-ex]. (Cited on pages 107 and 114.)

[178] M. Escalier et al., *Photon/jet separation with DC1 data*, ATL-PHYS-PUB-2005-018. (Cited on page 108.)

[179] M. Escalier, *Recherche expérimentale de la brisure spontanée de symetrie electrofaible dans le canal $H \to \gamma\gamma$ et d'une solution au problème de hiérarchie dans ATLAS*, Participation à la préparation de l'électronique du calorimètre electromagnétique, thèse Université de Paris Sud, numéro 7855. (Cited on page 108.)

[180] G. Corcella et al., *HERWIG 6: An Event generator for hadron emission reactions with interfering gluons (including supersymmetric processes)*, JHEP.0101:010, 2001. (Cited on page 108.)

[181] J. Tanaka, *Study of Systematic Uncertainty of Fake Photon Estimation: Difference Coming from MC Event Generators*, ATL-COM-PHYS-2009-420. (Cited on page 108.)

[182] M. Cacciari, G. Salam and G. Soyez, *The Catchment Area of Jets*, JHEP.0804:005, 2008, arXiv:0802.1188 [hep-ph]. (Cited on page 110.)

[183] M. Cacciari, G. Salam and S. Sapeta, *On the characterisation of the underlying event*, JHEP.1004:065, 2010, arXiv:0912.4926 [hep-ph]. (Cited on page 110.)

[184] W. Lampl, *Calorimeter Clustering Algorithms: Description and Performance*, ATL-LARG-PUB-2008-002. (Cited on page 110.)

[185] S. Laplace and J.B de Vivie, *Calorimeter isolation and pile-up*, ATL-COM-PHYS-2012-467. (Cited on pages 110 and 111.)

[186] ATLAS Collaboration, *Evidence for prompt photon production in pp collisions at $\sqrt{s} = 7$ TeV with the ATLAS detector*, ATLAS-CONF-2010-077. (Cited on pages 112 and 114.)

[187] N. Andari, *Plot of p_T/E_T for converted photons for approval*, ATL-COM-PHYS-2010-527. (Cited on page 115.)

[188] egamma public plot, `https://atlas.web.cern.ch/Atlas/GROUPS/PHYSICS/EGAMMA/PublicPlots/20100721/pTETConvertedPhotons/index.html` (Cited on page 115.)

[189] ATLAS Collaboration, *Background studies for $H \to \gamma\gamma$*, ATLAS-COM-PHYS-2011-782. (Cited on page 117.)

[190] ATLAS Collaboration, *Measurement of the isolated di-photon cross-section in pp collisions at $\sqrt{s} = 7$ TeV with the ATLAS detector*, Phys.Rev.D85.012003, 2012, arXiv:1107.0581. (Cited on page 117.)

[191] F. Alonso et al., *Background studies for the search of Higgs boson decaying to two photons with 4.9 fb^{-1} with the ATLAS experiment*, ATL-COM-PHYS-2012-515. (Cited on page 117.)

[192] F. Alonso et al., *Background study for $H \to \gamma\gamma$ with 8 TeV data*, ATL-COM-PHYS-2012-754. (Cited on page 117.)

[193] ATLAS Collaboration, *Measurements of the photon identification efficiency with the ATLAS detector using 4.9 fb^{-1} of pp collision data collected in 2011*, ATL-COM-PHYS-2012-123. (Cited on page 121.)

[194] K. Liu et al., *Measurement of the identification efficiency of isolated prompt photons using radiative $Z \to ll\gamma$ decays in 4.9 fb^{-1} of ATLAS data*, ATL-COM-PHYS-2012-382. (Cited on page 122.)

[195] M. Jimenez and K. Tackmann, *Photon identification efficiency extrapolated from electrons in $Z \to e^+e^-$ decays*, ATL-COM-PHYS-2012-241. (Cited on page 122.)

[196] K. Liu et al., *Measurement of the identification efficiency of isolated prompt photons using the matrix method and 4.9 fb^{-1} of ATLAS data*, ATL-COM-PHYS-2012-242. (Cited on page 122.)

[197] A. Bocci and F. Hubaut, *egamma meeting of june 7th 2012*, https://indico.cern.ch/getFile.py/access?contribId=0&resId=0&materialId=slides&confId=163472 (Cited on page 126.)

[198] M. Delmastro, *egamma meeting of may 30th 2012*, https://indico.cern.ch/getFile.py/access?contribId=2&resId=0&materialId=slides&confId=163471 (Cited on page 126.)

[199] ATLAS Collaboration, *Signal studies for $H \to \gamma\gamma$ 8 TeV* , ATL-COM-PHYS-2012-755. (Cited on page 126.)

[200] ATLAS Collaboration, *Measurement of the backgrounds to the $H \to \gamma\gamma$ search and reappraisal of its sensitivity with 37 pb^{-1} of data recorded by the ATLAS detector*, ATLAS-CONF-2011-004. (Cited on page 127.)

[201] ATLAS Collaboration, *Study of the Di-Photon Backgrounds to the $H \to \gamma\gamma$ Search with the ATLAS detector at $\sqrt{s} = 7$ TeV*, ATLAS-PHYS-INT-2011-011. (Cited on page 127.)

[202] ATLAS Collaboration, *Search for the Higgs boson in the diphoton final state with 38 pb^{-1} of data recorded by the ATLAS detector in proton-proton collisions at $\sqrt{s} = 7$ TeV*, ATLAS-CONF-2011-025. (Cited on page 131.)

[203] ATLAS Collaboration, *Search for the Higgs boson in the diphoton final state with 38 pb^{-1} of data recorded by the ATLAS detector at $\sqrt{s} = 7$ TeV*, ATLAS-PHYS-INT-2011-024. (Cited on page 131.)

[204] G. Unal, *HSG1 meeting of december 4th 2011*, https://indico.cern.ch/getFile.py/access?contribId=5&resId=0&materialId=2&confId=125835 (Cited on page 135.)

[205] N. Lorenzo, *HSG1 meeting of february 2nd 2011*, https://indico.cern.ch/getFile.py/access?contribId=4&resId=0&materialId=slides&confId=127678 (Cited on page 135.)

[206] ATLAS Collaboration, *Search for the Higgs Boson in the Diphoton Channel with the ATLAS Detector using 209 pb^{-1} of 7 TeV Data taken in 2011*, ATLAS-CONF-2011-085. (Cited on pages 136 and 176.)

[207] ATLAS Collaboration, *Search for Higgs boson decays in two photons with early 2011 data*, ATL-COM-PHYS-2011-515. (Cited on pages 136 and 142.)

[208] M. Escalier, L. Fayard and J-F. Marchand, *Reconstruction of the z vertex and direction of the photon*, ATL-PHYS-INT-2010-013. (Cited on page 137.)

[209] G. Unal, *HSG1 meeting of may 12th 2011*, https://indico.cern.ch/getFile.py/access?contribId=14&resId=0&materialId=slides&confId=130231 (Cited on pages 141 and 142.)

[210] J-F. Marchand and E. Scifo, *Oscillation of calorimeter pointing z position as a function of pseudo-rapidity in the end-cap*, ATL-COM-CAL-2012-003. (Cited on pages 141 and 153.)

[211] ATLAS Collaboration, *Search for the Standard Model Higgs boson in the two photon decay channel with the ATLAS detector at the LHC*, Phys.Lett.B705:452-470, 2011, arXiv:1108.5895v2 [hep-ex]. (Cited on pages 142 and 176.)

[212] S. Frixione, P. Nason and C. Oleari, *Matching NLO QCD computations with Parton Shower simulations: the POWHEG method*, JHEP.0711:070, 2007. (Cited on page 144.)

[213] ATLAS Collaboration, *Signal studies for $H \to \gamma\gamma$*, ATL-COM-PHYS-2011-781. (Cited on pages 147, 148 and 151.)

[214] G. Bozzi, S. Catani, D. de Florian and M. Grazzini, *Transverse-momentum resummation and the spectrum of the Higgs boson at the LHC*, Nucl.Phys.B737:73-120, 2006. (Cited on page 147.)

[215] T. Binoth, J.P. Guillet, E. Pilon and M. Werlen, *A Full next-to-leading order study of direct photon pair production in hadronic collisions*, Eur.Phys.J.C16:311-330, 2000. (Cited on page 152.)

[216] ATLAS Collaboration, *Search for the Standard Model Higgs boson in the diphoton decay channel with 4.9 fb^{-1} of ATLAS data at $\sqrt{s} = 7$ TeV*, ATLAS-CONF-2011-161. (Cited on page 152.)

[217] ATLAS Collaboration, *Search for the Higgs boson decaying to two photons with 4.9 fb^{-1}*, ATL-COM-PHYS-2011-1748. (Cited on page 154.)

[218] L. Dixon and M. Siu, *Resonance continuum interference in the diphoton Higgs signal at the LHC*, Phys.Rev.Lett.90:252001, 2003. (Cited on pages 154 and 212.)

[219] M. Kado and N. Lorenzo Martinez, *Impact of the destructive interference between continuum background and $gg \to H\gamma\gamma$ process on the $H \to \gamma\gamma$ signal yield*, ATL-COM-PHYS-2012-1174. (Cited on page 154.)

[220] M. Kado, N. Lorenzo Martinez and G. Unal, *Energy scale uncertainties for $H \to \gamma\gamma$*, ATL-COM-PHYS-2012-077. (Cited on page 156.)

[221] F. Gianotti on behalf of the ATLAS Collaboration, *CERN seminar of july 4th 2012*, `https://indico.cern.ch/conferenceDisplay.py?confId=164890` (Cited on pages 156 and 165.)

[222] ATLAS Collaboration, *Observation of a new particle in the search for the Standard Model Higgs boson with the ATLAS detector at the LHC*,

Phys.Lett.B716:1-29, 2012, arXiv:1207.7214v1 [hep-ex]. (Cited on pages 156, 158, 165, 173, 178, 190, 200, 201, 204, 205, 206, 207, 209, 214, xxi, xxii, xxiii and xxiv.)

[223] I. Koletsou, *Recherche du boson de Higgs dans le canal diphoton au LHC avec le detecteur ATLAS*, CERN-THESIS-2008-047. (Cited on page 158.)

[224] ATLAS Collaboration, *Update of $H \to \gamma\gamma$ analysis for the July paper*, ATL-COM-PHYS-2012-1207. (Cited on pages 158 and 165.)

[225] I. Stewart and F. Tackmann, *Theory Uncertainties for Higgs and Other Searches Using Jet Bins*, Phys.Rev.D85.034011, 2012. (Cited on page 164.)

[226] E. Petit, *HSG1 meeting of may 17th 2012*, https://indico.cern.ch/getFile.py/access?contribId=3&resId=0&materialId=slides&confId=166247 (Cited on page 164.)

[227] J. Campbell, K. Ellis and C. Williams, *Vector boson pair production at the LHC*, JHEP.1107:018, 2011. (Cited on page 164.)

[228] C. Balazs, E. Berger, P. Nadolsky and C-P. Yuan, *Calculation of prompt diphoton production cross-sections at Tevatron and LHC energies*, Phys.Rev.D76:013009, 2007. (Cited on page 184.)

[229] T. Gleisberg, S. Hoeche, F. Krauss, M. Schonherr, S. Schumann, F. Siegert and J. Winter, *Event generation with SHERPA 1.1*, JHEP.0902:007, 2009. (Cited on page 184.)

[230] O. Silbert, *statistics forum meeting of december 19th 2011*, https://indico.cern.ch/getFile.py/access?contribId=3&resId=0&materialId=slides&confId=164826 (Cited on pages 189 and 190.)

[231] B. Murray, *Implications of LHC results on march 28th 2012*, https://indico.cern.ch/getFile.py/access?contribId=6&resId=1&materialId=slides&confId=183986 (Cited on page 193.)

[232] N. Berger, *HSG1 sharepoint*, https://espace.cern.ch/atlas-phys-higgs-htogamgam/Lists/ICHEP8TeV2012/Attachments/48/bias.pdf (Cited on page 193.)

[233] L.D. Landau, *On the angular momentum of a system of two photons*, Dokl.Akad.Nawk.USSR60: 207, 1948. (Cited on page 203.)

[234] C.N. Yang, *Selection Rules for the Dematerialization of a particle into two photons*, Phys.Rev77: 242, 1950. (Cited on page 203.)

[235] S. Bolognesi, *ICHEP 2012 on July 7th 2012*, https://indico.cern.ch/getFile.py/access?contribId=473&sessionId=53&resId=0&materialId=slides&confId=181298 (Cited on page 203.)

[236] S. Bolognesi et al., *On the spin and parity of a single-produced resonance at the LHC*, arXiv:1208.4018 [hep-ph]. (Cited on page 203.)

[237] CMS Collaboration, *Observation of a new boson at a mass of* 125 *GeV with the CMS experiment at the LHC*, Phys.Lett.B716:30-61, 2012, arXiv:1207.7235 [hep-ex]. (Cited on pages 209, 214, 217 and 218.)

[238] CMS Collaboration, *Evidence for a new state decaying into two photons in the search for the standard model Higgs boson in pp collisions*, CMS PAS HIG-12-015. (Cited on pages 209, 212, 213 and 214.)

[239] K. Tackmann, *Higgs meeting of July 17th 2012*, https://indico.cern.ch/getFile.py/access?contribId=0&resId=0&materialId=slides&confId=199655 (Cited on page 214.)

[240] G. Unal, *Workshop Higgs Hunting 2012* , http://indico2.lal.in2p3.fr/indico/getFile.py/access?contribId=40&sessionId=1&resId=0&materialId=slides&confId=1747 (Cited on page 214.)

[241] S. Ganjour, *ICHEP 2012, July 7th 2012*, https://indico.cern.ch/getFile.py/access?contribId=431&sessionId=53&resId=0&materialId=slides&confId=181298 (Cited on page 216.)

Appendix

In the following are listed the invariant mass distributions of the selected diphoton events. The full 7 TeV dataset corresponding to an integrated luminosity of 4.8 fb^{-1} and the 8 TeV dataset corresponding to 5.9 fb^{-1} are shown separately. The analyses were described in sections 6.3 and 6.4. The distributions are given per category: "Unconverted central, low p_{Tt}", "Unconverted central, high p_{Tt}", "Unconverted rest, low p_{Tt}" and "Unconverted rest, high p_{Tt}", "Converted central, low p_{Tt}", "Converted central, high p_{Tt}", "Converted rest, low p_{Tt}" and "Converted rest, high p_{Tt}", "Converted transition" and "2-jet". A background-only fit is overlaid. The BEH boson expectation for a mass hypothesis of 126.5 GeV corresponding to the SM cross section is also shown.

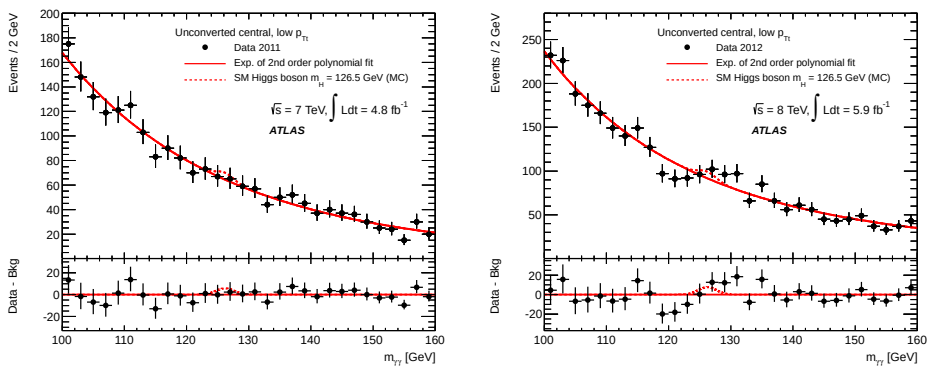

Figure 6: Background-only fits to the diphoton invariant mass spectra for categories "Unconverted central, low p_{Tt}", for $\sqrt{s} = 7$ TeV data sample on the left and $\sqrt{s} = 8$ TeV data sample on the right. The bottom inset displays the residual of the data with respect to the background fit. The BEH boson expectation for a mass hypothesis of 126.5 GeV corresponding to the SM cross section is also shown [222].

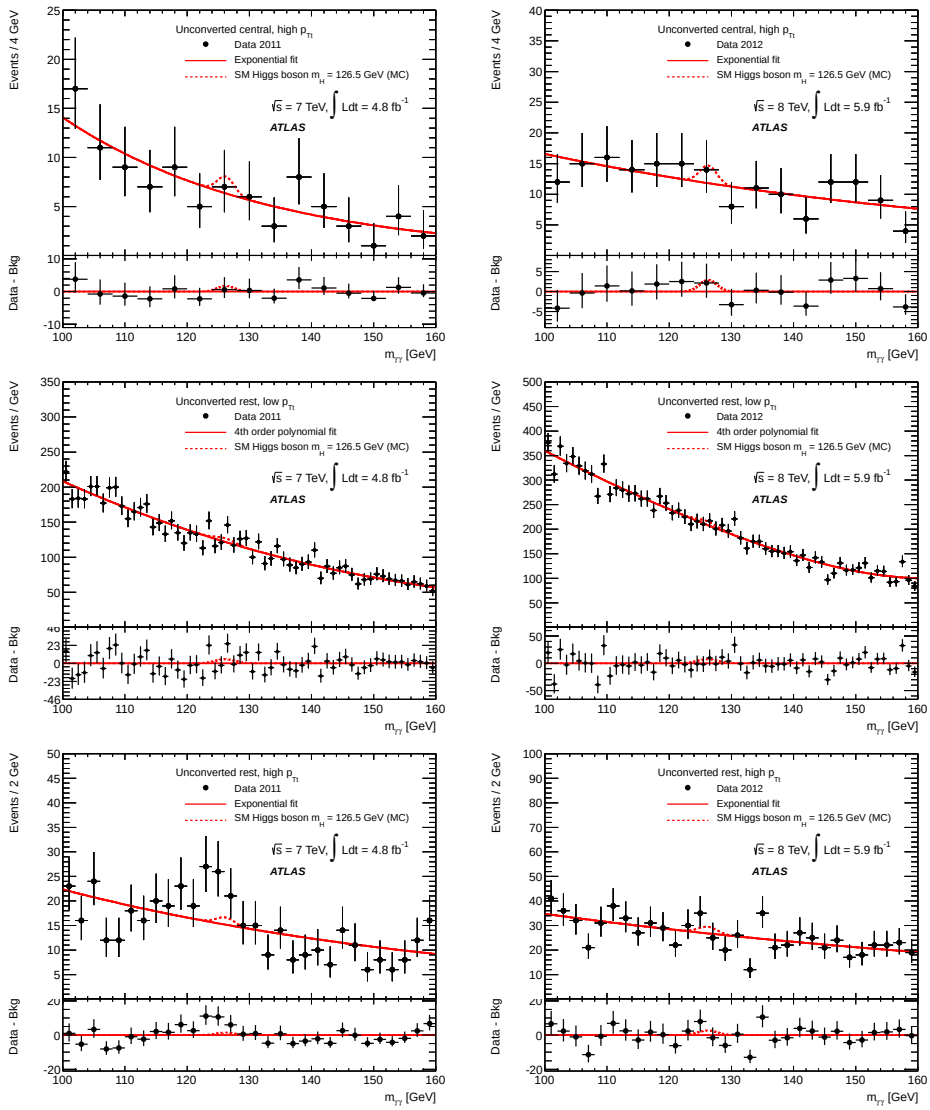

Figure 7: Background-only fits to the diphoton invariant mass spectra for categories "Unconverted central, high p_{Tt}", "Unconverted rest, low p_{Tt}" and "Unconverted rest, high p_{Tt}", for $\sqrt{s} = 7$ TeV data sample on the left and $\sqrt{s} = 8$ TeV data sample on the right. The bottom inset displays the residual of the data with respect to the background fit. The BEH boson expectation for a mass hypothesis of 126.5 GeV corresponding to the SM cross section is also shown [222].

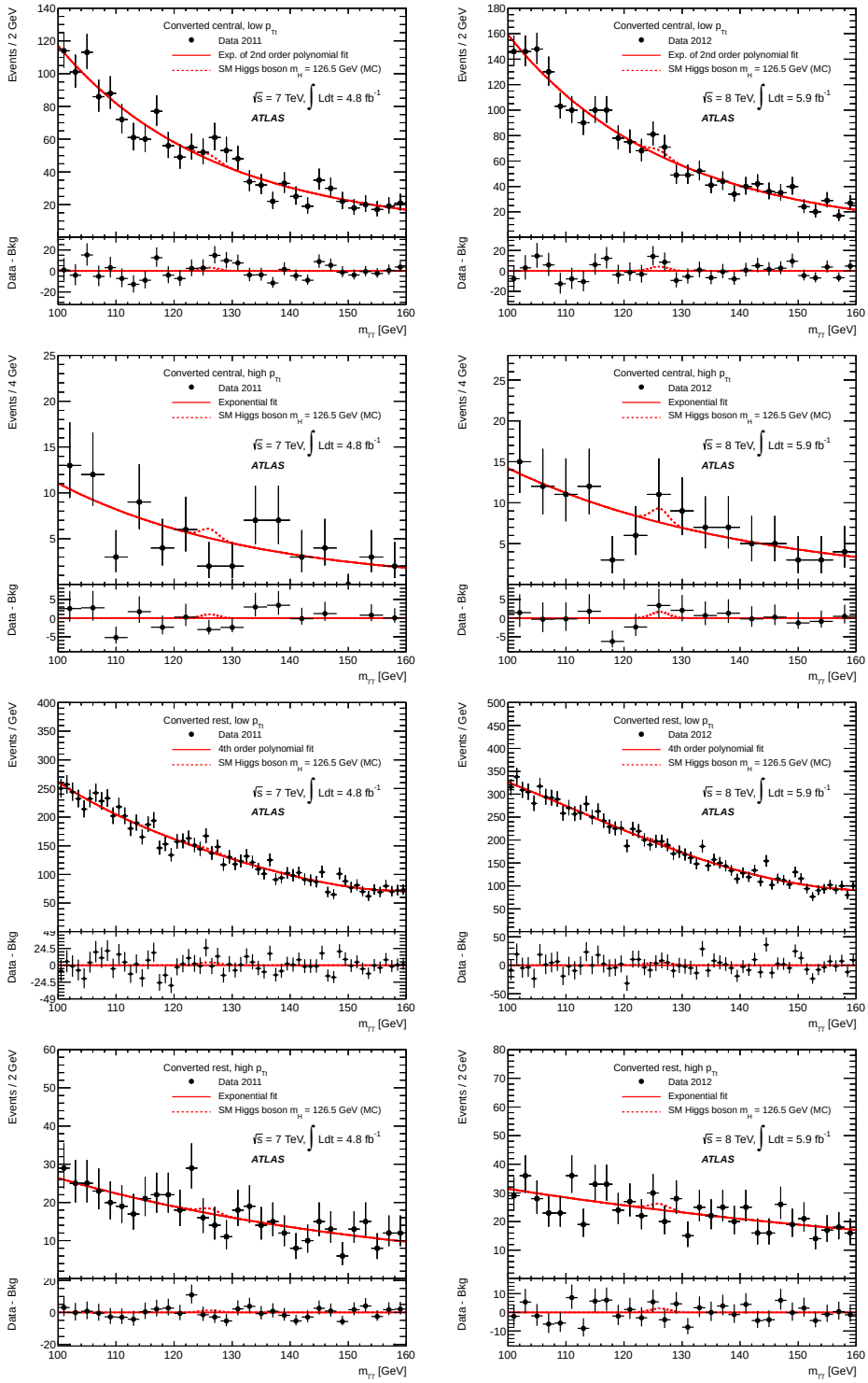

Figure 8: Background-only fits to the diphoton invariant mass spectra for categories "Converted central, low p_{Tt}", "Converted central, high p_{Tt}", "Converted rest, low p_{Tt}" and "Converted rest, high p_{Tt}", for $\sqrt{s} = 7$ TeV data sample on the left and $\sqrt{s} = 8$ TeV data sample on the right. The bottom inset displays the residual of the data with respect to the background fit. The BEH boson expectation for a mass hypothesis of 126.5 GeV corresponding to the SM cross section is also shown [222].

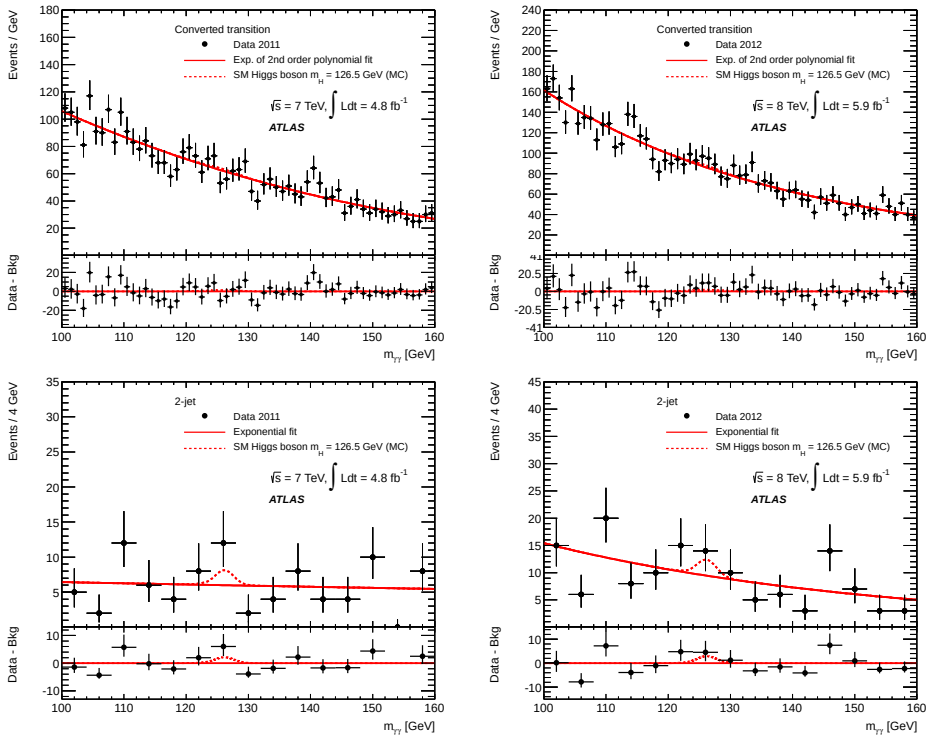

Figure 9: Background-only fits to the diphoton invariant mass spectra for categories "Converted transition" and "2-jet", for $\sqrt{s} = 7$ TeV data sample on the left and $\sqrt{s} = 8$ TeV data sample on the right. The bottom inset displays the residual of the data with respect to the background fit. The BEH boson expectation for a mass hypothesis of 126.5 GeV corresponding to the SM cross section is also shown [222].

Remerciements

Tout d'abord, je voudrais remercier Monsieur L. Fayard, qui avait dirigé ma thèse pendant trois années. Depuis mon stage du Master II jusqu'à la fin de la thèse, vous étiez toujours disponible pour moi, tous les jours et toutes les heures. Je ne peux évidemment vous remercier par quelques simples mots ni pour tout le temps que vous m'avez consacré ni pour tout ce que vous m'avez appris. Vous m'avez aidé dans ce trajet depuis le tout début. Vous m'avez appris la vie d'un chercheur, moi qui suis arrivée chez vous une étudiante qui avait l'habitude de trouver les réponses en cherchant dans les livres. Vous m'avez appris la méthodologie du travail et la vraie Physique: depuis les bases de la Physique fondamentale jusqu'à la Physique des collisionneurs, la Physique des détecteurs, la Physique hadronique et la Statistique. Vous m'avez appris à analyser, à chercher la précision dans les détails et à acquérir une curiosité de connaître. J'ai toujours admiré en vous la sensation que vous avez des "bugs" et surtout les idées originales que vous avez. J'ai beaucoup appris avec vous et je vous suis très reconnaissante pour tout. Je vous remercie aussi de m'avoir présenté à toutes les personnes que je connais actuellement dans le domaine. Je vous remercie de m'avoir appris à vivre et à travailler dans une collaboration et surtout "à essayer de ne regarder que le côté positif des gens". Vous n'étiez pas qu'un directeur de thèse, vous étiez un proche sur qui je pouvais compter pour n'importe quel type de problème. Je vous remercie de m'avoir supportée toutes ces années. Je souhaite à tous les prochains thésards d'avoir un directeur de thèse comme le mien.

Ensuite, je tiens à remercier très particulièrement Monsieur G. Unal. Sans toi Guillaume non plus, ma thèse n'aurait pas eu lieu, tu étais la clé de ma motivation. J'ai eu la plus grande chance pendant ma thèse de ne jamais s'inquiéter pour une question: je savais toujours que quelque soit le niveau de difficulté, j'aurai une réponse toujours correcte en te la posant. Je te remercie pour tout ce que tu m'as appris et tout ce que tu m'as expliqué (en répétant même plusieurs fois). Je te remercie pour ta disponibilité, je ne me rappelle pas d'un jour où tu n'étais pas là quand j'en avais besoin. Je te remercie également pour les discussions infinies et pour tous les conseils que tu m'as donnés. Je te suis très reconnaissante pour le temps que je t'avais pris, pour tous les mots d'encouragement, pour le soutien moral, pour ton extrême gentillesse et pour ta franchise. Je te remercie surtout d'avoir lu et corrigé ma thèse en entier! Merci pour tout!

Je voudrais remercier Messieurs G. Wormser et A. Stocchi pour m'avoir accueillie au laboratoire. Je remercie tout le service administratif du laboratoire, en particulier Sylvie, le service informatique en particulier Gérard et Damien et

le service des missions pour la gentillesse de ses dames. Je remercie Geneviève et Françoise pour leur soutien et encouragement. Je remercie le CNRS à l'origine de mon financement pendant ces trois années. Je remercie également le service administratif de l'Université Paris XI et de l'Ecole Doctorale. En particulier, je tiens à remercier Monsieur E. Khan. Je souhaite aussi remercier mon parrain de thèse Monsieur N. Delerue pour son soutien et ses conseils.

Je remercie également tous les membres du jury: Messieurs G. Cowan, L. Fayard, F. Englert, A. Stocchi, G. Unal, P. Verdier et T. Virdee. Que vous avez accepté de juger ma thèse m'est un grand honneur! Je remercie très particulièrement Monsieur F. Englert, sans vous on n'aurait pas eu de quoi chercher et Monsieur T. Virdee à l'origine des analyses de la désintégration du boson scalaire en paire de photons au LHC. Je remercie Messieurs G. Cowan et P. Verdier d'avoir accepté d'être rapporteurs de ma thèse: j'apprécie beaucoup le temps que vous avez pris à lire le manuscrit, merci pour vos corrections, vos commentaires et surtout pour votre patience et pour votre soutien.

Je tiens à remercier très particulièrement Monsieur R. Stora: je vous remercie pour les heures que vous avez passées à m'expliquer le phénomène de la brisure spontanée de la symétrie dans le cadre du Modèle Standard. Je vous remercie pour les lettres que vous m'aviez envoyées avec des explications détaillées, je vous remercie surtout d'avoir pris le temps de corriger mon chapitre théorique. Merci beaucoup pour votre gentillesse, pour ce que vous m'avez appris, pour votre soutien et pour votre encouragement! Je remercie également Monsieur J. Iliopoulos pour les explications très pédagogiques et les connaissances que vous m'avez apportées. Je remercie de même Monsieur J. Zinn-Justin pour les discussions très intéressantes.

J'aimerai exprimer ma gratitude à toute l'équipe ATLAS LAL. Très particulièrement, je voudrais remercier Monsieur M. Kado. Marumi, je vous remercie pour toutes les explications très pédagogiques, vous êtes *Le Professeur* du groupe. Je vous remercie pour toutes ces séances de discussions, pour tout ce que vous m'avez appris. Je vous dois la majorité de mes connaissances en Statistique. Merci d'avoir partagé vos idées toujours trés originales et votre très vaste connaissance. Je vous remercie surtout pour votre soutien, votre écoute pendant les moments difficiles, vos conseils et bien sûr pour votre extrême gentillesse. J'admire en vous la capacité de conviction, d'encouragement ainsi que votre optimisme. Merci d'avoir été pendant toutes ces années aussi la Sagesse de notre groupe!

Je remercie également Madame L. Fayard, merci pour votre patience, votre soutien et votre encouragement. J'ai beaucoup apprécié vos conseils pendant toute cette période. Je vous remercie pour votre aide particulièrement pendant les derniers jours avant la soutenance. Je remercie de même Monsieur D. Fournier, merci pour votre encouragement et votre guidance surtout pendant les derniers mois de la thèse. Grand merci pour le temps que vous avez mis à corriger les

premiers chapitres de ma thèse. Je dois aussi mes grands remerciements à Marc Escalier, merci pour tes aides, tes commentaires et surtout pour les “débuggages” de codes.

Je remercie également Francesco Polci qui a dirigé aussi mon stage et le début de ma thèse. Je te remercie pour ce que tu m’avais appris et pour ta gentillesse. Merci Jean-François Marchand pour ton aide, ta sympathie et tes conseils. Je remercie beaucoup Nicolas Berger, merci pour ton extrême gentillesse, ton soutien et ton encouragement surtout vers la fin de la thèse. Je te remercie aussi pour ton aide et ce que tu m’as appris durant nos discussions de Statistique. Special thanks to Aaron Armbruster and Haichen Wang for your help and the very useful discussions. I thank as well Junichi Tanaka for guiding our group in this last difficult year, thank you for your patience and your kindness. Many thanks to Alex Read and Kyle Cranmer for your help, your answers and your support. In particular, I thank Kerstin Tackmann, thank you for your kindness, your support and for summarizing such incredibly all the work done in the ICHEP conference note. Je remercie de même Madame S. Poulat pour votre aide pendant les mois les plus difficiles. Finally, I thank James Burkett for making many of my sentences english correct and especially for your friendship, I appreciate it a lot!

Mes chaleureux remerciements à mes collègues au laboratoire pour votre soutien et votre amitié: Karim, Narei, Marthe, Driss, Clément, Sébastien, Estelle et notre amie Pauline, Henso, Jean-Baptiste (les trois), Adrien, Lan et Samah. J’ai beaucoup apprécié de travailler avec vous aussi et j’espère qu’on aura maintenant plus d’occasions pour les sorties. Je souhaite également remercier mes collègues du Master de Physique théorique à l’ENS pour votre soutien et votre amitié Micha, Emmanuel (les deux), Bruno et Nicolas. Je remercie mes amis au Liban, en particulier Peter. Je remercie aussi mes amis libanais en France, en particulier Céline, Garabed, Samer, Wissam (mon ami de plus de 10 ans), vous m’étiez un grand support et bien sûr grand merci aussi pour Houssam qui était toujours là ces deux dernières années, merci pour tout ce que vous avez fait pour moi.

Je remercie mes professeurs à l’Université Libanaise, en particulier Messieurs J. Bechara et N. Kallas. Mes plus chers remerciements à mes premiers professeurs qui m’ont accompagné depuis le “petit jardin” à l’école maternelle Bon Pasteur jusqu’à ce jour-ci: Mesdemoiselles Rose-Marie et Reina, merci pour votre support et votre amour! Je vous aime beaucoup! Je remercie ma famille au Liban et en Russie, en particulier ma chère tante Reguina.

Finalement, je ne peux sans remercier les trois personnes grâce à qui j’ai pu faire la moindre chose de ma vie: papa, maman et ma soeur. Là, les remerciements dépassent les mots. Vous êtes toute ma vie!